MODELING INTERFACIAL SLAG LAYER PHENOMENA IN THE SHELL/MOLD GAP IN CONTINUOUS CASTING OF STEEL

BY

YA MENG

B.S., Central South University of Technology, 1995
M.E.N.G.R., Central South University of Technology, 1998

DISSERTATION

Submitted in partial fulfillment of the requirements
for the degree of Doctor of Philosophy in Materials Science and Engineering
in the Graduate College of the
University of Illinois at Urbana-Champaign, 2004

Urbana, Illinois

ABSTRACT

Heat transfer and lubrication of interfacial gap between the mold and the solidifying steel shell control the final product quality of continuous casting of steel. Previous solidification and heat transfer models for continuous casting of steel are evaluated, focusing on the treatment of the interfacial gap. Experimental work on mold slag properties and their effect on heat transfer and lubrication are reviewed.

A new lubrication and friction model of slag in the interfacial gap was combined into an existing 1-D heat transfer model, CON1D. Analytical transient models of liquid slag flow and solid slag stress have been coupled with a finite-difference model of heat transfer in the mold, gap and steel shell to predict transient shear stress, friction, slip and fracture of the slag layers. The consistency and accuracy of the model is validated by comparing with analytical solutions and with results from commercial codes.

Experimental work is conducted to measure the properties of slag powder, including the friction coefficient at different temperatures and viscosity at lower temperature than previously measured. DSC, dip thermocouple and atomization tests are conducted to construct CCT curves and to predict critical cooling rates of two slag powders, which have different crystallization tendencies. XRD, Polarized Transmission Light Microscopy and SEM are used to analyze the composition of the mold powder and re-solidified slag samples and to determine the crystalline/glassy microstructure.

The CON1D model predicts shell thickness, temperature distributions in the mold and shell, thickness of the re-solidified and liquid powder layers, heat flux profiles down the wide and narrow faces, mold water temperature rise, ideal taper of the mold walls,

and other related phenomena. Plants measurements from operating casters were collected to calibrate the model.

The model is then applied to study the effect of casting speed and mold powder viscosity properties on slag layer behavior between the oscillating mold wall and the solidifying steel shell. The study finds that liquid slag lubrication would produce negligible stresses. Lower mold slag consumption rate leads to higher solid friction and results in solid slag layer fracture and movement if it falls below a critical value. Crystalline slag tends to fracture near the meniscus and glassy slag tends to fracture near mold exit. Mold friction and fracture are governed by lubrication consumption rate, which is total consumption rate subtracting the slag consumption in the oscillation marks. Medium casting speed may be the safest to avoid slag fracture due to its having the lowest critical lubrication consumption rate. The high measured friction force in operating casters could be due to three sources: an intermittent moving solid slag layer, excessive mold taper or mold misalignment.

The model is also applied to interpret the crystallization behavior of slag layers in the interfacial gap between the mold and the steel shell. A mechanism for the formation of this crystalline layer is proposed that combines the effects of a shift in the viscosity curve, a decrease in the liquid slag conductivity due to partial crystallization, and an increase in the solid slag layer roughness corresponding to a decrease in solid layer surface temperature with distance down the mold. When the shear stress exceeds the slag shear strength before the axial stress accumulates to the fracture strength, the slag could shear longitudinally inside the layers.

To my family

ACKNOWLEDGEMENTS

I would like to express my sincere gratitude to my advisor, Professor Brian G. Thomas for his guidance, support and encouragement through out of this work. I feel fortunate for having opportunity to learning a great deal from him both academically and personally. Also thanks to my committee members, Prof. Jonathan Dantzig, Prof. Ian Robertson, Prof. Pascal Bellon, Prof. David Payne and Prof. Waltraud Kriven, who offered guidance and support.

I would like to thank members of the Continuous Casting Consortium at UIUC, including Accumold (Huron Park, Ontario, Canada), AK Steel (Middletown, OH), Allegheny Ludlum Corporation (Brackenridge, PA), Armco Inc. (Middletown, OH), Bethlehem Steel (Richfield, OH), BHP Steel (Australia), Columbus Stainless Pty Ltd. (Mpumulanga, South Africa), Hatch Associate Consultants (Buffalo, NY), Inland Steel Company (East Chicago, IN), LTV Steel Company (Richfield OH), Postech (Pohang, Kyoungbuk, Korea), and Stollberg (Niagara Falls, NY) for their continued support of my research.

Thanks to Dr. Ron J. O'Malley at Nucor Steel and Darrell Sturgill at Stollberg for their measurements and suggestions. Prof. Hani Henein and Arvind Prasad at University of Alberta, Canada help with CCT tests; Dr Xiaoqiang Hou at The Center for Cement Composite Materials, UIUC with DSC tests, Prof. Andreas Polycarpou and Tim Solzak at Mechanic Engineering Department with friction tests and Prof. Craig Lundstrom and Fang Huang at Geology Department with polarized microscopy, Mr. John Bukowski, Mr. Scott Robunson for help on analysis methods. Some analyses are carried out in the Center

for Microanalysis of Materials, University of Illinois, which is partially supported by the U.S. Department of Energy under grant DEFG02-91-ER45439.

I am greatly indebted to all members of Metals Processing Simulation research group, Dr. Chunsheng Li, Dr. Hua Bai, Dr. Lifeng Zhang, Dr. Young-Mok Won, Dr. Joydeep Sengupta, Lan Yu, Tiebiao Shi, Quan Yuan, Bin Zhao and Claudio Ojeda, I could not imagine being able to complete my research without their unselfish help, advice and encouragement.

Finally, I am thankful to all of my friends and my whole family: my parents, sister, my husband and my baby who endured this long process with me, always offering support and love.

TABLE OF CONTENTS

page

LIST OF TABLES

LIST OF FIGURES

page

NOMENCLATURE

Cp	specific heat (J/kgK)
d	depth/thickness (m)
d_b	diameter of the breakout hole (m)
d_{osc}	volume-averaged osc.-mark depth (mm)
$freq$	mold oscillation frequency (cpm)
f_{roll}	fraction of heat flow per spray zone going to roll (-)
f_s	solid steel fraction (-)
f_v	empirical solid slag layer speed factor (-)
g	gravity (9.81m/s^2)
H	enthalpy (kJ/kg))
h	heat transfer coefficient (W/m^{2}K)
h_{conv}	natural convection h in spray zones (W/m^{2}K)
h_{rad_spray}	radiation h in spray zones (W/m^{2}K)
h_{rad}	radiation h in slag layers (W/m^{2}K)
k	thermal conductivity (W/mK)
L	length (m)
L_f	latent heat of steel (kJ/kg)
L_{pitch}	distance between successive oscillation marks (m)
N	slab thickness (m)
n	exponent for temperature dependence of slag viscosity (-)
Pr_{waterw}	Prandtl number of water at mold cold face temperature ($C_p\mu/k$)
Q	average mold heat flux (kW/m^2)

Q_{slag}	mold slag consumption (kg/m^2)
Q_{water}	water flow rate in spray zones (l/m^{2}s)
q_{int}	shell/mold interface heat flux (kW/m^2)
q_{sh}	superheat flux (kW/m^2)
R	gas constant (8.314 J/Kmol)
Re_{waterf}	Reynolds number at average of mold cold face and cooling water temperatures ($DV\rho/\mu$)
$r_{contact}$	slag/mold contact resistance (m^{2}K/W)
s	mold oscillation stroke (mm)
T	temperature (^{o}C)
T_{fsol}	mold slag solidification temperature (°C)
T_{hotc}	mold copper hot face temperature (^{o}C)
T_{mold}	mold hot face temperature with coating (^{o}C)
T_{liq}	steel liquidus temperature (^{o}C)
T_{sol}	steel solidus temperature (^{o}C)
T_s	steel shell surface temperature (at oscillation mark root) (^{o}C)
T_s'	liquid slag layer hot-side temperature (^{o}C)
ΔT_{water}	cooling water temperature rise(°C)
TLE	thermal linear expansion (-)
t	time (s)
t_d	drainage time (s)
t_f	mold oscillation period (s)
t_p	mold oscillation positive strip time (s)

V_c	casting speed (m/s)
w	width (m)
W	slab width (m)
x	shell thickness direction (m)
z	casting-direction, distance below meniscus (m)
Z_{mold}	working mold length (m)
α	thermal linear expansion coefficient (K^{-1})
ε	surface emissivities (-)
ε_{th}	thermal strain of steel shell (%)
η	viscosity (Pa s) (used in literature)
μ	viscosity (Pa s)
ρ	density (kg/m^3)
σ	Stefan Boltzman constant (5.67×10^{-8} W/m^2K^4)
τ	shear stress (Pa)
ϕ	friction coefficient (-)

<u>Subscripts</u>:

air	air gap
ch	cooling water channel in mold
coat	mold coating layer
eff	effective oscillation mark (based on heat balance)
gap	shell/mold gap
mark	oscillation mark

mold	copper mold
scale	scale layer in mold cooling channel
slag	mold slag
solid, liquid	solid slag layer, liquid slag layer
spray	spray nozzle below mold
steel	steel slab
water	cooling water
$\alpha, \delta, \gamma, l$	α-Fe, δ-Fe, γ-Fe, liquid steel phases

CHAPTER 1. INTRODUCTION

1.1 Background

Though the continuous casting method was attempted by early workers in 1840s[1], it was not until 1960s that the continuous casting of steel began to be widely adopted. It is now the predominant method to solidify semi-finished shapes in the steelmaking industry. By 2002, 88.4% of 902 million metric tons world crude steel production was produced through continuous casting[2] because it is the most low-cost, efficient and high quality method to mass produce metal products in a variety of sizes and shapes. Experts predict that annual steel consumption could grow to 1.2 billion tonnes by 2020[3].

1.2 Process Overview

In the continuous casting process, as shown in Figure 1.1[4], molten steel flows from a ladle, through a tundish into the mold. Mold powder is added to the free surface of the liquid steel providing thermal and chemical insulation from the environment. Once in the mold, the molten steel freezes against the water-cooled copper mold walls to form a solid shell. This shell contains the liquid as the shell is withdrawn continuously from the bottom of the mold. The shell thickness increases down the length of the mold, typically reaching 10mm to 20mm by mold exit. The withdrawal rate, or “casting speed” depends on the cross-section and quality of the steel being produced and varies from 0.3m/min to 10m/min[3]. Below mold exit, the strand is further cooled by water sprays and rolls support the steel to minimize bulging due to ferrostatic pressure. Once the liquid steel

inside the shell completely solidifies, the strand can be severed into individual lengths to yield slabs, blooms or billets, depending on the cross-section of the mold.

Mold heat transfer and lubrication predominantly control the occurrence of catastrophic breakouts, where liquid steel bursts through the shell, and also affect strand surface quality[5]. Excessive and/or uneven heat removal is associated with longitudinal cracks and star cracks in the shell[6, 7]. Heat transfer in the continuous casting process is governed by many complex phenomena. Figure 1.2[8] shows a schematic of some of these. Liquid metal flows into the mold through a submerged entry nozzle, and is directed by the angle and geometry of the nozzle ports[9]. The direction of the steel jet controls turbulent fluid flow in the liquid cavity, which affects delivery of superheat to the solid/liquid interface of the growing shell. Synthetic casting powder added on the top surface of the molten steel sinters and melts into the top liquid slag layer. The heat flux across the slag layers between copper mold and steel shell depends on the powder consumption rate and slag layer thermal properties[10-12].

To avoid having the solidifying shell stick to the mold, which can lead to tearing, or even breakouts, the mold is reciprocated vertically to create “negative strip time” when the mold moves downward faster than the steel shell. Also, during each oscillation stroke, liquid slag is pumped from the meniscus into the gap between the steel shell and the mold wall[13], where it acts as a lubricant, so long as it remains liquid and thus also helps to prevent sticking. But the mold oscillation also creates periodic depressions in the shell surface, “oscillation marks”, which affect heat transfer and could be the initiation sites of transverse cracks[14]. A substantial fraction of slag consumed in the mold is entrapped in oscillation marks moving down at the casting speed. The remaining slag consumed is

mainly due to the flowing liquid layer when the solid layer stably attaches to the mold wall.

The hydrostatic or “ferrostatic” pressure of the molten steel pushes the unsupported steel shell against the mold walls, causing friction between the steel shell and the oscillating mold wall, which limits the maximum casting speed[15]. At the corners, the shell may shrink away to form a gap, so friction is negligible. However, friction at the bottom of the narrow faces becomes significant if excessive taper squeezes the wide face shell. Finally, misalignment of the mold and strand can cause friction, especially if the stroke is large. The interfacial friction could cause solid slag layer fracture and movement and then result in local heat flux variation. The accompanying temperature and stress variations in the steel shell could lead to quality problems, such as shear sticking, tearing and even breakouts[16-18].

Mold taper, distortion and steel shell shrinkage may generate contact resistance or a vapor-filled gap, which acts as a further interfacial resistance to heat transfer in addition to oscillation marks and slag layers. This can lead to local hot spots. Proper taper encourages uniform heat transfer between the mold and steel surfaces, without exerting excessive contact forces on the hot and weak shell. Insufficient taper causes reduced heat flux across the mold/strand interface, leading to a thinner, weaker shell[19]. This may cause breakouts or bulging below mold, which leads to longitudinal quality problems such as off-corner “gutter” and subsurface longitudinal cracks[20]. Excessive taper also causes many problems, including mold wear, friction leading to axial tensile stress causing transverse cracks, and even buckling of the wide face shell, gutter and associated problems[21] as mentioned above.

Finally, the flow of cooling water through vertical slots in the copper mold withdraws the heat and controls the temperature of the copper mold walls. If the “cold face” of the mold walls becomes too hot, boiling may occur, which causes variability in heat extraction and accompanying defects. Impurities in the water sometimes form scale deposits on the mold cold face, which can significantly increase mold temperature, especially near the meniscus where the mold is already hot.

After exiting the mold, the steel shell moves between successive sets of alternating support rolls and spray nozzles in the spray zones. The accompanying heat extraction causes surface temperature variations while the shell continues to solidify, which cause phase transformations and other microstructure changes that affect its strength and ductility. It also experiences thermal strain and mechanical forces due to ferrostatic pressure, withdrawal, friction against rolls, bending and unbending. These lead to complex internal stress profiles which cause creep and deformation of the shell. This may lead to further depressions on the strand surface, crack formation and propagation.

1.3 Mold Slag

Mold Fluxes are synthetic slags that are used in the continuous casting process. These synthetic slags are complex mixtures of raw minerals including ceramic based oxides, pre-reacted components, and carbon. Available in many particles sizes, shapes and types, mold flux primarily contains silica (SiO_2), lime (CaO), sodium oxide (Na_2O), fluorspar (CaF_2), and carbon. Other components of this slag system include alumina (Al_2O_3), magnesium oxide (MgO), other alkaline oxides (Li_2O, K_2O), and some metallic oxides of iron, manganese, titanium to achieve specific properties.

Continuous casting mold slag performs five important functions[22-24]:

1) Thermally insulates the molten steel meniscus to prevent premature solidification and meniscus “hook” defects;

2) Protects the molten steel from oxidation;

3) Absorbs non-metallic inclusions, such as Al_2O_3 and TiO_2 floating to the molten steel surface;

4) Provides a lubricating film of molten slag to prevent the steel from adhering to the mold wall and to facilitate strand withdrawal;

5) Provides homogenous heat transfer from strand to mold.

As shown in Figure 1.2, the slag above the molten steel consists of an unreacted powder layer and a melted liquid layer below. Depending on the melting characteristics of the slag, there will also be a sintered layer in between[25].

The slag layer adjacent to the cold mold wall cools and greatly increases in viscosity, thus acting as a re-solidified solid layer. Its thickness increases greatly just above the meniscus, where it is called the “slag rim”. Depending on its compositions and cooling history, the microstructure of this layer could be glassy, crystalline or mixtures of both[26]. Insights into this microstructure can be determined by measuring its Time-Temperature-Transformation (TTT) diagram[27, 28]. The solid layer often remains stuck to the mold wall, although it is believed to be sometimes dragged intermittently downward at an average speed far less than the casting speed[29]. However, the mechanism of slag layer flow, fracture, and attachment is not understood well yet.

The chemistry, viscosity, solidification point and crystallinity are typically considered the most important properties of slag, which decide the powder melting, infiltration and lubrication behaviors, which in turn, affect the mold heat transfer. Good

design of mold slag could avoid surface defects such as longitudinal, transverse and star cracks; enhance surface quality with the formation of uniform and shallow oscillation marks; prevent breakouts; and enable increased casting speed.

1.4 Objectives

Due to the importance and complexity of the continuous casting process, it is worthwhile to develop fundamentally based mathematical models combined with laboratory experiments such as slag TTT curves, and measurements on operating casters to improve understanding and product quality of this advanced process. The objectives of this study are:

1) To develop an efficient computational model of heat transfer phenomena in continuous casting with a detailed treatment of the interfacial gap, including the insulating mold powder layers, liquid slag layer flow and solid layer crystallization, friction and fracture behaviors.

2) To calibrate the mathematical model with plant measurements on operating casters.

3) To apply the model to interpret caster signals such as thermocouple measurements and friction signals and to develop a diagnostic tool for problems in continuous casting, such as, breakout danger, excessive mold friction and crack formation.

4) To apply the model to investigate the effects of various casting conditions on heat transfer and interfacial lubrication and to give optimum processing parameters.

1.5 Methodology

First, previous literature is reviewed to understand the effects of mold powder on interfacial heat transfer and lubrication behavior and to examine the various mathematical models that describe steel solidification, mold heat transfer and the interfacial gap. (Chapter Two)

Based on the previous heat transfer model[30-32], the lubrication and friction model of slag in the interfacial gap was combined into a 1-D heat transfer model, CON1D. The heat transfer results were obtained by inputting basic casting conditions such as steel grade, pouring temperature, casting speed etc. and assuming some intermediate variables such as slag consumption and oscillation mark size. The liquid slag layer velocity distribution was obtained by solving the Navier-Stokes equation including the effect of temperature dependent viscosity of the slag. The shear stress on the solid slag layer and the mold wall was derived according to the ferrostatic pressure from the liquid steel and the velocity gradient in the liquid slag. A stress calculation based on a force balance on the solid slag layer was performed to predict the possibility of solid layer fracture and sliding. The consistency and accuracy of the model is then validated by comparing with an analytical solution and with results from commercial codes, such as MATLAB and ANSYS. (Chapter Three)

Experiments are conducted on two types of slag: high tendency to be crystalline (slag S1) and high tendency to be glassy (slag S2). Slag composition, solidification temperature and viscosity curves were measured separately at Technical Data Sheet Laboratory, Stollberg Inc., Niagara Falls, NY and Metallurgica's Lab in Germany at the request of AK Steel Technology Center, Middletown, Ohio. DSC, Thermocouple DIP

tests and atomization tests are then conducted at CEE, UIUC and the Advanced Materials Processing Laboratory(AMPL), University of Alberta, Canada to collect data for CCT/TTT diagram of slag. Slag friction coefficient measurements were made at the Tribology and Micro-Tribology Lab at MIE, UIUC. The model predicted friction results were compared with reported friction measurements[33]. XRD, Polarized Transmission Light Microscopy and SEM are used to analyze the composition of the mold powder and re-solidified slag sample and determine the crystalline/glassy microstructure. (Chapter Four)

Plants measurements from operating casters were collected to calibrate the model. Molten steel temperature was measured at AK Steel, Mansfield, OH by constructing an apparatus to lower a thermocouple probe down through the top surface powder and slag layers into the flowing molten steel. The measured data was used to calculate the superheat into the solidifying shell[34]. Embedded mold thermocouples measurements and breakout shell were also obtained from AK steel caster under similar casting conditions. Other plants also supplied measured data for model calibration, including plain carbon casting at LTV steel, Cleveland Ohio[30]; stainless steel casting at Columbus Stainless Steel, South Africa[35]; billet casting at POSCO, South Korea[36]; and spray zone cooling at China Steel, Taiwan[37]. (Chapter Five)

The calibrated model was used to investigate the effect of various process conditions on heat transfer and mold friction, such as mold slag crystallization behavior, powder consumption rate and casting speed. The model is able to predict ideal taper, interpret caster signals and predict potential problems, e.g. cooling water boiling,

excessive mold friction, breakout danger and crack formation. Finally, the model will give optimum processing parameters to avoid problems. (Chapter Six, Seven)

1.6 Figures

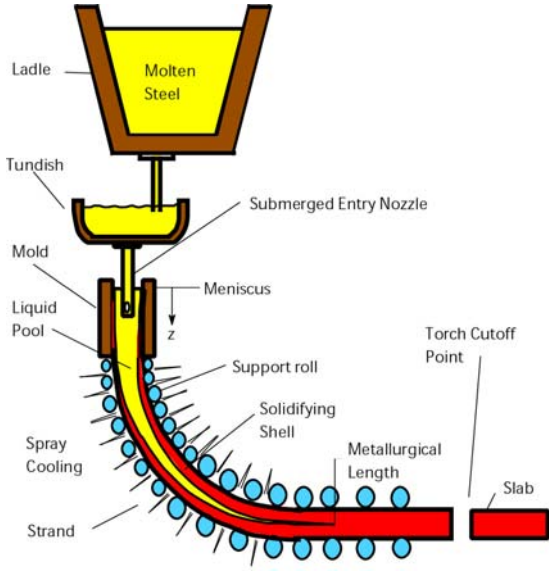

Figure 1.1 Steel continuous casting process[4]

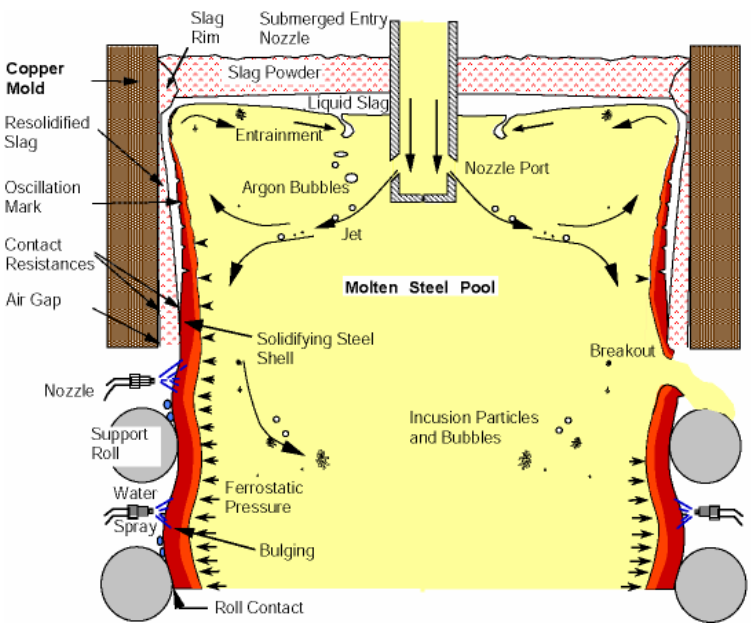

Figure 1.2 Schematic of CC phenomena showing slag layers[8]

CHAPTER 2. LITERATURE REVIEW

2.1 Mathematical Modeling

Many mathematical models have been applied to different aspects of continuous casting[38-40]. Generally, they are in one of the following four categories: 1) Fluid flow models; 2) Shell solidification and thermal-mechanical models; 3) Mold heat transfer and thermal distortion models; and 4) Mold/Shell interface heat transfer and lubrication models.

2.1.1 Steel Solidification Models[39]

The earliest solidification models used simple empirical equations and found application in the successful prediction of metallurgical length, which was easily done by solving the following simple empirical relationship for distance, z, with the shell thickness, S, set to half the section thickness.

$$S = K\sqrt{z/V_c} \tag{2.1}$$

where, K was found from evaluation of breakout shells and computations.

The first 1-D finite difference models to calculate the temperature field and growth profile of the continuous cast steel shell were given by Hills[41], Mizakar[42] and Lait[43]. By choosing a thin horizontal slice through the shell moving downward through the mold at casting speed, the models solved the 1-D transient heat conduction:

$$\rho\frac{\partial H}{\partial t} = \nabla\left(k\nabla T\right) \tag{2.2}$$

With the surface boundary conditions for the mold involving either a constant mold heat transfer coefficient or an empirical heat-flow relationship, these models calculate the

temperature evolution and growth of the solidifying steel shell. Many industrial models followed[44-46]. Such models found further application in trouble shooting the location down the caster of hot tear cracks initiating near the solidification front[47], and in the optimization of cooling practice below the mold to avoid subsurface longitudinal cracks due to surface reheating[48].

Since then, many advanced models have been developed to simulate further phenomena such as thermal stress and crack related defects[49-52] or turbulent fluid flow[53-57] coupled together with solidification. For example, a 2-D transient stepwise coupled elasto-viscoplastic finite-element model tracks the behavior of a transverse slice through a continuously cast rectangular strand as it moves down through the mold at casting speed[50]. This model is suited for simulating longitudinal phenomena such as taper design[58], longitudinal cracks[59] and surface depressions[20].

The complex turbulent flow in the liquid steel pool was usually considered by enhancing the liquid steel thermal conductivity by a factor of 6-8[42, 60], which does not take into account the effect of non-uniform super-heat dissipation to the narrow-faces more than the wide-faces[61]. Other casters have been modeled using 3-D coupled fluid flow–solidification models[55, 57] based on control-volume or finite difference approaches at the expense of greater computation time and memory.

2.1.2 Mold Heat Transfer and Distortion Model

The copper mold plays a critical role in the continuous casting process, which acts as a heat exchanger, a solidification and hydro-chemical reactor and a shaping die[62]. Calculation of temperature distribution and thermal distortion of the copper mold is very important for understanding the heat flux profile from the solidifying steel shell across

the interface. It provides clues for improving mold taper and cooling water channel design and increasing mold service life. Several models solve the steady-state heat conduction equation within the mold using either finite difference or finite element method[63-67]. The heat flux can be determined from measured mold wall temperature. Traditionally, a trial and error technique was used[68, 69]. Alternatively, the inverse heat conduction problem is solved[65, 67].

The temperature across the lower part of the mold is usually linear, showing a steady-state, 1-D heat conduction. But near the meniscus region, the temperature measurements show that the highest mold temperature is at about 20mm below the meniscus[38] due to the vertical heat conduction into the cold mold region above the meniscus. Therefore, 2-D heat flux calculation is required within the top part of the mold. Even 3-D finite-element thermal-stress models have been applied to determine the axial heat flux profile from the measured mold temperature data in order to account for the complex mold water channel geometry[64-66].

Some researchers used empirical equation for heat transfer in the mold as a function of dwell time, *t*, which was calculated by dividing distance below meniscus by the casting speed[43, 48, 70, 71]. For example, Brimacombe reported the average mold heat flux had the following relationship found from the heat balance on mold cooling water temperature increase[48]:

$$Q\left[kW/m^2\right] = 2680 - 222\sqrt{t\left[\sec\right]} \tag{2.3}$$

Wolf gave similar results for slab casting with mold powder[72]:

$$Q\left[kW/m^2\right] = 7300\Big/\sqrt{t\left[\sec\right]} \tag{2.4}$$

The calculated 2-D or 3-D heat flux and mold temperature distribution can also be input into mold thermal distortion models[21, 64, 73], which was used to predict ideal taper[21, 74] and crack formation in the mold[75]. Samarasekera[76] found an outward bulge of 0.1~0.3mm at the meniscus which gave a negative taper of 1~2%/m above the meniscus, and a positive taper of 0.4%/m below.

2.1.3 Interfacial Model

One of the greatest resistances to heat transfer from the liquid steel to the mold cooling water is the interface between the mold and the shell. Heat transfer across this interface is controlled by the thickness and thermal properties of the materials that fill the gap. Despite its known importance, most previous mathematical models characterize the interface as a boundary condition for a model of either the shell or the mold alone. Even models of both usually use a simplified treatment of the gap[74, 77, 78].

Previous interfacial heat transfer model have focused on simulating the heat flux through the different slag layers. The partition of slag into crystalline and glassy layers was investigated through mathematical models to determine the effect of slag layer formation on thermal resistance. Bagha[79] reported a greater thermal conductivity of crystalline slag than glass slag, which might due to ignoring the radiation across the transparent glassy phase[80]. Other models including the effect of both conduction and [81]thickness[12, 82].

A few researchers have attempted to couple the heat transfer to slag hydrodynamics. Riboud and Larrecq[83] first presented an analysis of the flow of the molten mold powder in the shell/mold gap, which included the effect of temperature dependent viscosity and ferrostatic pressure with the assumption of no mold oscillation.

Kor[84] was one of the first to solve the Navier-Stokes equation for a laminar incompressible fluid (the liquid mold powder), flowing between the moving steel shell and oscillating mold wall. It is assumed that the space between the mold wall and the steel shell was entirely filled with liquid slag with a constant viscosity and constant thickness. This model might be reasonable for the region of meniscus, where no air gap has yet formed and the solid slag layer is thin. Bland[85] and Hill[86] developed models which incorporated heat transfer through two layers: solid and liquid mold powder. The thickness of two layers was decided by the shrinkage of steel shell. It seems good only for round casters or near the corner, where shell can shrink such as used by Thomas[81, 87].

Bommaraju[88] and Dilellio[17] both used a temperature dependent viscosity curve to model viscous flow within the gap. The analysis assumed Couette flow between stationary mold plate and the strand moving at the casting speed. The model calculated the velocity profile of the slag and the shear stress at different locations. When the temperature dropped below its solidification point, solid-solid friction was assumed and the shear stress became significant. Dilellio also predicted large pressure fluctuations in the slag layer near the meniscus region, where the shell is thin and deformable.

It is generally believed that the mold friction is composed of liquid friction and solid (dry) friction[15, 18, 33, 89]. When the liquid slag film is present, the shear stress is decided by the slag viscosity and the relative motion between the shell and the mold:

$$\tau_{liquid} = \mu \frac{V_{mold} - V_c}{d_{liquid}} \tag{2.5}$$

The solid friction is the contribution from the contact between the shell and mold or solid slag film and mold, and is independent of relative velocity:

$$\tau_{solid} = \phi \, \rho_{steel} g \, z \tag{2.6}$$

Some later models used similar methods to simulate slag infiltration near the meniscus and to calculate slag layer velocity profile, shear stress, friction force and pressure variation in the gap. Of these, most assumed a linear velocity distribution through the liquid film thickness[12, 15, 89, 90]. Several previous models have concerned mold slag hydrodynamics by solving a Navier-Stokes equation[17, 84-86, 91-94]. In these models, the slag layer thickness either was an empirical constant[84, 92, 95], an input linear function[13, 91, 93] or assumed to equal the shrinkage of the steel shell[17, 85, 86, 88], which ignores important phenomena such as ferrostatic pressure. Japan researchers[96-98] give an empirical relationship between liquid slag film thickness and mold oscillation conditions:

$$d_{liquid}\left[mm\right] = 79.1 V_c \left[m/min\right]^{-0.6} T_{fsol}\left[°C\right]^{-0.9} s\left[mm\right]^{0.3} t_f\left[s\right]^{-0.08} t_p\left[s\right]^{0.12} \tag{2.7}$$

Assuming a constant liquid slag layer thickness and constant slag viscosity in the layer, the slag consumption rate was obtained by integrating slag velocity across the interfacial gap[96]:

$$Q_{slag} = \frac{\rho_{slag}}{2} d_{liquid} + \frac{g \rho_{slag}\left(\rho_{steel} - \rho_{slag}\right)}{12 \mu V_c} d_{liquid}{}^3 \tag{2.8}$$

Most previous models assumed constant slag viscosity in the gap[84, 91-93], which is contrary to the tremendous temperature dependency reported in measurements[99-101] and the high temperature gradient across the gap. Some researchers fit slag viscosity to a simple inverse function of temperature[17] or an Arrhenius equation[85, 88, 95]. However, the slag viscosity is usually only measured above the slag liquidus should be much higher on the mold side.

Some mechanical models were developed to predict the oscillation mark depth[102, 103], which can be connected with the slag consumption and lubrication. Thomas's research group have developed a simple 1-D transient solidification model of the shell, coupled together with a 2-D analytical solution of steady heat conduction in the mold[30], CON1D, which features a detailed treatment of the interfacial gap, including mass and momentum balance of the slag layers and the effect of oscillation marks. However, no mathematical model connects the slag crystallization with gap heat transfer. Moreover, no previous model predicts friction or describes solid layer fracture and the sliding behavior of the slag layers.

2.2 Plants Measurements

Extensive instrumentation is commonly utilized to monitor and analyze the continuous casting process, which can be used as an online problem-detection, quality control system and offline product quality analyses and trouble shooting. Mold instrumentation includes temperature measurement from embedded thermocouples, metal level monitor and load cells and strain gage for mold displacement and friction.

2.2.1 Thermal Response

The total heat extracted into the mold can be measured by the temperature rise from inlet to outlet of the cooling water flowing through the water channels[30, 104].

Thermocouples are often embedded in the copper mold to collect temperature measurements and can be interpreted with computational heat flow models[29, 105, 106]. Brimacombe, Samarasekera and co-workers at UBC continuous casting group have successfully instrumented molds especially billets with thermocouples to measure mold

wall temperature for the last two decades[68, 107-109]. Figure 2.1 shows a typical mold hot face temperature and heat flux profile with distance below meniscus, which were calculated from mold wall temperature measurements made along the mid-plane of the loose and narrow walls[110]. As expected, the temperature and heat fluxes on both walls decrease with increasing distance below the meniscus due to the increasing heat resistance from the solidifying steel shell and slag layer. The higher temperature and heat flux through the narrow face may be partly due to the molten steel flow from the bifurcated SEN being directed towards the narrow walls. From Figure 2.1, it can also be observed that the medium carbon steel showed lower mold heat removal.

The temperature signal can also help to understand other complex events occurring in the mold, such as mold level variation and related surface depressions[111] and sticker breakout prevention[112]. As shown in Figure 2.2, Ozgu[110] and Geist[113] both reported “saw-tooth” shaped temperature fluctuations low in the mold, which suggests periodic solid slag layer fracture and sheeting from the mold wall[29].

2.2.2 Friction Signal

Friction signals are obtained by installing lubrication sensor[114], load cells[115] or pressure sensors[116] on the mold to record the mold speed, load or pressure variation during mold oscillation. Figure 2.3(a) was obtained from pin forces and mold displacements measured during casting and cold oscillation tests[117]. Figure 2.3(b) shows an example of a load cell signal during casting of a 0.3%C-Boron alloyed steel with powder lubrication[118].

However, fundamental understanding of the meaning of these measurements and how to interpret them to solve problems is lacking. Currently mold friction measurements

are evaluated mainly as a means to detect problems with the oscillation system, such as mold misalignment. If the friction signal can be better understood, friction monitoring could be used to identify the status of mold lubrication to predict surface defects[114] and to help prevent breakouts[112].

2.3 Mold Powder Properties

Compared with oil lubrication, powder(/slag) lubrication leads to more uniform and usually lower heat transfer[5, 67]. The heat flux across the interfacial gap depends on the slag layer thermal properties[10-12] and thickness[119, 120] and friction, which is affected by slag properties such as melting, crystallization behavior and temperature dependent viscosity[121, 122].

2.3.1 Mold Powder Composition

The composition of mold powder varies with the properties required for different steel grades and casting conditions. The major constituents include CaO, SiO_2, Al_2O_3, CaF_2 and Na_2O. A ternary system that is relevant in understanding the behavior of mold slag compositions is the CaO-SiO_2-CaF_2 system, illustrated in Figure 2.4(a)[123]. In a typical mold slag composition range, the ternary compound cuspidine ($3CaO{\cdot}2SiO_2{\cdot}CaF_2$) equilibrates with $CaO{\cdot}SiO_2$, $3CaO{\cdot}2SiO_2$, $2CaO{\cdot}SiO_2$ and CaF_2 in solid state. Samples containing these compounds melt incongruently. The lines surrounding cuspidine represent isotherms on the liquidus surface, which vary in the temperature range from 1114°C to 1407°C in this ternary. Figure 2.4(a) also shows the composition of slag S1, which will be discussed in detail in Chapter 4. Figure 2.4(b)-(d)[124] show some other relevant ternary phase diagrams in mold slag systems. The

actual phases in mold slag film are even more complicated because all these components may react together to form new phases and change the eutectic point in addition to being affected by about ten other minor constitutes. Table 2.1 shows the typical composition range of commercial mold powders[25]. The basicity or V-ratio, which is usually calculated as CaO wt%/SiO_2 wt%, is an important index for mold powder properties, and ranges from 0.67~1.2[125].

The viscosity, melting range, glass transition and crystallization temperature depend on the powder composition. The building block of most mold slag is the SiO_4 tetrahedron. Each silicon-oxygen tetrahedron is linked to at least three other tetrahedra at the corners to form a three-dimensional network[126]. Each oxygen acts as a bridge between neighboring tetrahedra and hence is called a bridging oxygen (BO)[127]. Oxides with cations forming such coordination polyhedra, such as SiO_2, B_2O_3 etc, are termed a "network former" or "glass former"[128]. When an alkali or alkaline earth oxide is added into a slag system, it provides additional oxygen ions, which modify the network structure, so it is called a "network modifier". Its singly bonded oxygen does not participate in the network and so it is called a nonbridging oxygen (NBO). The modifying cations in the network modifier are located in the vicinity of the single-bonded oxygens to mantain local charge balance. The creation of NBO in the network lessens the connectivity, and causes the slag viscosity to decrease[127]. The network modifiers used in continuous casting slags include CaO, Na_2O, MgO, K_2O, Li_2O, BaO and SrO etc. The effect of Al_2O_3 depends on the average number of oxygens per network-forming ion. In the case of slag systems based on silicate glasses containing more alkali and alkaline earth oxide than Al_2O_3, the Al^{3+} is believed to occupy the centers of AlO_4 tetrahedra.

Hence, the addition of Al_2O_3 introduces only 1.5 oxygens per network-forming cation, and the NBOs of the structure are used up and converted to BOs[128], which enhance network and cause viscosity to increase. However, if Al_2O_3/CaO ratio is greater than one, it is hypothesized that octahedrally co-ordinated AlO_6^{9-} ions enter the melt and serve to disintergrate the complex aluminosilicate ion chain[129-131], which is not considered in this mold slag systems. Compounds containing F, such as CaF_2, are added to provide fluorine(F^-) ion in order to decrease the viscosity of the slag by replacing the divalent oxygen ion and causing the breakdown of the Si-O-Si bond[129, 132]. Table 2.2 summarizes the effect of these components on viscosity and crystallization of mold slags[25]. Carbon is added to slow the melting rate and make it more uniform.

It should be noted that the slag composition changes during the casting process, such as the carbon burning out as the powder melts and collecting in the sintered layer. In addition, the slag absorbs re-oxidation products, especially when casting Al-killed steel, the alumina in the slag can rise 3~15%[133].

2.3.2 Viscosity

Viscosity, which characterizes the slag fluidity, is highly temperature dependent. Figure 2.5 shows how the viscosity of some commercial silicate glasses vary with temperature[126]. The viscosity of liquid slag at high temperature is usually measured with a rotating viscometer[99, 134], in which the toque of a rotating spindle, immersed in the slag that is contained in a cylindrical crucible, is measured. Owing to the strength of the spindle, seldom are viscosity measurements reported greater than 10Pa·s. Thus, the viscosity-temperature curve near the solidifying temperature is yet unclear for mold slag used in continuous casting process.

Most slags are considered to be Newtonian fluids. The viscosity is often expressed as an Arrhenius-type relationship:

$$\mu = A\exp\left(\frac{E}{RT}\right) \tag{2.9}$$

where A is a constant, E is the activation energy for viscous flow. To account for the effect of activation energy changing with temperature, several slag viscosity models have been developed based on measurements of slag viscosity with different composition[83, 99, 130, 135].

Riboud at IRSID carried out viscosity measurements on a set of 23 synthetic mixtures of the system CaO-Al_2O_3-SiO_2-Na_2O-CaF_2 and 22 industrial continuous casting slags. From these measurements, an interpolation formula was derived[83, 99]:

$$\begin{aligned}
&\mu\left[Pa\ s\right] = A\cdot T\left[K\right]\cdot\exp\left(B/T\left[K\right]\right)\\
&\ln A = -19.81 + 1.73X_{CaO^*} + 7.02X_{Na_2O^*} + 5.82X_{CaF_2} - 35.76X_{Al_2O_3}\\
&B = 31140 - 23896X_{CaO^*} - 39159X_{Na_2O^*} - 46356X_{CaF_2} + 68833X_{Al_2O_3}\\
&X_{CaO^*} = X_{CaO} + X_{MgO} + X_{FeO} + X_{MnO} + X_{B_2O_3}\\
&X_{Na_2O^*} = X_{Na_2O} + X_{K_2O}\\
&X = Molar\ \ fraction
\end{aligned} \tag{2.10}$$

Kayama developed a different empirical formula that includes the effect of SiO_2, MgO and Li_2O individually[130]:

$$\begin{aligned}
&\ln\mu\left[poise\right] = \ln A + B/T\left[K\right]\\
&\ln A = -4.82 - 0.06X_{CaO} - 0.12X_{MgO} - 0.19X_{Na_2O} + 0.06X_{CaF_2} - 0.24X_{Al_2O_3}\\
&B = 29012.5 - 92.6X_{SiO_2} - 165.6X_{CaO} - 413.6X_{CaF_2} - 455.1X_{Li_2O} + 283.2X_{Al_2O_3}\\
&X = Mole\%
\end{aligned} \tag{2.11}$$

I.R. Lee's model is similar to Koyama's, but adds the component B_2O_3 into the system[135]:

$$
\begin{aligned}
&\log \mu\left[Pa\cdot s\right] = \log A + B/T\left[K\right] \\
&\log A = -2.307 - 0.046X_{SiO_2} - 0.07X_{CaO} - 0.095X_{B_2O_3} \\
&\qquad - 0.041X_{MgO} + 0.035X_{CaF_2} - 0.185X_{Al_2O_3} \\
&B = 6807.2 + 70.68X_{SiO_2} + 32.58X_{CaO} + 59.7X_{B_2O_3} - 34.77X_{Na_2O} \\
&\qquad - 176.1X_{CaF_2} + 312.65X_{Al_2O_3} - 167.4X_{Li_2O} \\
&X = Mole\%
\end{aligned}
\tag{2.12}
$$

These models provide a method to design the slag composition to achieve a desired viscosity curve. However, none of them can accurately predict the viscosity near the solidification temperature. These models are only good for low viscosity, high temperature range (<10^3poise) and cannot accommodate the sharp viscosity increase that occurs at lower temperature. Moreover, the form of Eq.(2.9) is not suitable for an analytical derivation of slag rheology.

2.3.3 Solidification Temperature

During a cooling cycle, there is a point where the slag viscosity increases suddenly and the slag becomes non-Newtonian. This is referred to as the crystallization temperature, solidification temperature or break temperature. This is a relatively vague concept because it could be a temperature range, depending on the fraction of crystalline formation and varied with cooling rates.

I.R. Lee also gave a relationship for break temperature based on composition[135]:

$$
\begin{aligned}
&T_{fsol}\left[{}^{o}C\right] = 1241.6 - 2.15X_{MgO} - 15.28X_{B_2O_3} - 4.49X_{Na_2O} \\
&\qquad - 8.55X_{CaF_2} - 1.41X_{Al_2O_3} - 6.41X_{Li_2O} \\
&X = Mole\%
\end{aligned}
\tag{2.13}
$$

Sridhar reported a better fitted relation based on viscosity measurements carried out at NPL for both steady and dynamic state[136]:

$$Steady\ Condition:$$

$$T_{fsol}\left[{}^{o}C\right] = 1180 - 3.94X_{Al_2O_3} - 7.87X_{SiO_2} + 11.37X_{CaO} - 9.88X_{MgO} + 24.34X_{Fe_2O_3} + 0.23X_{MnO} - 308.7X_{K_2O} + 6.96X_{Na_2O} - 17.32X_{F}$$

$$Dynamic\ Condition\ (CR = 10^{o}C/\min):$$

$$T_{fsol}\left[{}^{o}C\right] = 1120 - 8.43X_{Al_2O_3} - 3.3X_{SiO_2} + 8.65X_{CaO} - 13.86X_{MgO} - 18.4X_{Fe_2O_3} - 3.21X_{MnO} - 9.22X_{TiO_2} + 22.86X_{K_2O} - 3.2X_{Na_2O} - 6.46X_{F} \quad (2.14)$$

$$X = wt\%$$

2.3.4 Crystallization Behavior

Laboratory experiments show that heat transfer across the gap is significantly affected by the crystallization of the slag film while it is insensitive to chemical composition[137]. Gas bubbles were sometimes observed in the crystalline slag samples[138]. Radiation plays an important role in the glassy film[138-140]. Wang [141] also reported that a glassy slag is preferred. The crystalline slag tends to increases slag scale on surface of strands and also leads to the cracks or breakouts because of lower local heat transfer.

Slag crystallization temperature is defined as the temperature at which crystals begins to precipitate in the amorphous matrix, which depends on cooling rate. Several studies were conducted using differential thermal analysis (DTA)[27, 121, 142], single or double hot thermocouple technique (SHTT/DHTT)[28, 143], Confocal Microscopy[144] and by devitrification, examining the fraction of crystalline phase after heating a previous quenched sample to a specific temperature and holding[145]. The isothermal transformation diagrams (TTT diagram) and continuous cooling transformation diagrams (CCT diagram) of slag have been measured recently in controlled laboratory conditions [27, 28, 143, 144, 146-150]. Figure 2.6 shows some of their results. However, most of

those methods are limited to a very low cooling rate ($1^oC/min$~$900^oC/min$). While average cooling rate of the mold slag in the longitudinal (meniscus to mod exit) and transverse (mold hot face to steel shell surface) directions may be about 20~$25^oC/sec$, the local cooling rate maybe as high as 50~$100^oC/sec$, especially near the meniscus where the maximum heat flux crosses into the mold. Therefore, the method of achieving higher cooling rate for studying mold slag crystallization is required.

Larson[151], Lanyi[100, 152], Lin [153] and Wang[141] show that alumina tends to increase viscosity and decrease the crystallization temperature. This makes the slag easier to be glassy[141, 151]. The TTT curves of typical crystalline and glassy slags are shown in Figure 2.7[143, 144]. The increase of Al_2O_3 delays and narrows the crystallization region and increases the crystallization temperature at the same time.

The high basicity and highly glassy characteristics of mold slags are usually inversely proportional[141]. A high basicity system has low viscosity and a high tendency to crystallize[151]. So slag basicity has been suggested as an empirical indicator to predict the tendency to crystallize. Basicity is defined by the concentration ratio of oxides of network modifiers to oxides of network formers[129-131]:

$$BI = \frac{1.53X_{CaO} + 1.51X_{MgO} + 1.94X_{Na_2O} + 3.55X_{Li_2O} + 1.53X_{CaF_2}}{1.4X_{SiO_2} + 0.1X_{Al_2O_3}} \tag{2.15}$$

Deploymerization index (DI) was also proposed as indicator[154]:

$$DI = \frac{X_{SiO_2} + X_{Na_2O} + X_{CaO} + X_{Al_2O_3}}{X_{SiO_2} + X_{Al_2O_3} + X_{B_2O_3}} \tag{2.16}$$

The higher the deviation of DI from unity, the faster the the crystallization is.

2.3.5 Thermal Conductivity

The effective thermal conductivity of a mold slag contains contribution from phonon (lattice) conduction and photon (radiation) conduction[137, 139]. The latter is especially important for liquid and glassy slags. In general, the crystalline phases have higher lattice conductivity than the glassy phases.

The thermal diffusivities of different slags were measured using the laser pulse method[137, 155]. The results indicated that slag thermal diffusivities are insensitive to chemical composition[137]. High solidification temperature crystalline slag usually reduces mold heat transfer[122]. This is likely due to: 1) the decrease of effective conductivity of the solid phase owing to the high porosity of crystalline slag[138]; 2) the increased thermal contact resistance caused by the increase of surface roughness that develops during crystallization[119, 140]; and 3) the thicker solid slag layer that accompanies the higher solidification temperatures.

2.3.6 Slag Selection Criteria

The optimum mold powder application varies with casting conditions such as, steel grade, casting speed, oscillation practice and mold design etc. The criteria for slag selection have been established based on the functions the slag is expected to serve.

The two most important functions of mold powder are uniform heat transfer and good lubrication. An empirical parameter, $\eta \cdot Vc$, has been used to combine the effect of slag viscosity and casting speed. Conditions are recommended to maintain a high slag film stability and lubrication efficiency[156]. Figure 2.8(a) shows the effect of $\eta \cdot Vc$ on mold heat transfer[157]. In the $\eta \cdot Vc$ range of 1 to 3.5(poise·m/min), the variation in mold

heat transfer is a minimum, indicating uniform powder infiltration between the mold and the strand. Figure 2.8(b) shows the effect of η·Vc on measured mold friction force. The minimum is proposed to indicate the best lubrication[16].

Figure 2.9 shows a useful diagram for selecting the viscosity and break temperature of powders for various casting speeds[158]. Crack sensitive (medium-carbon) steel grade should be cast using a mold powder with a high break temperature (low heat transfer), whereas sticker and bulging sensitive grades should be cast with a low break temperature powder (high heat transfer leading to a thick shell).For all other grades, a powder between the two bounds was recommended[120, 136]. This empirical criterion has not been fundamentally understood, however.

2.4 Tables and Figures

Table 2.1 Typical Chemistry Range for Mold Slag[25]

CaO:	25~45%	MgO:	0~10%	MnO:	0~10%
SiO_2:	20~50%	K_2O:	0~5%	TiO_2:	0~5%
Al_2O_3:	0~10%	FeO:	0~6%	BaO:	0~10%
Na_2O:	1~20%	B_2O_3:	0~10%	C:	1~25%
F:	4~10%	Li_2O:	0~4%		

Table 2.2 Effect of Components on Viscosity (μ) and Crystallization Temperature (T_{CR}) of Mold Slags[25]

Component	Effect on μ	Effect on T_{CR}	Component	Effect on μ	Effect on T_{CR}
CaO	Decrease	Increase	MnO	Decrease	Decrease
SiO_2	Increase	Decrease	MgO	Decrease	Decrease
Cao/ SiO_2	Decrease	Increase	B_2O_3	Decrease	Decrease
Al_2O_3	Increase	Decrease	BaO	Decrease	Decrease
Na_2O	Decrease	Decrease	Li_2O	Decrease	Decrease
F	Decrease	Increase	TiO_2	No change	Increase
Fe_2O_3	Decrease	Decrease	K_2O	Decrease	Decrease

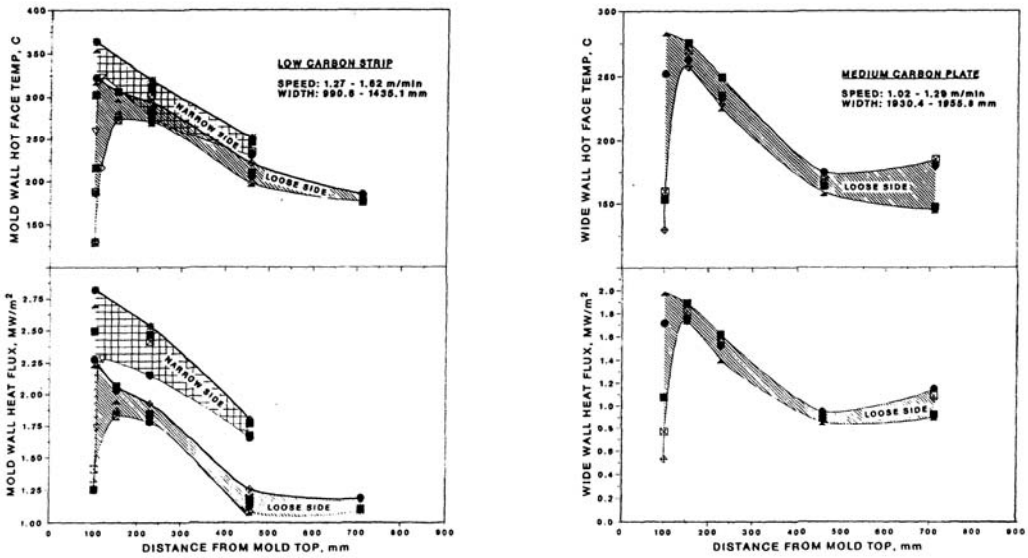

(a) Low carbon steel **(b) Medium carbon steel**

Figure 2.1 Variation of mold hot face temperature and heat flux[110]

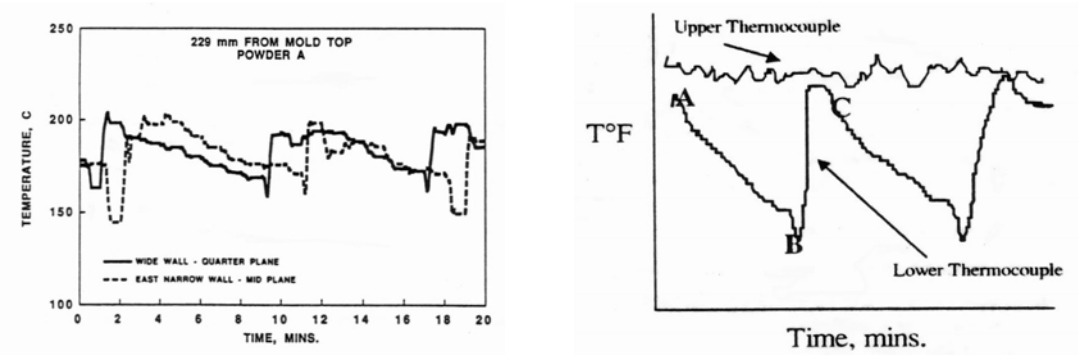

(a) [110] **(b) [113]**

Figure 2.2 Sawtooth-like temperature variation on mold wall

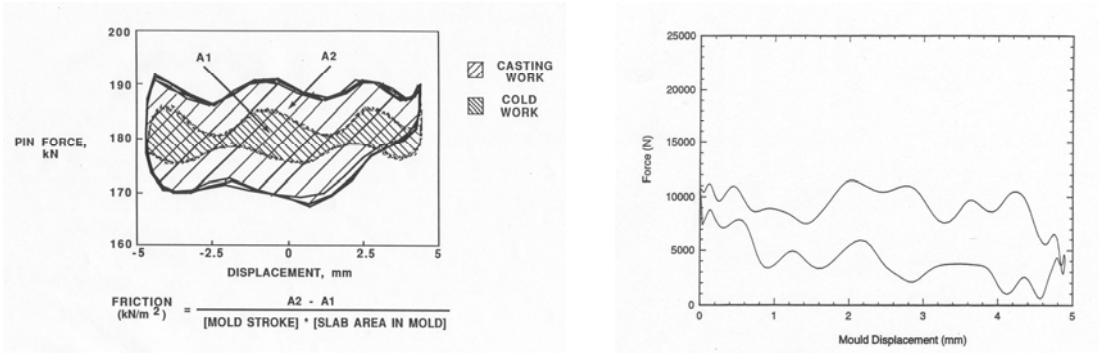

(a) Pin force during casting and cold oscillation[117] **(b) Load cell signal[118]**

Figure 2.3 Friction force vs. displacement

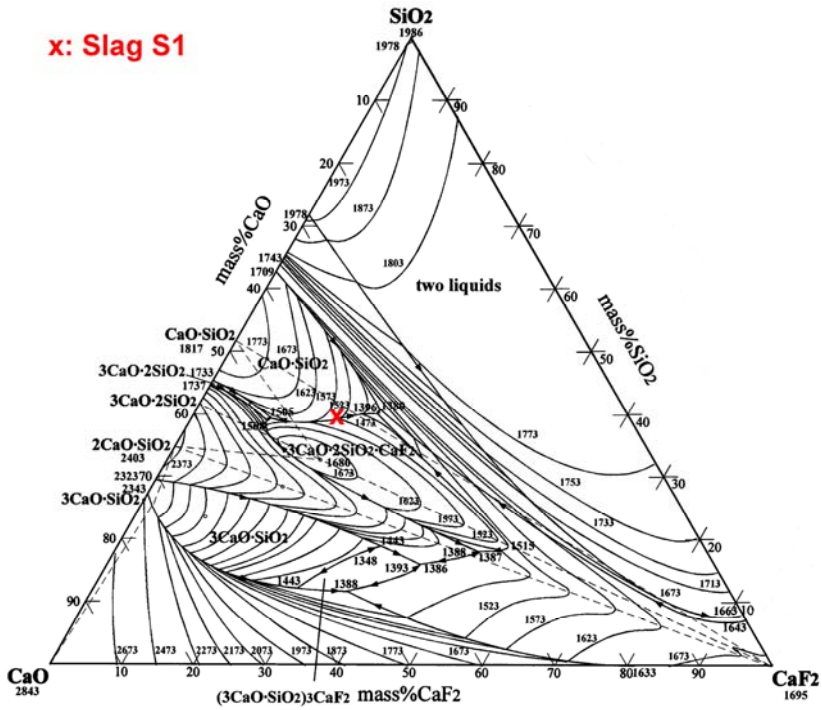

(a) CaO-SiO$_2$-CaF$_2$[123]

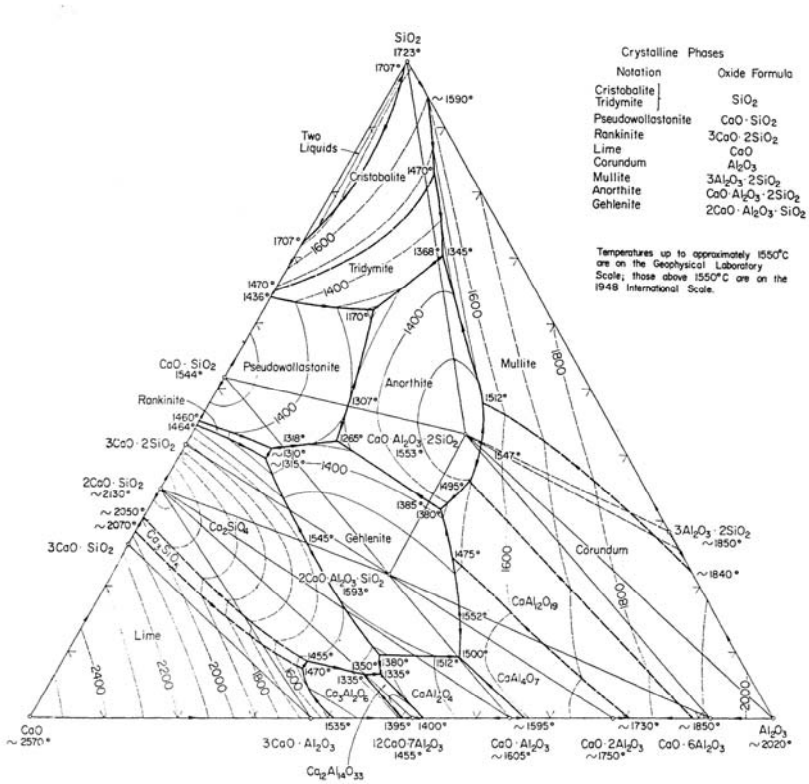

(b) CaO-SiO$_2$-Al$_2$O$_3$[124]

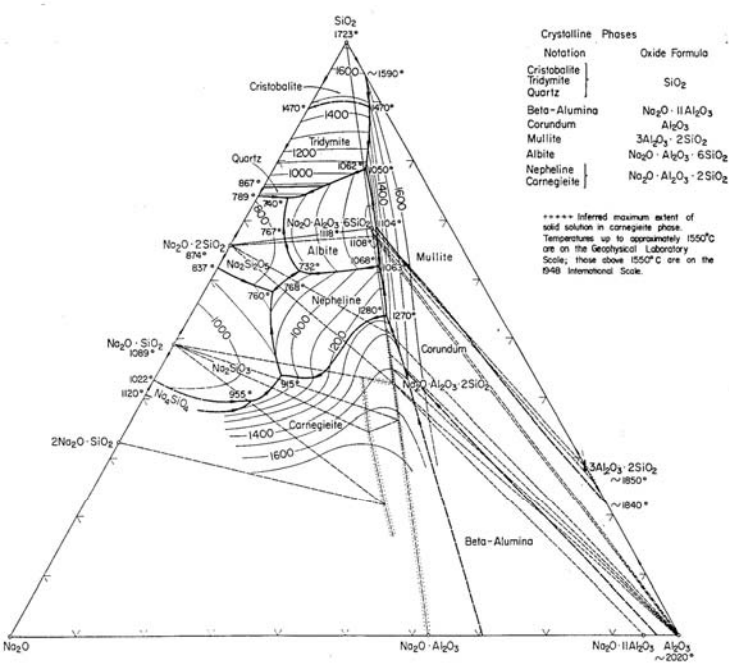

(c) SiO_2-Al_2O_3-Na_2O[124]

Compounds	CaO	Na_2O	SiO_2	Temp.	
SiO_2			100.0	1710	M
α CaO·SiO_2	48.3		51.7	1540	M
β CaO·SiO_2	48.3		51.7	1180	I
Na_2O·SiO_2		50.8	49.2	1088	M
Na_2O·$2SiO_2$		34.1	65.9	874	M
$2Na_2O$·CaO·$3SiO_2$	15.6	34.4	50.0	1141	D
Na_2O·3CaO·$6SiO_2$	28.5	10.5	61.0	1047	D
Na_2O·2CaO·$3SiO_2$	31.6	17.5	50.9	1284	M

M = Melting Point
D = Decomposition Point
I = Inversion Point

Point		Crystal Phases	CaO	Na_2O	SiO_2	Temp.
△	A	NS-N_2CS_3	3.0			1060
•	B	N_2CS_3-NC_2S_3	11.5			1141
△	C	NC_2S_3-αCS	33.0			1280
△	D	αCS-S	37.0		63.0	1436
⊙	E	T-Quartz		24.3	75.7	870
△	F	Quartz-NS_2		26.4	73.6	790
✻	K	NS_2-NS-N_2CS_3	1.8	37.5	60.7	821
○	L	N_2CS_3-NC_2S_3-NS_2	2.0	36.6	61.4	827
○	N	NS_2-NC_2S_3-NC_3S_6	5.2	24.1	70.7	740
✻	O	NC_3S_6-Q-NS_2	5.2	21.3	73.5	725
⊙	P	Q-NC_3S_6-T	7.0	18.7	74.3	870
○	Q	T-βCS-NC_3S_6	12.9	13.7	73.4	1035
○	R	NC_3S_6-NC_2S_3-βCS	14.5	19.0	66.5	1030
•	S	βCS-NC_2S_3-αCS	19.5	17.7	62.8	1110
•	T	αCS-S-βCS	15.6	11.4	73.0	1110
△	I	NS-NS_2		38.0		840

△ Binary Eutectic
✻ Ternary Eutectic
• Decomposition Point
○ Reaction Point
⊙ Inversion Point
C = CaO N = Na_2O
S = SiO_2 Q = Quartz
T = Tridymite

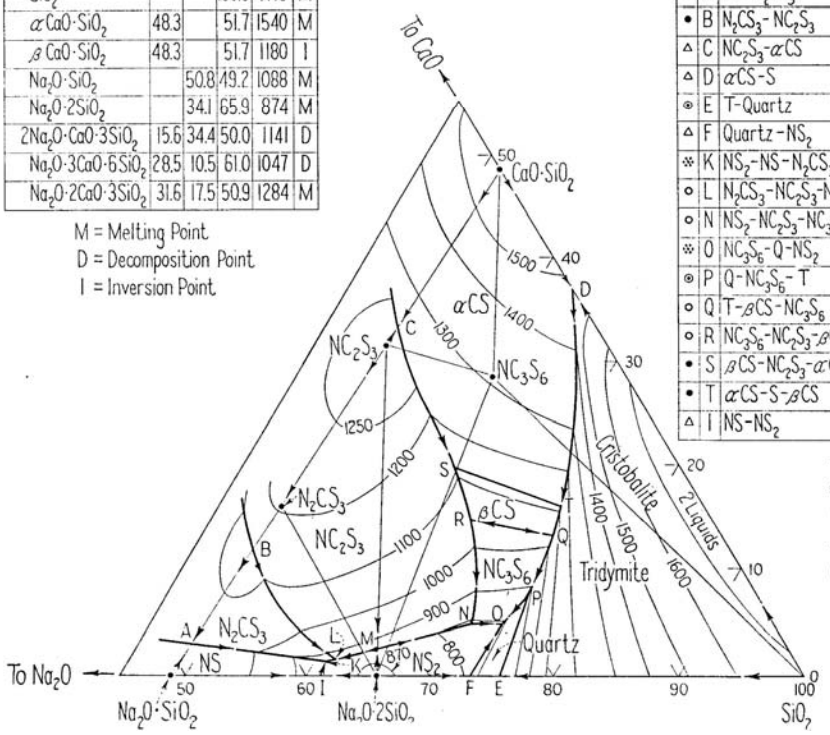

(d) CaO-SiO_2-Na_2O[124]

Figure 2.4 Ternary phase diagrams showing liquidus temperature contours

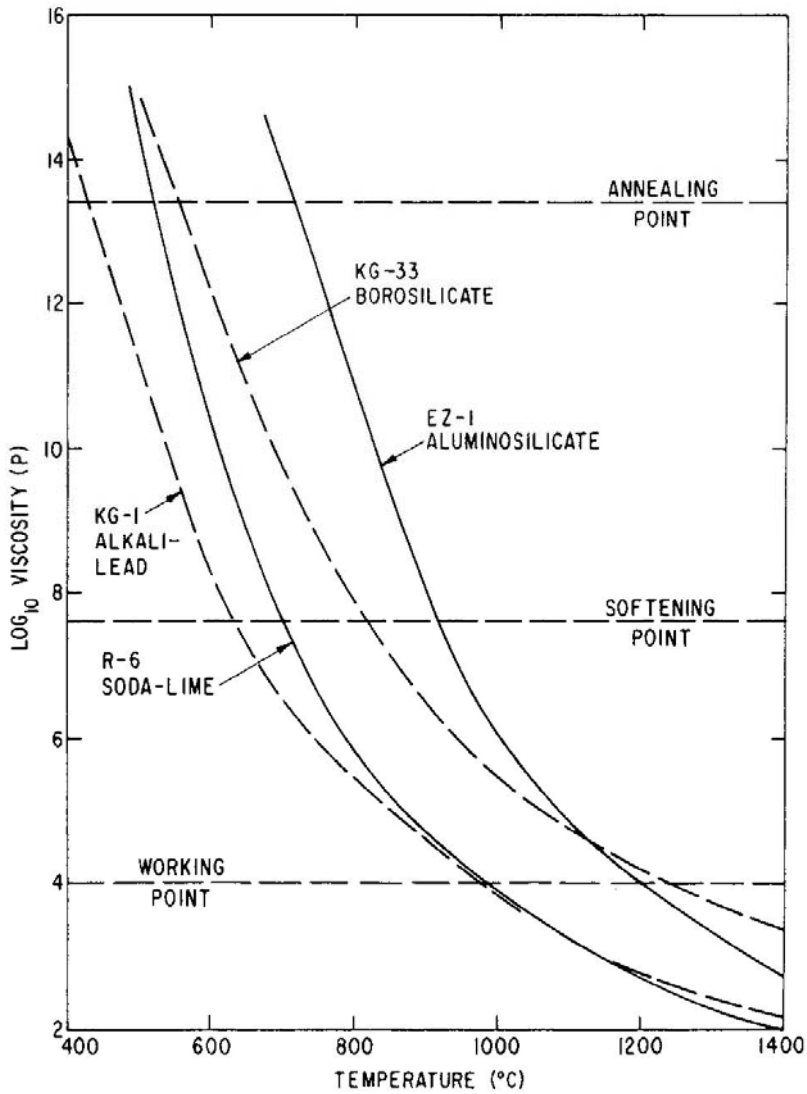

Figure 2.5 Viscosity of some commercial silicate glasses[126]

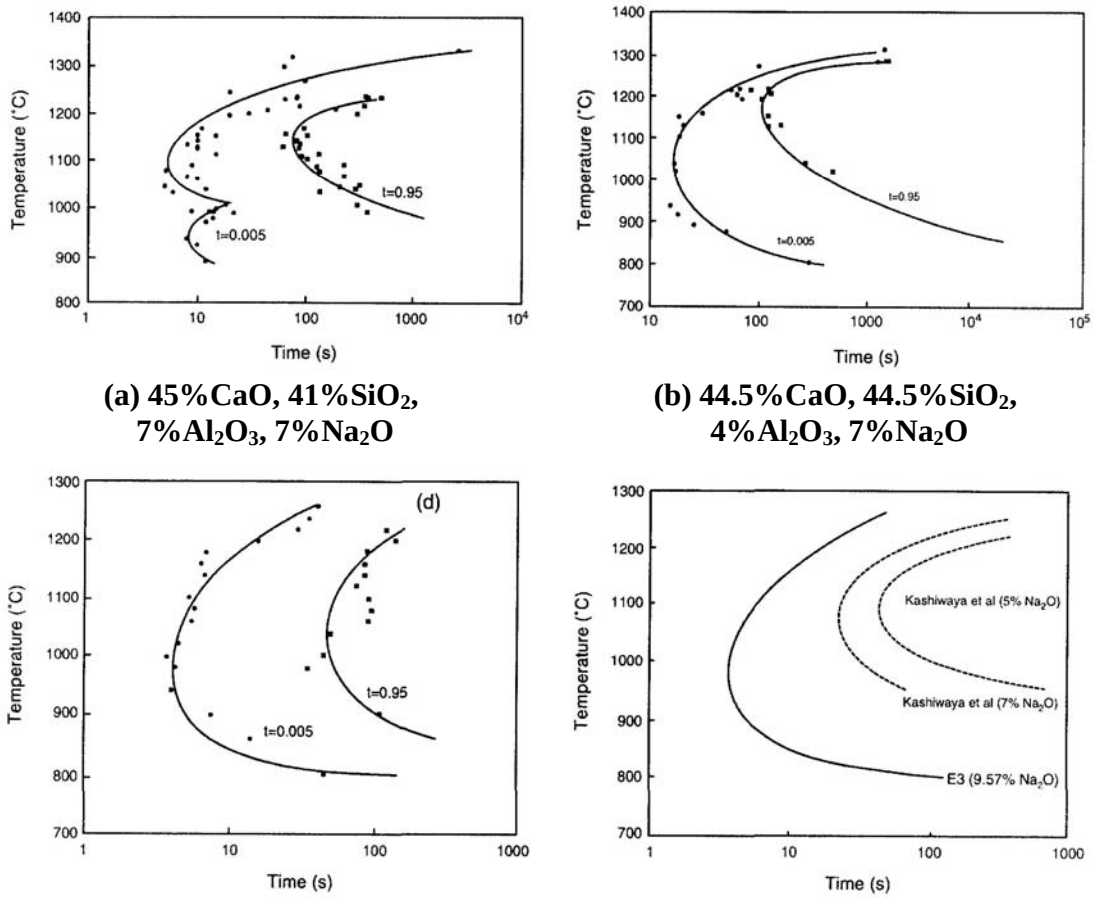

(a) 45%CaO, 41%SiO_2, 7%Al_2O_3, 7%Na_2O

(b) 44.5%CaO, 44.5%SiO_2, 4%Al_2O_3, 7%Na_2O

(c) 39.6%CaO, 40.9%SiO_2, 6.9%Al_2O_3, 9.6%Na_2O

(d) 43~44%CaO, 43~44%SiO_2, 7%Al_2O_3, 5~7%Na_2O

Figure 2.6 TTT curves obtained by double thermocouple technique[145]

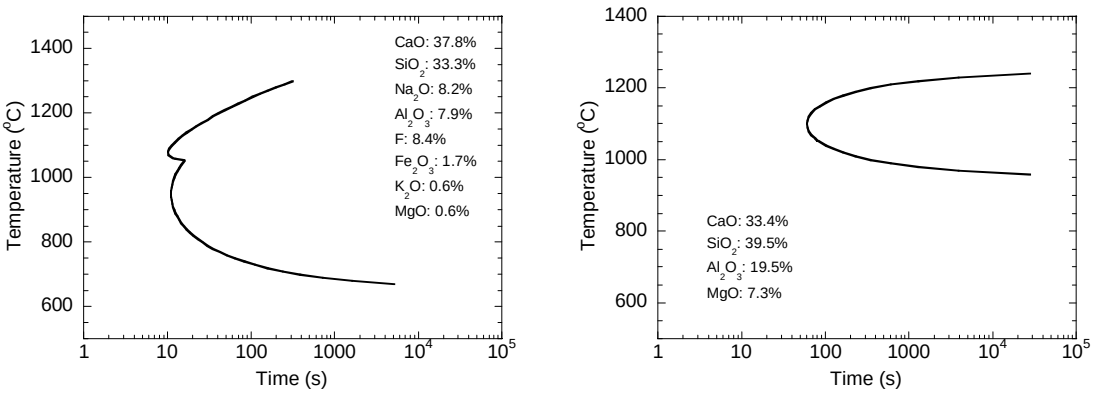

(a) Typical crystalline slag[143]

(b) Typical glassy slag[144]

Figure 2.7 TTT curves of typical crystalline and glassy slag

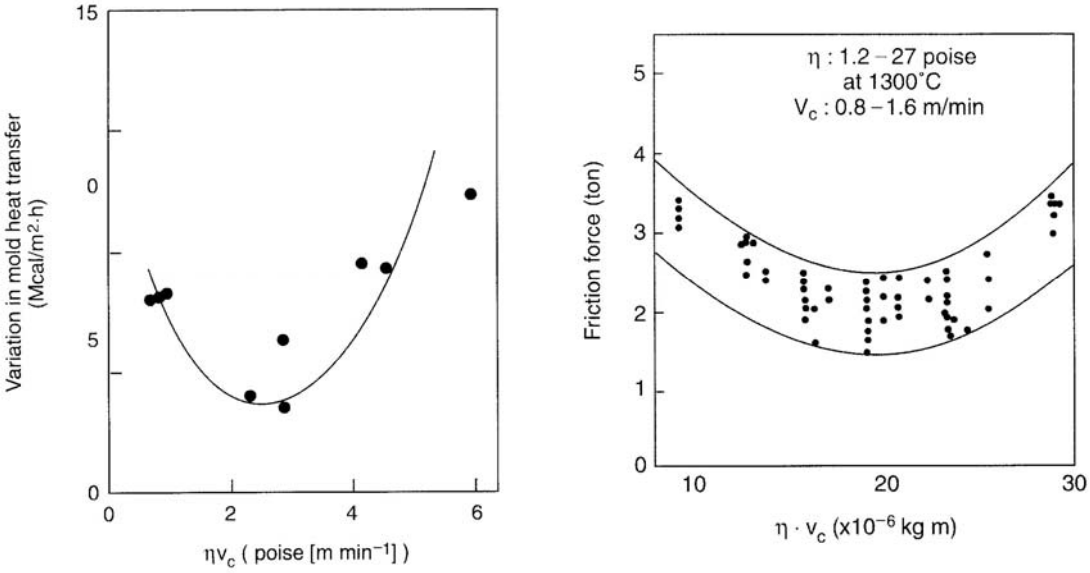

(a) Variation in heat transfer[157] **(b) Friction force[16]**

Figure 2.8 Effect of parameter η·Vc

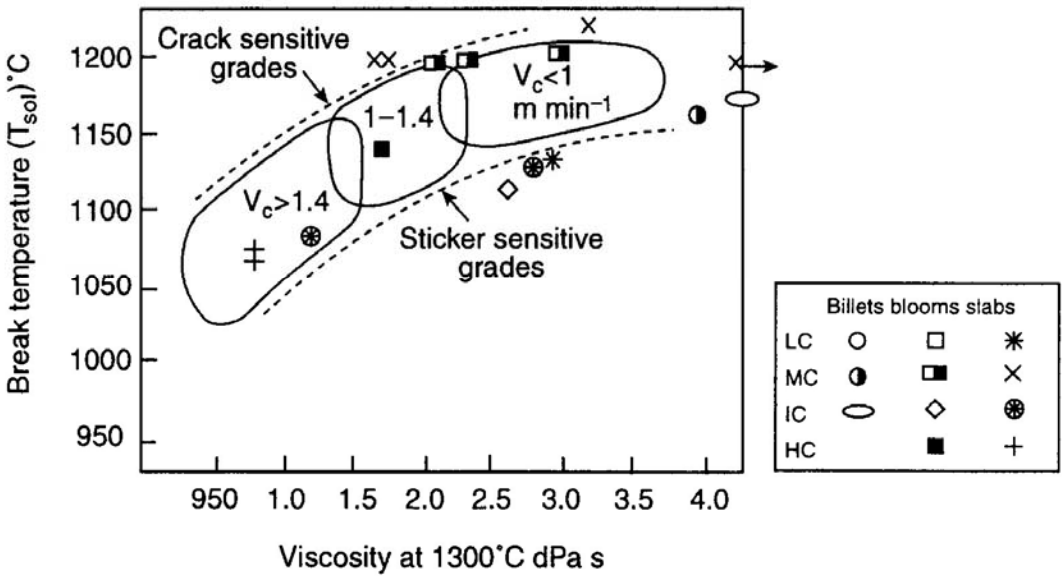

Figure 2.9 Relation between slag properties and casting speed[158]

CHAPTER 3. MODEL DESCRIPTION AND VALIDATION

3.1 Steel Solidification Model

The model in this work computes 1-D transient heat flow through the solidifying steel shell, coupled with 2-D steady-state heat conduction within the mold wall. Superheat from the liquid steel was incorporated as a heat source at the steel solid/liquid interface. The model features a detailed treatment of the interfacial gap, including mass and momentum balances on the liquid and solid slag layers, friction between the slag and mold, and slag layer fracture. The model simulates axial (z) behavior down a chosen position on the mold perimeter. Wide-face, narrow-face and even corner simulations can thus be conducted separately.

3.1.1 Superheat Delivery

Before it can solidify, the steel must first cool from its initial pour temperature to the liquidus temperature. Due to turbulent convection in the liquid pool, this “superheat” contained in the liquid is not distributed uniformly. A small database of results from a 3-D fluid flow model[61] is used to determine the heat flux, q_{sh}, delivered to the solid/liquid interface due to the superheat dissipation, as a function of distance below the meniscus. The initial condition of the liquid steel at the meniscus is then simply the liquidus temperature.

Previous work[61] found that this “superheat flux” varies linearly with superheat temperature difference and also is almost directly proportional to casting speed. The

superheat flux function in the closest database case is adjusted to correspond with the current superheat temperature difference, ΔT_{sup}, and casting speed, V_c, as follows:

$$q_{sh} = q_{sh}^{o} \frac{\Delta T_{\sup}}{\Delta T_{\sup}^{o}} \frac{V_c}{V_c^{o}} \tag{3.1}$$

where q_{sh}^{o} is the superheat flux profile from the database case with conditions of superheat temperature difference $\Delta T_{\sup}^{o}$ and casting speed V_c^{o}. Further adjustments are made to translate the heat flux peak to account for differences in nozzle configuration between the current conditions and the database. Examples of the superheat flux function are included in Figure 3.1, which represents results for a typical bifurcated, downward-directed nozzle[61]. The influence of this function is insignificant to shell growth over most of the wide face, where the superheat flux is small and contact with the mold is good.

3.1.2 Heat Conduction in the Solidifying Steel Shell

Temperature in the thin solidifying steel shell is governed by the 1-D transient heat conduction equation, which becomes the following on applying the chain rule to the temperature-dependent conductivity:

$$\rho_{steel} Cp_{steel}^{*} \frac{\partial T}{\partial t} = k_{steel} \frac{\partial^2 T}{\partial x^2} + \frac{\partial k_{steel}}{\partial T} \left(\frac{\partial T}{\partial x} \right)^2 \tag{3.2}$$

Temperature dependent properties for carbon steel are given in Appendix B[159]. Both sensible and latent heat of steel are included in the effective specific heat, Cp_{steel}^{*}, explained in Section 3.1.5-C.

This equation assumes that axial (z) heat conduction is negligible in the steel, which is reasonable past the top 10mm, due to the large advection component as indicated by the large Péclet number:

$Pe = \frac{V_c Z_{mold} \rho_{steel} Cp_{steel}}{k_{steel}} = \frac{0.0167 \times 0.81 \times 7400 \times 670}{30} = 2236$. The simulation domain for this portion of the model is a slice through the liquid steel and solid shell, which moves downward at the casting speed, as pictured in Figure 3.1 and Figure A1 together with typical interface conditions. At the internal solid/liquid steel interface, the "superheat flux", q_{sh}, delivered from the turbulent liquid pool, (section 3.1.1), is imposed as a source term. From the external surface of the shell, interfacial heat flux, q_{int}, is lost to the gap, which depends on the mold and slag layer computations, described in the following two sections. Appendix A provides the explicit finite-difference solution of Eq.(3.2), including both of these boundary conditions.

3.1.3 Microsegregation Model

The previous model uses the equilibrium Fe-C phase diagram to calculate steel liquidus, solidus, peritectic temperature and phase fractions which include the influences of Mn, Si, Al, S, P etc. 14 elements[8, 160]. To model realistic microsegregation during solidification of steel, an analytical model[161] based on the Clyne-Kurz equation has been added into CON1D. The non-equilibrium model is extended to take into account the effect of multiple components, a columnar dendrite microstructure, coursing, and the δ/γ transformation, which was developed by Won[161]. This model is implemented in this work and applied to predict phase fractions during solidification, microsegregation of solute elements, the solidus temperature and the secondary dendrite arm spacing. The phase fractions are then used for calculating temperature dependent steel thermal properties[159, 162]

Liquidus, solidus and peritectic temperatures depend on steel composition and cooling rate, C_R, as following:

$$T_{liq} = T_{pure} - \sum_i m_i \cdot C_{0,i} \tag{3.3}$$

$$T_{sol} = T_{pure} - \sum_i m_i \cdot C_{L,i}\left(C_{0,i}, C_R, k_i, D_i, f_s = 1\right) \tag{3.4}$$

$$T^{\delta/\gamma} = T^{\delta/\gamma}_{pure} - \sum_i n_i \cdot k_i^{\delta/L} \cdot C^{\delta}_{L,i} \tag{3.5}$$

Extended data needed for this model are listed in Table 3.1 and include the partition coefficients, k_i, diffusion coefficients, D_i, for each phase, the slopes of the equilibrium liquidus, m_i, and the slopes of Ar_4 lines, n_i, for the pseudo-binary alloys of 14 elements with iron. The results are not very sensitive to cooling rate, as the accompanying dendrite arm spacing change tends to compensate[161].

3.1.4 Ideal Taper

The narrow-face of the mold should be tapered to match the shrinkage of the steel shell, which is cooling against the wide face. Previous work has determined that this shrinkage depends mainly on the surface temperature of the shell and the steel grade[50]. The model predicts ideal average taper, by dividing the thermal strain, ε, by distance down the mold (instantaneous taper) or by the mold length (total taper per m). Thermal shrinkage strain is estimated here in two different ways, firstly ε_{th1}, by:

$$\varepsilon_{th1} = TLE(T_{sol}) - TLE(T_s) \tag{3.6}$$

Another method to calculate shrinkage was developed by Dippenaar[73, 74]. The strain ε_{th2}, is computed by summing the average thermal linear expansion of the solid portion of the shell between each pair of consecutive time steps:

$$\varepsilon_{th2} = \sum_{t=0}^{t}\left(\left(\frac{1}{i}\right)\sum_{i=1}^{solid\ nodes}\left(TLE\left(T_i^t\right) - TLE\left(T_i^{t+\Delta t}\right)\right)\right) \tag{3.7}$$

Here, TLE is the thermal linear expansion function for the given steel grade, calculated from weighted averages of the phases present. This model also includes the effect of mold distortion, slag layer thickness and funnel mold extra length (if present). It has been applied elsewhere to predict ideal taper[21]

3.1.5 Steel Properties

The program includes several different choices for steel properties, including simple constants input by the user. By default, the liquidus temperature, solidus temperature, phase fraction curve, thermal conductivity, specific heat and thermal linear expansion are all calculated as functions of composition and temperature. Steel density, ρ_{steel}, latent heat, L_f, and steel surface emissivity, ε_{steel}, are constants. For carbon steel: ρ_{steel} =7400kg/m^3, L_f =271kJ/kg, ε_{steel} =0.8

A. Phase Fraction

By default, equilibrium lever-rule calculations are performed on an Fe-C phase diagram, whose phase field lines are specified as simple linear functions of alloy content (including the influences of Si, Cr, Mn, Ni, Mo, Cu, Ti, P, S, Al, V, N, Nb and W) reported by Kagawa[160] in order to calculate steel liquidus, solidus, peritectic temperature and phase fractions. Alternatively, the user can choose a non-equilibrium micro-segregation model[161] to find these values, which was extended in this work to include the effects of 14 elements, given in Table 3.1. For a 0.044%C, 0.022%Mn, 0.006%S, 0.01%P, 0.009%Si 0.049%Al plain carbon steel, the equilibrium phase diagram model calculates T_{liq}=1528°C, T_{sol}=1509°C, while with 10°C/second cooling rate,

the segregation model gives T_{liq}=1532°C, T_{sol}=1510°C. Figure 3.2 shows the solid fraction temperature curve in the mushy zone obtained from both models. Both models produce similar results. The surprising finding that the equilibrium model produces slightly lower transformation temperatures shows that differences in the coefficients which define the alloy-dependent equilibrium lines are more important than the non-equilibrium effects due to segregation at the typical cooling rates, dendrite arm spacing, and compositions considered.

B. Thermal Conductivity of Steel

The thermal conductivity of carbon steel is calculated as a function of temperature, carbon content and phase fraction, which was fitted from measured data compiled by K. Harste[159]. The specific functions are listed in Appendix B. Stainless steel thermal conductivity is calculated according to the fitted equation based on measured data compiled by Pehlke[162]. Figure 3.3 compares some typical plain-carbon steel, austenitic-stainless steel and ferritic stainless steel conductivities. Thermal conductivity of the liquid is not artificially increased, as common in other models, because the effect of liquid convection is accounted for in the superheat flux function, which is calculated by models[61] which fully incorporate the effects of turbulent flow.

C. Effective Specific Heat of Steel

Specific heat is calculated as a function of temperature, carbon content, phase fraction and steel grade. Appendix B gives the specific heat functions for carbon steel, found by differentiating the enthalpy curve from K. Harste[159]. Refer to Pehlke[162] for the specific heat functions of stainless steel. When the steel temperature is between the

solidus and liquidus temperatures, latent heat, L_f, is evolved using the liquid phase fraction curve found previously. The effective specific heat is then defined as:

$$C_p^* = \frac{dH}{dT} = C_p - L_f \frac{df_s}{dT} \tag{3.8}$$

Figure 3.4 shows the specific heat curve of AISI 1026 carbon steel using the micro-segregation model compared with measured data[162]. The curves for other alloys, such as used later, are similar except for within the mushy region. So long as it properly matches the total latent heat, its exact shape has little effect on shell growth or surface temperature.

D. Thermal Linear Expansion of Steel

By default, the thermal linear expansion, TLE, needed for shrinkage and ideal taper calculations is computed as a function of steel density,

$$TLE = \sqrt[3]{\frac{\rho_0}{\rho(T)}} - 1 \tag{3.9}$$

where $\rho_0 = \rho_{steel}$. The composition and temperature-dependent steel density function for carbon steel, $\rho(T)$ is taken from measurements tabulated by Harste[159] and is listed in Appendix B. Constant density, ρ_{steel} is adopted for the heat flow calculations in order to enforce constant mass in the fixed-domain computation.

Alternatively, the user may input a thermal linear expansion coefficient, α, so:

$$TLE = \alpha\left(T - T_{sol}\right) \tag{3.10}$$

This is done for stainless steel, where α is taken from Pehlke[162].

3.1.6 Steel Solidification Model Validation

The solidification model is verified here through comparison with an analytical solution for 1-D heat conduction with phase change[163]. This solution assumes constant shell surface temperature and constant steel properties. Table 3.2 lists the constants used in both the analytical solution and the CON1D validation case, which are chosen for typical conditions expected in practice. The difference between the steel liquidus and solidus temperatures is only 0.1^{o}C to approximate the single melting temperature assumed in analytical solution, which is set to the mean of T_{liq} and T_{sol} used in CON1D. The pour temperature is set to the liquidus because superheat is neglected in the analytical solution. For the CON1D model, the time step size Δt is 0.004second and node spacing is 0.5mm.

Figure 3.5 compares results from the analytical solution and CON1D for (a) the temperature distribution through the shell at different times and (b) the growth of shell thickness with time. The results show that the predictions of the CON1D model is very accurate, so the same time step and mesh size are used in the following cases.

3.2 Heat Transfer and Mass Balance in Slag

3.2.1 Heat transfer Across the Interfacial Gap

Heat transfer across the interfacial gap governs the heat flux leaving the steel, q_{int}, to enter the mold. To calculate this at every position down the mold, the model evaluates an effective heat transfer coefficient, h_{gap}, between the surface temperature of the steel shell, T_s, and the hot face of the mold wall, T_{mold}:

$$q_{\text{int}} = h_{gap}\left(T_s - T_{mold}\right) \tag{3.11}$$

$$h_{gap} = 1\Big/\left(\left(r_{contact} + \frac{d_{air}}{k_{air}} + \frac{d_{solid}}{k_{solid}}\right) + 1\Big/\left(1\Big/\left(\frac{d_{liquid}}{k_{liquid}} + \frac{d_{eff}}{k_{eff}}\right) + h_{rad}\right)\right) \tag{3.12}$$

Heat conduction depends on the thermal resistances of four different layers of materials contained in the gap: oscillation marks, liquid slag, solid slag and a possible air gap. These depend on the time-averaged thickness profiles down the mold of the different layers and their corresponding thermal conductivities. The model for gap heat conduction is illustrated in Figure 3.6 and Figure 3.7. The most important resistances are usually the slag layers, whose thicknesses are calculated as described in the next section. The latent heat evolved by liquid slag solidification is less than 1% of the heat transferred across the gap, so it is neglected in this model (refer to Appendix C for detailed calculation).

The equivalent air gap, d_{air}, is specified as input data and includes the contact resistances[164] at the slag/shell and slag/mold interfaces. It may also include a gap due to shrinkage of the steel shell, which can be calculated using a separate thermal-stress model[50]. The shrinkage gap is affected by the mold taper and also by mold distortion, which can be calculated by another model[64]. This gap is important when simulating down positions near the corner.

All non-uniformities in the flatness of the shell surface are incorporated into the model through the prescribed oscillation mark depth, d_{mark}, and width, L_{mark}, as pictured in Figure 3.8. Assuming shallow triangle-shaped marks or depressions, d_{osc} is the volume-averaged oscillation mark depth:

$$d_{osc} = \frac{0.5 L_{mark} d_{mark}}{L_{pitch}} \tag{3.13}$$

where L_{pitch} is the ratio of the casting speed V_c to the oscillation frequency, *freq*.

The oscillation marks affect heat transfer in two different ways. Firstly, the oscillation marks consume mold slag, so affect the slag layer thicknesses, as described in next section. Secondly, they reduce heat conduction by effectively providing an extra gap. This extra gap is represented by d_{eff}, calculated based on a heat balance[31] which produces the same total heat flux as found by combining the heat fluxes across the two parallel conduction paths (at or adjacent to the oscillation mark), averaged spatially (z-direction) using an appropriate weighted average:

$$d_{eff} = \frac{0.5\, L_{mark} d_{mark}}{\left(L_{pitch} - L_{mark}\right)\left(1 + 0.5 \frac{d_{mark}}{d_{liquid} + d_{solid}} \frac{k_{gap}}{k_{mark}}\right) + L_{mark}} \tag{3.14}$$

$$k_{gap} = \left(d_{liquid} + d_{solid}\right) \Bigg/ \left(\frac{d_{solid}}{k_{solid}} + 1 \Bigg/ \left(\frac{k_{liquid}}{d_{liquid}} + h_{rad\_liquid}\right)\right) \tag{3.15}$$

The oscillation marks are assumed to be filled with either slag, air, or a mixture, depending on the local shell surface temperature. This governs the value of k_{mark}.

Except for perhaps a microscopically thin glassy surface layer, experience has shown that the cold slag layer adjacent to the mold wall is usually crystalline[142, 165], and thus opaque. Thus, radiation occurs only across the semi-transparent hot glassy or liquid layer above T_{fsol}[137, 166], according to Eq.(3.16), as shown in Figure 3.6:

$$h_{rad} = \frac{m^2 \sigma \left(T_{sK}^2 + T_{fsol\,K}{}^2\right)\left(T_{sK} + T_{fsol\,K}\right)}{0.75 a \left(d_{liquid} + d_{eff}\right) + \frac{1}{\varepsilon_{slag}} + \frac{1}{\varepsilon_{steel}} - 1} \qquad \left(T_{mold} < T_{fsol}\right) \tag{3.16}$$

where m is slag refractive index; T_{sK} and $T_{fsol\,K}$ are T_s and T_{fsol} expressed in Kelvin, a is average absorption coefficient of the slag, assuming graybody radiation (ε_{slag} =0.9). If the liquid slag runs out, so that $T_s < T_{fsol}$, then h_{rad}=0. In the unlikely event that $T_{mold} \geq T_{fsol}$,

ε_{slag} would be replaced by ε_{mold}, and T_{fsol} by T_{mold} in Eq.(3.16). Jenkins showed that this simple equation to characterize radiation with absorption across a gap, Eq.(3.16), is accurate to within 10% relative to a full multi-view factor analysis including radiation-conduction[82]. This is sufficiently accurate because the radiation component itself usually contributes only on the order of 10% of the gap heat transfer.

3.2.2 Mass and Momentum Balance on Powder Slag Layers

Slag is assumed to flow down the gap as two distinct layers: solid and liquid. The solid layer is assumed to move at a time-average velocity, V_{solid}, which is always between zero and the casting speed, V_c, according to the input solid slag speed ratio, f_v.

$$V_{solid} = f_v \cdot V_c \tag{3.17}$$

The downward velocity profile across the liquid slag layer is governed by the simplified Navier-Stokes equation, assuming laminar Couette flow:

$$\frac{\partial}{\partial \mathrm{x}}\left(\mu \frac{\partial V_z}{\partial \mathrm{x}}\right) = \left(\rho_{steel} - \rho_{slag}\right) g \tag{3.18}$$

A small body force opposing flow down the wide face gap is created by the difference between the ferrostatic pressure from the liquid steel, $\rho_{steel}\, g$, transmitted through the solid steel shell, and the average weight of the slag, $\rho_{slag}\, g$. The time-average velocity of the liquid slag described by Eq.(3.18), V_z, is subjected to boundary conditions constraining it to the casting speed, V_c on its hot side and to the solid slag velocity, V_{solid} on its cold side.

The temperature dependent viscosity of the liquid slag is fit to a simple power-law relation, which better represents low-temperature high-viscosity behavior than a simple Arrhenius equation[99]:

$$\mu = \mu_o \left(\frac{T_o - T_{fsol}}{T - T_{fsol}} \right)^n \tag{3.19}$$

where the parameters T_{fsol} and n are chosen empirically to fit measured data and μ_o is the viscosity measured at the reference temperature, T_o, usually chosen to be 1300°C. Using only few important slag properties, T_{fsol}, μ_{1300}, and an empirical index n, this equation reasonable models the entire viscosity curve, and also enables an analytical solution for slag flow in the gap as derived in the following sections. A typical curve obtained with this function is shown in Figure 3.9 together with the measured viscosities by Lanyi that it was fit to match[100]. Mold slags in service absorb some Al_2O_3 from the steel, which changes their properties, including decreasing the solidification temperature[100, 151]. The second curve in Figure 3.9 was constructed for a reported solidification temperature T_{fsol} of 1045°C and viscosity at 1300°C of 1.1Poise, and was used later in model calibration.

By approximating temperature across the gap to vary linearly, Eq.(3.17) through Eq.(3.19) can be solved for the time-averaged velocity distribution across the slag layers, which is illustrated in Figure 3.7. Integrating across the liquid region yields an average velocity for the liquid layer, $\overline{V}_{liquid}$:

$$\overline{V}_{liquid} = \frac{\left(\rho_{slag} - \rho_{steel}\right) g d^2_{liquid}}{\mu_s \left(n+2\right)^2 \left(n+3\right)} + \frac{V_c + V_{solid}\left(n+1\right)}{\left(n+2\right)} \tag{3.20}$$

where μ_s is the slag viscosity at liquid layer/steel shell interface. A mass balance was imposed to match the measured (known) powder consumption, Q_{slag}(kg/m^2), with the total molten slag flow rate past every location down the interfacial gap, neglecting the carbon content component, which burns off. This consumption rate is expressed as mass

of slag per unit area of the strand surface, which can be found from the consumption per mass of product, M_{slag}(kg/ton) :

$$Q_{slag}\left(kg/m^2\right) = M_{slag}\left(kg/ton\right) \times \rho_{steel} \times \frac{W \times N}{2\left(W+N\right)} \tag{3.21}$$

where W is slab width and N is slab thickness. Slag can be carried downward by the solid layer, the liquid layer, and in the oscillations marks:

$$\frac{Q_{slag} \times V_c}{\rho_{slag}} = V_{solid} d_{solid} + \overline{V}_{liquid} d_{liquid} + V_c d_{osc} \tag{3.22}$$

The liquid and solid layer thicknesses are obtained by solving a fourth order polynomial equation found by combining Eq.(3.12) and Eq.(3.22). The transport of slag by the oscillation marks depends on the lubrication state, discussed next.

Three different regions are distinguished down the mold, according to the lubrication condition. Close to the meniscus, a solid slag rim exists against the mold wall. Its thickness profile must be specified, as it depends on transient phenomena not yet in the model.

The second region, shown in Figure 3.7, allows the solid slag layer to move at the slow time averaged velocity V_{solid}. It always also includes oscillation marks filled with molten slag and a continuous liquid slag layer, which remains present so long as the outer surface temperature of the steel T_s' exceeds the slag solidification temperature, T_{fsol}:

$$T_s^{'} = T_s - q_{\text{int}} \cdot \frac{d_{eff}}{k_{mark}} \tag{3.23}$$

Slag in the oscillation marks remains liquid longer, due to the higher local shell temperature at their roots, T_s. Once the oscillation mark roots cool below the slag solidification temperature, however, the slag entrapped in them solidifies. This defines

the third region, which consists of totally solid slag, moving downward at the uniform speed, V_{solid}. The oscillation marks no longer transport slag, so become filled with air. The transition between the second and third regions is gradual.

3.3 Lubrication and Friction Model in Gap

It is important to emphasize that the above interfacial heat transfer model represents steady, time-averaged behavior only. To investigate transient phenomena, a transient version of this model is developed in this work to calculate liquid flow and solid slag stress during the oscillation cycle, which is applied to predict transient shear stress, friction, slip and fracture of the slag layers. Figure 3.10 shows the domain used in this transient model. Table 3.3 gives the typical casting conditions and simulation parameters used in model validation.

3.3.1 Liquid Slag Layer Flow Model

For simplicity, the slag is treated as two layers each with variable thickness in the vertical (z-) direction: a rigid solid layer and a laminar liquid layer with temperature dependent viscosity. A schematic profile of the mold, slag and steel shell velocities is shown in Figure 3.11 for the case when the solid slag layer is stuck to the mold wall so its average downward velocity, V_s, is zero. The steel shell moves downward at the casting speed V_c, and the mold oscillates in the vertical direction with the sinusoidal displacement function:

$$Z_m = Z_0 + \frac{s}{2}\sin\left(2\pi ft\right) \tag{3.24}$$

A mass balance on the liquid slag layer gives the following continuity equation, assuming incompressible flow, constant density and identical behavior within any vertical slice, so velocity across the slab width, V_y is zero:

$$\frac{\partial V_x}{\partial x} + \frac{\partial V_z}{\partial z} = 0 \tag{3.25}$$

The following Navier-Stokes equation characterizes the laminar viscous flow of liquid slag vertically within the gap:

$$\begin{aligned} &\rho_{slag} \cdot \left(\frac{\partial V_z}{\partial t} + V_x \cdot \frac{\partial V_z}{\partial x} + V_y \cdot \frac{\partial V_z}{\partial y} + V_z \cdot \frac{\partial V_z}{\partial z} \right) \\ &= -\frac{\partial P}{\partial z} + \frac{\partial \tau_{xz}}{\partial x} + \frac{\partial \tau_{yz}}{\partial y} + \frac{\partial \tau_{zz}}{\partial z} + \rho_{slag} g \end{aligned} \tag{3.26}$$

In the horizontal direction, the internal pressure, P, is assumed to equal the ferrostatic pressure, which is transmitted directly across the steel shell, so:

$$\frac{\partial P}{\partial z} = \rho_{steel} g \tag{3.27}$$

This is reasonable everywhere except near the corners that support themselves and near the meniscus where pressure fluctuates. Thus, this model is appropriate within most of the gap over the unsupported wide faces of slab casting.

In Eq.(3.26), $V_y \frac{\partial V_z}{\partial y}$ and $\frac{\partial \tau_{yz}}{\partial y}$ can be neglected because V_y=0. The three terms $\rho_{slag} V_x \frac{\partial V_z}{\partial y}$, $\rho_{slag} V_z \frac{\partial V_z}{\partial z}$ and $\frac{\partial \tau_{zz}}{\partial z}$ are shown to be negligible in the next section for typical continuous casting conditions. Thus Eq.(3.26) simplifies to the following as gravity and downward viscous drag by the steel shell must balance the upward squeezing from the ferrostatic pressure:

$$\rho_{slag} \cdot \frac{\partial V_z}{\partial t} = \frac{\partial \tau_{xz}}{\partial x} + \left(\rho_{slag} - \rho_{steel}\right) g \tag{3.28}$$

Shear stress in the liquid slag layer depends on the velocity gradient at each point across the channel:

$$\tau_{xz} = \mu \frac{\partial V_z}{\partial x} \tag{3.29}$$

Setting temperature at the hot liquid layer side, T_s', as the reference temperature, Eq.(3.19) is rewritten as:

$$\mu = \mu_s \left(\frac{T_s^{'} - T_{fsol}}{T - T_{fsol}} \right)^n \tag{3.30}$$

Assuming that temperature across the liquid slag layer thickness is linear gives:

$$T = \frac{x}{d_l}\left(T_s^{'} - T_{fsol}\right) + \ T_{fsol} \tag{3.31}$$

Substituting Eq.(3.31) into Eq.(3.30) and replacing the viscosity term in Eq.(3.29) with this position dependent viscosity yields:

$$\tau_{xz} = \mu_s \frac{d_l^n}{x^n} \frac{\partial V_z}{\partial x} \tag{3.32}$$

Differentiating Eq.(3.32) and substituting into Eq.(3.28), yields the following momentum equation, governing the velocity distribution in the liquid film:

$$\rho_{slag} \frac{\partial V_z}{\partial t} = \mu_s \frac{d_l^n}{x^n} \frac{\partial^2 V_z}{\partial x^2} \ - \mu_s \frac{n d_l^n}{x^{n+1}} \frac{\partial V_z}{\partial x} + \left(\rho_{slag} - \rho_{steel}\right) g \tag{3.33}$$

Differentiating Eq.(3.24) to get mold velocity V_m, and assuming the solid slag is attached to the mold wall, the boundary conditions for the liquid slag layer model, Eq.(3.33), are:

$$\text{solid/liquid slag layer interface:} V_z \Big|_{x=0} = V_s = V_m = \pi s f \cdot \cos\left(2\pi f t\right) \tag{3.34}$$

liquid slag/steel shell interface: $V_z \big|_{x=d_l} = V_c$ (3.35)

Neglecting $\frac{\partial V_z}{\partial t}$ and applying the boundary conditions Eqs.(3.34) and (3.35), Eq.(3.33) can be integrated to obtain the following "pseudo-transient" analytical solution:

$$V_z = \frac{-\left(\rho_{slag} - \rho_{steel}\right) g x^{n+2}}{\mu_s \left(n+2\right) d_l^n} + \left(\frac{\left(V_c - V_s\right)}{d_l} + \frac{\left(\rho_{slag} - \rho_{steel}\right) g d_l}{\mu_s \left(n+2\right)} \right) \frac{x^{n+1}}{d_l^n} + V_s \tag{3.36}$$

3.3.2 Liquid Slag Layer Flow Model Validation

To check the validity of the assumptions made to obtain Eq.(3.36), a fully transient numerical solution was obtained using an explicit finite-difference discretization of Eq.(3.33) with a central difference scheme:

$$\begin{aligned} V_z^{i\,(t+\Delta t)} &= V_z^{i\,(t)} + \frac{\Delta t}{\rho_{slag}} \\ &\left(\mu_s \frac{d_l^n}{x^n} \frac{V_z^{i+1(t)} - 2V_z^{i\,(t)} + V_z^{i-1(t)}}{\Delta x^2} - \mu_s \frac{n d_l^n}{x^{n+1}} \frac{V_z^{i+1(t)} - V_z^{i-1(t)}}{\Delta x} + \left(\rho_{slag} - \rho_{steel}\right) g \right) \end{aligned} \tag{3.37}$$

A MATLAB[167] program was coded to solve this equation with boundary conditions Eqs.(3.34) and (3.35) at different z-distances. Table 3.4 gives the parameters of 4 cases used in the MATLAB program. Cases (a)-(b) are based on heat transfer results for typical casting conditions as shown in Table 3.3; and Cases (c)-(d) use an extremely thick liquid layer (2mm) from Chavez's work[95]. Discretizing the continuity equation Eq.(3.25) and processing the results at different z-distances (specifically z=53mm and z=54mm for case (b)) allow computations of the other terms in Eq.(3.26).

Table 3.5 shows values of the different terms in Eq.(3.26) for case (b) at *t*=0.18s, x=0.16mm. Note that $\rho_{slag} V_x \frac{\partial V_z}{\partial x}$, $\rho_{slag} V_z \frac{\partial V_z}{\partial z}$ and $\frac{\partial \tau_{zz}}{\partial z}$ are negligible compared to the

other terms. Also note that the transient term $\rho_{slag}\frac{\partial V_z}{\partial t}$ contributes less than 1.5%, so can justifiably be neglected too.

Figure 3.12 shows typical velocity profiles computed with these models. For constant viscosity and a thin liquid layer, Figure 3.12(a), the velocity profiles are linear. Otherwise, nonlinearity is significant. Figure 3.12 also compares the numerical solution and the pseudo-transient analytical solution. It shows that the transient effect is negligible for a film thickness of 0.2mm. Even for an extreme case, 2mm thick liquid film, Figure 3.12(c), (d), the maximum transient effect is barely perceptible. Therefore the pseudo-transient analytical solution to the liquid slag layer flow equation, Eq.(3.36) is a reasonable approximation of the full transient solution.

Substituting Eq.(3.36) into Eq.(3.32) gives:

$$\tau_{xz} = \frac{(n+1)\mu_s(V_c - V_s)}{d_l} + \frac{(\rho_{slag} - \rho_{steel})g((n+1)d_l - (n+2)x)}{n+2} \tag{3.38}$$

Evaluating Eq.(3.38) at $x=d_l$ gives the shear stress at the slag/steel interface when a liquid slag layer is present:

$$\tau_{liquid\ flux/steel} = \mu_s\frac{(n+1)(V_c - V_s)}{d_l} - \frac{(\rho_{slag} - \rho_{steel})gd_l}{(n+2)} \tag{3.39}$$

3.3.3 Solid Slag Layer Stress Model

Near the meniscus, the solid slag layer attaches to the mold wall and oscillates with the mold. However, if the solid slag layer breaks, and where it breaks, could greatly affect heat transfer across the gap. A stress model is developed to investigate force balances and possible fracture in the solid slag layer.

The equilibrium force balance in the axial z-direction is:

$$\frac{\partial \tau_{xz}}{\partial x} + \frac{\partial \sigma_z}{\partial z} + F_z = 0 \tag{3.40}$$

Knowing that body forces F_z are negligible in the solid layer, Figure 3.13 illustrates the force balance in a solid slag layer discretization element cut from Figure 3.10 for four typical cases. Evaluating τ_{xz} in Eq.(3.38) at x=0 gives the shear stress boundary condition at the interface between the liquid and solid slag layers:

$$\tau_{s/l} = \mu_s \frac{(n+1)\left(V_c - V_s(t)\right)}{d_l} + \frac{(n+1)}{(n+2)}\left(\rho_{slag} - \rho_{steel}\right) g d_l \tag{3.41}$$

Note that this shear stress varies greatly during the oscillation cycle.

The maximum shear stress transmitted to the mold by Coulomb friction with the solid slag layer, due to relative motion of the mold and shell is:

$$\tau_{max} = \phi_{static} \cdot \sigma_x \tag{3.42}$$

The normal stress, σ_x, comes from the liquid steel ferrostatic pressure and the liquid slag pool above the meniscus, which generates a tiny additional head:

$$\sigma_x = -\left(\rho_{slag} g h_0 + \rho_{steel} g z\right) \tag{3.43}$$

Shear stress must be continuous across the gap, including both the boundaries at the mold and steel shell surfaces. When the liquid layer/steel interface shear stress is smaller than the maximum solid contact shear stress, then the friction force drops to match it, as shown in Figure 3.13(a). In this “liquid shear stress limited” case, Figure 3.13(a), the friction force is less than the maximum possible static friction given in Eq.(3.42). Ferrostatic pressure then generates axial stress σ_z in the solid layer that is compressive:

$$\sigma_z = -\frac{\upsilon}{1-\upsilon}\sigma_x \tag{3.44}$$

so *xz*-shear stress at the mold side can be calculated from Eqs.(3.40), (3.43), and (3.44)] as follows:

$$\tau_{mold} = -\int_{x=0}^{d_s} d\sigma_z / dz \cdot dx + \tau_{s/l} = \frac{\upsilon}{1-\upsilon}\rho_{steel} g d_s + \tau_{s/l} \tag{3.45}$$

Alternatively, if the liquid layer shear stress is larger than the maximum static friction, $\tau_{mold} = \tau_{max}$, then axial stress develops in the solid layer to compensate. In order to satisfy the force balance Eq.(3.40):

$$d\sigma_z = -d\tau_{xz} \cdot dz / dx \tag{3.46}$$

Discretizing Eq.(3.46) axially, and integrating across the thickness, the axial stress in the solid slag layer at $z+\Delta z$ is:

$$\sigma_{z+\Delta z} = \sigma_z - \frac{\tau_{max} - \tau_{s/l}}{d_s}\Delta z \tag{3.47}$$

Specifically, axial stress is tensile during the up-stroke and compressive in the down-stroke for this “mold friction limited” case shown in Figure 3.13(b). Furthermore, the axial tension accumulates over successive slices of the solid slag layer. The shear stress transmitted to the mold wall is the minimum of the maximum static friction stress and the solid/liquid interface stress:

$$\tau_{mold} = min\left(\frac{\upsilon}{1-\upsilon}\rho_{steel} g d_s + \tau_{s/l}, \tau_{max}\right) \tag{3.48}$$

3.3.4 Solid Slag Layer Stress Model Validation

To validate the stress model of the solid slag layer, a simplified case was solved using elastic finite-element stress analysis with ANSYS[168]. Figure 3.14 shows the

ANSYS model domain and mesh. The boundary condition at the mold side had displacements fixed to zero and at the liquid side was normal ferrostatic pressure, σ_x, from Eq.(3.43) and tangential shear stress, $\tau_{s/l}$ (from CON1D). Table 3.3 gives the input conditions and simulation parameters used in CON1D. Figure 3.15 compares the stress results from ANSYS and CON1D using Eqs.(3.47) and (3.48) and assuming the solid slag layer is stably attached to the mold wall. The CON1D model matches ANSYS except within 10mm near mold exit, where the real axial stress must quickly tend to zero (to match ambient atmospheric pressure).

3.3.5 Solid Slag Layer Fracture Model

If the axial stress exceeds the fracture strength, the solid slag layer will break, and be dragged down the mold wall. The shear stress on the mold/slag interface for this condition is:

$$\tau_{mold} = \phi_{moving} \cdot \sigma_x \tag{3.49}$$

Substituting Eqs. (3.41) and (3.49) into Eq.(3.45) can solve for the solid layer velocity V_s after it detaches from the mold wall. Fracture and sliding of the solid slag layer tend to create a gap between the upper attached solid layer and the lower moving layer. This gap may re-fill with liquid slag, and the solid layer might re-attach to the mold wall when the instantaneous velocity of the oscillating mold wall equals the moving solid slag layer velocity. The time for the liquid slag to fill the gap and the solid slag to re-attach depends on the slag consumption rate and liquid slag fluidity. The fracture and filling process requires extra slag consumption, which decreases the liquid layer thickness and increases shear stress(/friction) for the whole mold.

3.3.6 Mold Friction

The friction measured in operating casting molds may come from mold/slag contact, excessive taper, misalignment or a combination of the three.

A. Slag-layer friction

Previous research has suggested that friction against the slag layer is important[103]. The liquid slag-layer flow model and solid slag-layer stress model described in this work give the shear stress on the mold wall, τ_{mold}, due to mold/slag contact. Integrating the shear stress over the mold face gives the total friction force due to contact between the mold and slag layers:

$$F_{contact} = \int_0^{Z_{mold}} \tau_{mold} \cdot 2(W+N) \cdot dz \tag{3.50}$$

where, Z_{mold}: working mold length; W: slab width; N: slab thickness.

This model has been incorporated into CON1D, and is used for the study described in later chapters.

B. Excessive taper

If the solid slag layer remains attached to the mold wall all the way down the mold, there will be a continuous, thick liquid slag layer (to provide slag consumption) and a thick solid slag layer, leading to low heat transfer across the mold/shell gap. Then the shell will have relatively high surface temperature and small shrinkage. In this case, excessive narrow face taper may squeeze the steel shell and therefore lead to increased friction. The maximum force from squeezing the shell occurs if the shell buckles, leading to longitudinal surface depressions, such as off-corner gutter in extreme cases[20], as

shown in Figure 3.16. Applying the Eular critical buckling load equation with rigid ends yields an estimate of the normal stress on the mold wall, F_{cr}:

$$F_{cr} = \frac{4\pi^2 EI}{L_{eff}^{\ 2}} = \frac{4\pi^2 E}{L_{eff}^{\ 2}} \frac{b^3 h}{12} \tag{3.51}$$

Where, b is the shell thickness, h is the vertical contact length along the narrow face, L_{eff} is the unsupported shell width across the wide face from the corner and E is the effective elastic modulus of the hot steel shell. So the friction due to buckling for each narrow face is:

$$F_{excessive\ taper} = 2\phi_{static} \cdot F_{cr} \tag{3.52}$$

C. Excessive taper

Misalignment of the mold and strand is another important potential cause of friction. The friction force during each oscillation cycle is inferred from the difference between the force transducer measurements with and without molten steel in the mold[169]. Currently, such friction signals can be used to monitor and detect misalignment problems in operating casters.

3.4 Mold Heat Transfer Model

3.4.1 Heat Conduction in the Mold

Two dimensional, steady state temperature within a rectangular vertical section through the upper portion of the mold is calculated assuming constant conductivity:

$$\frac{\partial^2 T}{\partial x^2} + \frac{\partial^2 T}{\partial z^2} = 0 \tag{3.53}$$

This equation is solved using a standard Fourier series product solution[170] applying fixed heat flux, $q_{int} = -k_{mold} \partial T / \partial x$, and convection, h_{water} and T_{water} as boundary conditions, as shown in Figure 3.17(a) (refer to Appendix D[171]). This copper domain is generally chosen to extend from the top of the mold to 100mm below the meniscus.

Below this meniscus region, heat flow is one-dimensional through the thickness. Temperature at the copper hot face, T_{hotc}, is then:

$$T_{hotc} = T_{water} + q_{\text{int}} \left(\frac{1}{h_{water}} + \frac{d_{mold}}{k_{mold}} \right) \tag{3.54}$$

where d_{mold} is the copper mold thickness calculated in Appendix E[171]. Coating layers and air gap are incorporated as needed to find the mold hot face temperature, T_{mold}, by adding extra d_{coat}/k_{coat} and d_{air}/k_{air} resistances to Eq.(3.54) as needed. In addition to the heat flux across the interface, q_{int}, this calculation requires the initial cooling water temperature, T_{water}, input as a boundary condition, and the effective water heat transfer coefficient, h_{water}, discussed next.

3.4.2 Convection to the Cooling Water

The effective heat transfer coefficient between the cooling water and the cold face ("water-side") of the mold, h_{water}, is calculated including a possible resistance due to scale deposits on the surface of the cooling water channels:

$$h_{water} = 1 \Big/ \left(\frac{d_{scale}}{k_{scale}} + \frac{1}{h_{fin}} \right) \tag{3.55}$$

To account for the complex nature of heat flow in the undiscretized width direction of the mold, the heat transfer coefficient between the mold cold face and the

cooling water, h_{fin}, incorporates heat flow to both the root and sides of the water channels, the latter treated as heat-transfer fins.

$$h_{fin} = \frac{h_w w_{ch}}{L_{ch}} + \frac{\sqrt{2h_w k_{mold}\left(L_{ch} - w_{ch}\right)}}{L_{ch}} \tanh\sqrt{\frac{2h_w d_{ch}^2}{k_{mold}\left(L_{ch} - w_{ch}\right)}} \tag{3.56}$$

where the mold geometry parameters, L_{ch}, w_{ch}, and d_{ch} are shown in Figure 3.17(b). The heat transfer coefficient between the water and the sides of the water channel, h_w, is calculated assuming turbulent flow through an equivalent-diameter pipe using the empirical correlation of Sleicher and Reusse[172], which is reported[173] to be more accurate than other relations such as Dittus and Boelter[174]:

$$h_w = \frac{k_{water}}{D}\left(5 + 0.015\,\mathrm{Re}_{waterf}^{c_1}\,\mathrm{Pr}_{waterw}^{c_2}\right) \tag{3.57}$$

where $D = \dfrac{2w_{ch}d_{ch}}{w_{ch} + d_{ch}}$ is the equivalent diameter of the water channel, $c_1 = 0.88 - 0.24/\left(4 + \mathrm{Pr}_{waterw}\right)$, $c_2 = 0.333 + 0.5e^{-0.6\,\mathrm{Pr}_{waterw}}$ are empirical constants. The water properties could be constants specified by user input, or they are calculated based on the bulk temperature in cooling channel and wall temperature at mold cold face accordingly, as given in Appendix F[171]

The presence of the water slots can either enhance or diminish the heat transfer, relative to a plate-shaped mold wall with uniform thickness, $d_{mold,}$ such as used in billet casting. Deep, closely spaced slots augment the heat transfer coefficient, (h_{fin} larger than h_w) while shallow, widely spaced slots inhibit heat transfer. In most molds, h_{fin} and h_w are very close.

Although it slightly underpredicts mold temperature, Eq.(3.56) was shown, through comparison with many 3-D computations for a variety of typical slab casting

mold geometries and conditions, to match the temperature within 1% at the water slot root and from 0.1% to 6% at the hot face [31, 175]. For a typical hot face temperature of 190°C and water temperature of 30°C, it gives maximum errors of 2°C and 10°C. It is most accurate for molds with either deep, closely-spaced slots[31] or very wide slots[175], where cold face temperature is most nearly constant as assumed in Eq.(3.56).

3.5 Spray Zones

The secondary cooling zones begin right after the mold exit and are divided into different zones according to the different support roll diameter or different cooling water flow rates from spray nozzles, which are assumed in the middle between two rolls, as shown in Figure 3.18(a). Heat flux from the strand surface varies greatly between each pair of support rolls according to spray nozzle cooling (based on water flux), h_{spray}; radiation, h_{rad_spray}; natural convection, h_{conv}; and heat conduction to the rolls, h_{roll}, as shown in Figure 3.18(b). Incorporating these phenomena enables the model to simulate heat transfer during the entire continuous casting process. The heat extraction due to water sprays is a function of water flow[176], of the following form:

$$h_{spray} = A \cdot Q_{water}^{c} \cdot \left(1 - b \cdot T_{spray}\right) \tag{3.58}$$

where Q_{water} (l/m^{2}s) is water flux in the spray zones, and T_{spray} is the temperature of the spray cooling water. In Nozaki's empirical correlation[177], A=0.3925, c=0.55, b=0.0075, which has been used successfully by other modelers[176, 178].

Radiation is calculated by:

$$h_{rad\_spray} = \sigma \cdot \varepsilon_{steel} \left(T_{sK} + T_{ambK}\right)\left(T_{sK}^{2} + T_{ambK}{}^{2}\right) \tag{3.59}$$

where T_{amb} is ambient temperature, T_{sK} and T_{ambK} are T_s and T_{amb} expressed in Kelvin. Natural convection is treated as a constant input for every spray zone. For water-cooling only, it is not very important, so was simplified to 8.7W/m^{2}K everywhere. Larger values can be input for h_{conv} to reflect the stronger convection when there is air mist in the cooling zone. Heat extraction into the rolls is calculated based on the fraction of heat extraction to the rolls, f_{roll}, which is calibrated for each spray zone:

$$h_{roll} = \frac{f_{roll}}{L_{roll\ contact} \cdot (1 - f_{roll})} \left(\begin{array}{l} \left(h_{rad\_spray} + h_{conv} + h_{spray} \right) \cdot L_{spray} + \\ \left(h_{rad\_spray} + h_{conv} \right) \cdot \left(L_{spray\ pitch} - L_{spray} - L_{roll\ contact} \right) \end{array} \right) \quad (3.60)$$

Heat extraction is a maximum directly beneath the spray nozzle (assumed centered between the rolls) and at the roll/shell contact region. The relative size of this maximum is governed by the fraction of heat specified to leave relative to that removed by the spray cooling water. A typical f_{roll} value of 0.05 produces local temperature drops beneath the rolls of about 100°C. Beyond the spray zones, heat transfer simplifies to radiation and natural convection.

3.6 Solution Methodology

The model requires simultaneous solution of three different systems of equations: 1-D transient heat conduction and solidification of the steel shell, 2-D steady state heat conduction in the mold, and the equations balancing heat, mass, momentum and stress in the gap. The simulation starts by setting the initial steel and mold temperatures to the pouring temperature and inlet cooling water temperature respectively. Phase transformation temperatures and phase fraction temperature curves are then calculated, using either equilibrium phase diagram or microsegregation model. Then, each time step begins by rearranging and solving Eqs.(3.12) and (3.22) simultaneously for d_{liquid} and

d_{solid}, based on heat and mass balances at the previous time step. The heat flux q_{int} is then calculated according to Eqs.(3.11) and (3.12), which is the boundary condition for both steel and mold domains. The heat transfer coefficient, h_{water} is calculated according to cooling channel conditions with Eqs.(3.55) to (3.57), and used to obtain mold temperatures. Applying the superheat flux boundary condition, Eq.(3.1), as an internal heat source at the steel solid/liquid interface, the model uses an explicit, central-finite difference algorithm originally developed by Pehlke[179] to solve Eq.(3.2) for the shell temperature at each time step (Appendix A). This limits the maximum time step size, Δt. When a node temperature drops below the liquidus temperature, its solid fraction is calculated from the latent heat evolved, and then the node temperature is adjusted[180] (Eq.(A6)) according to the phase fraction-temperature curves, described in Section 3.1.5-A. The results are used as initial conditions for the 2-D mold calculation, which solves Eq.(3.53) analytically (Appendix D[171]), relating distance down the mold, z, to time in the shell through the casting speed. Subsequently, the entire 1-D shell solidification model in the 2-D mold region is recomputed using the new 2-D mold temperatures as its boundary condition. This stepwise coupling procedure alternates between models until the 1-D mold temperatures converge to match the 2-D results within 3°C. This produces a self-consistent prediction, which is stable for almost all coupled simulations investigated and usually converges in 3-4 iterations.

Nest the model calculates velocity and shear stress distribution in the liquid slag layer (Eq.(3.36)) based on the temperature distribution solved by Eq.(3.31). Solving the force balance equation in the solid layer, Eq.(3.40), gives the axial stress, which is used to decide if the solid layer fractures. The friction force on the mold wall is obtained finally

by integrating the shear stress over the whole mold faces (Eq.(3.50)). Figure 3.19 gives a flow chart of the whole procedure.

The model has been incorporated into a user-friendly FORTRAN program, CON1D[171]. A 100-second long simulation with 0.004sec time step and 100-node mesh runs on a Pentium III personal computer (using 3.1Mbytes of memory) in about 30 seconds. Appendix I gives the sample input and output files of CON1D version7.5.

3.7 Tables and Figures

Table 3.1 Equilibrium Partition Coefficient, Diffusion Coefficient, and Liquidus Line Slopes of the Solute Elements

Element	$k^{\delta/L}$	$k^{\gamma/L}$	D^{δ} (cm2/sec)	D^{γ} (cm2/sec)	m (°C/%)	n (°C/%)
C	0.19	0.34	0.0127exp(-19450/RT)	0.0761exp(-32160/RT)	78.0	-1122
Si	0.77	0.52	8.0exp(-59500/RT)	0.3exp(-60100/RT)	7.6	60
Mn	0.76	0.78	0.76exp(-53640/RT)	0.055exp(-59600/RT)	4.9	-12
P	0.23	0.13	2.9exp(-55000/RT)	0.01exp(-43700/RT)	34.4	140
S	0.05	0.035	4.56exp(-51300/RT)	2.4exp(-53400/RT)	38.0	160
Cr	0.95	0.86	2.4exp(-57310/RT)	0.0012exp(-52340/RT)	1.04	13.4
Ni	0.83	0.95	1.6exp(-57360/RT)	0.34exp(-67490/RT)	4.69	-28.6
Cu	0.53	0.88	2.6exp(-57360/RT)	0.7exp(-68350/RT)	5.32	-10.4
Mo	0.80	0.585	3.47exp(-57690/RT)	0.068exp(-59000/RT)	2.6	77.6
Ti	0.38	0.33	3.15exp(-59200/RT)	0.15exp(-59980/RT)	10.24	120.5
V	0.93	0.63	4.8exp(-57360/RT)	0.284exp(-61900/RT)	12.95	85.5
Nb	0.40	0.22	50.2exp(-60220/RT)	0.83exp(-63690/RT)	10.24	70.8
W	0.85	0.45	1.57exp(-58200/RT)	0.13exp(-57300/RT)	0.24	18.8
N	0.25	0.48	0.008exp(-18900/RT)	0.91exp(-40270/RT)	60.0	-

Note: R is gas constant of 1.987cal/mol K, and T is temperature in Kelvin.

Table 3.2 Constants Used in Analytical Solution and Validation Casefor Steel Solidification Model

Conductivity, k_{steel}	30.0	W/mK
Specific Heat, Cp_{steel}	670.0	J/kgK
Latent Heat, L_f	271.0	kJ/kg
Density, ρ_{steel}	7400.0	kg/m^3
Melting Temperature, T_{melt}	1509.05	^{o}C
Liquidus Temperature, T_{liq}	1509.1	^{o}C
Solidus Temperature, T_{sol}	1509	^{o}C
Shell Surface Temperature, T_s	1000	^{o}C

Table 3.3 Typical Casting Condition and Simulation Parameters for Transient Interfacial Gap Model

Carbon Content, *C%*	0.05	%
Liquidus Temperature, T_{liq}	1529	^{o}C
Solidus Temperature, T_{sol}	1509	^{o}C
Steel Density, ρ_{steel}	7400	kg/m^2
Fraction Solid for Shell Thickness Location, f_s	0.3	-
Mold Powder Solidification Temperature, T_{fsol}	950	^{o}C
Mold Powder Viscosity at 1300°C, μ_{1300}	4.3	Poise
Exponent for Temperature dependence of Viscosity, n	1.6	-
Slag Density, ρ_{slag}	2500	kg/m^3
Mold Powder Conductivity, k_{solid}, k_{liquid}	1.5, 1.5	W/mK
Poisson's Ratio of Slag, υ	0.17	-
Mold Slag Consumption Rate, Q_{slag}	0.41	kg/m^2
Mold Slag Lubrication Consumption Rate, Q_{lub}	0.2	kg/m^2
Solid layer/mold Interface Friction Coefficient, ϕ_{static}, ϕ_{moving}	0.4, 0.4	-
Solid slag layer velocity, V_s	0.	m/s
Casting Speed, V_c	1.0	m/min
Pour Temperature, T_{pour}	1550	^{o}C
Slab Section Size, $W \times N$	1500×230	mm$\times$mm
Working Mold Length, Z_{mold}	800	mm
Oscillation Mark Geometry, $d_{mark} \times w_{mark}$	0.45×0.45	mm$\times$mm
Mold Oscillation Frequency, f	83.3	cpm
Oscillation Stroke, s	7.8	mm
Negative Strip Ratio of velocity, *NS%*	0.3	-
Liquid Slag Pool depth, h_0	10	mm
Time Step, dt	0.002	s
Mesh Size, dx	0.5	mm

Table 3.4 Simulation Parameters in Liquid Slag Layer Model Validation Cases

	Case (a)	Case(b)	Case (c)	Case (d)	
Temperature dependent viscosity exponent, n:	0	1.6	0	1.6	-
Liquid film thickness, dl:	0.2		2.0		mm
Viscosity at shell surface side, μ_s:	0.53		0.50		Pas
Density, ρ_{slag}:	2500		4000		kg/m^3
Casting speed, V_c:	1.0		1.5		m/min
Mold oscillation stroke, s:	7.8		20		mm
Mold oscillation frequency, f:	1.389		1.5		cps
Steel density, ρ_{steel}:	7400		7400		kg/m^3
Time Step, Δt:	5.0E-7				s
Mesh Size, Δx:	0.04				mm

Table 3.5 Terms in Eq.(3.26) for Case (b) at t=0.18s, x=0.16mm (unit: N/m^3)

$\rho_{slag}\frac{\partial V_z}{\partial t}$	$\rho_{slag}\cdot V_y\cdot\frac{\partial V_z}{\partial y}$	$\rho_{slag}\cdot V_z\cdot\frac{\partial V_z}{\partial z}$	$\left(\rho_{slag}-\rho_{steel}\right)\cdot g$	$\frac{\partial \tau_{yz}}{\partial y}$	$\frac{\partial \tau_{zz}}{\partial z}$
-335.	0.0304	0.0431	-48020.	47683.	-1.0624

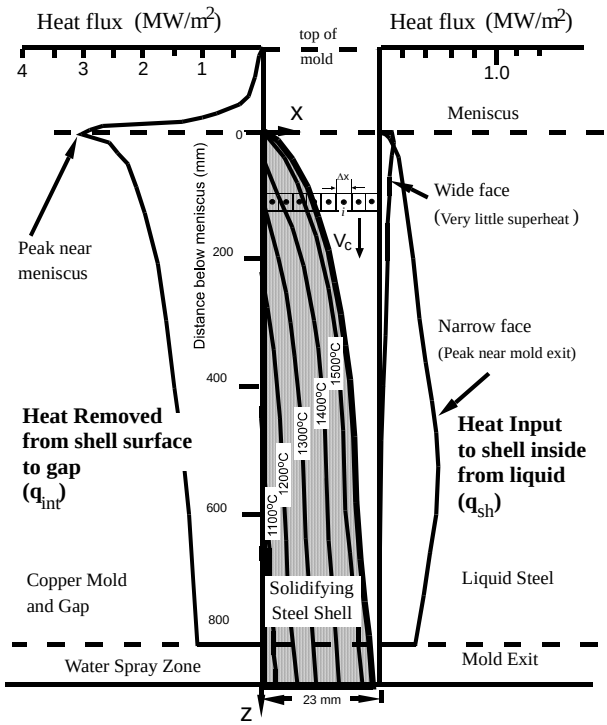

Figure 3.1 Model of solidifying steel shell domain showing typical isotherms and heat flux conditions

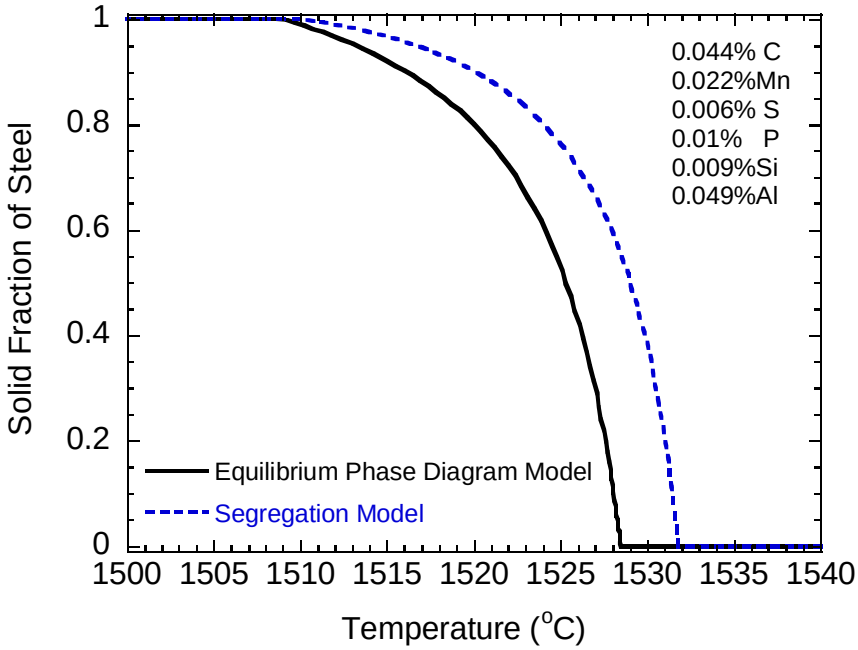

Figure 3.2 Phase fraction variation with temperature in mushy zone

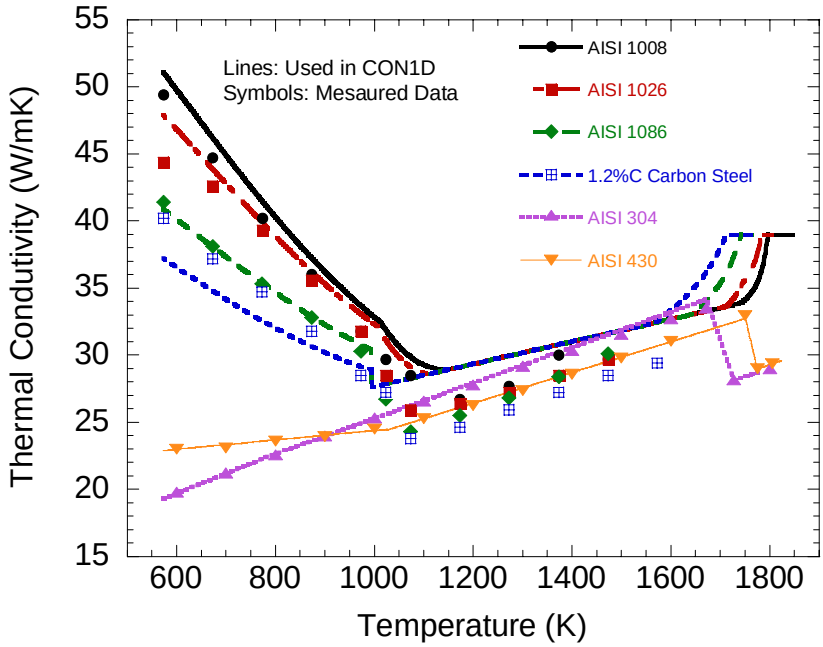

Figure 3.3 Comparison of model thermal conductivities and measurements[162]

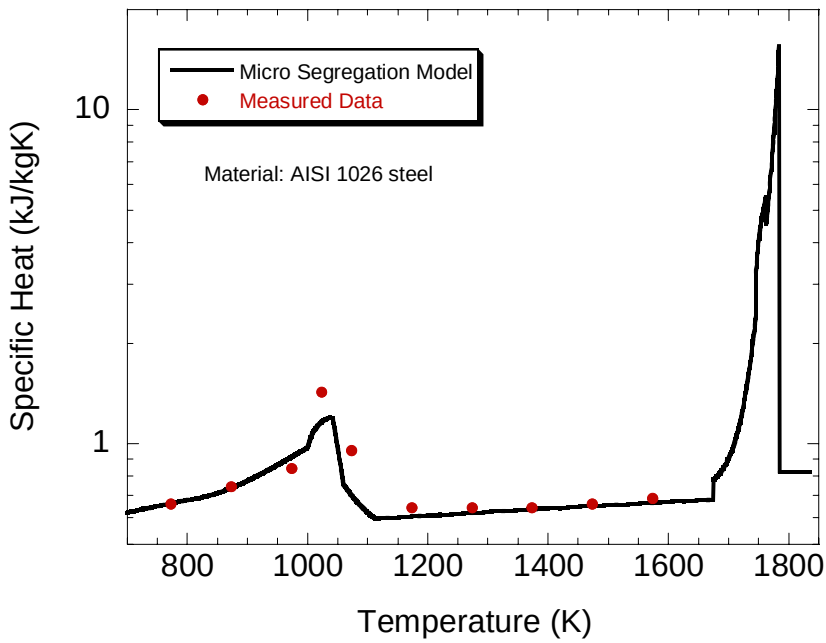

Figure 3.4 Comparison of model specific heat curve and measurements [162]

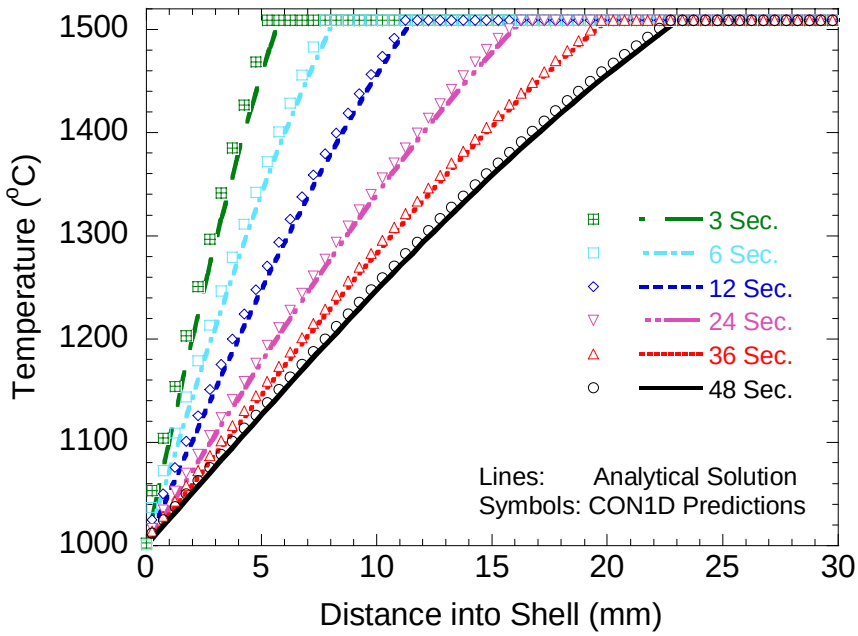

(a) Shell temperature distribution

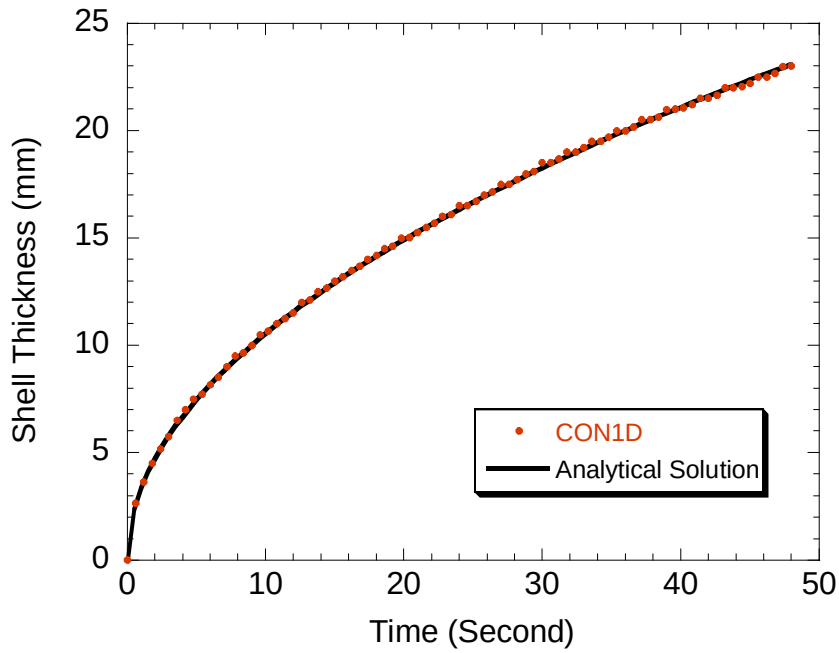

(b) Shell growth

Figure 3.5 Comparison of CON1D steel solidification model results and analytical solutions

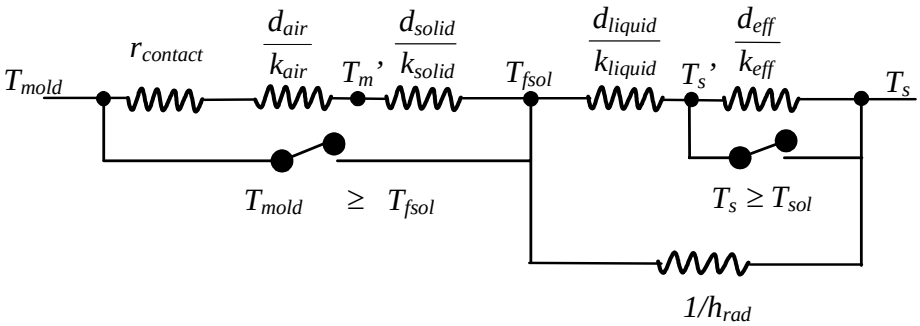

Figure 3.6 Thermal resistances used in the interface model

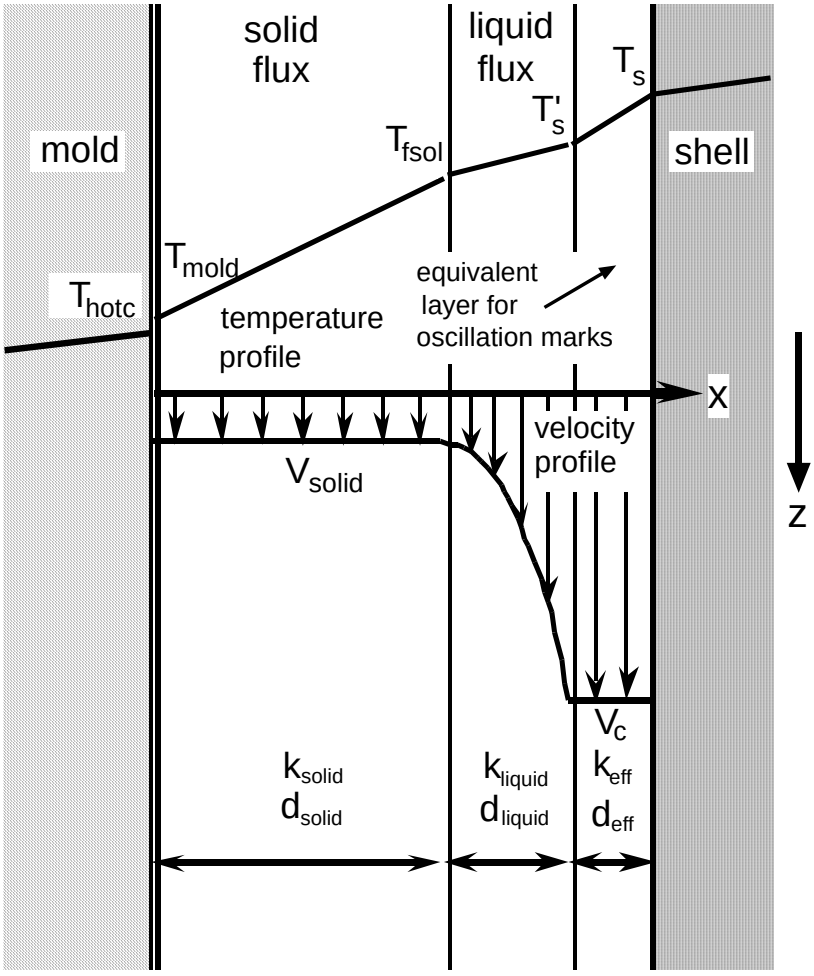

Figure 3.7 Velocity and temperature profiles assumed across interfacial gap[171]

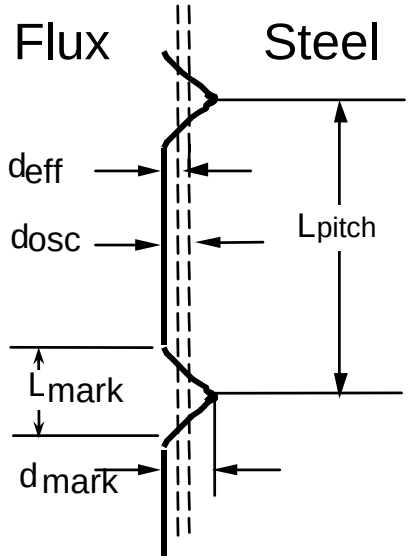

Figure 3.8 Model treatment of oscillation marks[171]

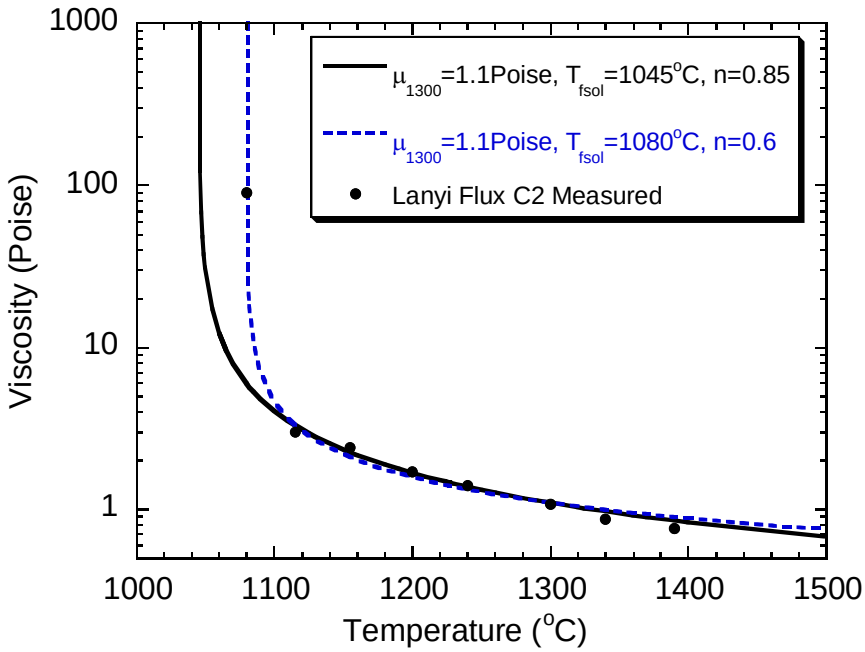

Figure 3.9 Comparison of model mold slag viscosity curves and measurements[100]

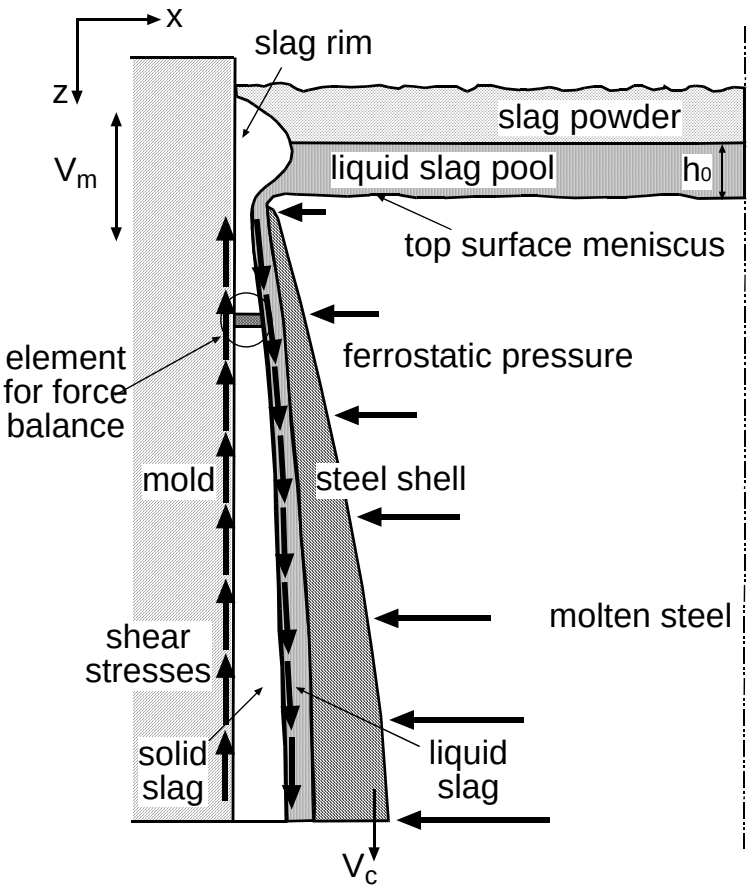

Figure 3.10 Schematic of interfacial gap in oscillating mold

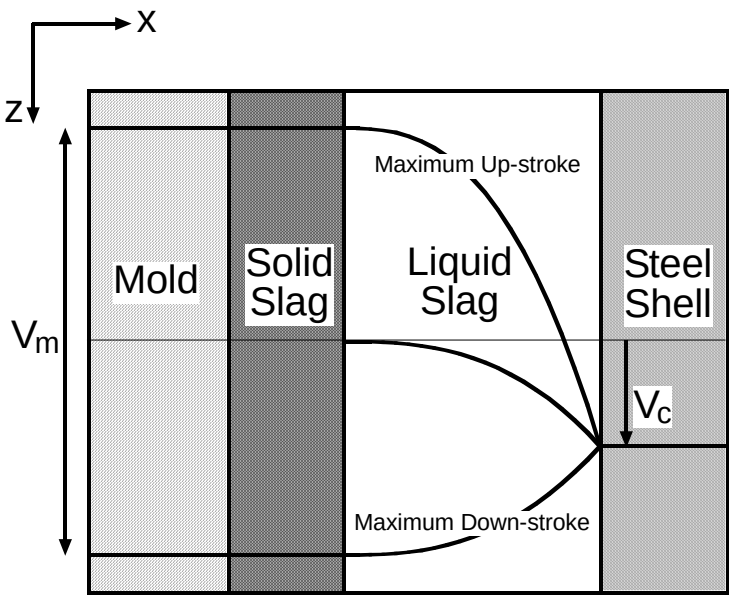

Figure 3.11 Schematic profile of slag velocity during oscillation cycle

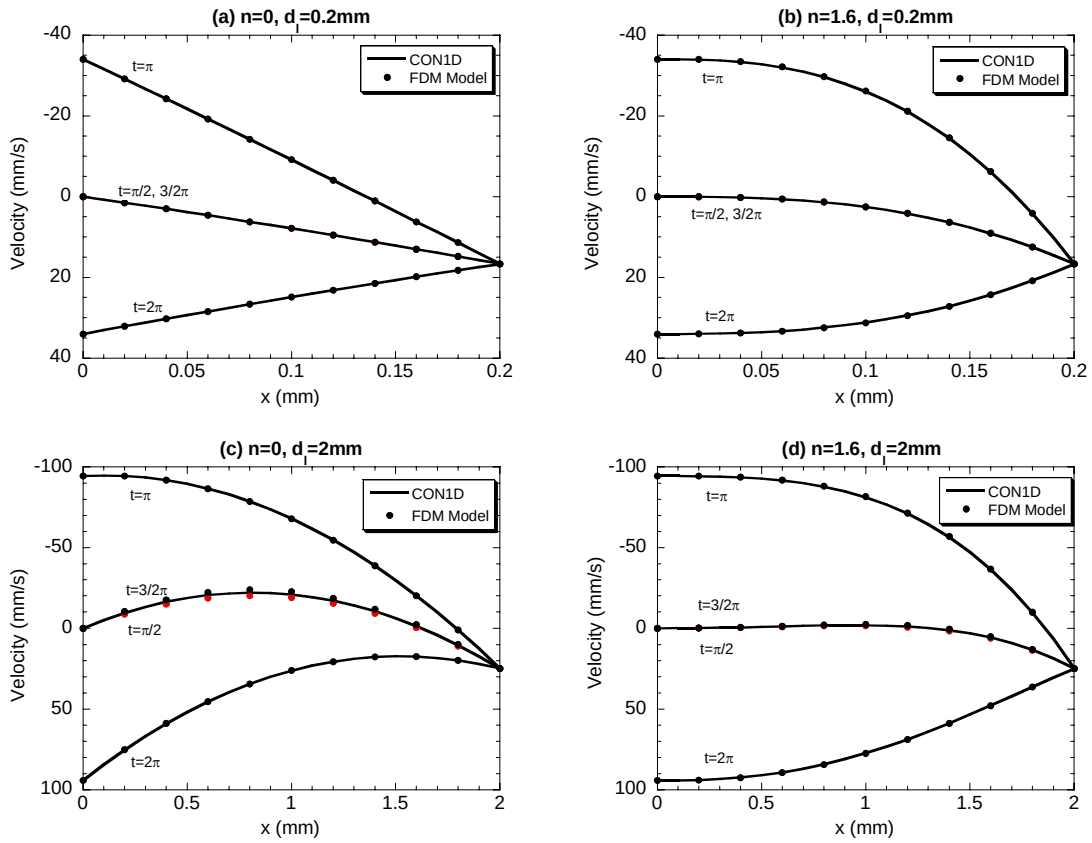

Figure 3.12 Velocity profiles in liquid flux layer

(for different viscosity exponent(0/1.6) and film thickness (0.2/2mm))

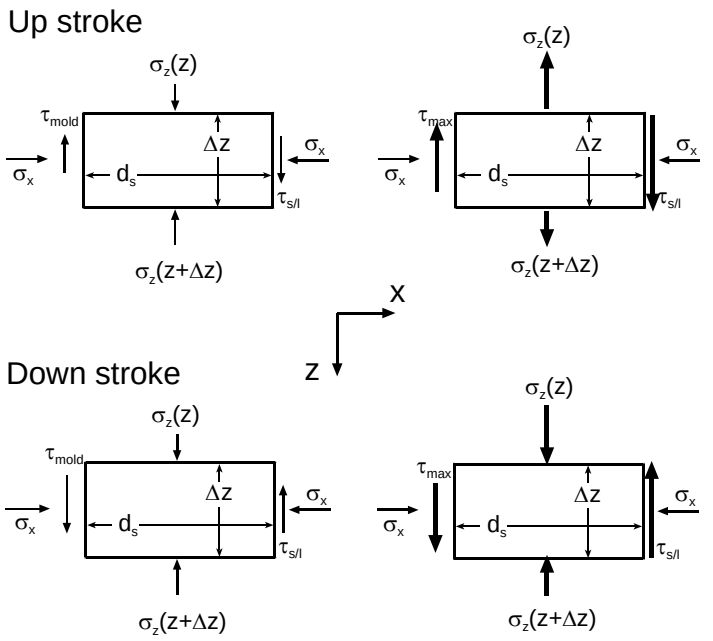

(a) liquid shear stress limited (b) friction coefficient limited

Figure 3.13 Force balance on solid slag layer section

(mold wall friction left, liquid layer shear stress right and axial stress)

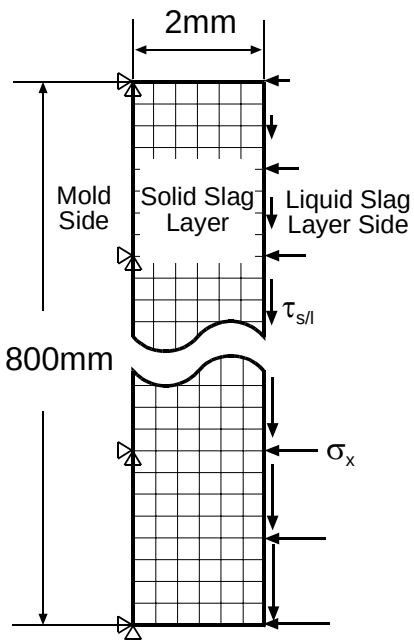

Figure 3.14 ANSYS solid slag stress model domain, mesh and BCs

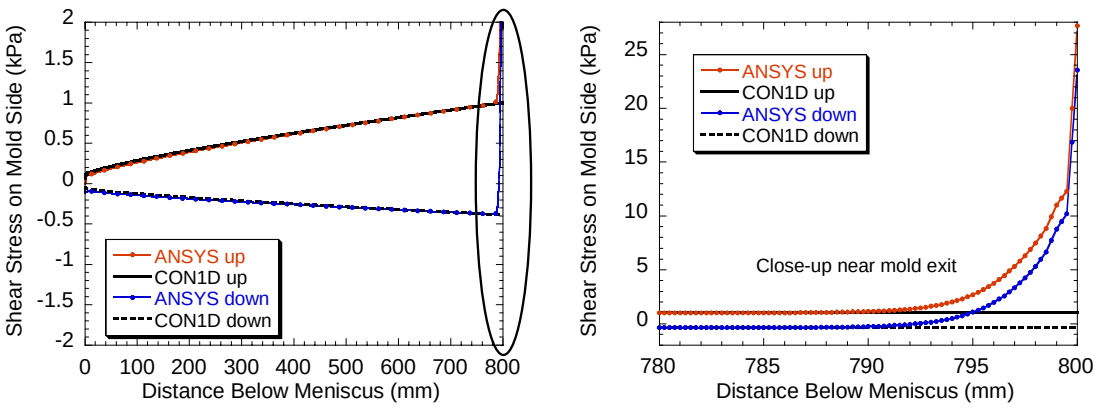

(a) Shear stress on mold side

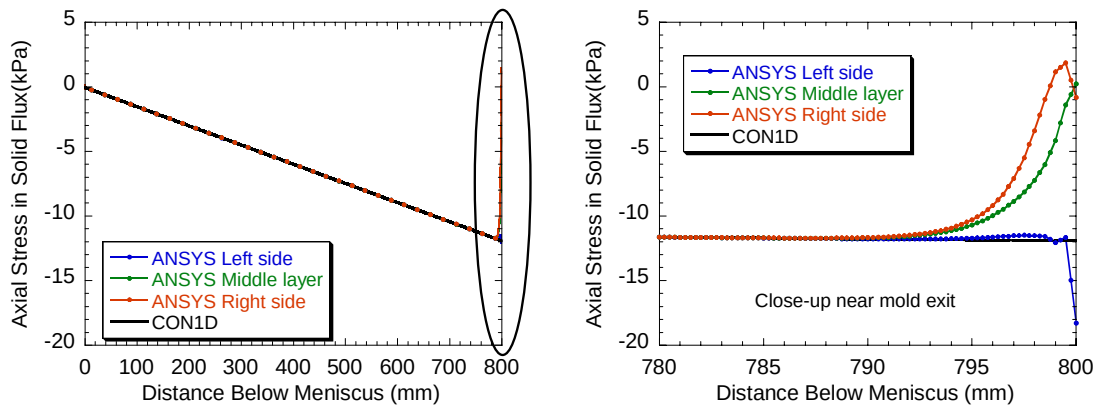

(b) Axial stress in sold slag layer

Figure 3.15 Comparison of CON1D solid layer stress model and ANSYS results

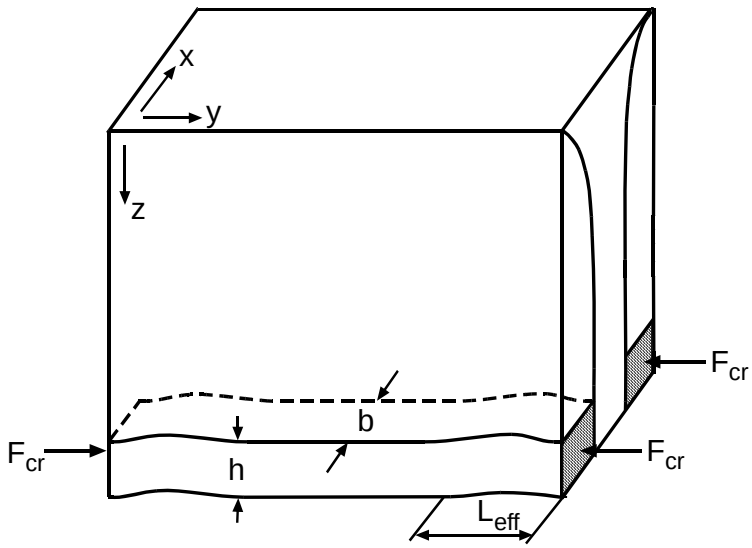

Figure 3.16 Schematic of friction forces from excessive taper of narrow mold faces

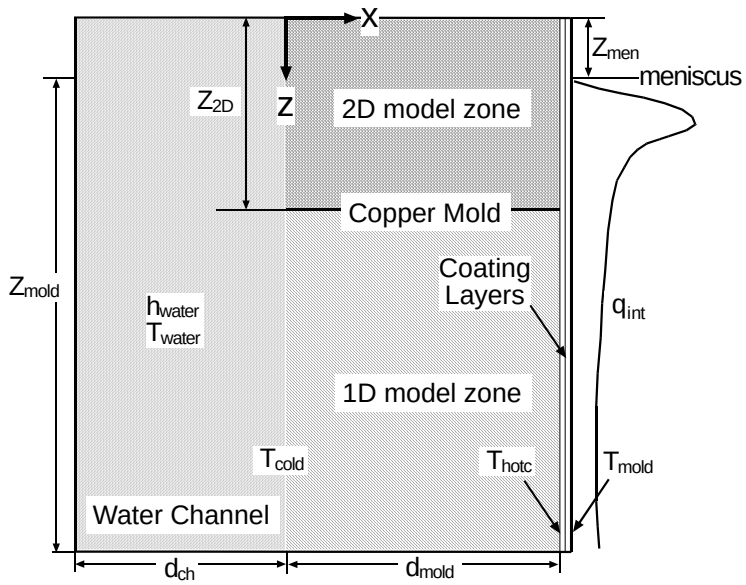

(a) Vertical section along casting direction

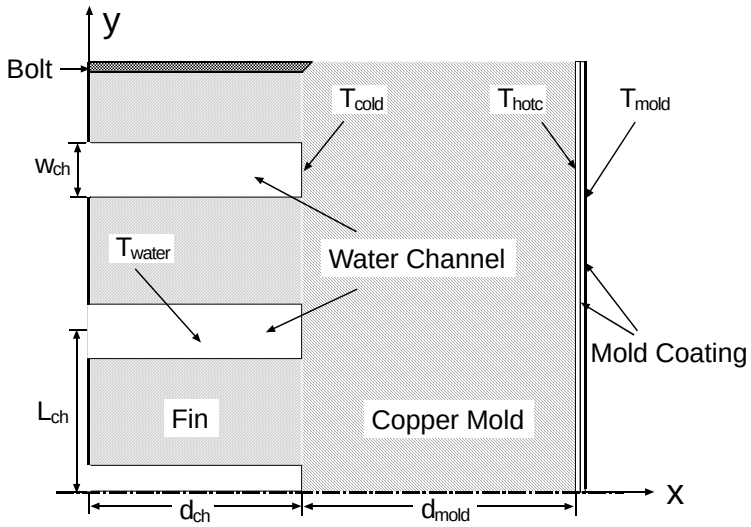

(b) Horizontal section through mold

Figure 3.17 Simulation domain in mold

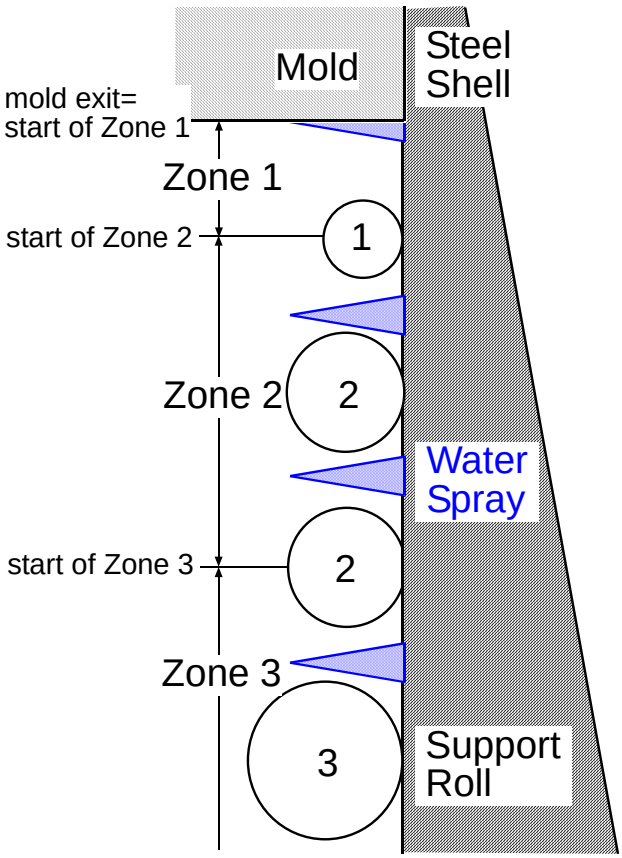

(a) Typical spray zone configuration

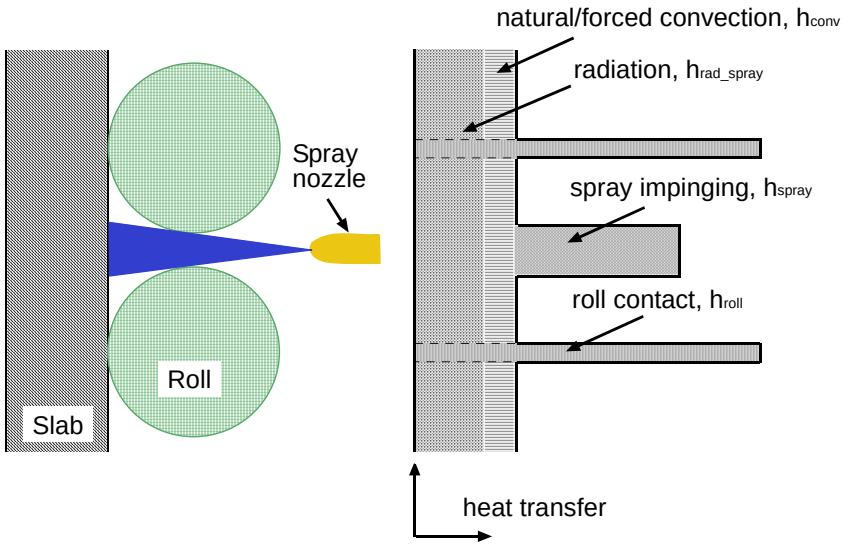

(b) Heat transfer between one pair of rolls

Figure 3.18 Schematic of spray zone region

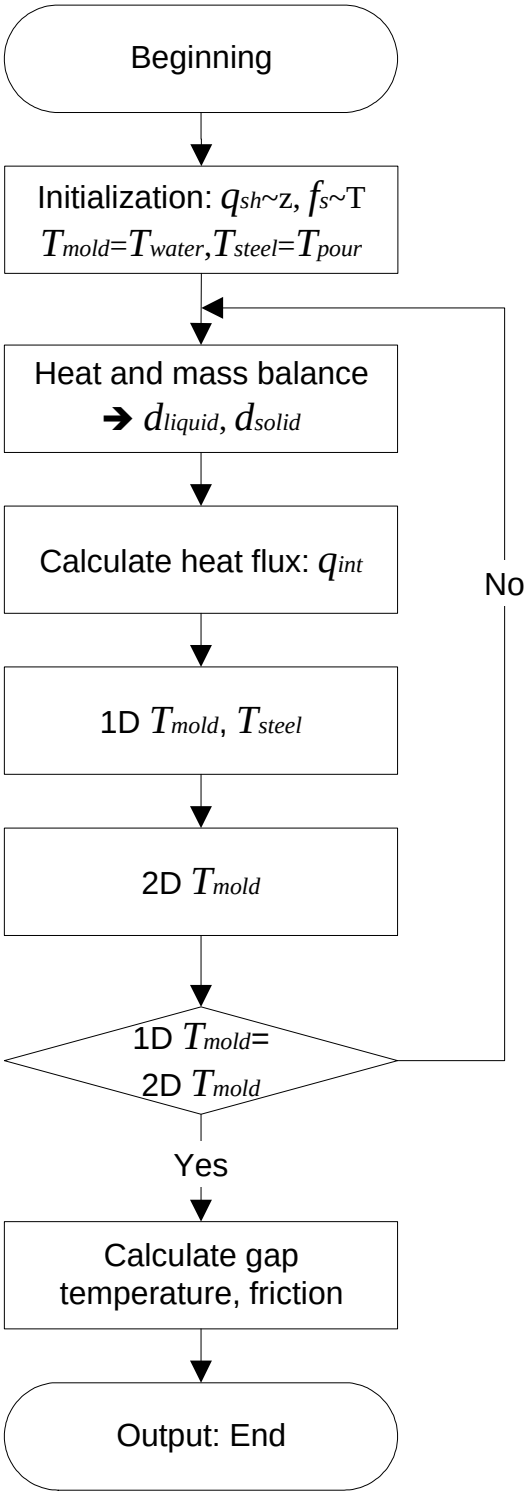

Figure 3.19 Flow chart of CON1D program

CHAPTER 4. SLAG PROPERTY MEASUREMENTS AND CHARACTERIZATION

The previous chapter described the mathematical model CON1D. It was shown that by supplying the model with accurate information, extensive insight can be gained into steel product behavior and potential quality concerns. Most of the parameters, such as casting conditions and mold geometry, can be directly obtained from the operating caster of interest. The heat transfer and lubrication in the interfacial gap depends mainly on the properties of the slag filling the gap. These properties include chemical composition, viscosity, friction coefficient and crystallization behavior. Because some of these properties have not been recorded in previous work, an experimental investigation was undertaken to gain better understanding of these important mold slag properties.

4.1 Chemical Composition

In this study, four different mold powder or slag-layer-film samples taken during tail-out were investigated. These four slags are S1 and K1 crystalline slags, S2 glassy slag, and H1 tail-out film. The chemical compositions of the four slag powder are listed in Table 4.1, which have been re-calculated from the original suppliers report (Appendix G[181-183]) by converting F to CaF_2. It must be noted that the carbon is added to slow down the mold powder melting and thereby control melting uniformity during the casting process. This carbon burns out during the powder sintering and melting process, so is not generally present in the liquid slag layer or in the re-solidified slag film in the gap. The powder for slag samples S1 and S2 were prepared without adding the carbon in order to reproduce the actual molten slag in the continuous casting mold without having to experience the difficulties associating with decarburization.

4.2 Friction Coefficient

The modeling work in Chapter 3 shows that the slag properties near the solidification temperature are very important to interfacial lubrication. However, previous research focuses only on the properties at high temperature (greater than 1000°C)[99, 101, 130, 135, 136, 151-153, 184], The lubrication properties of flux near the softening temperature are rarely reported. Thus, laboratory experiments measuring the friction coefficient of the solid slag layer from room temperature up to 1000°C were conducted.

4.2.1 Sample Preparation and Instrumentation

The prepared relatively carbon free mold powder was melted in a graphite crucible (with Zr coating) at 1400°C for an hour, and then poured into a preheated metal dish (Steel/high temperature Ni alloy). The inner diameter of each sample holder is 20-30mm and the depth is 5mm. The sample surface was polished using 120~600 grit coarse sand paper to get a flat surface with roughness R_a about 0.2μm~0.6μm, as measured using a Dektak 3030 profilometer at the Center for Microanalysis of Materials (CMM) at UIUC. Each sample was then tested with a High Temperature Tribometer (HTT) at the Tribology and Micro-Tribology Lab at Department of MIE, UIUC, shown in Figure 4.1.

The HTT can measure detailed friction and wear data on material test specimens up to 1000°C. It consists of a rotating/oscillating spindle on which the plate specimen is mounted and a special holder applies the contact load through a pin while measuring both the normal and friction forces. The pin, holder and sample are contained within a cylindrical furnace that features spiral heat coils and is insulated with special reflective film to encourage uniform radiative heating in the interior. The entire unit is enclosed in a

sealed bell jar. Vertical movement of the specimen into and out of the furnace and precise control of the movement to regulate the pin loading are provided by a remotely operated drive system[185].

4.2.2 Experimental Procedure

The pin is a 0.25inch diameter steel ball bearing except for run #A, which used a ring shaped pin with a flat surface(D_o/D_i=1”/0.25”). The wear track diameter is set to 0.375inch except for Run #8. The spindle velocity is varied from 50rpm to 300rpm, which corresponds to speeds of 25mm/sec to 150mm/sec. For run #8, the track diameter is 0.715inch. To keep same velocity range, the rotating frequency is adjusted to 26~158rpm correspondingly.

The first series of experiments began from room temperature and increased every 100°C until the machine limit (~900°C). It took 3~5 minutes for temperature to reach each set point, which was increased in 100°C intervals. After waiting 5 minutes, data was recorded from the display every two seconds for two minutes, giving 60 data points for each state.

To investigate reproducibility and the importance of time in the apparatus, the second series of experiments was conducted by heating to the highest temperature in only 40 minutes and recording data during decreasing temperature intervals using the above recording procedure. Wear track depths were measured with a profilometer which is able to quantify depth from 0.02mm to 25mm[186].

4.2.3 Results and Discussion

Table 4.2 gives the temperature process of each different run and the corresponding maximum wear track depth. The machine was calibrated after run #2. Comparing the HTT LCD displayed friction coefficient and the real friction coefficient during calibration using known weights applied tangentially and normally, Figure 4.2 shows the deviation is in a reasonable measurement error range. However, runs #A and #1 were conducted before machine calibration, so we can only rely on the tendency of the friction coefficient as the values appear to be too large.

Figure 4.3(a) shows a sample of data recorded for slag S1 in run #5 at 400°C. The variation is different for different conditions. Figure 4.3(b) plots the average friction coefficient for 25mm/s velocity, with the variation range at every temperature shown as error bars. Higher velocity slightly increases the friction coefficient, but this effect is negligible for temperatures above 500°C, as shown in Figure 4.3(c).

Figure 4.4 gives the results of four runs for slag S1. The direction of the arrow on each line shows evolution of temperature during heating or cooling. The value of the friction coefficient varies between runs with average value 0.16 ± 0.1 excluding run #1. Increasing temperature above 800°C causes the friction coefficient to begin to drop. This decrease might correspond to the oxidation layer formed on the top steel ball bearing pin or alternatively to material softening. In general, there seems to be a slight trend of decreasing friction with increasing temperature which is consistent with a softening phenomenon. However there is lots of variation that can be explained by oxidation. An oxide layer is believed to lubricate the metal/slag interface[187]. Thus, run #7 shows a hysteresis loop with lower friction at later time at the same temperature due to oxide layer

build-up. The increase of friction just after starting to decrease temperature at the beginning of runs #5 and #8 might be due to spalling of the oxide. Figure 4.5 shows pictures of the specimens after the friction tests. Two different friction mechanisms seem to have affected these two runs. Run #1 shows adhesive friction while run #5 is more likely to be abrasive friction. The measurement of wear track depth shows that run #5 has much deeper wear than run #1 (152μm vs. 24μm), which is consistent with the two proposed mechanisms.

Figure 4.6 shows the friction coefficient as a function of temperature for slag S2 based on runs #3, #4 and #6. It appears that the friction has a slight drop from room temperature to 500°C. Just above 500°C, the friction coefficient increases sharply from 0.1 to 0.5. This is because the specimen begins to soften. Instead of wear, the ball bearing plows through the tacky slag layer and causes an artificially high increase of friction coefficient. Figure 4.7 shows pictures of slag S1 before and after the test. It confirms that the sample got soft and deformed greatly during the experiment. With increasing temperature, the specimen became too soft to withstand any normal force. After this softening and accompanying deformation, decreasing temperature caused the friction coefficient to fluctuate between 0 and 1.5. This indicates that the surface was too rugged to make any effective measurement, which also happened to a specimen where open bubble holes appeared in the wear track. For the test with slag K1, a similar friction increase with material softening was observed at 720°C as shown in Figure 4.8. The more gradual increase for this test might be due to the use of a different top pin with a flat surface.

The results show that the friction is relatively insensitive to the microstructure of the slag. It generally stays below 0.2 before softening. The softening of the slag, indicated by the apparent dramatic increase in friction coefficient occurs at much lower temperature than previously supposed. This work, for the first time, enables a way to extend the viscosity curves to a lower temperature range.

4.3 Viscosity

Viscosity and solidification temperature have been identified as the key physical properties in selecting a powder with suitable heat transfer properties[5]. Together with the chemical composition, Powder manufacturers commonly measure viscosity at high temperature, as shown in Figure 4.9. Only the low viscosity part of the curve(<400poise) can be measured with a viscometer. Note that the viscosity of slag H1 was fitted from measurements using Eq.(3.19) with μ_{1300}=3.1poise, T_{fsol}=1130°C and n=1.682[183].

From the high temperature friction test, we know that slags S2 and K1 soften at 500°C and about 720°C, and that slag S1 will likely begin to soften at 1000°C or above. For slag S2, the normal force dropped from 10N to 7N in about one minute while the wear check depression grew to 0.5mm deep. The magnitude of the slag viscosity at the softening point can be estimated roughly from its definition assuming Newtonian flow:

$$\mu = \frac{\tau_{\theta z}}{\dot{\gamma}_{\theta z}} \tag{4.1}$$

The shear stress, $\tau_{\theta z}$ can be estimated from the recorded friction force, F, and the contact area, A:

$$\tau_{\theta z} = \frac{F}{A} = \frac{F}{\pi r h} = \frac{3.0N}{3.14 \times 3.175mm \times 0.01mm} \approx 30 \times 10^6 Pa \tag{4.2}$$

Where, r is the radius of the ball bearing, h is the increase in depression depth over one revolution. The strain rate, $\dot{\gamma}_{\theta z}$ can be estimated by assuming $\frac{\partial v_z}{\partial \theta} = 0$:

$$\dot{\gamma}_{\theta z} = \frac{\partial v_\theta}{\partial z} + \frac{1}{r}\frac{\partial v_z}{\partial \theta} = \frac{\partial v_\theta}{\partial z} \approx \frac{\Delta v_\theta}{\Delta z} \approx \frac{25mm/\sec}{5mm} = 5\sec^{-1} \tag{4.3}$$

Where, Δz is the slag layer total thickness, v_θ is the rotation speed. Combining equations (4.1)-(4.3) gives a viscosity of about $6\times10^7\,Poise$. This value matches with the viscosity of common glass at its softening point shown in Figure 2.5[126]. Thus, we can extend the viscosity curves to the low temperature-high viscosity (10^8poise) region, as shown in Figure 4.9. This figure also shows the CON1D model fit through the data points using Eq.(3.19). It is interesting to note that the measurements show inflection(s) occur in the high temperature portion of each curve perhaps due to partial crystallization. The data for slag K1 and this work both show that the inflections are just a minor fluctuation in the entire curve. The CON1D model fitting equation does not capture this effect.

4.4 Crystallization Study

It is well known that the proportion of crystalline and glassy phases in the slag film is important to the control of heat transfer in the mold[139, 140, 188] A thicker crystalline layer decreases heat transfer and is helpful to reduce surface defects for peritectic steels[189, 190]. However, slag with a high crystallization tendency is also reported to increase the friction between the mold and the strand which might cause sticking type breakouts[69, 191]. A series of experiments were conducted to study the crystallization behavior of slags S1 and S2.

4.4.1 Experimental Methods

The onset of crystallization is a strong function of cooling rate in slags because they do not crystallize easily. Three methods were used to investigate time temperature transformation phenomena in slags S1 and S2 over a wide cooling rate range.

A. Differential Scanning Calorimetry (DSC) (CCT tests)

DSC is a common technique used to determine phase transformations at slow cooling rate. The test material is subjected to a controlled temperature program by online feedback control of the heat input simultaneously with a reference substance that experiences no phase transformation over the temperature range of interest. The difference of heat flow between the two samples is recorded. The signal is then corrected by subtracting the heat flow difference signal obtained from a calibration (baseline) run using two identical reference samples. Deviations in the heating or cooling rate are attributed to phase transformations in the test sample. An endothermic phase transformation causes a dip in the heating rate curve during a heating test. During a cooling test, the reverse phase transformation is exothermic, causing a peak spike in the cooling rate curve. The onset temperature of the exothermic peak is an indicator of a crystallization reaction. In a slag with only one peak, this is often called the "Crystallization Temperature" of the mold slag[143].

The DSC experiments were conducted on a Netzsch STA 409 at the Center for Cement Composite Materials (CCM), UIUC, which is capable of both gravimetric (TG) and thermal analysis simultaneously. The temperature range for TG/DSC is -100 to 1600°C.

Slags S1 and S2 were analyzed by TG/DSC. 60~80mg of decarbonized mold powder was poured into a platinum micro-crucible. Pure alumina (Al_2O_3) was selected as the reference for all tests conducted. The temperature was increased from room temperature to 1300°C for slag S1 and 1100°C for slag S2 at a heating rate of 10°C/min. These temperatures were sufficient to fully melt each powder. Each sample was then cooled to room temperature at cooling rates of 1°C/min, 5°C/min and 30°C/min in separate tests. The heat flow vs. temperature/time curve was recorded and corrected with the reference baseline run.

B. Dip thermocouples (CCT Tests)

To investigate intermediate cooling rates, a series of thermocouple dip tests were conducted at the Advanced Materials and Processing Laboratory (AMPL), University of Alberta, Canada. In these tests, a thermocouple is dipped into the slag melt in a Zr coated graphite crucible. It takes a few seconds for the thermocouple to heat up to the slag temperature and reach thermal equilibrium. Then the thermocouple is withdrawn into the air, with a droplet of the slag stuck around the thermocouple bead. The temperature of the thermocouple is continuously recorded by the data acquisition system using InstruNet v2.0. By adjusting the initial melt temperature, or by exposing the dip around the thermocouple to different atmospheric conditions, such as forced convection, a range of cooling rates, 0.5°C/sec~50°C/sec, could be achieved. Table 4.3 lists the cooling rate ranges of different dip thermocouple tests.

C. Atomization (Glass formation)

The real continuous casting process involves rapid initial quenching of the liquid slag against the mold wall followed by slower cooling at different temperatures according

to position in the slag layer (see Figure 6.3). To reproduce the high cooling rates, an Impulse Atomization Process (IAP) was used. The IAP is a single fluid atomization technique capable of producing droplets of a predictable mean particle size and a relatively tight standard deviation under controlled atmospheric conditions, which is available at the AMPL, Alberta Canada[192]. Here the mold powder was placed in a graphite crucible and heated in an enclosed tower in a nitrogen atmosphere. At the bottom of the crucible, an array of orifices was machined. By vibrating a plunger inserted into the melt, the molten slag is forced out of the orifices at the bottom of the crucible. The streams are disintegrated into droplets and fall through the chamber. A mathematical model of droplet solidification which was developed by researchers in the AMPL was used to predict the cooling history of the droplets[193]. By varying the atomization parameters, particle cooling rates due to the radiation and convection were obtained ranging from 100°C/sec to 13000°C/sec depending on particle size. Figure 4.10 shows the schematic of the Impulse Atomization Process[192].

D. Furnace holding (Devitrification tests)

The atomized material was confirmed to be in a fully glassy state through XRD measurements (described in the next section). This material was then subjected to reheating and furnace holding to investigate devitrification. The amorphous particles were put into a preheated furnace maintained at different temperatures (500°C to 1100°C). After the sample had been held for a set time as shown in Table 4.4, it was taken out, water quenched to room temperature and analyzed with XRD.

4.4.2 X-ray Diffraction (XRD)

The treated samples were submitted for XRD analysis to examine the phases present in order to investigate the evolution of crystallization. This study used a Rigaku Geigerflex Powder Diffractometer with a Co tube ($K_{\alpha 1}$ λ=1.78897Å) and a graphite monochromator to filter the K_{β} wavelength at the Department of Earth & Atmospheric Sciences, University of Alberta, Canada with operation conditions of 40kV and 30mA, and the Rigaku D-Max X-ray diffractometer using Cu radiation ($K_{\alpha 1}$ λ=1.54056Å) at the CCM, UIUC with operation conditions of 40kV and 20mA. At the CCM, each XRD spectrum was collected between 5° and 70° 2θ angle. A step size of 0.02^{o} was used at a scanning speed of 1.2^{o}/min. The collected data were analyzed using analytical software, Jade6.5. The XRD results using different radiation sources were converted with the following relation:

$$\frac{\sin(\theta_{Cu})}{\sin(\theta_{Co})} = \frac{\lambda_{Cu}}{\lambda_{Co}} \tag{4.4}$$

After this conversion, the results for the same specimen from the different X-ray diffractometers matched very well.

4.4.3 Results and Discussion

A. DSC curves

Figure 4.11 shows the DSC curves for slags S1 and S2 generated at a constant heating rate of 10°C/min and different cooling rates of 1°C/min, 5°C/min or 30°C/min. The sharp endothermic trough of the heating curves at 100°C is due to water evaporation. Figure 4.11(a) also show two endothermic troughs occurred around 450°C and 750°C,

which are associated with the decomposition of carbonates. The carbonates normally used in casting powders are $CaCO_3$, and Na_2CO_3. The 450^oC endotherm might be due to the decomposition of Na_2CO_3 and the 750^oC endotherm is probably related to the decomposition of $CaCO_3$[194]. This is confirmed by the accompanying weight loss included in Figure 4.11(a) (TG), which is expected because of the volatization of CO_2. The series of endothermic peaks above 1000^oC on the heating curve indicates that the powder began to melt incongruently. The end of the last peak encountered on heating presumably represents the liquidus temperature. This is seen to be 1235^oC for slag S1.

During the cooling process, the phase transformations are very different from heating, owing to the irreversible chemical reactions that occur during melting. Several exothermic peaks were observed, where again phase transformations are indicated. On cooling, the phase transformation is believed to begin at the inflection point starting each peak. For slag S1 at 1^oC/min cooling rate, shown in Figure 4.11(a), the exothermic peaks begin at 1234^oC, 1160^oC and 1022^oC, which might correspond to the onset of three different crystalline phases forming.

In general, a higher cooling rate increases the peak height, whereas a lower rate yields higher resolution[195]. Higher cooling rates delay both the onset and finish of each phase transformation. The corresponding temperatures are also labeled in Figure 4.11(a).

Similar analysis is conducted for slag S2. The results show a lower liquidus temperature of 1050^oC and different exothermic peaks during cooling, as labeled in Figure 4.11(b). The information in Figure 4.11 is presented later to construct continuous cooling transformation curves.

B. Thermocouple dip tests cooling curves

The cooling curves recorded during the thermocouple dip tests were smoothed using the Savitzky-Golay polynomial smoothing filter to eliminate noise[167]. The Savitzky-Golay algorithm is based on performing a least squares linear regression fit of a polynomial of degree K over at least K+1 data points around each point to smooth the data. The filter coefficients: the order of the polynomial, K, the number of passes, P and the frame size, F are taken to be 2, 3, 9. These values are chosen to preserve higher moments in the data, thus reducing the distortion of essential features of the data such as peak heights and line widths in the spectrum, while efficiently suppressing random noise that degrades derivative calculation. Figure 4.12(a) compares the recorded thermocouple temperature and the filtered curve.

The temperature history curves were numerically differentiated with second order accuracy to distinguish points where the thermal gradient changes would be indicative of crystallization. As an example, Figure 4.12(b) shows two points marking the onset of sharp drop in cooling rate where the beginning of crystallization is believed to occur for slag S1 test K. Figure 4.12(c), (d) show temperature gradient profiles of thermocouple dip tests for both slags with labeled points of interest. These points were used for constructing CCT curves.

C. X-Ray diffraction results

XRD was carried out for the initial decarbonized slag powder, re-solidified atomization particles and samples after thermocouple dip tests and furnace holding tests. Figure 4.13 displays the intensity distribution as a function of diffraction angle of the slag powders before melting, and indicates that the six main phases are: silica (SiO_2), calcium

fluoride (CaF_2), wollastonite ($CaSiO_3$), calcite ($CaCO_3$), calcium silicate (Ca_3SiO_5) and sodium carbonate (Na_2CO_3).

The crystalline phases identified in the thermocouple dip tests and furnace holding devitrification tests are summarized in Table 4.5 and Table 4.6. The atomized particles had no peaks for crystalline phases, indicating that all droplets of both slags were completely amorphous. The peaks are weaker relative to the background noise for all samples, compared with the slag powder, indicating that the melting and re-solidification produced some glass in every test. Cuspidine ($3CaO•2SiO_2•CaF_2$ or $Ca_4Si_2O_7F_2$) is identified in all non-amorphous specimens. The thermocouple dip tests for slag S1 with slower cooling rates (Test D, K, I) indicate calcium silicon oxide fluoride ($SiO_2•2CaF_2$ or $Ca_2SiO_2F_4$)[196] phase also, as shown in Figure 4.14. This shows that cuspidine crystallizes easily and that perhaps $Ca_2SiO_2F_4$ crystallization is suppressed by the higher cooling rate.

Figure 4.15 indicates the evolution of crystalline phase(/s) forming at progressively longer holding times in the furnace devitrification tests from the glassy state at 700°C. In slag S1, the first (easiest) phase to form is cuspidine which first appears after holding at 700°C for 30 minutes. With increasing furnace temperature, different phases are found as shown in Figure 4.16. Nepheline ($Na_2O•Al_2O_3•2SiO_2$ or $NaAlSiO_4$) is found in slag S1 at temperatures greater than 900°C. Holding slag S1 longer than one hour at 1100°C causes the peaks of nepheline to disappear and a new phase, gehlenite ($2CaO•2Al_2O_3•SiO_2$ or $Ca_2Al_2SiO_7$) to form, as shown in Figure 4.16(a). This phenomenon was also observed by Grieveson[197] and O'malley[198].

For slag S2, no crystalline phase forms at 500°C even after two hours of holding. Besides cuspidine, some new phases such as nepheline and calcium silicate ($2CaO•SiO_2$ or Ca_2SiO_3, $8CaO•5SiO_2$ or $Ca_8Si_5O_{18}$) are found in slag S2 when holding at 700°C for two hours. Instead of gehlenite in slag S1, a sodium calcium silicate phase ($Na_2O•2CaO•3SiO_2$ or $Na_2Ca_2(SiO_3)_3$) is found at 900°C. When the holding temperature is near to the slag melting temperature, only a small amount of crystalline cuspidine phase is observed in the amorphous background(Figure 4.16(b)). This might due to the lower driving force for crystallization at higher temperature.

D. CCT curves

From the time-temperature profiles recorded during the DSC tests and thermocouple dip tests, CCT diagrams were constructed by taking time starting at zero when the cooling curves crossed the liquidus temperature (1235°C for slag S1 and 1050°C for slag S2). Figure 4.17(a) shows the CCT diagram for slag S1. The critical cooling rate to maintain the amorphous structure is estimated to be 50°C/s. At slower cooling rate, the first crystalline phase appears at around 1200°C, which should be cuspidine ($Ca_4Si_2O_7F_2$) according to the XRD analysis. Watanabe measured that the liquidus of cuspidine varies between 1114°C (55% CaF_2) and 1407°C (20% CaF_2) in the CaO-SiO_2-CaF_2 ternary system(Figure 2.4(a))[123]. For the slag S1, Figure 2.4(a) shows a liquidus temperature of 1250°C, which almost matches with the result in this work. As slag S2, the liquidus temperature is found to be lower. This might be due to the effect of many other compounds in the slag, especially Na_2O, Al_2O_3 etc, which decrease the system melting temperature. When the cooling rate is slower than 10°C/s, a second crystalline phase is formed at around 1100°C, which could be silicon oxide fluoride

($Ca_2SiO_2F_4$) phase. The DSC tests with very slow cooling rate (<5°C/min) shows a third peak near 900°C as shown in Figure 4.11(a), implying the existence of a third phase, which could not be distinguished in the XRD pattern of the thermocouple dip tests. The cooling curves of the dip tests are more ambiguous but do not appear to show the third phase either. This suggests that this phase is suppressed at the faster cooling rate in comparison to the DSC tests. The XRD results from furnace heating devitrification tests confirm that more crystalline phases form at 900°C to 1100°C. Comparing these results with the phase diagrams in Figure 2.4, these phases generally shows lower liquidus line which is due to the eutectic reaction between each other.

Similarly, Figure 4.17(b) shows the CCT diagram for slag S2 featuring a critical cooling rate of only 20°C/sec. This low critical cooling rate confirms the conjecture that slag S2 is glassy. The cuspidine ($Ca_4Si_2O_7F_2$) phase starts to form at around 1050°C. Other crystalline phases were observed from isothermal aging tests as described in previous section, though they are difficult to be distinguished unambiguously in the XRD pattern and cooling curves of thermocouple dip tests.

4.5 Slag Film Microscopy

4.5.1 Polarized Transmitted Light Microscopy

Polarized Light Microscopy is a technique that examines a material's optical properties to investigate its microstructure. It can be best applied to materials that are anisotropic and have two indices of refraction. These materials are called "birefringent". When polarized light enters a birefringent material, it splits up into two rays that vibrate along the two principal directions of the anisotropic crystal lattice. One of these rays is called the fast ray, and the other the slow ray. By the time the rays emerge from the

specimen, one of them has been retarded, or slowed down, more than the other and this angle of retardation can be used to deduce the crystal structure of the material[199]. Specifically, retardation measurements are typically applied to distinguish between isotropic and anisotropic materials.

Isotropic materials, which include gases, liquids, and glasses, demonstrate the same optical properties in all directions. They have only one refractive index and no restriction on the vibration direction of light passing through them. Thus when the isotropic specimen is examined under cross polarized light, no retardation of either ray occurs, so total extinction of the reassembled light is observed. Anisotropic materials, in contrast, have optical properties that vary with the orientation of incident light with the crystallographic axes. They demonstrate a range of refractive indices depending both on the propagation direction of light through the substance and on the vibrational plane coordinates. More importantly, anisotropic materials act as beam splitters and divide light rays into two parts. The technique of polarizing microscopy exploits the interference of the split light rays, as they are re-united along the same optical path to extract structure information about these materials.

A piece of film of slag H1 from interfacial steel shell/mold gap was caught as it folded off the mold wall during tail-out after continuous casting process[200]. The slag film was cut into thin slices only 0.03mm thick and mounted on microscope slides, which are called “thin sections”. The thin section specimen was then observed under polarized light microscopy, which was carried out at the Department of Geology, UIUC.

Figure 4.18(a) shows the different layers and cracks in the slag film under plane polarized light. Figure 4.18(b) to (d) are the images under cross polarized light obtained

by rotating the specimen stage. The extinction on the steel side layer proves that it is isotropic. Because crystals of any size or composition have some anisotropic properties, this indicates that the layer is a glassy layer. This suggests that the layer was formed from air quenching the liquid slag while obtaining the sample. Note that the critical cooling rate for obtaining glass is well below typical cooling rates encountered during air cooling, so this finding is reasonable. (Lumped parameter cooling analysis with slag layer thickness of 2mm, heat transfer coefficient of 200W/m^{2}K and conductivity of 1.5W/mK produce the Biot number of 0.26 and a cooling rate of 80°C/sec)

4.5.2 Scanning Electron Microscopy (SEM)

To further investigate the morphology and composition distribution of the slag film, an SEM microstructure analysis was carried out on the Zeiss DSM 960 with an energy dispersive x-ray spectroscopy system (EDX), which is available at the Center for Microanalysis of Materials (CMM) at UIUC. It has a LaB_6 source to provide a stable beam for quantitative analysis and is also equipped with a system for the observation of backscattering patterns.

Figure 4.19(a) shows the backscatter electron image (BSE) of the slag H1 film. Figure 4.19(b) is a close-up of the interface between the two layers. Crystals on the left can be clearly seen growing into the glassy layer on the right. To investigate the composition distribution in the specimen, a series of EDX mapping was performed. Each image was created by mapping the X-ray intensity at each point for a specific element. As shown in Figure 4.20, the bright region indicates where the specific element has a high concentration. On the right side of each image, all elements are distributed homogenously, which again confirms the glassy microstructure of the right side. The

EDX spectrum was also used to identify the element composition of different regions in the sample. The crystalline side (left) is composed of high-calcium grains (point B) in a high-silicon background (Point D). These likely represent crystals of cuspidine that precipitated. Figure 4.21(a)-(c) indicate that the area average composition is almost the same for the crystal and glassy regions, which indicates that no severe macro-segregation occurred in the gap during casting.

4.6 Tables and Figures

Table 4.1 Mold Powder Composition (wt%)

	S1	S2	K1	H1
SiO_2	34.33	38.33	31.38	36.01
CaO	29.69	13.30	21.52	35.74
Al_2O_3	5.55	2.43	4.85	4.63
CaF_2	15.93	14.05	28.12	6.82
Na_2O	4.75	13.44	9.57	6.04
MgO	3.05	1.45	0.84	<3.0
TiO_2	<1.0	<0.5	-	<3.0
Fe_2O_3	<1.5	<1.5	0.20	<3.0
MnO	<1.0	<0.5	0.01	<3.0
K_2O	<1.0	<0.5	0.80	<3.0
Li_2O	-	<1.0	-	-
B_2O_3	-	1.41	-	-
C-Total	4.11	11.49	2.36	5.73
CO_2	3.22	3.78	2.75	-
C-Free	3.23	10.46	1.61	

Table 4.2 HTT Friction Tests

Test #	Slag	Process	Maximum wear track depth (μm)
Run #A	K1	Increase Temperature from 25°C to 870°C	- (softened)
Run #1	S1	Increase Temperature from 25°C to 980°C	24
Run #5	S1	Decrease temperature from 920°C to 80°C	152
Run #7	S1	Increase Temperature from 25°C to 900°C, then decrease temperature from 900°C to 200°C	249
Run #8	S1	Decrease temperature from 890°C to 200°C	102
Run #3	S2	Increase Temperature from 25°C to 300°C	-
Run #4	S2	Increase Temperature from 25°C to 550°C	2254 (softened)
Run #6	S2	Increase Temperature from 25°C to 550°C	1460 (softened)

Table 4.3 Dip Thermocouple Tests Cooling Rates Range (°C/sec)

Slag S1	Test F	Test E	Test D	Test K	Test I
CR range	22~40	20~50	10~16	0.7~20	1.1~15
Slag S2	Test 1	Test 2	Test 9		
CR range	1.3~20	0.7~15	0.5~6		

Table 4.4 Slag Annealing Treatment

	1min	10min	30min	60min	120min
500°C		S2	S2	S2	S2
700°C	S1, S2		S1, S2	S1	S1, S2
900°C	S1, S2	S1, S2	S1, S2	S1, S2	S1, S2
1000°C		S2			
1100°C	S1	S1	S1	S1	

Table 4.5 Phases Present in Slag S1 from Dip TC Tests and Devitrification Tests

Phases \ Test	F	E	D	K	I	700°C 1min	700°C 30min	700°C 60min	900°C 1min	900°C 120min	1100°C 1min	1100°C 60min
Glass	X	X				X	X					
Cuspidine ($Ca_4Si_2O_7F_2$)	X	X	X	X	X		X	X	X	X	X	X
Calcium silicon oxide fluoride ($Ca_2SiO_2F_4$)			X	X	X				X	X	X	X
Nepheline ($NaAlSiO_4$)									X	X	X	
Gehlenite ($Ca_2Al_2SiO_7$)												X

Table 4.6 Phases Present in Slag S2 from Dip TC Tests and Devitrification Tests

Phases \ Test	1	2	9	500°C 120min	700°C 1min	700°C 30min	700°C 120min	900°C 1min	900°C 60min	1000°C 10min
Glass	X	X		X	X	X				X
Cuspidine ($Ca_4Si_2O_7F_2$)		X	X			X	X	X	X	X
Calcium silicate (Ca_2SiO_4)						X	X	X	X	
Nepheline ($NaAlSiO_4$)							X			
Calcium silicate ($Ca_8Si_5O_{18}$)							X	X		
Sodium calcium silicate ($Na_2Ca_2(SiO_3)_3$)									X	

Figure 4.1 High Temperature Tribometer

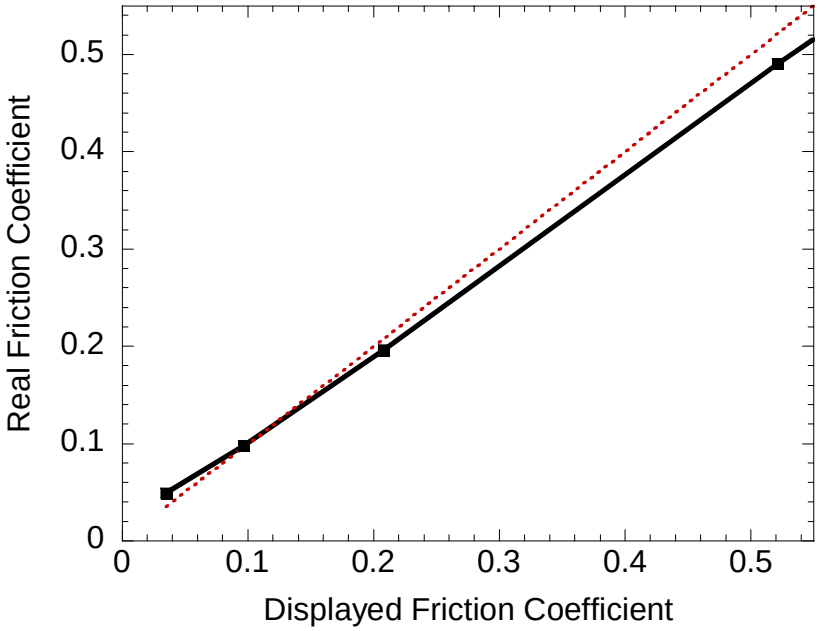

Figure 4.2 Comparison of HTT displayed friction coefficient and real friction coefficient

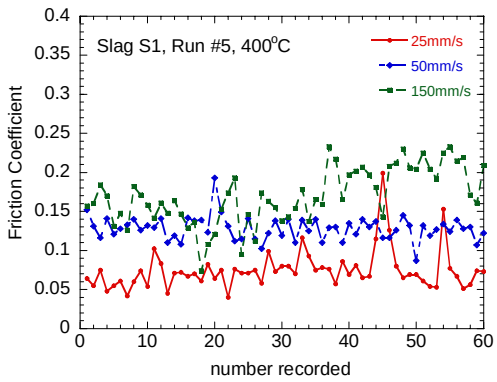

(a) Friction variation with time

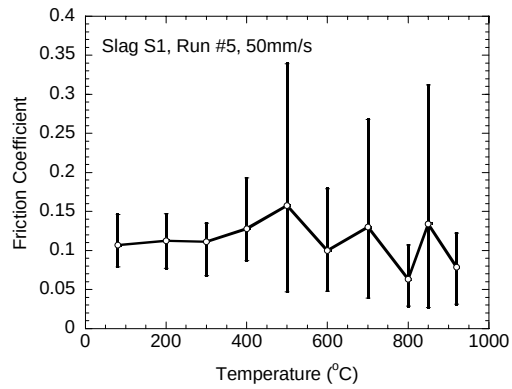

(b) Friction variation with temperature including "error bars" to indicate data ranges

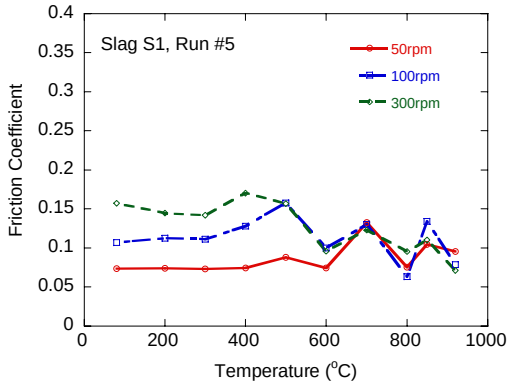

(c) Average friction coefficient vs. temperature at different speeds

Figure 4.3 Friction coefficient for slag S1 Run #5

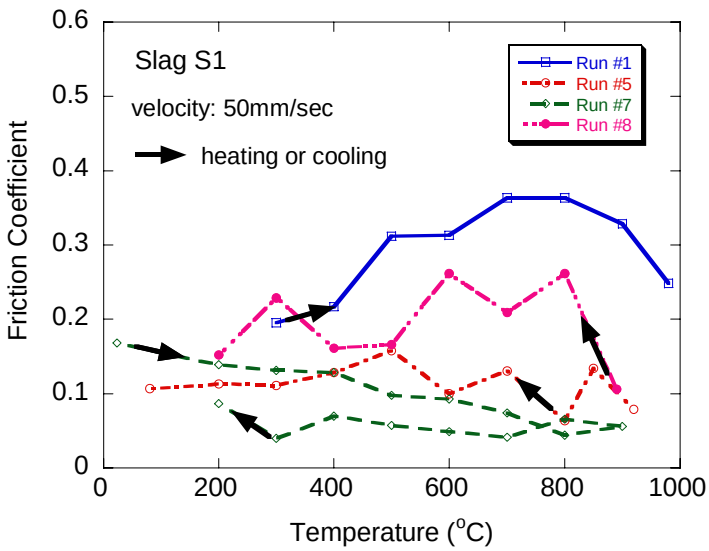

Figure 4.4 Friction coefficient vs. temperature for slag S1

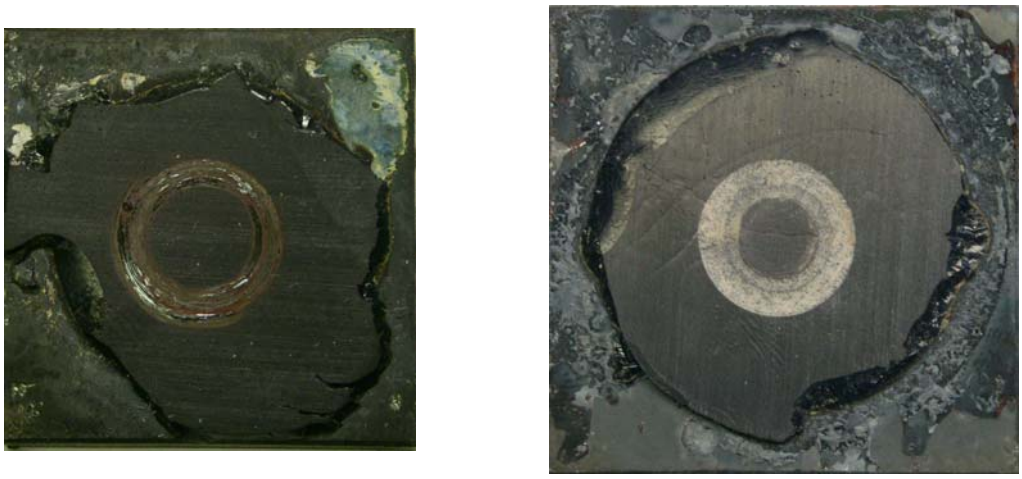

(a) Run #1 **(b) Run #5**

Figure 4.5 Picture of the specimen for slag S1 after tests

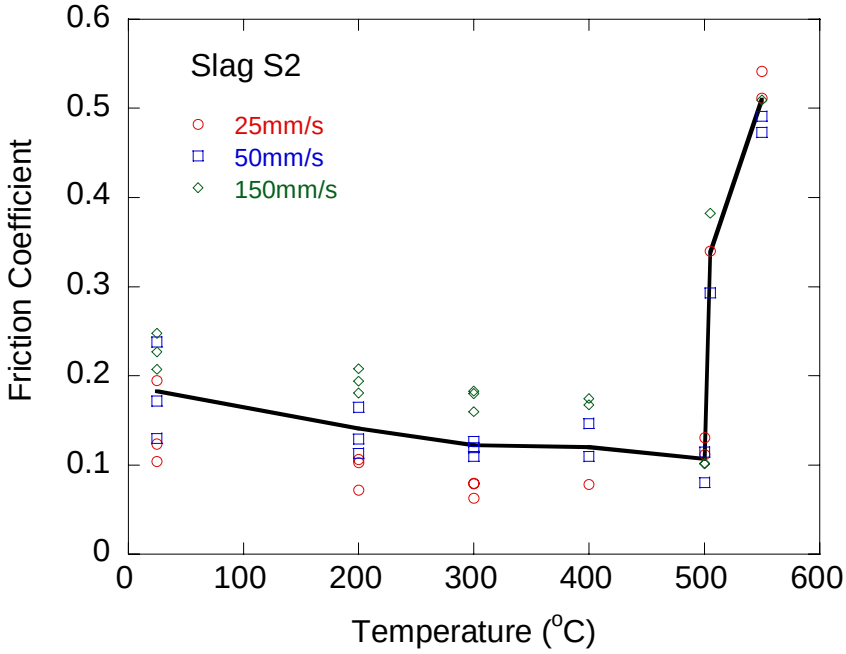

Figure 4.6 Friction coefficient vs. temperature for slag S2 (Runs #3, #4 and #6)

(a) Before Test **(b) After Test**

Figure 4.7 Picture of the friction specimen for slag S2 (Run #6)

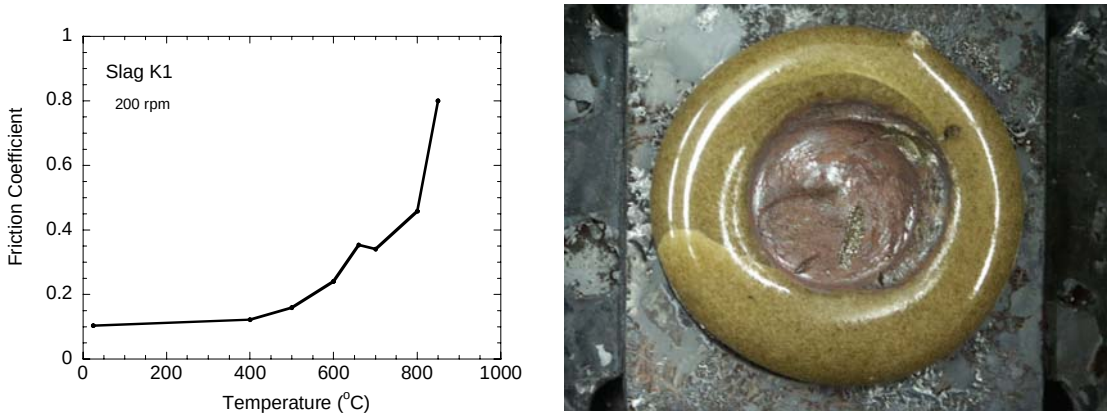

(a) Friction Coefficient **(b) After Test**

Figure 4.8 Friction test for slag K1 (Run #A)

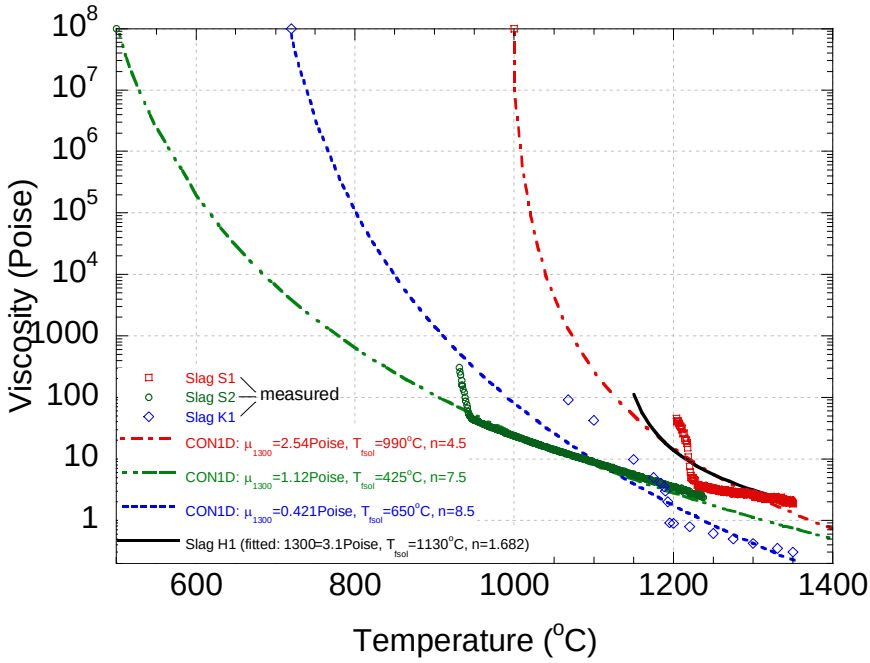

Figure 4.9 Measured slag viscosity with CON1D fitted curves

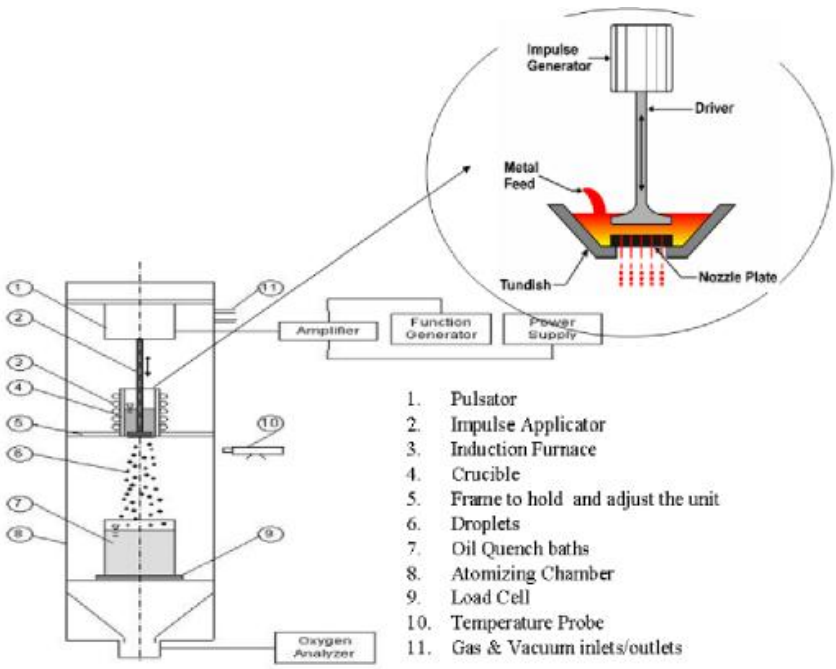

Figure 4.10 Impulse Atomization Process[192]

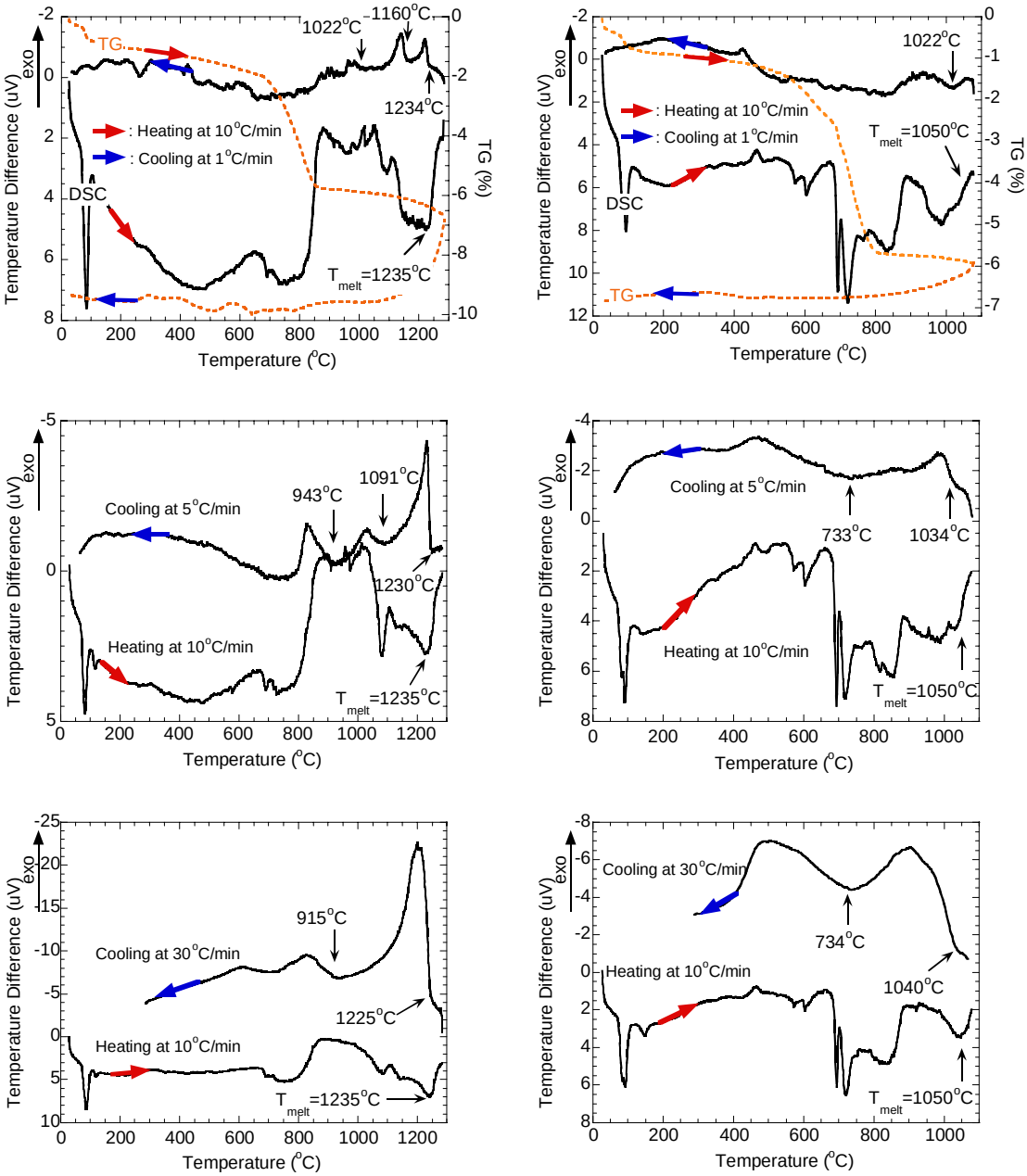

(a) Slag S1 **(b) Slag S2**

Figure 4.11 DSC/TG curves for slag S1, S2 at 10°C/min heating rate and 1°C/min, 5°C/min or 30°C/min cooling rate

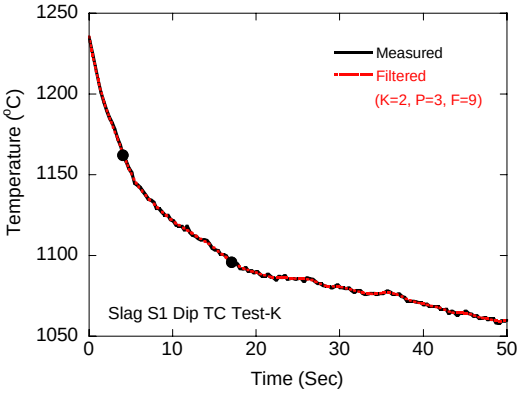

(a) Temperature History of Test K

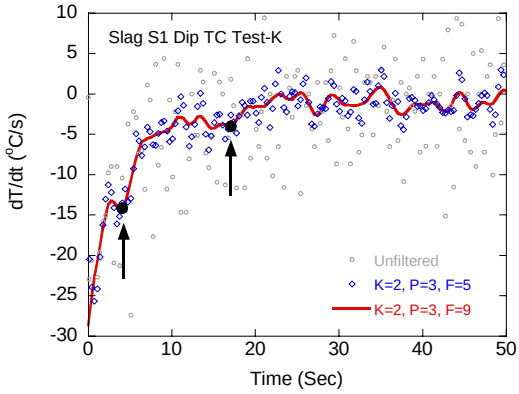

(b) Temperature derivative of Test K

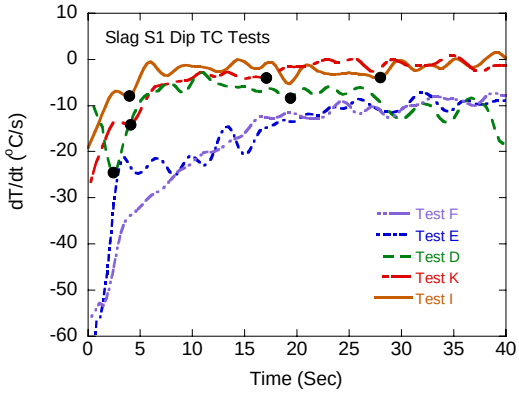

(c) Temperature derivative of Slag S1

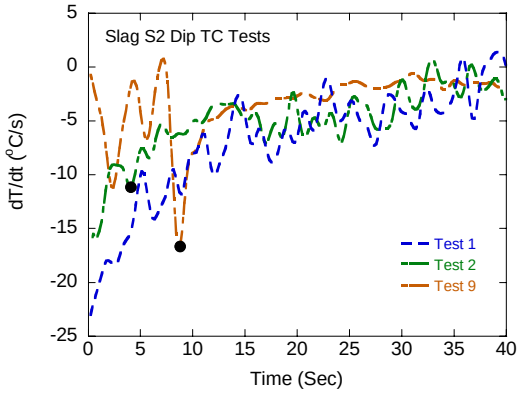

(d) Temperature derivative of Slag S2

Figure 4.12 Analysis of TC cooling curves in dip tests

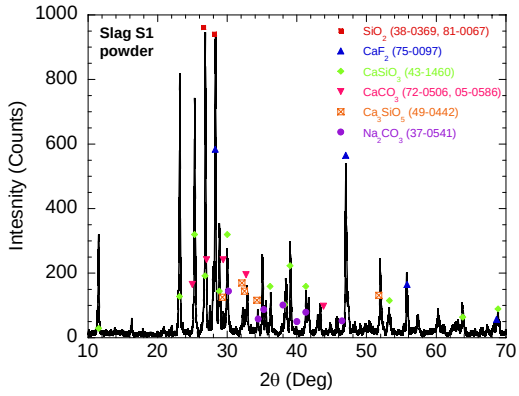

(a) Slag S1

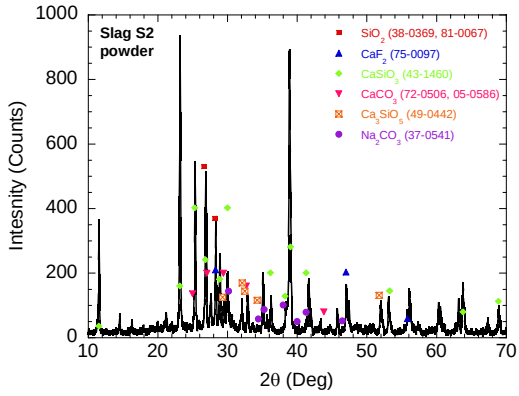

(b) Slag S2

Figure 4.13 XRD pattern of slag powder

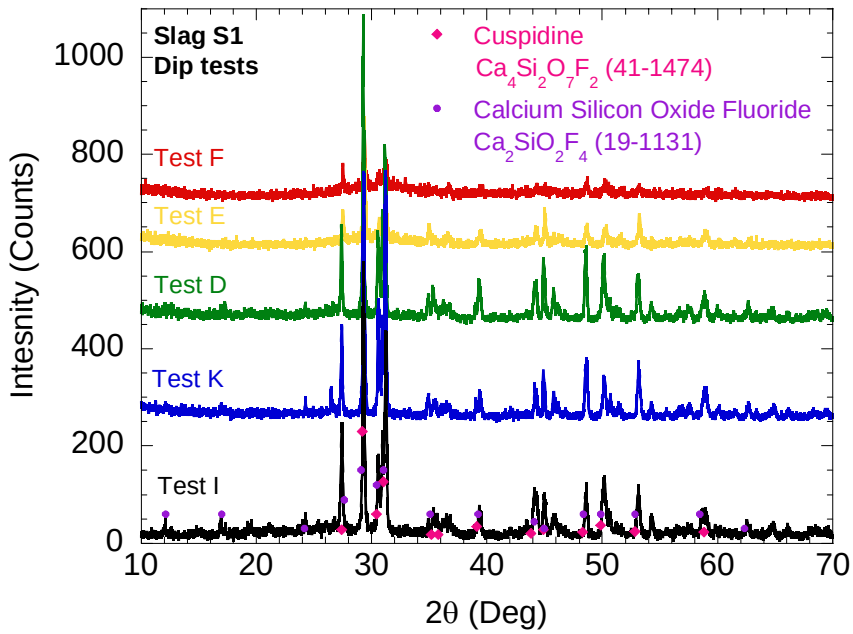

(a) Slag S1

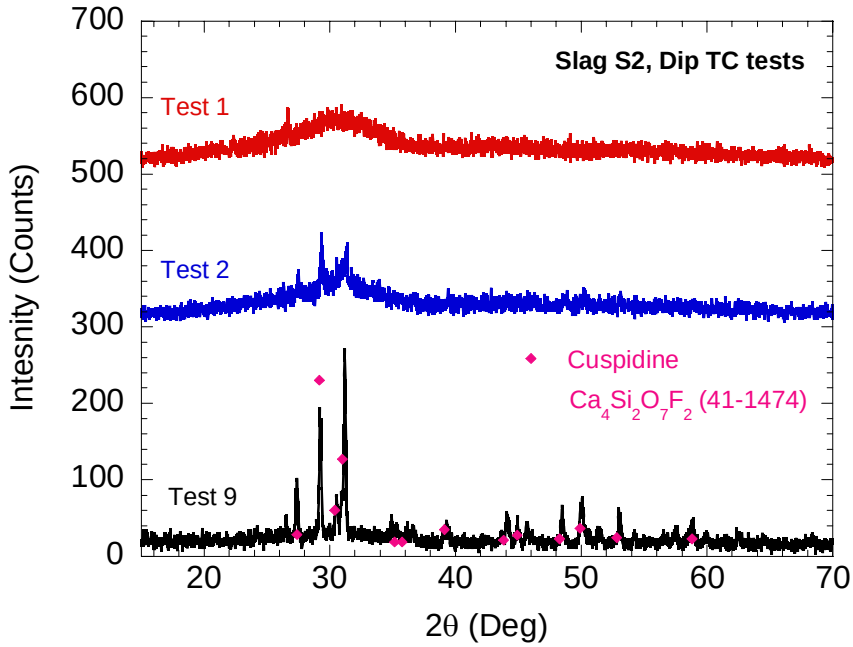

(b) Slag S2

Figure 4.14 XRD pattern of dip TC tests

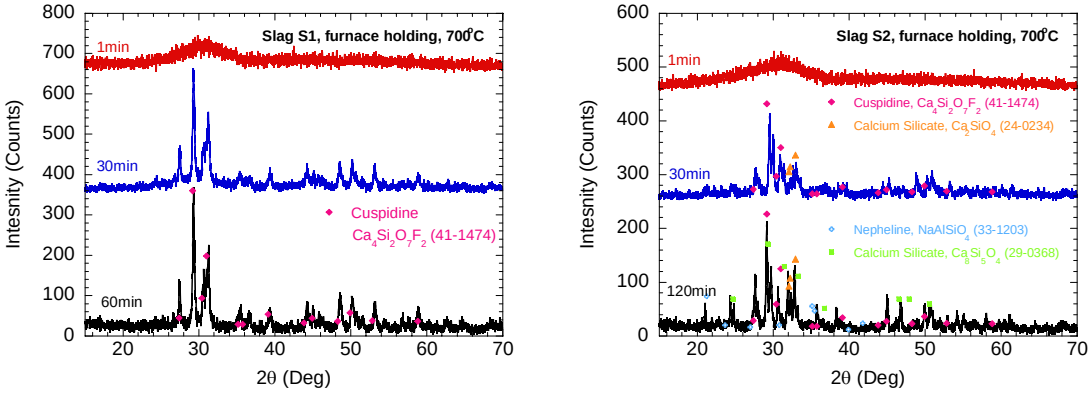

(a) Slag S1 **(b) Slag S2**

Figure 4.15 XRD pattern of slag devitrification tests at 700°C

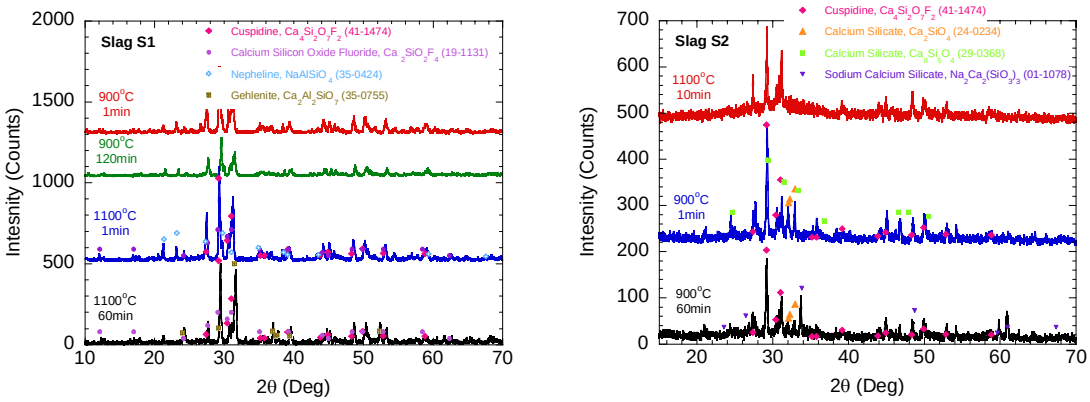

(a) Slag S1 **(b) Slag S2**

Figure 4.16 XRD pattern of slag devitrification tests at high temperature

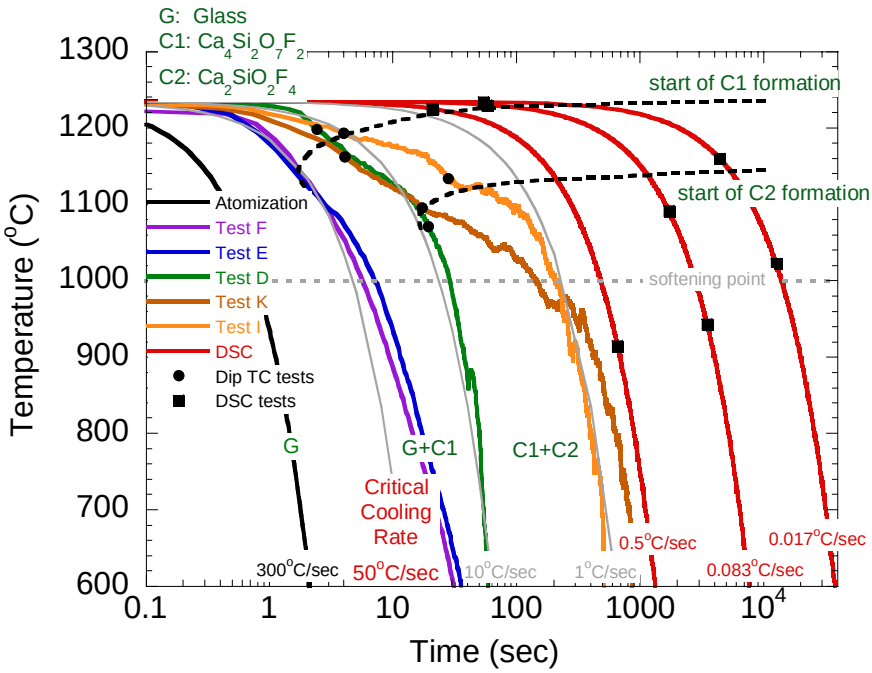

(a) Slag S1

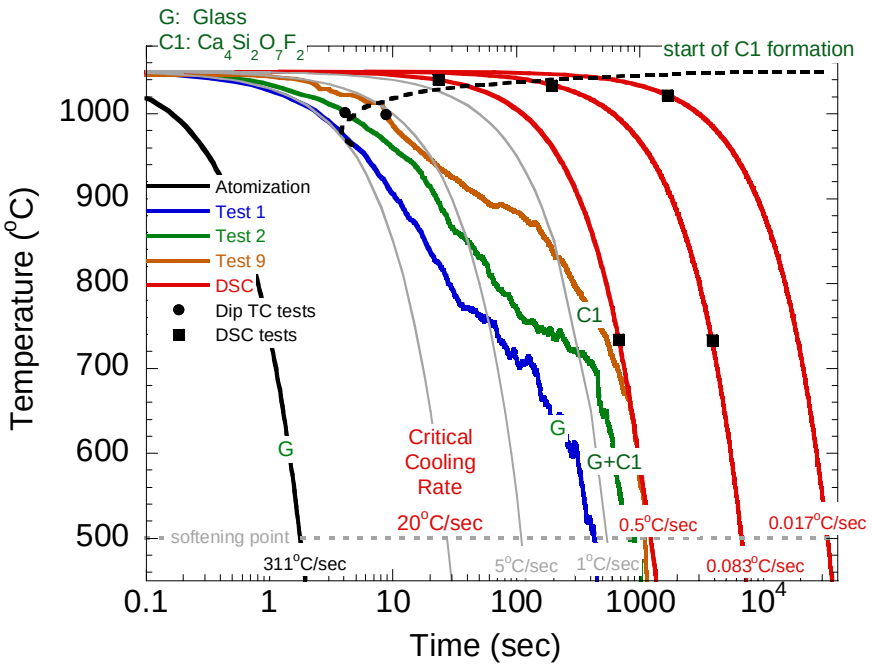

(b) Slag S2

Figure 4.17 CCT diagram

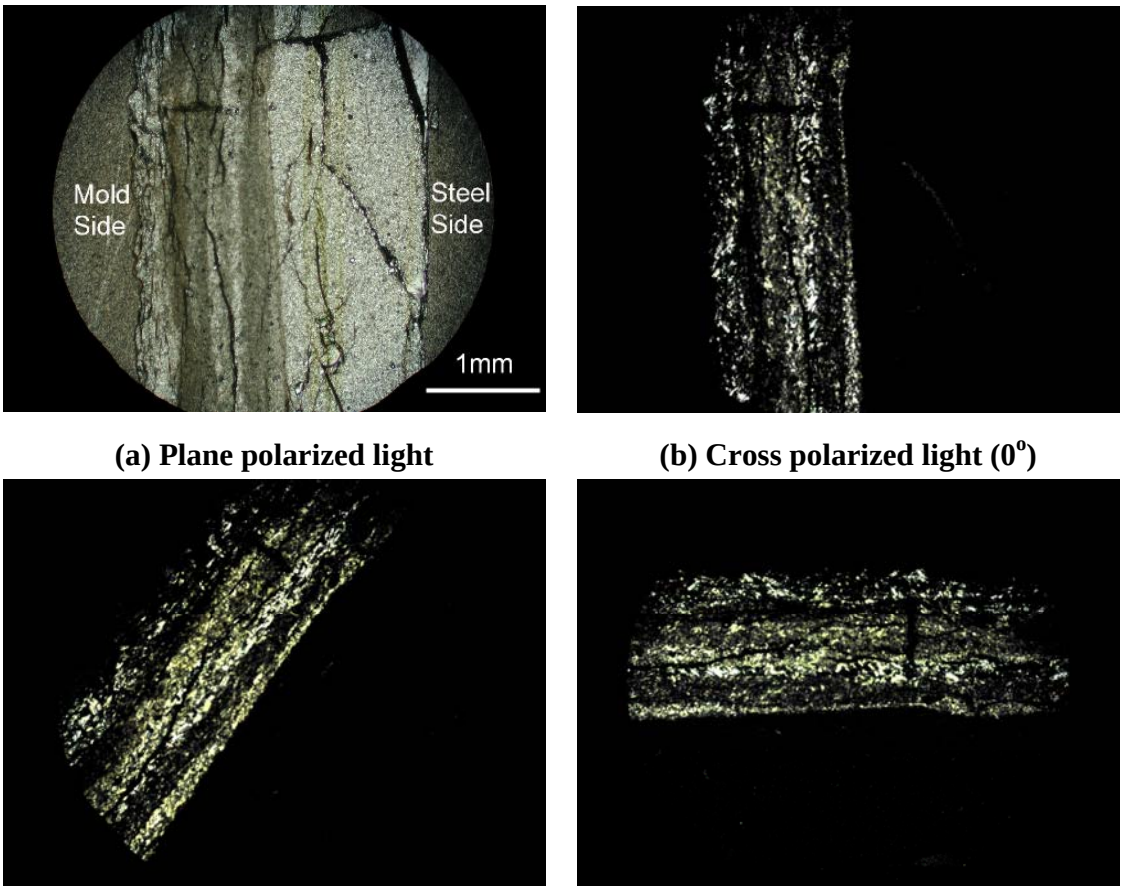

(a) Plane polarized light **(b) Cross polarized light (0°)**

(c) Cross polarized light (45°) **(d) Cross polarized light (90°)**

Figure 4.18 Polarized light microscopy (slag H1)

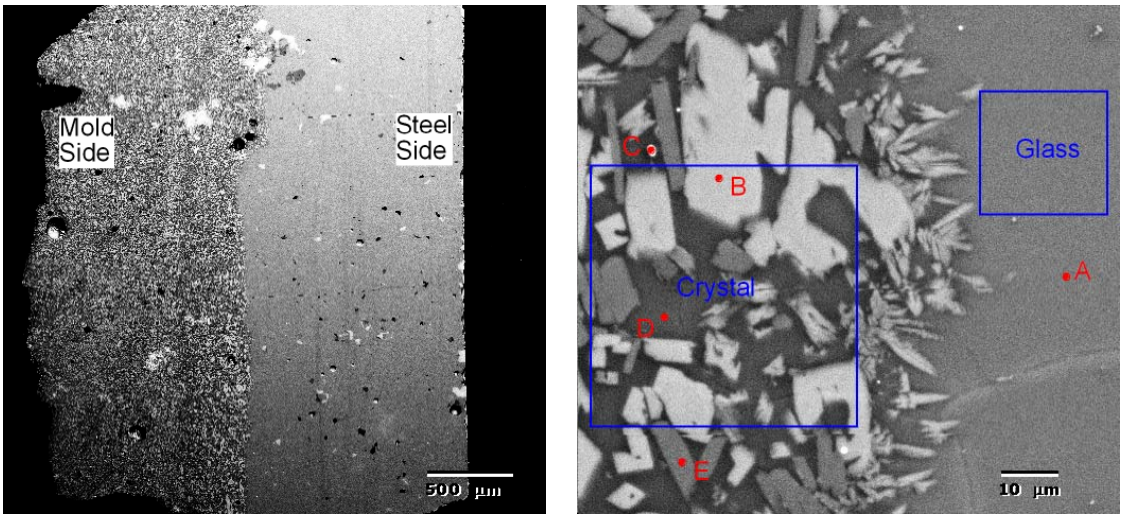

(a) **(b)**

Figure 4.19 BSE image of slag H1 film

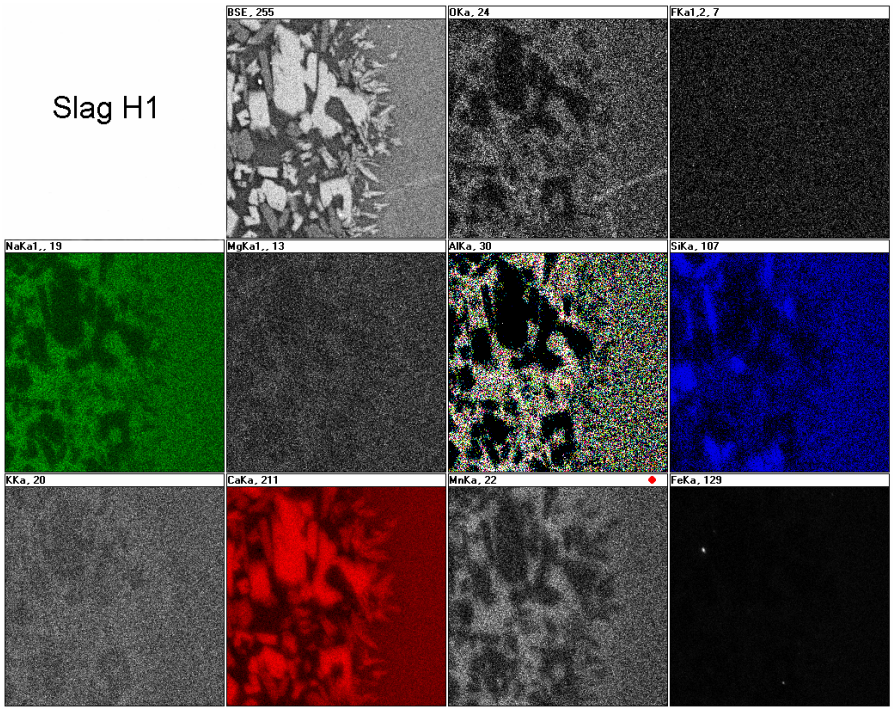

Figure 4.20 EDX mapping of slag H1 film

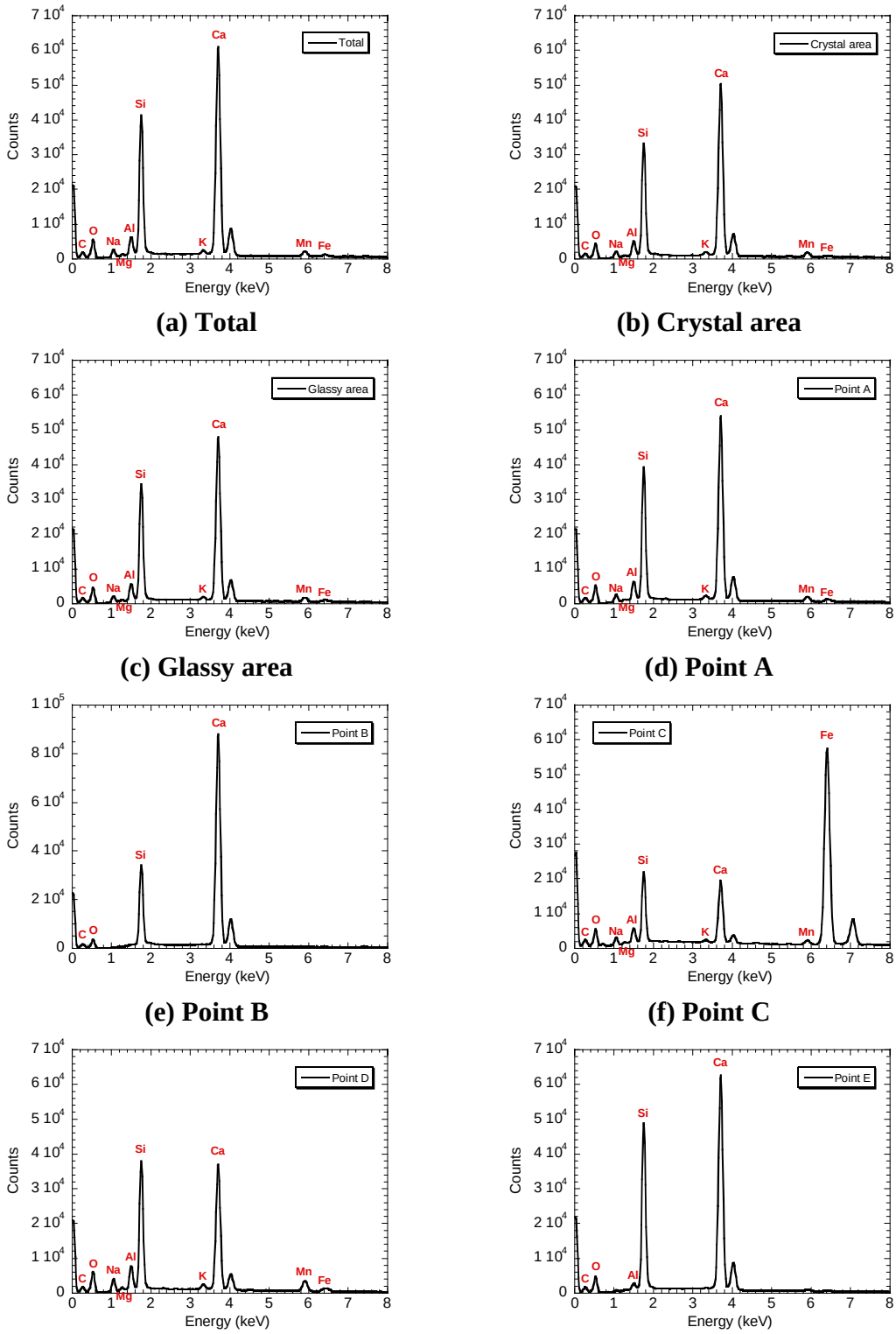

(a) Total (b) Crystal area

(c) Glassy area (d) Point A

(e) Point B (f) Point C

(g) Point D (e) Point E

Figure 4.21 EDX spectrum of slag H1 film for points and areas in Figure 4.19(b)

CHAPTER 5. MODEL CALIBRATION

Having shown the model to be internally consistent, it cannot be used quantitatively until it is calibrated to match measurements on the specific operating caster of interest. This step is necessary because so many of the inputs to the model are uncertain.

To date, the model has been calibrated to match many different casters, including slabs at BHP LPD in Whyalla, South Australia; LTV Steel in Cleveland, OH[201], AK Steel in Mansfield, OH[34], Allegheny Ludlum in Brackenridge, PA[202], Columbus Stainless Steel in Middleburg[35], South Africa, Siderar in Argentina, and China Steel in Taiwan, ROC; thin slabs at Nucor in Crawfordsville, IN[203] and POSCO in Seoul, S. Korea[204]; blooms at BHP RBPD in Newcastle, New South Wales[205]; and billets at POSCO Pohang in S. Korea[36]. In order to calibrate the model, it is simply run several times, using trial and error to find values of the model parameters that allow the model predictions to match all of the known measurements for a given set of casting conditions. Those measurements can include the cooling water temperature rise, the time-average temperature of any thermocouples embedded in the mold, the thickness profile of breakout shells, the thickness of solidified mold powder layers and slag rims, and the temperature histories of any thermocouples embedded in the strand.

Specifically, adjustments can be made to the velocity of the solid slag layer, the value of the contact resistances down the mold, and even the thermal properties of the mold slag. Other influential input parameters include the average powder consumption rate and the average oscillation mark depth and width.

In a slab caster with properly designed taper, there should not be any air gap due to shrinkage down the center of the wide face. This is because ferrostatic pressure pushes the long, wide, weak shell against the mold to maintain as close a contact as possible. This greatly simplifies model calibration when simulating a slice through the wide face of the mold and shell.

Input parameters for the standard case, Table 5.1, were calibrated to match the casting conditions of the 0.225m$\times$1.78m slabs of low-carbon steel cast at LTV Steel Cleveland, OH, where cooling water temperature rise, mold thermocouple temperatures, and breakout shell measurements were available[30, 206]. The steel composition is 0.044% C, 0.022%Mn, 0.006%S, 0.01%P, 0.009%Si and 0.049%Al.

5.1 Mold Cooling Water Temperature Rise

The first step in model calibration is to match the total heat extracted in the mold, Q, with the measured temperature increase of the mold cooling water. The average rate of heat extracted from the mold per unit surface area, Q, is found from:

$$Q = \frac{V_c}{Z_{mold}} \sum_{mold} q_{\text{int}} \Delta t \tag{5.1}$$

This heat transfer rate should equal the temperature increase of the mold cooling water, ΔT_{water}, flowing through the "hot" channels, located adjacent to the slab width area:

$$\Delta T_{water\_hot\ channels} = \sum_{mold} \frac{q_{\text{int}} L_{ch} V_c \Delta t}{\rho_{water} C_{pwater} V_{water} w_{ch} d_{ch}} \tag{5.2}$$

This equation assumes that the cooling water slots have locally uniform rectangular dimensions, w_{ch} and d_{ch}, and spacing, L_{ch}. Heat entering the hot face (between two water

channels) is assumed to pass straight through the mold to heat the water flowing through the cooling channels.

To compare with the measured water temperature increase, the above prediction is modified as follows to account for missing slots due to bolts or water slots, or slots that are beyond the slab width, so do not participate in heat extraction:

$$\Delta T_{water\_total\ channels} = \Delta T_{water\_hot\ channels} \frac{w_{ch} \cdot d_{ch} \cdot W / L_{ch}}{total\ channel\ area} \tag{5.3}$$

Using reported slag properties and consumption rate (Table 5.1), heat flux was calibrated to match the measured temperature rise of 7.1 deg C by adjusting the solid slag speed ratio, f_v, to 0.175. The corresponding temperature rise in just the hot channels is predicted to be 7.5 deg C.

5.2 Mold Temperatures

The next step in calibration of CON1D is to further adjust the model parameters to match the measurements of thermocouples embedded in the walls of the operating casting mold. This step is very constrained, however, as every change that causes a local increase in heat flux must be balanced by a corresponding decrease elsewhere, in order to maintain the balance with the cooling water already achieved.

In this example, Table 5.1, the slag rim shape in region I was chosen to decrease linearly from 0.8mm at the meniscus to 0.5mm at 15mm below the metal level, which is near to the position of peak heat flux. The peak heat flux position should not be confused with the location of peak mold temperature, which is usually about 35mm below the heat flux peak (55 mm below the meniscus in this case). Assuming no air gap in the interface for this wide face simulation, the contact resistances and scale thicknesses are other

adjustable input conditions to match the mold thermocouple measurements. Here a 0.02mm scale layer was assumed for the top 305mm, where special designed inserts had been installed to increase the local cooling water velocity[206] and 0.01mm scale for the bottom remainder of the mold. These thicknesses are in accordance with plant observations that the hot region had a thicker scale layer[63].

Figure 5.1 compares the calibrated and measured temperatures at several locations down the LTV mold. The thermocouples were all 18.8mm below the mold hot face. The agreement indicates the calibration of the model for these typical casting conditions. This figure also shows the predicted hot face and cold face temperature profiles. The sharp change in temperature is due to a sudden increase in water channel depth, produced by experimental inserts used in the trial[206]. Note that the observed scale layer greatly increased the mold temperature, especially in the hot portion that contained the insert. Based on this insight, steps were taken to improve water quality to prevent this scale and improve mold life[206].

5.3 Shell Thickness

Having calibrated the model, the predicted shell thickness profile is compared with measurements down a breakout shell that occurred under very similar castings conditions, as given in Figure 5.2. Shell thickness is defined in the model by interpolating the position between the liquidus and solidus isotherms with the temperature corresponding to the specified solid fraction, f_s, according to the phase fraction-temperature relationship in Figure 3.2. In this sample case, f_s=0.1, which is the only adjustable parameter remaining for model calibration. This fraction is reasonable as inter-dendritic liquid is held by surface tension during draining of the breakout.

To compare the predicted steady shell thickness with that of a breakout shell, a correction is needed to account for the solidification time that occurred while the liquid metal was draining during the breakout[207]. Thus, time in the steady simulation corresponds to distance down the breakout shell according to the relation:

$$t = \frac{z}{V_c} + t_d \tag{5.4}$$

where the "drainage time" t_d is the time for the metal level to drop from the meniscus to the breakout slice of interest, z. Drainage time is calculated based on the Bernoulli equation and a mass balance[208]:

$$t_d = \frac{\sqrt{Z_b} - \sqrt{Z_b - z}}{C_D \frac{\pi d_b^2}{4NW} \sqrt{\frac{g}{2}}} \tag{5.5}$$

where the drainage coefficient C_D =1. For the present case, the position of the breakout hole from the meniscus, Z_b=1.524m; slab thickness, N=0.225m; slab width, W=1.78m. Assuming that steel flow to the mold was shut off simultaneously with the metal level starting to drop below the meniscus, and the breakout hole diameter d_b began at 50mm and linearly grew to 90mm by the time all liquid steel had drained, a transient shell profile can be calculated. Figure 5.2 gives the predicted shell thickness at both steady state and transient conditions, compared with the break-out shell measurements. The generally close match with the transient predictions tends to validate the model. The underpredicted shell thickness near the meniscus is likely due to a short interval of increased liquid flow into the mold after the breakout started and before level control and flow were shut off. This would have allowed the liquid level to move downward with the top of the breakout shell for a short time interval (not included in the model), thus

providing additional solidification time at the very top of the breakout shell. This effect is commonly observed in breakout shells.

Growth of the shell naturally depends on both the interfacial and superheat fluxes. The superheat distribution is important to the narrow face, as Figure 3.1 shows that the two curves are of the same magnitude low in the mold where the hot molten steel jet impinges against the solidifying shell. Figure 5.2 shows the shell thinning of the narrow face due to this jet impingement effect.

Variation in the superheat flux is critical to shell growth down the narrow face and off-corner regions, where problems such as inadequate taper sometimes produce significant air gap(s). Together, the large superheat combined with decreased heat transfer across the interfacial gap can reduce shell growth. This was the subject of a significant study using the model, which was reported elsewhere[19].

5.4 Powder Layer Thickness

The model predicts the thickness and velocity profiles expected in the powder layers in the interfacial gap. For example, Figure 5.3 shows the solid and liquid slag layer thickness profiles expected for the standard conditions investigated here (Table 5.1). It shows that the liquid slag layer runs out at 380mm below the meniscus, where the liquid slag layer/steel shell interface temperature T_s' drops below the slag solidification temperature of 1045°C as shown in Figure 5.4. The total slag thickness continues to increase while there is still liquid coming from the oscillation marks. This is indicated in Figure 5.4, where the shell surface temperature at the oscillation mark roots, T_s, still exceeds 1045°C at mold exit. Although no reliable slag samples were obtained from this

caster, these slag thickness predictions of 0.5 to 1.5mm are consistent with samples measured at similar plants[31, 204].

5.5 Shell Surface Temperature

Typical model predictions of the surface temperature in the mold are shown in Figure 5.4 for standard conditions. When liquid slag layer runs out at 380mm below the meniscus (Figure 5.3), the liquid entrapped in the oscillation marks flows out and air fills in. This increases the resistance of the oscillation mark, so the temperature difference between the oscillation mark root and peak increases also, as shown in Figure 5.4.

After exiting the mold, the slab surface quickly reheats, and then fluctuates greatly as it travels through the spray zones. Heat is extracted rapidly during contact with the support rolls and when passing through the impingement zone of the cooling water from the spray nozzles, which each cause great temporary drops in surface temperature.

Lacking accurate spray and roll contact heat transfer coefficients, calibration of temperature predictions below the mold can be calibrated by adjusting the model parameters f_{roll} and spray coefficients to match measurements such as roll cooling water heat extraction rate, and thermocouple temperatures embedded in the strand. An example of such calibration is shown in Figure 5.5 for casting conditions measured at China Steel #1 slab caster in Taiwan, ROC, given in Table 5.2 and Table 5.3. The temperature measurements were achieved by feeding a block containing several thermocouples into the mold just before “tail-out” at the end of casting[37]. The thermocouple tips extending through the bottom of the block were soon frozen into the strand. Being positioned before the last several meters of steel before the end of the cast ensured that the recorded temperature histories would be typical, while allowing the insulated tube of thermocouple

wires extending from the top of the block to follow the strand through the caster with minimal damage. The distance of each thermocouple from the surface was measured after sectioning the final product.

Internal temperature histories measured at three places beneath the surface are included in Figure 5.5. Both surface thermocouples needed about 500 mm to heat up to their surrounding shell temperatures, and later suffered from internal debonding, so their results are reliable only between 500 and 3000 mm. The centerline thermocouple needed almost 2m to heat up and appears to be accurate within 10°C. Both the internal temperatures and the amplitude of their wiggles are roughly matched, indicating the degree of calibration. Temperature fluctuations at the thermocouple location are quite small, compared with the surface, which varies over 100°C over a single roll pitch. Near the top of the caster, the greatest surface temperature drop occurs beneath each spray jet, while a tiny dip occurs at each small region of direct contact with a support roll. Lower in the caster, the relative size of the dips becomes closer, with deep sharp drops caused by the high local heat extraction rate during roll contact under high ferrostatic pressure

Optical pyrometers are also useful for model calibration[176], but are adversely affected by intermittent changes in surface scale emissivity and steam density from evaporating spray water, so are most accurate when located below the spray chamber. Attaching thermocouples directly to the strand surface is another difficult experimental method that can be used for model calibration[46].

5.6 Tables and Figures

Table 5.1 Standard Input Conditions for Model Calibration

Carbon Content, *C%*	0.044	%
Liquidus/Solidus Temperature, T_{liq}/ T_{sol}	1529/1509	^oC
Steel Density, ρ_{steel}	7400	kg/m^3
Steel Emissivity, ε_{steel}	0.8	-
Fraction Solid for Shell Thickness Location, f_s	0.1	-
Mold Thickness at Top (Outer face, including water channel)	56.8	mm
Mold Outer Face Radius, R_o	11.985	m
Mold Dimensions, $Z_{mold\_total} \times W_{mold}$	900×1876	$mm \times mm$
Scale thickness at mold cold face (inserts region/ below), d_{scale}	0.02/0.01	mm
Initial Cooling Water Temperature, T_{water}	30	^oC
Water Channel Geometry, $d_{ch} \times w_{ch} \times L_{ch}$	$25 \times 5 \times 29$	mm^3
Cooling Water Velocity, V_{water}	7.8	m/s
Mold Conductivity, k_{mold}	315	W/mK
Mold Emissivity, ε_{mold}	0.5	-
Mold Powder Solidification Temperature, T_{fsol}	1045	^oC
Mold Powder Conductivity, k_{solid}/k_{liquid}	1.5/1.5	W/mK
Air Conductivity, k_{air}	0.06	W/mK
Slag Layer/Mold Resistance, $r_{contact}$	5.0E-9	m^2K/W
Mold Powder Viscosity at 1300°C, μ_{1300}	1.1	Poise
Exponent for Temperature dependence of Viscosity, *n*	0.85	-
Slag Density, ρ_{slag}	2500	kg/m^3
Slag Absorption Factor, *a*	250	m^{-1}
Slag Refractive Index, *m*	1.5	-
Slag Emissivity, ε_{slag}	0.9	-
Mold Powder Consumption Rate, Q_{slag}	0.6	kg/m^2
Empirical solid slag layer speed factor, f_v	0.175	-
Casting Speed, V_c	1.07	m/min
Pour Temperature, T_{pour}	1550	^oC
Slab Section Size, $W \times N$	1780×225	$mm \times mm$
Nozzle Submergence Depth, d_{nozzle}	265	mm
Working Mold Length, Z_{mold}	810	mm
Oscillation Mark Geometry, $d_{mark} \times w_{mark}$	0.45×4.5	$mm \times mm$
Mold Oscillation Frequency, *freq*	84	cpm
Oscillation Stroke, *stroke*	10	mm
Time Step, *dt*	0.004	s
Mesh Size, *dx*	0.5	mm

Table 5.2 Input Conditions for Sub-Mold Calibration (China Steel Case)

Carbon Content, *C%*	0.45	%
Mold Thickness at Top (including water channel)	51	mm
Initial Cooling Water Temperature, T_{water}	35	^oC
Water Channel Geometry, $d_{ch} \times w_{ch} \times L_{ch}$	$25 \times 5 \times 28$	mm^3
Cooling Water velocity, V_{water}	7.62	m/s
Casting Speed, V_c	0.55	m/min
Pour Temperature, T_{pour}	1510	^oC
Slab Geometry, $W \times N$	1560×270	$mm \times mm$
Nozzle Submergence Depth, d_{nozzle}	200	mm
Working Mold Length, Z_{mold}	600	mm
Mold Oscillation Frequency, *freq*	120	cpm
Oscillation Stroke, *stroke*	4	mm
Cooling Water Temperature in Spray Zones, T_{spray}	35	^oC
Spray Length of Spray Zone Nozzle, L_{spray}	0.05	m
Spray Zone Roll Contact Angle	7	Degree
Coefficients in Nozaki Eq.(3.58), *A/b/c*	0.3925/0.0075/0.55	-

Table 5.3 Input Spray Zone Variables (China Steel Case)

Zone #	Zone Starts at (mm)	Roll # in Zone	Roll Radius (mm)	Water Flow Rate (l/min/row)	Spray Width (m)	f_{roll}
1	600.0	2	70	27.5	1.3	0.05
2	906.9	5	70	14.86	1.2	0.05
3	1840.8	5	100	14.86	1.2	0.05
4	3034.3	5	125	11.84	1.2	0.2
5	4520.5	10	150	8.8	1.2	0.2
6	7977.9	10	175	7.15	1.2	0.2
7	11883.1	11	210	2.5	1.56	0.2
8	17050.7	18	240	0.0	1.56	0.2
	26440.7	End of last spray zone				

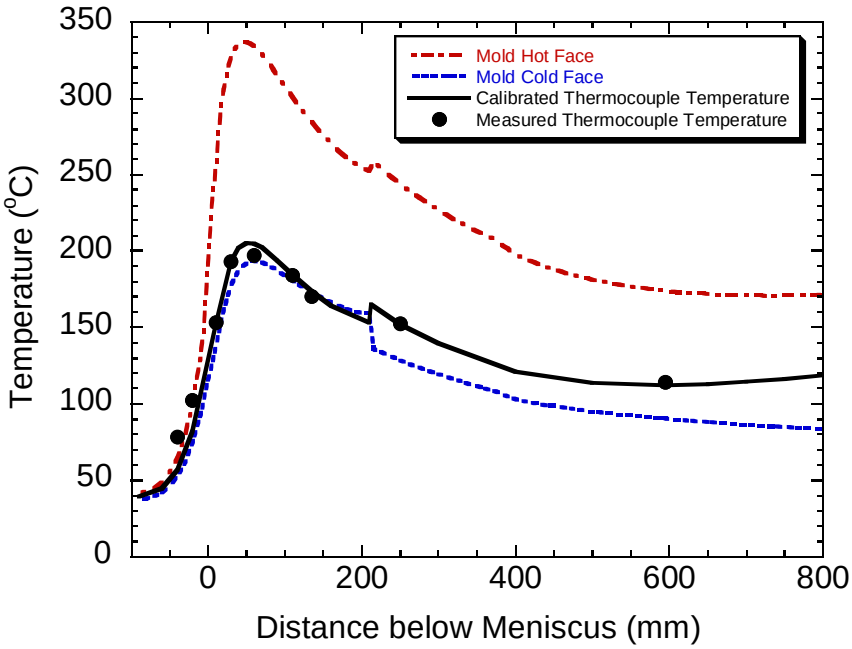

Figure 5.1 Comparison of CON1D calibrated and measured mold temperature

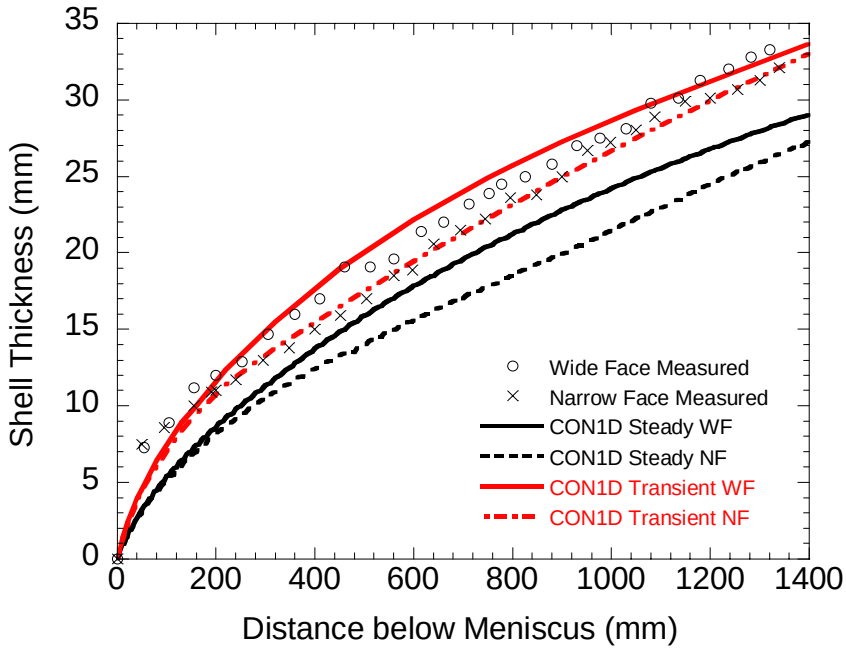

Figure 5.2 Comparison of CON1D predicted and measured shell thickness

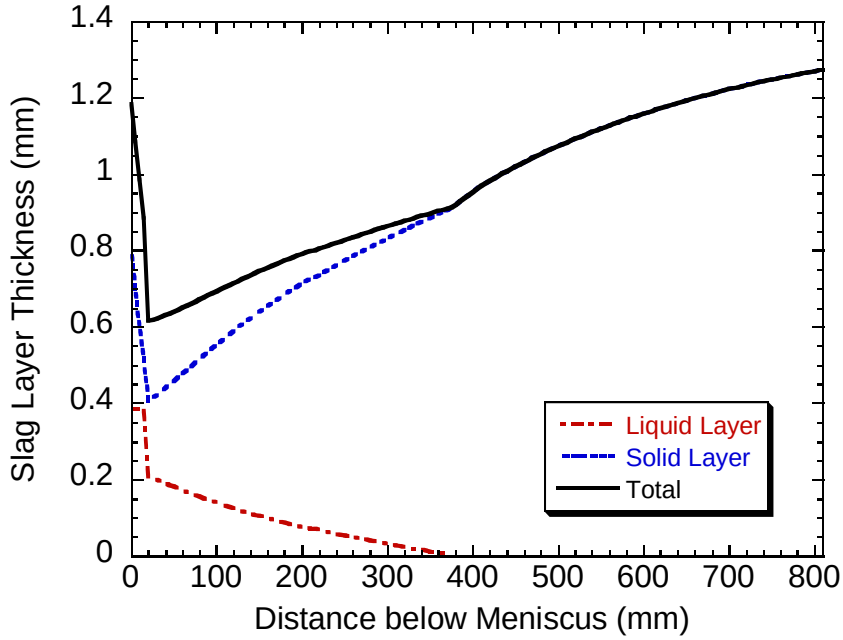

Figure 5.3 Predicted slag layer thickness profiles

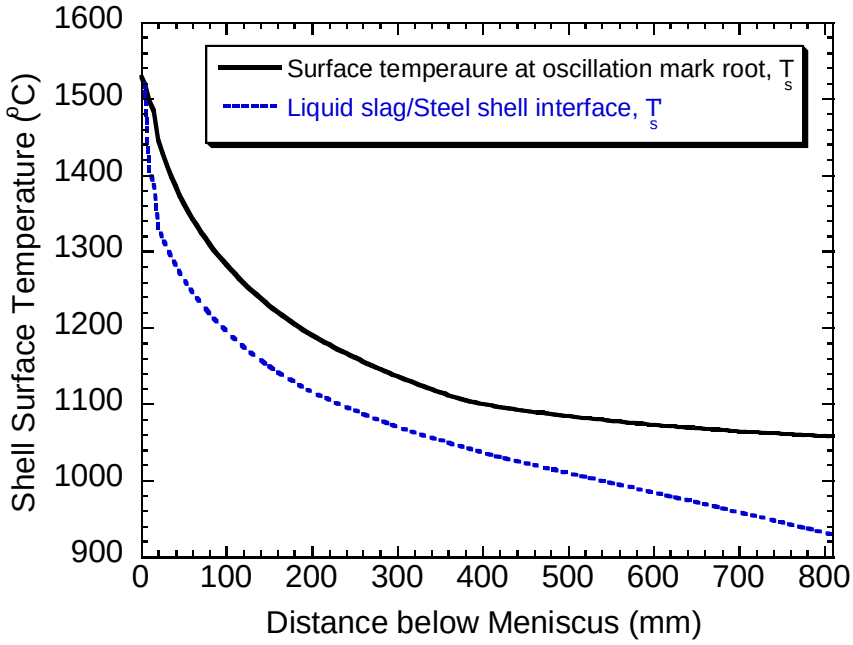

Figure 5.4 Predicted shell surface temperature

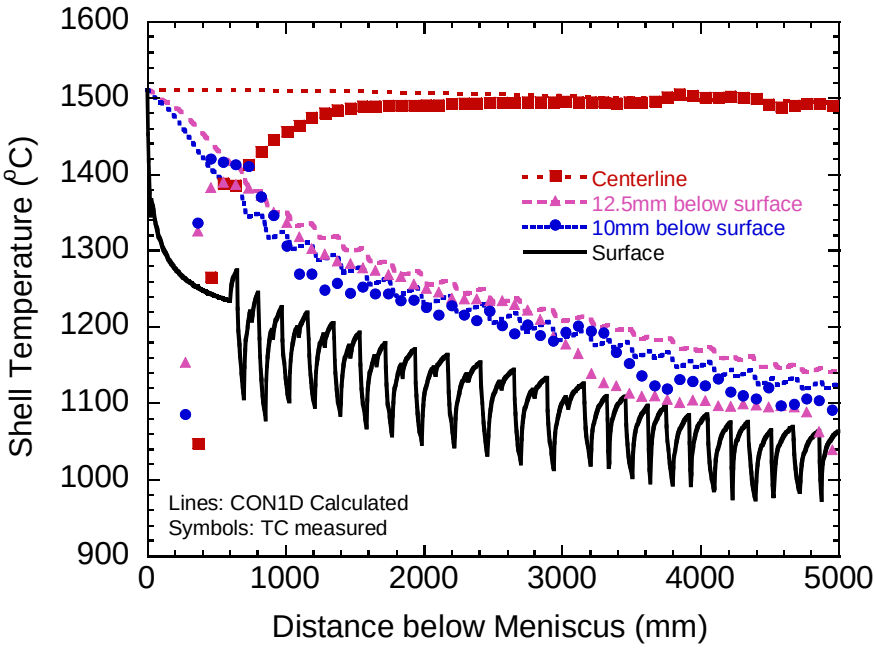

Figure 5.5 Shell temperature (China Steel Case)

CHAPTER 6. MODEL APPLICATIONS

The calibrated model has many applications for both design and operation of continuous casting machines. Firstly, it can help to investigate the effect of various process conditions on the fundamentals of mold heat transfer. Most parameters, such as oscillation practice, powder type, casting speed, and steel grade, affect heat transfer in several different ways, which can only be isolated and quantified independently using a model. The model is currently being extended to predict liquid layer lubrication and solid slag-layer fracture from excessive mold friction and the accompanying heat flux variations,

The CON1D model is first used to simulate behavior for the typical casting conditions listed in Table 3.3. To study the effect of slag type, three slags were chosen. Figure 6.1 shows the viscosity curves vs. temperature assumed for these three slags, which were chosen to match with slag viscosity data measured by Lanyi[100]. The typical continuous casting Slag A might be crystalline or glassy (Slag A2 in Lanyi[100]); Slag C is readily crystalline (Slag A6 in Lanyi[100]). Slag G is Slag C with 25% additional alumina, which has a high tendency to be glassy[100]. The composition and properties of these three slags are listed in Table 6.1.

The "lubrication consumption rate", Q_{lub} is a useful concept for comparing different powder consumption rates. It is introduced here as the rate of slag consumption neglecting the slag carried in the oscillation marks:

$$Q_{lub} = Q_{slag} - Q_{osc} \tag{6.1}$$

Oscillation marks filled with slag and moving at the casting speed consume slag at the following rate, Q_{osc}:

$$Q_{osc} = \rho_{slag} \cdot d_{osc} = \frac{0.5\rho_{slag} \cdot d_{mark} \cdot w_{mark}}{L_{pitch}} \tag{6.2}$$

Thus, the total consumption rate of slag, Q_{slag}, depends greatly on the oscillation mark shape, while lubrication depends mainly on Q_{lub}, and mold heat transfer depends on both.

The liquid slag represented by Q_{lub} acts to lubricate the mold-shell interface and thereby lower friction. The CON1D model is run with different mold slags, consumption rates and casting speeds to study the effect of mold powder properties and oscillation practice. The related parameters are listed in Table 6.1 and Table 6.2.

6.1 Typical Results

Simulations were first run for typical low friction conditions, Case I (Table 3.3), assuming that all solid slag is attached to the mold wall and constant lubrication consumption rate Q_{lub}, of 0.2kg/m^2. At 1.0m/min casting speed, total consumption rate, Q_{slag} is 0.41kg/m^2. Figure 6.2 shows typical results with Slag A. The mean heat flux in the mold is 1.24MW/m^2 and the shell thickness is 20.4mm at mold exit (based on a solid fraction of 0.3). A uniform liquid slag layer of 0.29mm is predicted, Figure 6.2(d), while the solid layer continually increases down the mold. Such a thick solid layer could build up over time starting during initial mold filling with starter slag. Once it reaches steady state, it does not consume any new mold powder. Increasing casting speed is naturally predicted to raise heat flux but lower shell growth.

6.2 Crystallization Behavior

Figure 6.3 shows the cooling history of various points in the slag layer for Case I with Slags A and G. The superimposed TTT curve of a conventional industrial mold slag (7.9%Al_2O_3)[143] is used to estimate the onset of crystallization for Slag A. Figure 6.3(a) predicts crystallization in most of the slag layer (including the oscillation marks) except in the very thin (0.2mm) layer adjacent to the mold wall, which is quenched rapidly and remains glassy. Extra alumina in the slag delays the onset of crystallization and increases the temperature range of crystallization, so the TTT curve of a slag with 19.5% Al_2O_3[144] is used to estimate the onset of crystallization for Slag G. Figure 6.3(b) shows that no points within Slag G cross the TTT curve, so no crystalline phase is predicted. This agrees with the assumption that Slag G tends to be glassy.

Shear stress and axial stress along the solid slag layer was plotted in Figure 3.15. It shows that the solid slag layer is in compression almost everywhere. Therefore the attached solid slag layer is stable and no fracture should occur. This can happen in practice, as evidenced by the recovery of a solid slag layer attached to the mold wall after one hour of casting, which contains trace elements only found in the starter slag (consumed in the first few minutes)[157, 200]. The accompanying stable, thick liquid layer ensures a very low friction force on the mold wall.

Figure 6.4(a) predicts the slag layer thicknesses of the glassy and crystalline slags, assuming the same consumption rate and other conditions (Table 3.3). The glassy layer of slag G is thinner due to its lower solidification temperature. Therefore it produces a slightly higher heat flux and lower shell temperature than the crystalline slag, as shown in Figure 6.4(b)(c). If the lower consumption rate that generally accompanies higher

viscosity slags in a real caster[6, 209] were taken into account, these differences would be even greater. In either case, this prediction matches well-known measured behavior[6, 138, 210].

Note that the crystalline slag is predicted to have lower friction on the mold wall, Figure 6.4(d). This is mainly because of its lower viscosity gradient at high temperature (Figure 6.1), which helps the solid crystalline layer to stay attached to the mold wall and prevent fracture.

6.3 Critical Slag Consumption Rate

Lowering the slag consumption rate, Q_{lub}, leads to higher shear stress at the liquid/solid slag interface. If friction on the mold side cannot balance the shear stress along the solid/liquid interface, axial tensile stress must build up in the solid slag layer to compensate. When axial stress in the solid slag exceeds the slag fracture strength, the solid slag breaks and is dragged down the mold wall. The critical consumption rate is the minimum consumption rate needed to keep solid slag attached to the mold wall without breaking or sliding. In order to find it, the complete CON1D model was run several times with different consumption rates, Case II, assuming slag fracture strength of 80MPa[211]. Figure 6.5 shows the axial stress and shear stress distribution of slags A and G along the mold wall at their corresponding critical consumption rates. It shows that tensile axial stress accumulates in the solid slag only when liquid shear stress exceeds maximum static solid friction. In each case, fracture is predicted during the upstroke when axial stress just exceeds the slag fracture strength. All stresses are compressive during the down stroke.

Slag G has 60% larger critical lubricating consumption rate, Q_{lub}, 0.12kg/m^2 than Slag A, 0.075kg/m^2. Slag C has similar behavior to Slag A, but with an even lower

critical Q_{lub}, 0.05kg/m^2. It confirms the general observations that crystalline slags are more stable than glassy slags. Combined with their thicker layer and lower heat flux, this may explain why such crystalline slags are better for depression and crack sensitive steel grades[210, 212].

Another important difference between Slag A/C and G is the position of slag fracture. As consumption rate lowers, the glassy slag drops below the critical consumption rate first and fractures first near the mold exit. For crystalline slags A and C, the solid slag layer fractures within 100mm near the meniscus. These results show that the sharpness of the slag viscosity increase near the solidification temperature is more important than the popular slag property, slag viscosity at 1300°C.

Figure 6.6 shows the heat flux and mold temperature of these two critical cases. Relative to Case I, very high heat flux is predicted near the meniscus. This is also indicated by the high mold temperature at that region. This also implies that in a real caster, if an abnormal high mold temperature is observed near the meniscus, it may be due to a temporary consumption rate drop regardless of slag type. This should also correlate with solid slag breaking and moving down the mold wall. Slag fracture in turn will cause temporary gaps, heat flux drops, and thermal stresses in the shell. The phenomena of high meniscus heat flux and high variations are known to correlate with strand defects[97, 213], which is consistent with the model prediction here.

6.4 Mold Friction

6.4.1 Attached Solid Slag Layer

When casting with a stable conventional consumption rate (Q_{slag}=0.41kg/m^2), the model predicts a stable solid slag layer and a very low friction force. For the cases

studied here, the mold wall shear stress amplitude is 0.85MPa for slag A, and 2.52MPa for slag G, which are far lower than reported measured friction data[33]. The high friction force measured in operating casters likely comes from three possible causes: a moving solid slag layer (and accompanying thinner liquid layer), excessive taper or misalignment.

6.4.2 Moving Solid Slag Layer

If the liquid slag level at the meniscus varies, it cannot keep a steady flow into the mold/strand gap even if the mold taper and alignment are reasonable and do not contribute to friction. The solid slag layer may break and move along the mold wall, accounting for part of the slag consumption. For a given consumption rate, the liquid slag layer is thinner when the solid layer moves. This leads to higher heat flux and higher friction and therefore perpetuates the slag fracture and motion. The fracture position predicted for slag A (Case II with critical consumption rate) is near the meniscus. Thus, the low viscosity liquid layer may quickly fill in the gap due to facture, and the solid slag layer might reattach to the mold wall until the next fracture. For slag G, if the consumption temporarily drops lower than the critical consumption rate, the solid slag layer fracture will occur further above mold exit.

To model a moving solid slag layer, its average velocity is simply assumed to be some small constant percentage of the casting speed, v_f. In case III, assuming $v_f \approx 5\%$ produces total friction force predictions within the measured range of 15~23kPa[33]. Note the average “moving” solid slag layer velocity is actually the time average of a highly transient process, calculated with an intermittent procedure of solid layer fracture, movement and re-attachment. Most of the time, the solid layer still sticks to the mold

wall, so the shear stress can still be calculated based on liquid layer friction and the maximum static friction between mold and solid layer. Figure 6.7 shows that both liquid and solid moving layers are thinner than for the attached case. In particular, the liquid slag layer gets thinner with distance down the mold and nearly runs out by mold exit. This increases friction greatly. (Appendix I gives a complete list of input and output files of the run with moving solid slag layer with Slag A)

6.4.3 Friction Variation during an Oscillation Cycle

Figure 6.8(a) shows the mold velocity and casting speed profile during half of one oscillation cycle. It shows that at one instant, 0.24second, the mold velocity equals the casting speed, so there is no shear stress. After that time, the mold moves down faster than the shell during the period of “negative strip”. Thus, the stress acting on the slag layer shifts from tension to compression during that instant. Figure 6.8 also shows that the shear stress on the mold wall with a “moving” solid slag layer, (c), is much higher than with an attached layer, (b). Shear stress increases with distance along the mold length, and the transition from tension to compression becomes sharper for a moving layer. In the upper mold, liquid slag controls the friction between mold and shell, so the shear stress is nearly sinusoidal. In the lower mold region, the solid slag layer controls friction and the shear stress profile tends toward a square wave.

Figure 6.9 shows the shear stress down the mold at different times during the oscillation cycle. For all times, there is a transition from curved to straight, where liquid slag layer control transfers to solid slag layer control. The "average" is the mean of the absolute values of all the shear stresses over the whole oscillation cycle, and is very near to the curve when V_m is zero. This means that the average friction force can be estimated

with a simple static mold model. Integrating the shear stress over each mold face at each instant gives the total friction force history during each oscillation cycle, as shown in Figure 6.10 for different cases.

6.4.4 Total Mold Friction Force

Figure 6.10 shows that the friction due to shear stress is very small if the solid slag layer is attached and there are no other sources of friction. Friction with an intermittent attached solid layer is 10X larger and has a sharper transition from tension to compression. Another possible cause of high friction may be squeezing of the steel shell due to excessive narrow face taper. This is most likely when the shell temperature is high and shrinkage is small at high casting speed. A rough estimation of the magnitude of this friction is 15kN on each narrow face, based on Eqs.(3.51),(3.52), assuming buckling happens over the last 10mm (h=10mm) near mold exit, shell thickness b=20mm, L_{eff}=600mm, E=25GPa at 1100°C. This corresponds to an average friction stress over a 800mm long 230mm thick and 1500mm wide slab mold of 10kPa, which is similar to measured data[33]. Figure 6.10 shows that the friction force during an oscillation cycle for excessive taper can be identified by its almost-square shape. In contrast, liquid slag lubrication produces a smooth curve with a very gradual transition. Thus the lubrication/friction state of the mold can be identified from the shape of the friction force curve during an oscillation cycle in addition to its magnitude. Misalignment friction curves are expected to be curved according to gradual changes in its extent during the cycle.

6.5 Other Applications

The model can make predictions of potential quality problems, which have more relevance in practice than simple heat transfer. For example, a warning of possible boiling in the cooling water channels is issued when the mold surface temperature exceeds the pressure-dependent water boiling temperature. The model is also being used to make other warnings such as breakout danger from excessive shell thinning at mold exit, and crack formation etc. Finally, the model should predict optimum casting conditions to avoid problems, whenever possible. Initial features of the model toward this goal include a prediction of ideal mold taper. Together with other resources, CON1D is a powerful tool to investigate the cause and prevention of quality problems and to investigate potential design and operation improvements prior to costly experimental implementation.

6.5.1 Boiling Prediction

The model issues a warning that boiling is possible, if the mold cold face temperature exceeds the boiling temperature for the given operating pressure in the cooling water channels[214]:

$$Boiling\ if: T_{cold}\left(^{o}C\right) > 100\left(P\left(MPa\right)/0.10135\right)^{0.27} \tag{6.3}$$

Boiling in the water channels changes the rate of heat removal and causes temperature fluctuations that together pose a serious potential quality problem. Figure 5.1 shows that boiling is indeed possible for the conditions investigated here. This is due to the 0.02mm thick layer of scale on the mold cold face near the meniscus, which raises the mold face temperature ~70°C. On the other hand, adding a 0.5 mm thick protective Ni

coating to the hot face is predicted to have only a minimal effect on heat flux and cold face temperature. The CON1D model is ideal for quantifying effects such as these.

6.5.2 Breakout Analysis

The model can be used to help understand how a breakout may have arisen. Sticker breakouts are easily identified by their characteristic effect on mold thermocouple histories. Other breakouts, such as those caused by inadequate taper, can be more difficult to identify. For example, the model could be used to determine whether a given narrow-face breakout was more likely caused by excessive superheat resulting from a clogged nozzle, or from insufficient mold taper, causing an excessive gap. Either condition could produce a narrow-face shell that is too hot and thin to have the hot strength needed to avoid rupture. Further calibration may allow the model to accurately warn of a potential breakout when shell growth is predicted to fall below a critical value. Initial work towards this end is reported elsewhere[59].

6.5.3 Crack Formation Analysis

As with previous continuous casting models, CON1D can be used to locate where defects are formed. Hot tear cracks form near the location of the solidus isotherm is tracked by CON1D. For example, by accurately predicting the shell thickness exiting the mold, the model can identify whether a subsurface crack formed in or below the mold. This can be difficult to tell, particularly near the narrow face, where shell growth is slower. Here, a crack forming below the mold might appear to have formed in the mold without an accurate calculation of shell growth that incorporates superheat delivery. The model can also simulate phenomena below the mold, such as reheating of the shell

surface, which can lead to surface cracks. Sub-mold bulging and crack formation requires accurate prediction of the temperature variation between rolls, so the model is useful for designing spray water-cooling systems.

6.6 Tables and Figures

Table 6.1 Slag Composition and Properties

Slag	CaO	SiO_2	Al_2O_3	MgO	Na_2O	K_2O	F_2	FeO	MnO	B_2O_3	T_{fsol}	n	μ_{1300}
	wt%	wt%	wt%	wt%	wt%	wt%	wt%	wt%	wt%	wt%	^oC	-	P
A	32.3	36.4	8.9	0.7	5.0	1.9	8.3	3.0	-	3.4	950	1.6	4.3
G	27.5	30.3	21.4	0.9	5.6	-	12.0	1.1	1.3	-	850	3.2	5.0
C	34.8	38.3	0. 5	1.2	7.1	-	15.2	1.4	1.6	-	980	1.6	1.7

Table 6.2 Case Study Parameters

	Case I	Case II	Case III
Lubrication Consumption, Q_{lub}:	0.2kg/m^2	critical	0.2kg/m^2
Solid Layer Status:	attached	attached	moving

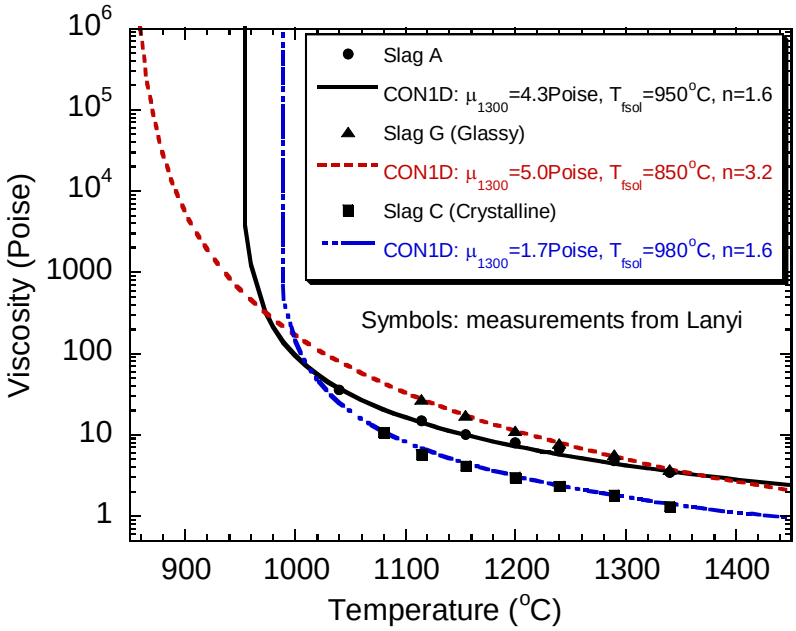

Figure 6.1 Mold slag viscosities used in cases study

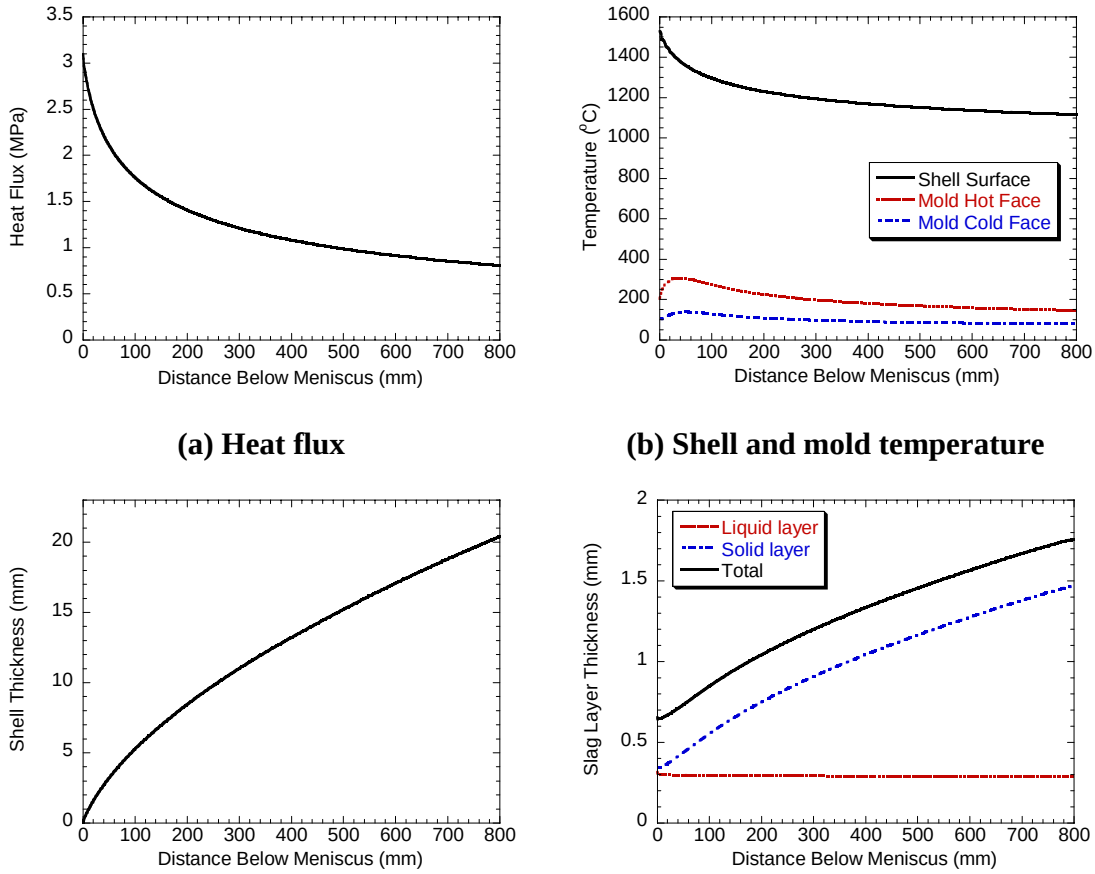

(a) Heat flux **(b) Shell and mold temperature**

(c) Steel shell thickness **(d) Slag layer thickness**

Figure 6.2 Typical results of Case I with slag A

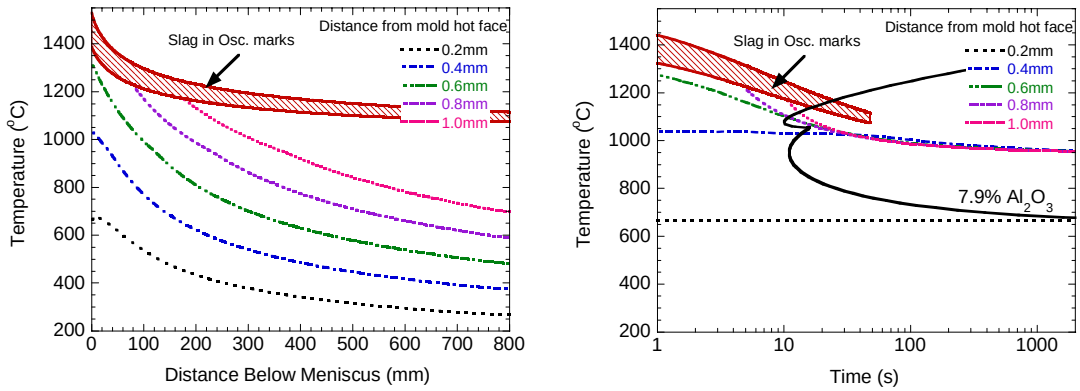

(a) Slag A (crystalline)

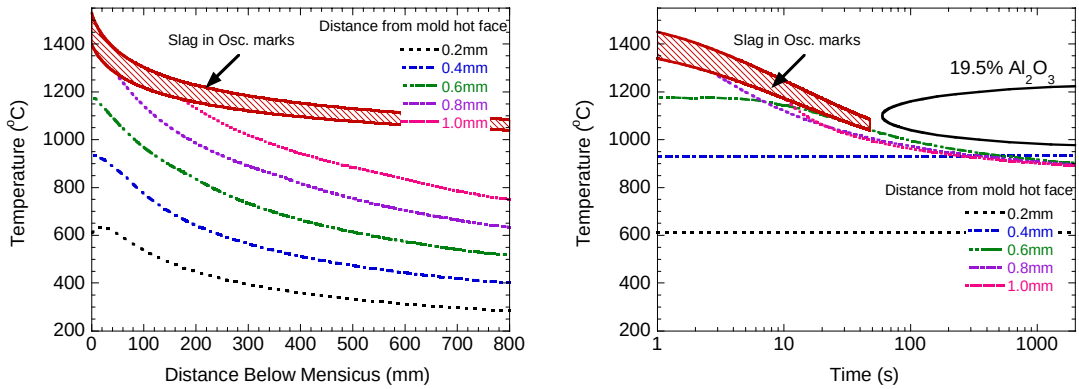

(b) Slag G (glassy)

Figure 6.3 Slag layer cooling history with TTT curves

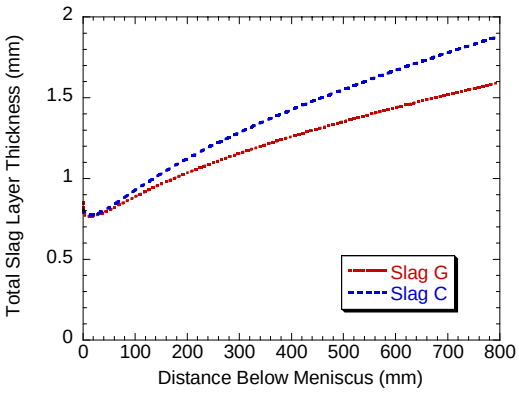

(a) Slag layer thickness

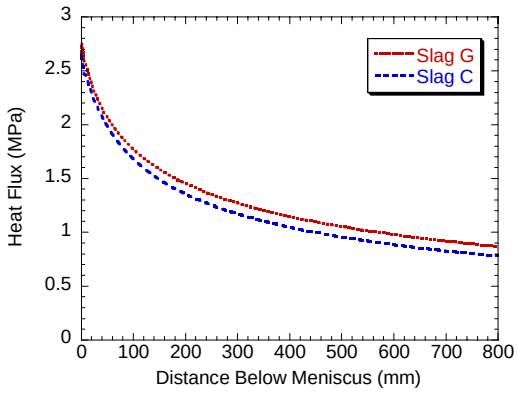

(b) Heat flux

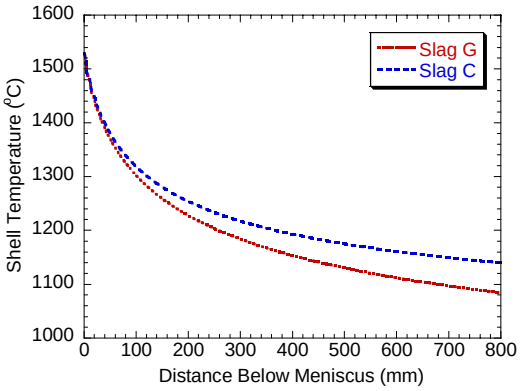

(c) Shell temperature

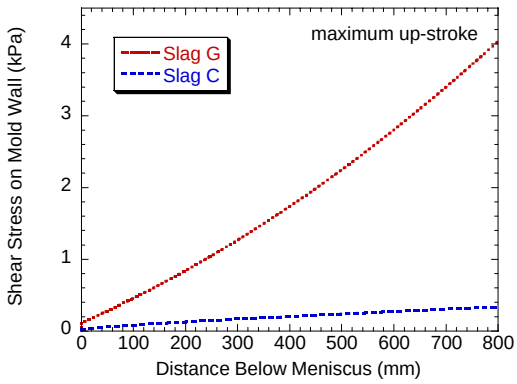

(d) Mold friction

Figure 6.4 Effects of slag type

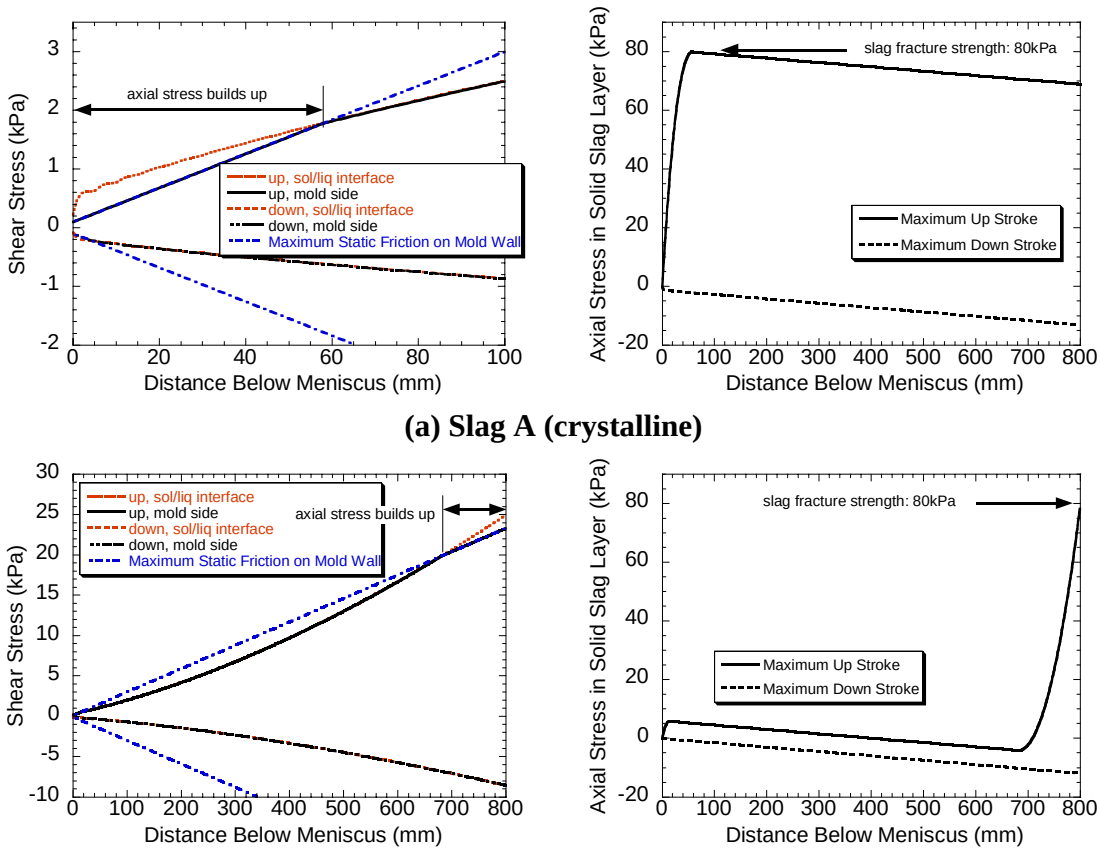

(a) Slag A (crystalline)

(b) Slag G (glassy)

Figure 6.5 Effect of Slag type on axial stress build up in solid layerfor critical Q_{lub}(Case II)

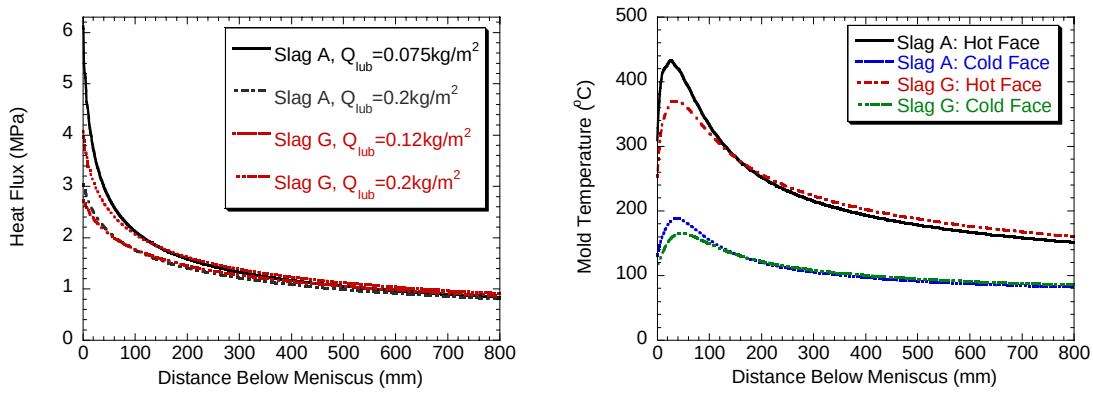

(a) Heat flux **(b) Mold temperature**

Figure 6.6 Comparison of heat flux and mold temperature with critical consumption rate (Case II)

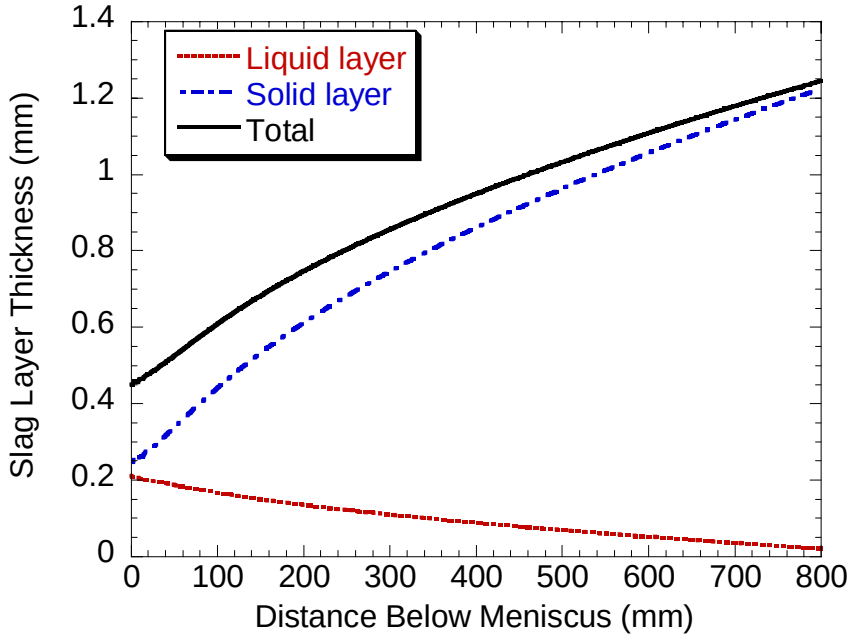

Figure 6.7 Slag layer thickness with "moving" solid layer (Case III with Slag A)

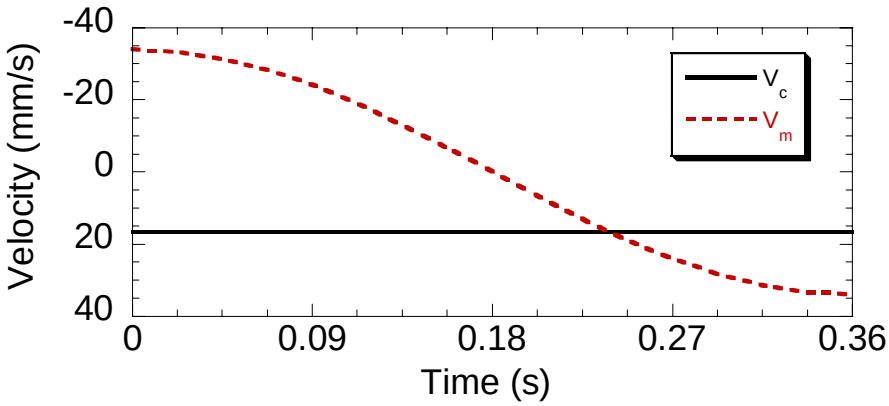

(a) Casting speed and mold velocity

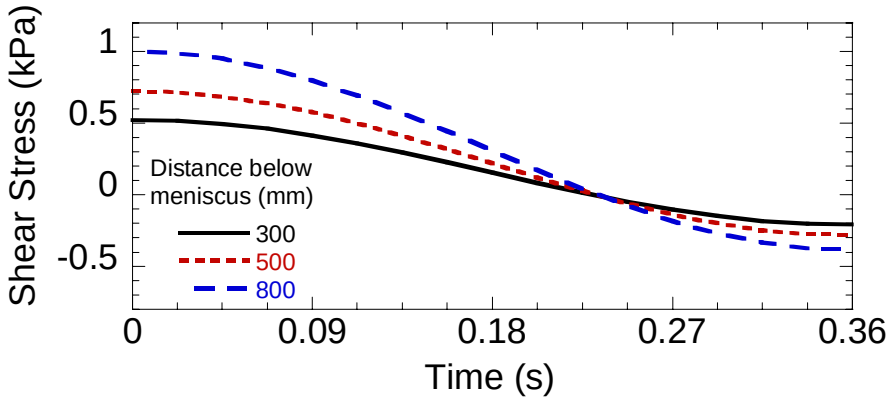

(b) Attached solid layer (Case I)

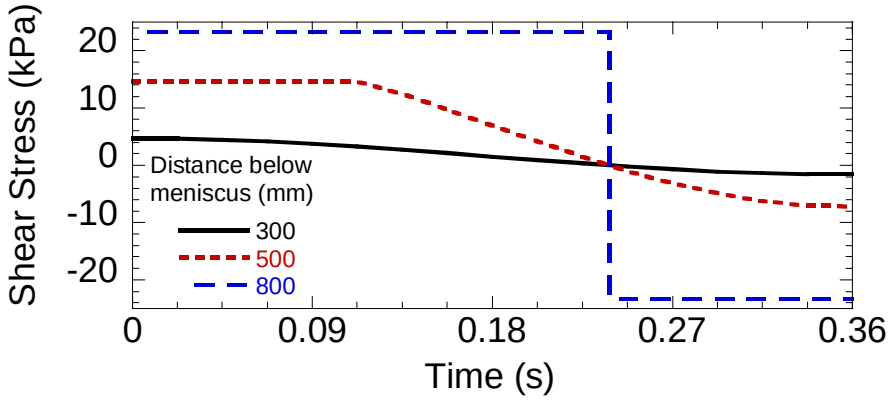

(c) "Moving" solid layer (Case III)

Figure 6.8 Velocity and shear stress during half oscillation cycle (Slag A)

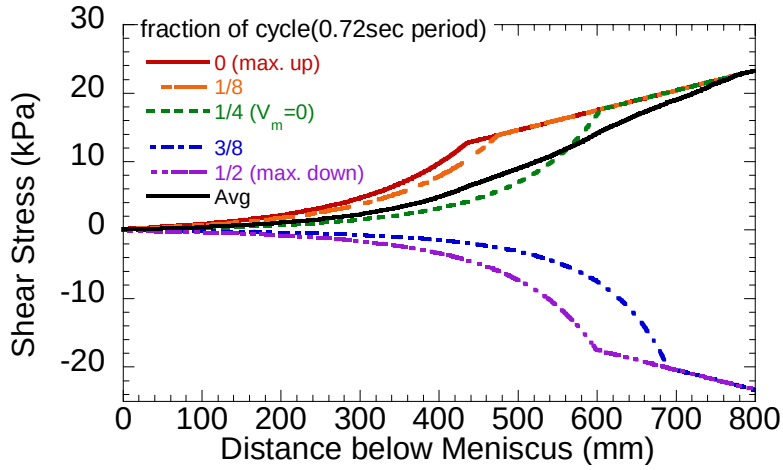

Figure 6.9 Shear stress down the mold wall with "moving" solid layer (Slag A)

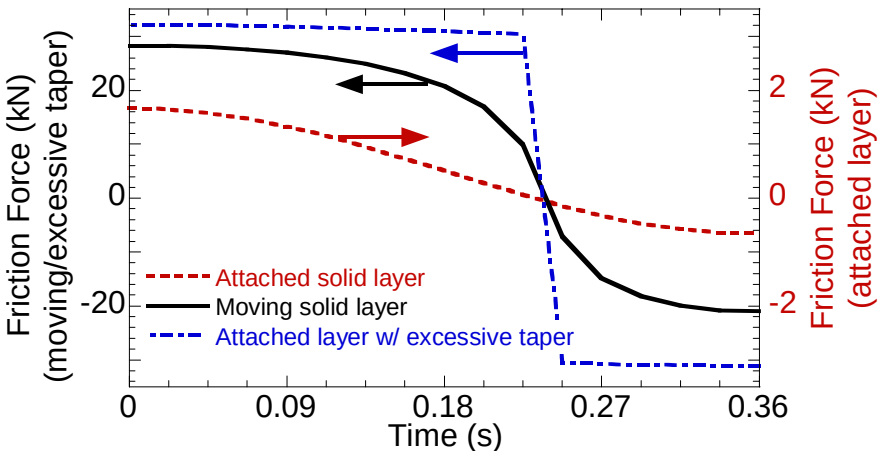

(a) Casting speed and mold velocity

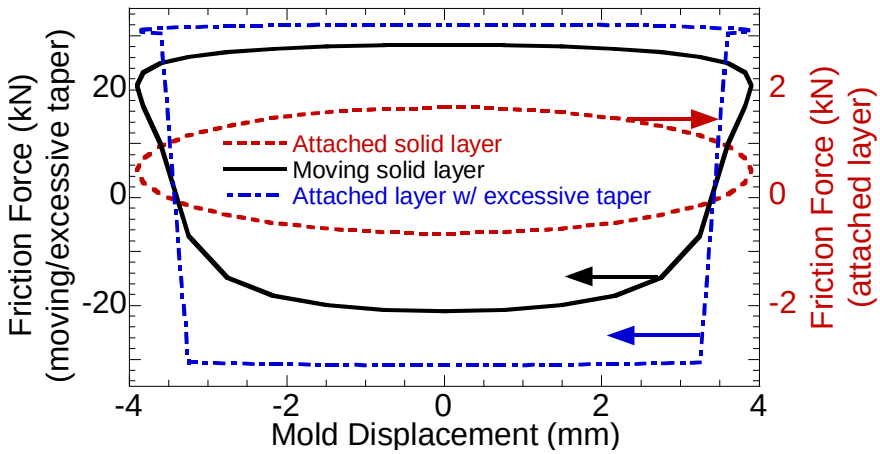

(b) Attached solid layer (Case I)

Figure 6.10 Friction force over oscillation cycle (Slag A)

CHAPTER 7. SLAG CONSUMPTION AND CASTING SPEED STUDY

7.1 Effect of Casting Speed on Heat Transfer and Shell Growth

As an example to illustrate the use of the model to understand fundamental phenomena in the mold, simulations were performed to investigate just two of the many interdependent parameters: casting speed and mold powder consumption. It is well known that increasing casting speed causes changes to other parameters, such as decreased mold powder consumption rate and shallower oscillation marks. To investigate the effect of increasing casting speed in a typical real caster, oscillation frequency was increased proportionally with speed, according to plant practice, and oscillation mark depth was decreased, such that the negative strip ratio and the lubrication consumption rate , Q_{lub} remained constant.

To investigate the effect of mold powder consumption rate, an intermediate case of standard (low) casting speed with decreased consumption rate is also included. The three cases in this study are listed in Table 7.1, with other conditions given in Table 5.1. The lubrication consumption rate for all 3 cases is 0.4kg/m^2.

Figure 7.1 presents the heat flux profiles down the mold wide face calculated for all three cases. Decreasing the powder consumption rate at constant casting speed (Case 2) is seen to increase heat flux in the top portion of the mold, relative to standard conditions (Case 1). This is because the average thickness of the slag layers decreases, thus lowering the interfacial resistance. This effect diminishes with distance down the mold, (as the importance of interfacial resistance to heat transfer decreases relative to that from increasing steel shell thickness).

The practical case of increasing casting speed and simultaneously decreasing total powder consumption rate and oscillation mark depth (Case 3) also increases heat flux toward the bottom of the mold. This is due to the lower thermal resistance of a thinner steel shell produced with less solidification time, which becomes increasingly important with distance down the mold. The net result of increasing casting speed (comparing Case 3 with Case 1) is to increase heat flux almost uniformly down the mold. This is reflected in uniformly higher mold temperatures, as seen in the model predictions in Figure 7.2. This prediction also matches mold thermocouple measurements obtained for Case 3 conditions, as included in Figure 7.2. The higher speed leads to a thinner steel shell and higher steel surface temperature so the liquid slag layer persists further down the mold, as shown in Figure 7.3, Figure 7.4 and Figure 7.5 respectively. But the higher heat flux for higher casting speed also lowers the shell surface temperature, which partially cancels the effect of higher temperature due to thinner shell. For these cases, the surface temperatures at the oscillation marks root near mold exit are almost the same, as shown in Figure 7.4 and Figure 7.6. Figure 7.6 compares the shell temperature profiles at mold exit.

The model is suited to many further fundamental parametric studies of this kind. For example, steel grade affects the average oscillation mark size, powder consumption rate, air gap size due to thermal contraction (narrow face), and steel strength. Mold powder properties and oscillation practice have similar interdependent effects. The effect of oscillation mark depth, for example, is quantified in a model application reported elsewhere[201].

For the sample cases, the higher speed causes a hotter shell with less shrinkage, shown in Figure 7.7, so needs slightly less narrow face mold taper. The shrinkage ε_{th1},

based on surface temperature only, is generally less than ε_{th2}, and is almost independent of casting speed, due to the cancellation effect discussed previously. With a linear taper, the narrow-face shell attempts to shrink away from the upper portion of the mold, while it pushes against the lower portion of the mold. To match the shrinkage, it is clear that taper should be increased high in the mold and decreased lower down. Mold distortion, viscoplastic creep of the steel, and other factors should also be taken into account when designing a non-linear mold taper. These calculations require sophisticated thermal-stress models, to calculate temperatures, stresses, and shrinkage, including the formation of an air gap near the corners, and its effect on heat flow across the mold/shell interface. The calibrated CON1D model is currently being used to provide calibrated heat transfer data to these models to evaluate and improve taper optimization.

7.2 Effect of Slag Properties on Critical Consumption Rate

The most important parameter affecting slag shear stress and fracture was found to be the liquid slag consumption rate. So long as consumption rate exceeds a minimum critical rate, the slag will not fracture. A parametric study was conducted on the minimum critical consumption to keep a stable attached solid slag layer using conditions in Table 3.3. Doubling the fracture strength of the crystalline mold slag allows the critical Q_{lub} for slag A to decrease by only 7% and delays the fracture position from 60mm to 100mm below the meniscus. The fracture strength has even less effect for slag G. The effects of slag Poisson's ratio, liquid slag pool depth, and mold thickness on critical consumption rate were negligible.

Maintaining a high mold/slag friction coefficient is important to lowering the critical consumption. As shown in Figure 7.8, especially for slag G, when the friction

coefficient is lower than 0.15, the slag layer can fracture, even for a stable conventional consumption rate.

Oscillation marks act as an extra resistance layer between the liquid slag layer and the steel shell. Thus they slightly lower temperature in the liquid layer, which leads to higher viscosity liquid, higher shear stress, easier flux fracture and higher critical consumption. Specifically, 0.45mm*4.5mm oscillation marks cast at 1.0m/min increase Q_{lub} by 0.01kg/m^2 for both slags (15% for slag A and 9% for slag G) relative to cases with no oscillation marks

7.3 Effect of Casting Speed on Critical Consumption Rate

The influence of casting speed on mold friction and interface heat flux has been investigated in a parametric study. Based on Case I, the casting speed was varied from 1.0m/min to 5.0m/min. The stroke was fixed at 7.8mm, and oscillation frequency adjusted to keep a constant negative strip ratio of 0.3 and a constant pitch length of 12mm. Negative strip time thereby decreases with increasing casting speed, so oscillation mark depth decreases[215]. The powder consumption rate thus decreases due to the shallower oscillation marks and higher oscillation frequency[216]. Oscillation mark depth becomes negligible when casting speed is greater than 2m/min. Table 7.2 gives the mold oscillation parameters used. Those parameters are chosen based on some previous plant measurements of oscillation marks depth[215] and total mold powder consumption rate[15, 31, 97, 217] as shown in Figure 7.9 and Figure 7.10.

Figure 7.10 also compares measured consumption rates[15, 31, 97, 217] with critical consumption rates calculated in this study. Measured consumption rates exceed the critical rates, which indicates that slag fracture should be a rare transient event. If the

total consumption rate can be steadily maintained, the strand should be well lubricated and a stable solid slag layer should remain attached to the mold. Figure 7.10 shows that measured consumption rates decrease with increasing casting speed. When there is significant consumption by the oscillation marks, Q_{osc}, the critical consumption also decreases with increasing casting speed. This is because oscillation mark depth decreases, carries less slag and increases the lubrication consumption component, thus helping to keep the solid layer attached to the mold wall as explained above. However, at higher casting speed (>2m/min), when the oscillation mark effect is negligible, the critical consumption rate increases slightly with casting speed.

Figure 7.11 shows two opposing effects of casting speed on solid slag fracture, excluding oscillation marks and their effects. Increasing casting speed increases the velocity difference between mold and shell, which tends to increase friction. It also increases shell surface temperature, which tends to decrease slag viscosity and friction. For slag A, the first effect prevails, so the slag always fails near the meniscus and higher casting speed is more dangerous to slag fracture. To be specific, increasing V_c from 1.0m/min to 2.0 m/min, requires the critical Q_{lub} to increase by 25%. Also, the fracture position occurs closer to the meniscus (moving from 60mm to 30mm). When the critical fracture position is near to the mold exit, such as slag G at less than 3.0m/min, the effect of higher surface temperature predominates, so higher casting speed helps to avoid slag fracture, as shown in Figure 7.11(b). Thus, increasing casting speed from 1.0m/min to 2.0m/min decreases critical Q_{lub} by 8%. However, further increasing casting speed above 3.0m/min causes the critical fracture position to move to near the meniscus, and increases the critical Q_{lub} as for slag A.

Note that the minimum critical consumption rate occurs at intermediate speed (~2m/min) for the conditions of the study with Slag G, which is the safest speed for slag layer stability. Measured consumption rates exceed the calculated critical consumption rates by the largest factor (~3X) for this intermediate speed. Safety margins are less at both lower speed and higher speed. At very high speed, ~5m/min, measured consumptions approach critical levels. This indicates that solid slag layer stability becomes a general problem at high speed (unless consumption or another condition assumed here is changed).

Figure 7.12 compares the average heat flux with measured and fitted data[43, 59, 72, 218]. Average mold heat flux increases with higher casting speed (shorter dwell time), with lower consumption rate or with a moving solid slag layer. Note that the average heat flux of the cases with moving slag or with critical consumption rate (just about to move) almost hit the upper bound of measurements. High and variable heat flux is another indication of slag layer fracture.

7.4 Effect of Casting Speed on Friction Stress

Finally, CON1D was run with a detached solid slag layer assumed to be moving at an average velocity of 5% of the casting speed (Case III). The lubrication consumption rate Q_{lub} was assumed to remain the same, 0.2kg/m^2, for all cases. The solid friction force with moving slag is much higher than for the attached cases, and increases with decreasing casting speed. These predictions compare with measured data[33], as shown in Figure 7.13. The agreement at lower casting speed is consistent with the prediction that solid slag fracture and movement increases at lower speed. The high friction measured at high speed might be due to other friction sources such as excessive mold taper. Also note

that for the same average solid layer moving speed, glassy slag has higher friction than crystalline slag. It is interesting speculate that the drop in friction at intermediate speed might correspond to the minimum in critical consumption rate and maximum safety factor predicted in this work. It implies that solid slag layer fracture may be more likely at both low and high casting speed, perhaps increasing the higher average solid layer moving speed, which would increase friction. This is consistent with measurements in Figure 7.13.

7.5 Tables and Figures

Table 7.1 Parametric Study Conditions for Effect of Casting Speed

	Casting Speed V_c (m/min)	Oscillation frequency *freq* (cpm)	Total Consumption Rate Q_{slag} (kg/m^2)	Osc. Mark Size $d_{mark} \times w_{mark}$ (mm^2)
Case 1	1.07	84	.60	.45×4.5
Case 2	1.07	84	.56	.45×4.5
Case 3	1.25	98	.56	.40×4.0

Table 7.2 Mold Oscillation Practice with Casting Speed

Casting Speed, V_c	Oscillation frequency, *f*	Negative Strip Time, *NST*	Negative Strip ratio, *NS%*	Osc. Mark, $d_{mark} \times w_{mark}$	Osc. Marks Consumption, Q_{osc}
m/min	cpm	s	-	mm×mm	kg/m2
1.0	83.3	0.24	0.3	.45*4.5	0.21
1.3	108.3	0.19	0.3	.30*3.0	0.094
1.6	133.3	0.15	0.3	.16*1.6	0.027
2.0	166.7	0.12	0.3	0*0	0
3.0	250.0	0.08	0.3	0*0	0
5.0	416.7	0.05	0.3	0*0	0

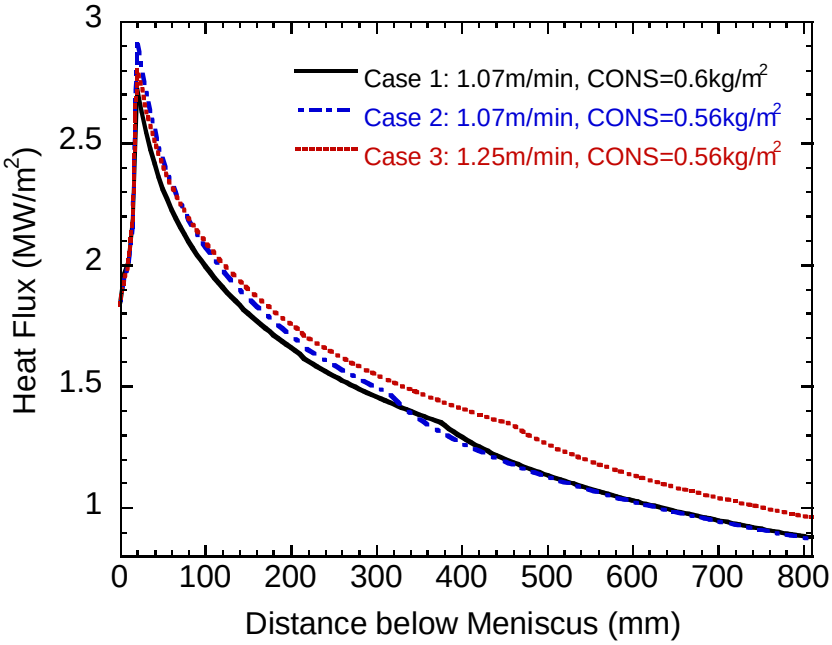

Figure 7.1 Effect of casting speed and powder consumption on the heat flux profile

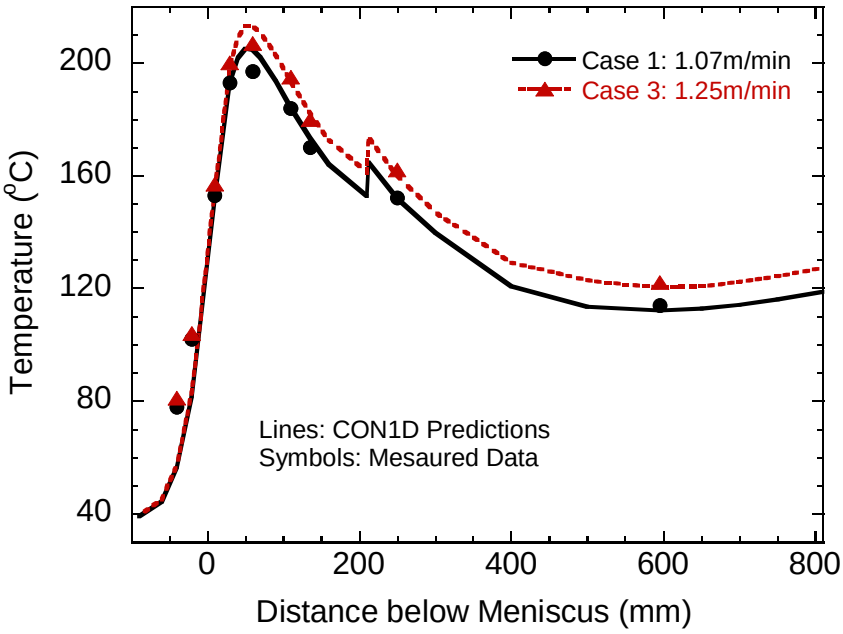

Figure 7.2 Effect of casting speed on mold temperature

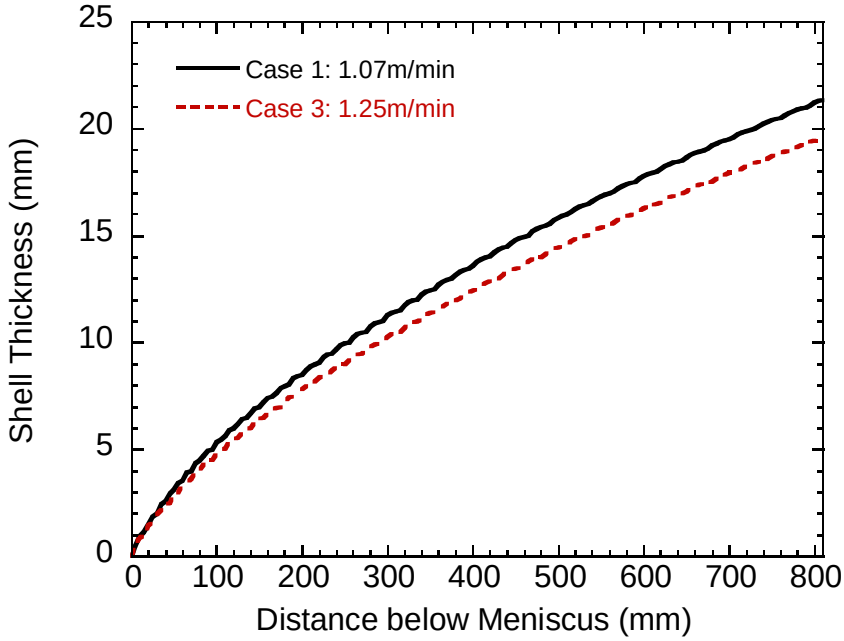

Figure 7.3 Effect of casting speed on steel shell thickness

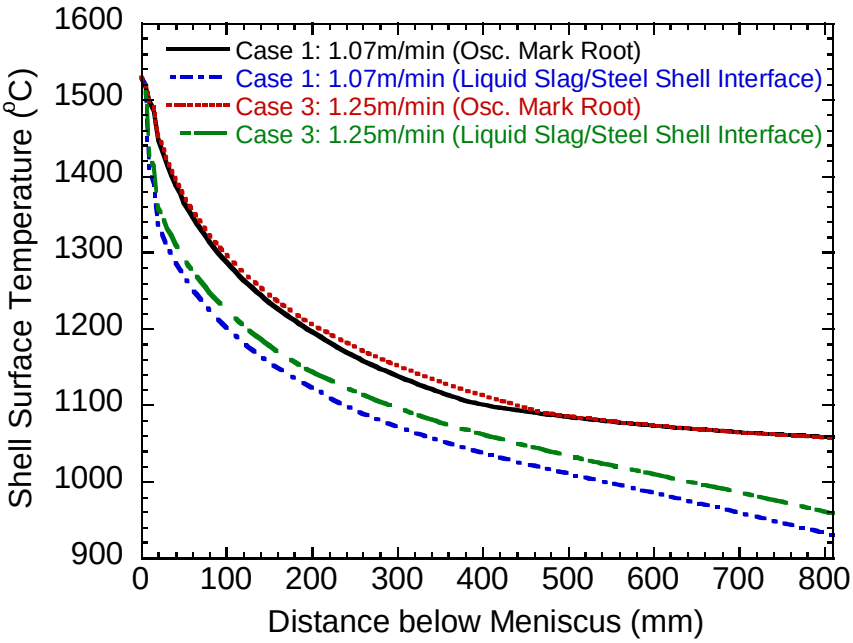

Figure 7.4 Effect of casting speed on steel shell surface temperature

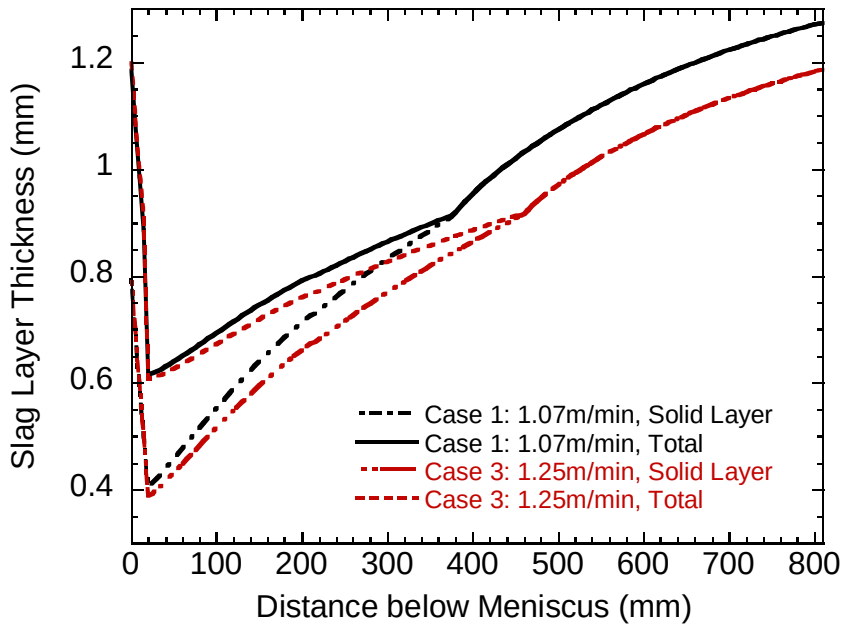

Figure 7.5 Effect of casting speed on slag layer thickness

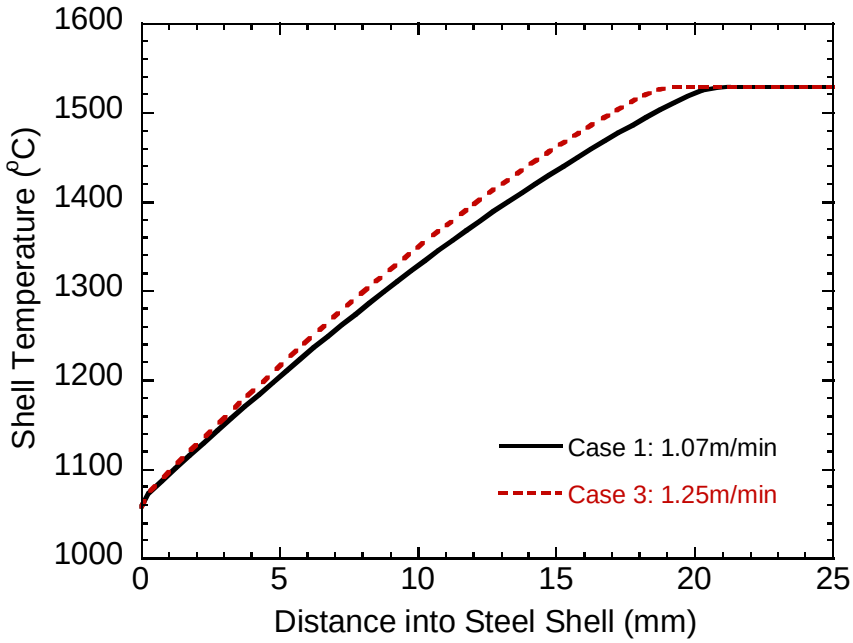

Figure 7.6 Effect of casting speed on steel shell temperature profile at mod exit

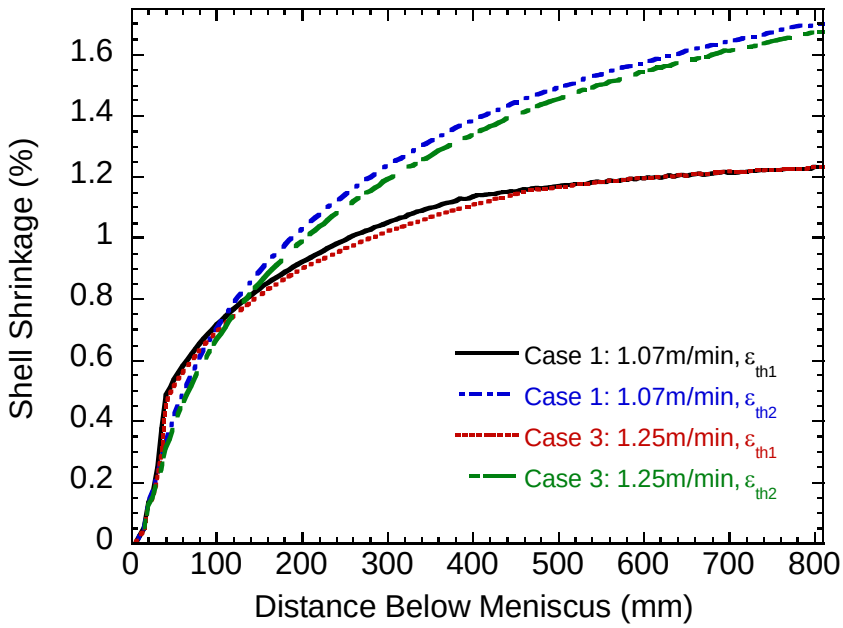

Figure 7.7 Effect of casting speed on steel shell shrinkage

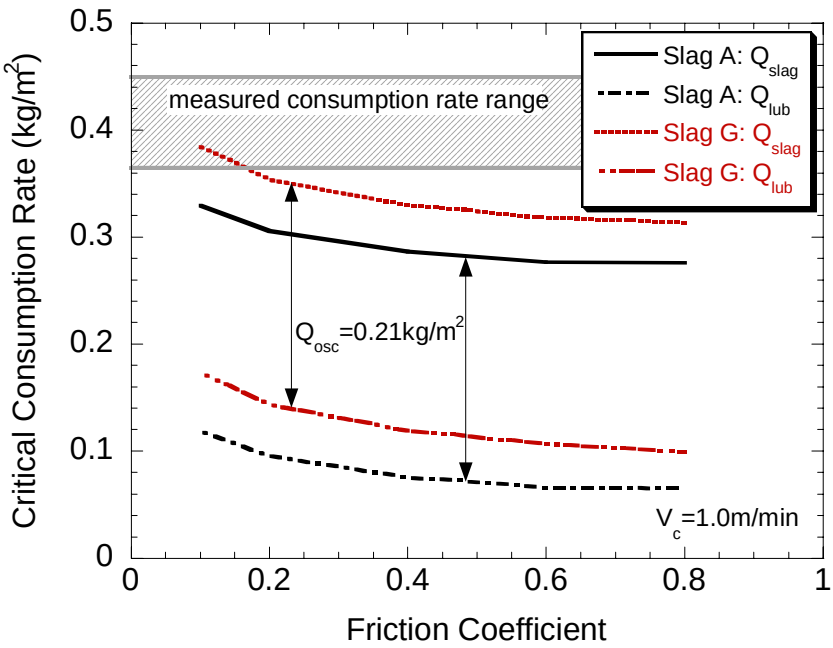

Figure 7.8 Effect of friction coefficient on critical consumption rate

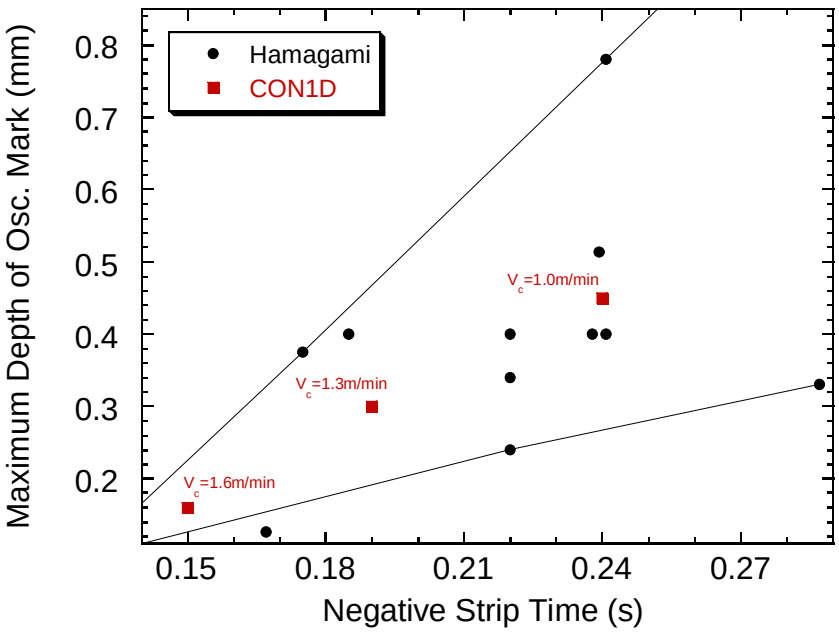

Figure 7.9 Maximum oscillation mark depth

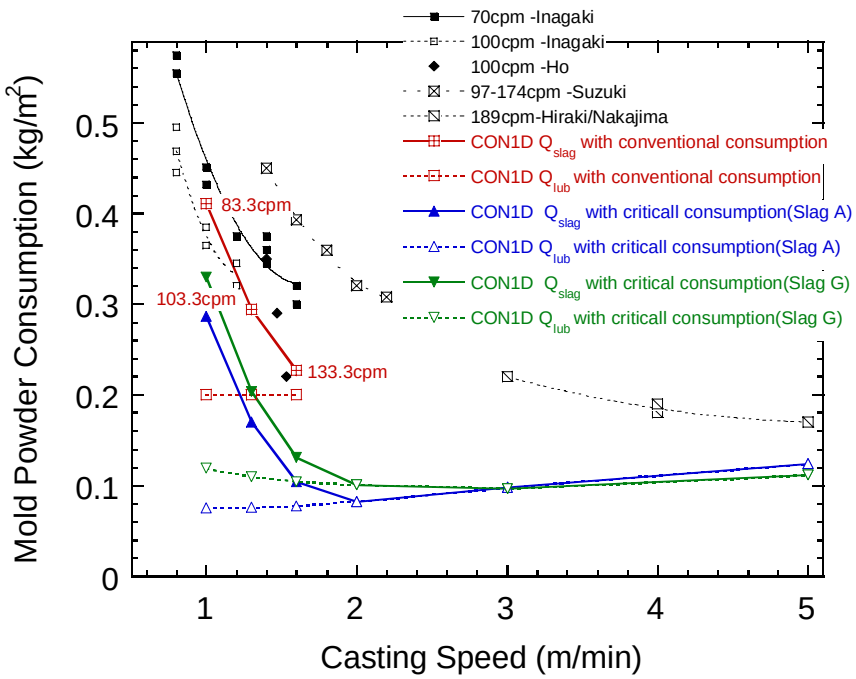

Figure 7.10 Powder consumption rates

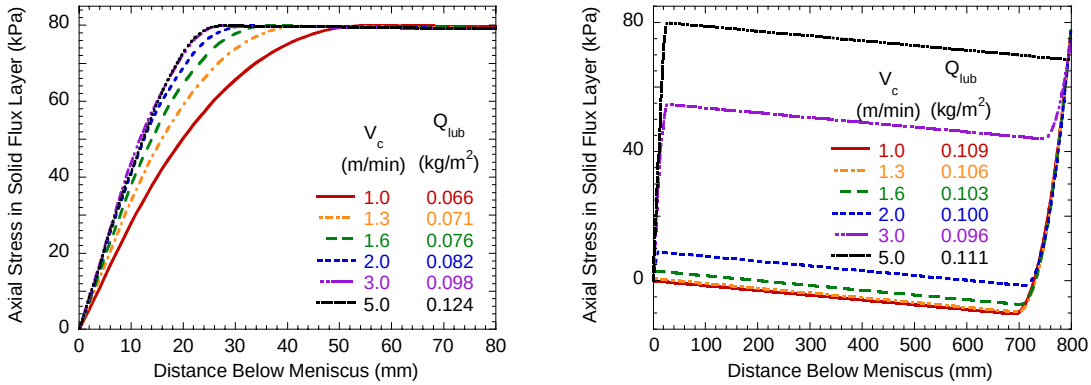

(a) Slag A **(b) Slag G**

Figure 7.11 Effect of casting speed on solid slag fracture (no oscillation marks)

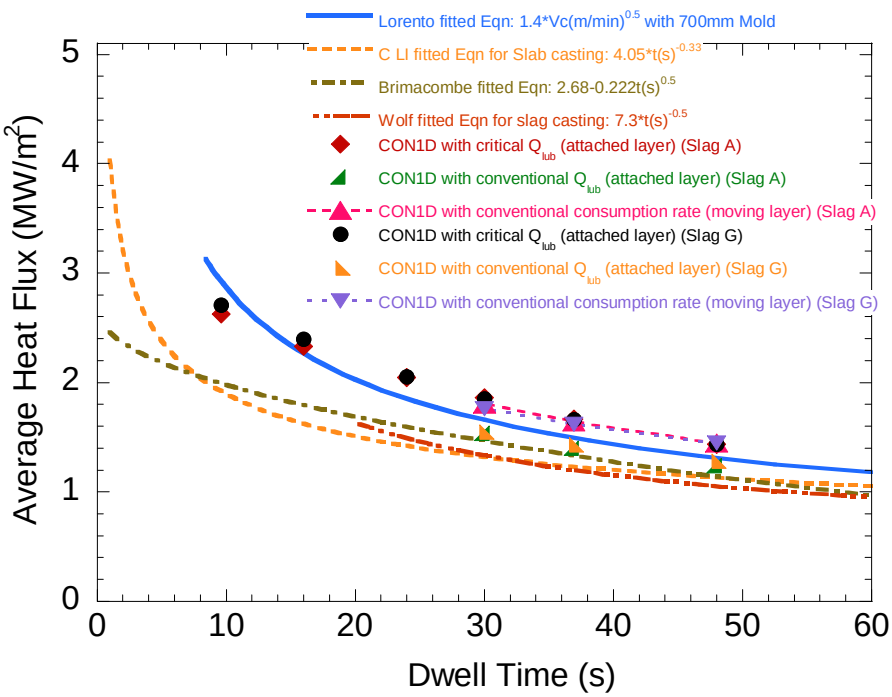

Figure 7.12 Average heat flux vs. dwell time

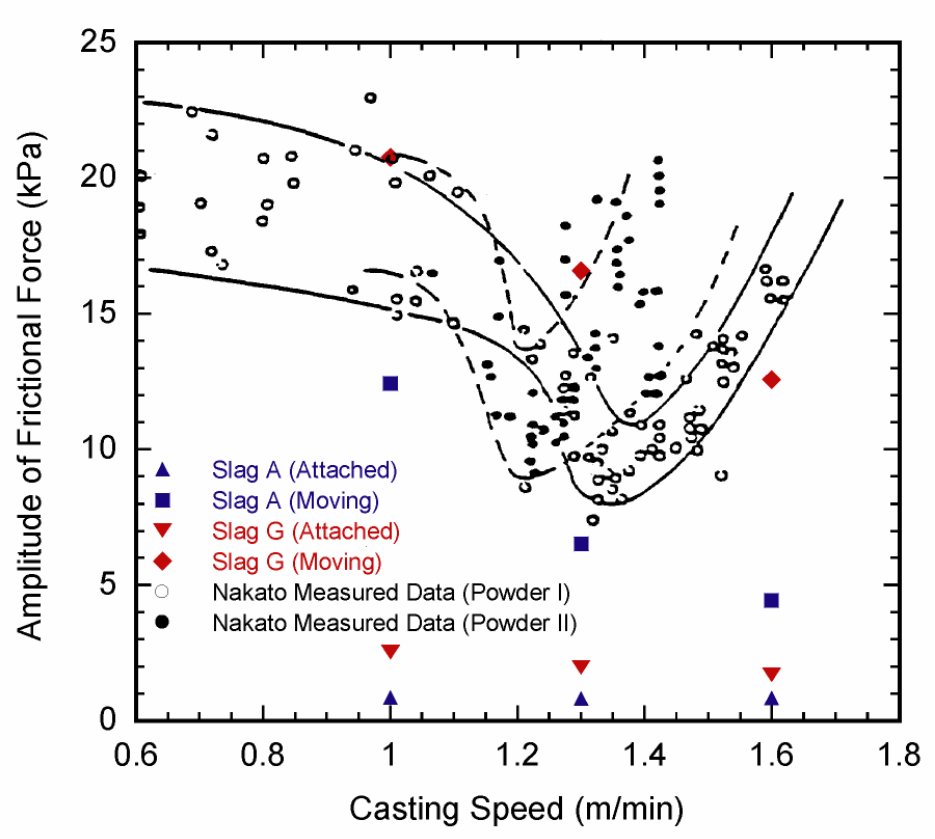

Figure 7.13 Effect of casting speed on friction force measurement and prediction

CHAPTER 8. CASE STUDY: INTERFACIAL GAP ANALYSIS FOR AK STEEL CASTER

In Chapter 4, improved understanding of the mold powder properties were obtained, including the entire viscosity-temperature curve and slag crystallization behavior of slag K1 used at AK steel. Using these new measurements, a case study analysis of the AK steel caster is conducted in this chapter to interpret caster signals such as thermocouple measurement and other interfacial slag gap phenomena. Specifically, the CON1D program described in Chapter 3 is used to predict temperature in the mold and shell, shell growth, interfacial slag layer thickness and microstructure, and friction phenomena. The predictions are compared wherever possible with measurements, available in previous work[138], and through further metallurgical investigation here.

8.1 Input Conditions

Casting powder K1 in Chapter 4 is used in this case. The measured viscosity data and CON1D fitted lines using Eq.(3.19) are plotted in Figure 8.1 using parameters given in Table 8.1. This figure also gives the calculated viscosity curves using Eqs. (2.10)~(2.12) based on slag composition listed in Table 4.1. Although these equations predict the viscosity at high temperature reasonably, they greatly underpredict the sharp viscosity increase measured at lower temperature. Furthermore, Eq.(2.13) predicts a break temperature of 983°C, which is much higher than the measured softening temperature.

The CON1D viscosity model, on the other hand, reasonably matches the measured data. In addition, it enables modeling of the likely viscosity change at low temperature due to slag crystallization by adjusting the solidification temperature, T_{fsol},

and index, *n*, as shown in Figure 8.1. To include this effect, a gradual shift in the viscosity curve is proposed between 250mm to 500mm below the meniscus, as shown in Figure 8.2(a). This distance corresponds roughly with the time needed for transformation of each part of the layer, which is discussed later.

The solid layer is attached to the mold wall near the meniscus. Down the mold, the increased friction likely causes it either to begin to move down along the mold wall or to shear longitudinally between the layers. Figure 8.2(a) also shows how the solid layer velocity is assumed to increase, which will be explained in detail later.

Due to the wide temperature range (650°C-1300°C) for the liquid slag used in this model, the conductivity uses an average value, 1.0W/mK, at the meniscus based on measurements[219]. And it gradually drops to 0.5W/mK. This might be due to the onset of the crystallization in the liquid slag layer, accompanied by gas bubble formation that decreases the conductivity. The conductivity curve assumed for the simulation is given in Figure 8.2(b), which shows the expected drop with distance below the meniscus. The conductivity of the solid slag layer is set to be a constant of 0.5W/mK[138].

Measurements show that with decreasing temperature of the slag cold surface, the contact resistance between the mold and solid layers increase due to an increase of the solid slag layer surface roughness[119]. A 5μm to 15μm air gap is assumed to account for this roughness change, which corresponds to a contact resistance of 0.83×10^{-4} -2.5×10^{-4}m^{2}K/W and agrees with Yamauchi's measurements[140]. Other input conditions are listed in Table 8.1. All input parameters governing the interfacial gap properties are chosen to be consistent with the conditions actually experienced in the gap according to measurements in this or previous work.

8.2 Heat Transfer Results

Figure 8.3(a)~(d) show heat transfer predictions for this AK steel case as a function of distance down the mold. With the measured total consumption rate of 0.3kg/m^2(Q_{lub}=0.09kg/m^2), the mean flux in the mold is 1.21MW/m^2, which gives a 5.6^{o}C cooling water temperature increase. This matches with the measured 6.1^{o}C within a reasonable measurement error range. Figure 8.3(a) shows the heat flux profile with distance down the mold. The radiation is about 22% of total heat flux. This should drop after partial crystallization, owing to increase in absorption coefficient, *a*, which is not included in current model yet.

Because the mold geometry near the embedded thermocouples is complicated[105], 3-D heat computations were performed by Langeneckert et al on regions of this copper mold near the thermocouples[175], including heat losses along the thermocouple wire itself. From these results, an offset of 4.5mm toward the mold hot face was found to adjust the CON1D prediction to match the 3-D model predictions for this mold[34, 175]. Figure 8.3(b) compares the measured thermocouple temperature and predictions (using this offset) for the central region of the mold wide face. The agreement indicates the consistency between the mold thermocouple measurements and the cooling water temperature measurement.

In addition to the mold hot face and cold face temperature, Figure 8.3(c) gives the temperature profile on the solid slag layer cold surface. The temperature difference between the mold hot face and the slag layer surface corresponds to the contact resistance between the mold and the slag layer. The contact resistance is low at the meniscus because the high temperature softens the solid slag layer and allows its surface to

smoothen. Down the mold, the slag surface temperature decreases, so the slag layer roughness increases. This increases the contact resistance between the sold layer and the mold.

The predicted shell thickness profiles are presented in Figure 8.3(d) with measurements down a breakout shell that occurred under similar casting conditions. The transient profile was simulated using the procedure explained in Section 5.3 with data given in Appendix H[32, 105]. Reasonable agreement is obtained, assuming a solid fraction of 0.1.

Figure 8.4(a) gives the velocity distribution of slag computed across the thickness at two locations, 200mm and 500mm below the meniscus. The profile varies during the oscillation cycle in a similar manner to Figure 3.11. Besides the thickness difference, there is a slight difference in solid slag velocity. The shift of the viscosity curve, together with the slight movement of the solid slag layer, accounts for some of the slag consumption and also increases the liquid layer velocity. Together, this causes the decrease in the liquid layer thickness, shown in Figure 8.4(b). The solid layer thickness increases with distance down the mold, according to the lower heat flux, and corresponding lower temperature, especially with the increased softening temperature. Together, the total slag layer thickness has relatively little change over the whole mold length, which agrees with the observation in the real operating casters[220]. The slag layer varies in thickness according to the depth of the oscillation marks. The average equivalent thickness of the oscillation marks, d_{eff}, is included in Figure 8.4(b).

It is noted that the slag layer softening interaction with surface roughness may set up a stabilizing effect on heat transfer. A rougher slag surface tends to create a larger

interfacial resistance, and consequently hotter slag layer. This in turn causes the solid layer to become thinner, and lowers the gap resistance. The net effects roughly cancel. Furthermore, minor changes in surface roughness tend to be compensated by softening due to corresponding changes in slag cold surface temperature.

8.3 Crystallization Behavior

Figure 8.5 shows the cooling history of different layers in the interfacial gap. The measured CCT curve for crystalline slag S1 (refer to Chapter 4) is superimposed on Figure 8.5(b) to estimate the onset of crystallization of slag K1 since they are both crystalline slags. It is seen that the slag layer in the oscillation marks begins to cross the CCT curve at ~100mm below the meniscus (~4 seconds). This indicates the onset of crystallization, which was expected to accompany the decrease in liquid slag conductivity (Figure 8.2(b)). Therefore, the heat flux is impeded and the temperature in the slag layers decreases. This temperature decrease in turn leads to an increase in roughness of the solid slag layer cold surfaces. Other locations in the slag layer crystallize after longer times, but at a similar distance down the mold owing to the slower average downward movement of the colder layers.

As the fraction of crystals in the liquid layer increases, the viscosity and softening temperature of the slag might also increase. Thus, the solidification temperature, T_{fsol}, and viscosity index, n, are adjusted according to Figure 8.1. The thinner liquid layer (see Figure 8.4(b)) causes shear stress and axial tensile stress to build up in the liquid layer. If the slag layer shear stress reaches its shear strength before the axial stress accumulates to the fracture strength, the slag layer could be sheared longitudinally inside of the film. This would release the axial stress and avoid the serious slag fracture and shear off from

the mold wall. Furthermore, the increased slag cold surface roughness might help the solid slag layer to attach to the mold wall and overcome the high fracture strength of the slag film and promote the inter-layer shearing. In the simulation, either fracture (see Chapter 6 and 7) or shearing was roughly approximated by giving the solid layer the average velocity profile shown in Figure 8.2(a). This solid layer movement accelerates the slag consumption, so the liquid layer thickness decreases quickly. Correspondingly, the heat flux is enhanced and the slag layer temperature rebounds. This causes a slight temperature hump in the middle of the mold, which is confirmed by the thermocouple measurements in the AK steel caster[29, 221]. When the whole slag layer enters the crystallization region, the heat transfer is relatively stable with a slight decrease due to the slightly thicker slag layer.

Figure 8.6(a) proposes a schematic of the microstructure distribution in the interfacial gap, based on the simulation results for this caster. According to the results, crystalline layers dominate the slag film. Sheared layers are mostly likely near the middle of the film, at the interface between the liquid and solid layers at the locations down the mold where the shear stress exceeds the slag strength. Figure 8.6(b)shows a micrograph of a cross section through a piece of slag film taken from the mold wall at the end of casting (cap-off) at about 300mm from the top of the mold, that has only slightly different composition with slag K1 and is about 0.9mm thick[29, 221]. This is consistent with predicted thickness that varied from a minimum of ~0.5mm (see Figure 8.4(b)) to a maximum of 0.9mm in oscillation marks. It appears to show sheared layers in the film[29], at the same general location predicted in Figure 8.6(a). The model predicts a short length of liquid layer on the steel side near the meniscus, which should be observed

as glass if the air-quenched cap-off sample could be obtained. On the mold side, a thin (~0.05mm) glassy layer is also predicted due to fast cooling to a sustained low temperature. This is not seen in the cap-off film obtained for slightly different conditions. It is likely due to the devitrification of the glassy layer, which would happen if the contact resistance were able to increase the slag surface temperature to above a critical temperature. TTT results of this work suggests that the critical temperature for devitrification is around 500~600°C, which is consistent with previous measurements of 650°C for industrial slags and a few hundred Celsius degrees higher for synthetic slags[28, 143]

Slag film samples were taken from an experimental apparatus, which was constructed to simulate the gap in the real caster[138]. The slag composition, B2 given in Table 1 in reference [138], is same as that of slag K1. The samples were observed under SEM and Figure 8.7 show the backscatter electron (BSE) images. This figure reveals a complex multiple-layered structure that is similar in appearance to the slag sample removed from the operating continuous casting mold. The layers appear mainly crystalline, and correspond to different cooling rates. On the mold side, the fine and close dendrite structure is consistent with the fast cooling experienced there. In the middle of the film, the grains are uniform with a larger size. The steel side shows uneven-sized grains, which indicates that there was a significant growth of a few grains, formed during slow cooling, within a glassy background, that was likely formed during fast air cooling after the sample was removed.

8.4 Friction Results

In Chapter 4, the friction measurements give a relatively stable sliding friction coefficient of 0.2, which is also assumed to be the static friction coefficient in this case. Figure 8.8 shows that the axial stress builds up quickly in the solid slag layer at about 400mm below the meniscus. This indicates the possible slag shear or fracture position.

Figure 8.9 shows the shear stress down the mold predicted from the CON1D model at different times during the oscillation cycle. The shear stress increases with distance down the mold. The liquid-layer-controlled friction (near sinusoidal shape over oscillation cycle) transfers to solid-layer-controlled friction (more square-shaped) at around 400mm below the meniscus, where the sheared slag layers occur.

Integrating each shear stress line gives the total friction force over the mold face during the half oscillation cycle, which is shown in Figure 8.10(a). This stress acting on the slag layer shifts from tension to compression when the oscillation cycle shifts from positive strip to negative strip. Its amplitude is roughly consistent with the mold friction stresses measured in steel plants (see Figure 7.13). The corresponding total mold force varies from 7.6 to -6.7kN over the cycle as shown in Figure 8.10(b), which is obtained by multiplying the results Figure 8.10(a) by the mold area.

8.5 Tables and Figures

Table 8.1 Input Conditions for AK Steel Case

Carbon Content, *C%*	0.047 (SS430)	%
Liquidus/Solidus Temperature, T_{liq}/ T_{sol}	1502/1477	^oC
Steel Density, ρ_{steel}	7000	kg/m^3
Fraction Solid for Shell Thickness Location, f_s	0.1	-
Mold Thickness at Top (Outer face, including water channel)	35	mm
Mold Dimensions, $Z_{mold\_total} \times W_{mold}$	1200×1560	mm$\times$mm
Initial Cooling Water Temperature, T_{water}	25	^oC
Water Channel Geometry, $d_{ch} \times w_{ch} \times L_{ch}$	$5 \times 16 \times 21.5$	mm^3
Cooling Water Velocity, V_{water}	11.67	m/s
Mold Conductivity, k_{mold}	315	W/mK
Mold Powder Solidification Temperature, T_{fsol}	650→850	^oC
Mold Powder Conductivity, k_{solid}/k_{liquid}	1.0→0.5	W/mK
Air Conductivity, k_{air}	0.06	W/mK
Slag Layer/Mold Resistance, $r_{contact}$	$0.83 \rightarrow 2.5 \times 10^{-4}$	m^2K/W
Mold Powder Viscosity at 1300°C, μ_{1300}	0.421	Poise
Exponent for Temperature Dependence of Viscosity, *n*	8.5→6.0	-
Slag Density, ρ_{slag}	2500	kg/m^3
Slag Absorption Coefficient, *a*	250	1/m
Slag Index of Refraction, *m*	1.5	-
Slag Friction Coefficient, ϕ	0.2	-
Mold Powder Consumption Rate, Q_{slag}	0.3	kg/m^2
Empirical solid slag layer speed factor, f_v	0→0.04	-
Casting Speed, V_c	1.524	m/min
Pour Temperature, T_{pour}	1563.	^oC
Slab Section Size, $W \times N$	984×132	mm$\times$mm
Nozzle Submergence Depth, d_{nozzle}	127	mm
Working Mold Length, Z_{mold}	1096	mm
Oscillation Mark Geometry, $d_{mark} \times w_{mark}$	0.42×4.0	mm$\times$mm
Mold Oscillation Frequency, *freq*	150	cpm
Oscillation Stroke, *stroke*	7.5	mm
Time Step, *dt*	0.005	s
Mesh Size, *dx*	0.66	mm

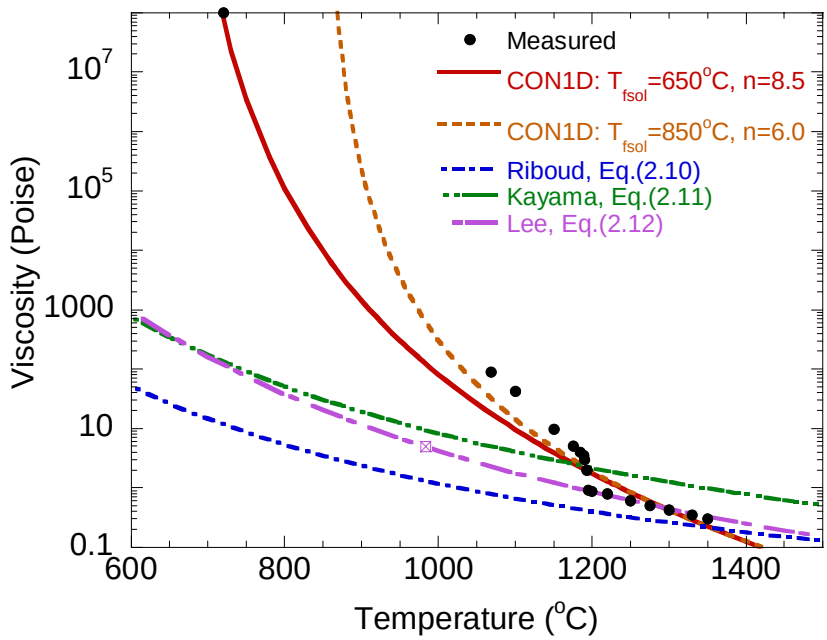

Figure 8.1 Viscosity of slag K1

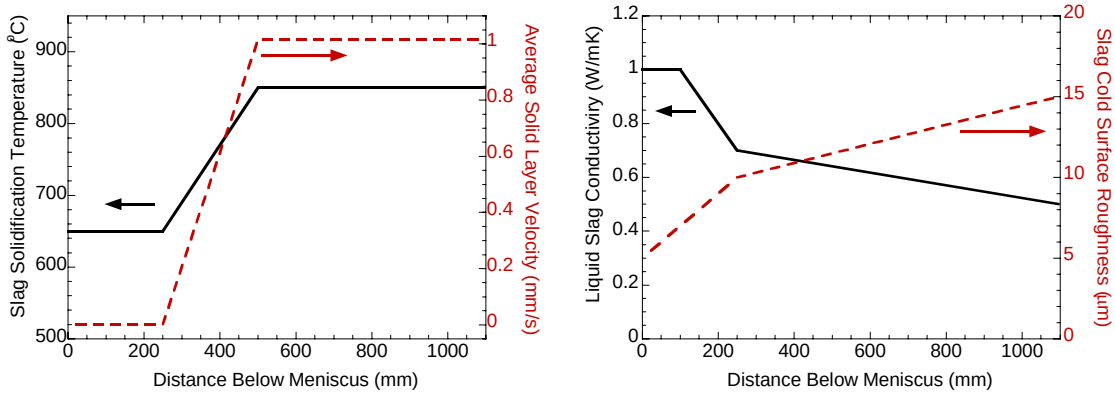

(a) Slag Solidification Temperature and Average Solid Layer Velocity **(b) Liquid Slag Conductivity and Slag Cold Surface Roughness**

Figure 8.2 Variable parameters used in AK steel Case

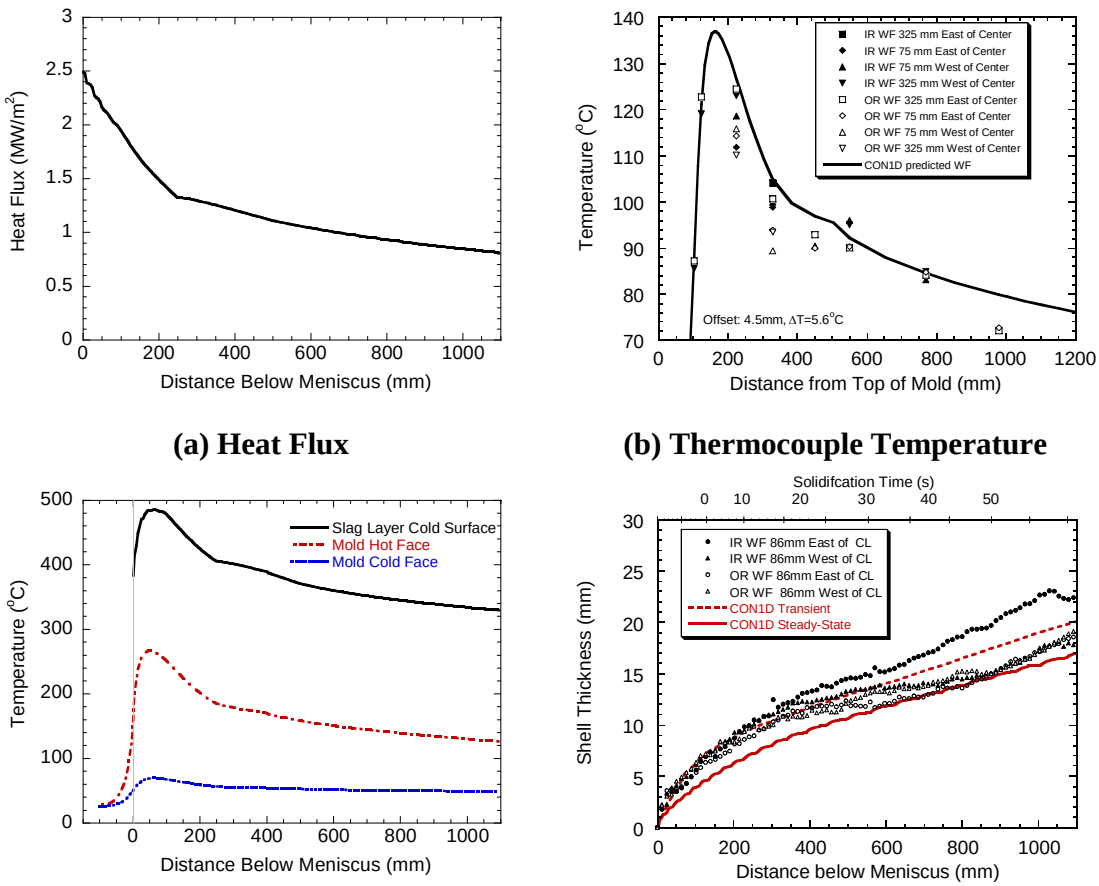

(a) Heat Flux **(b) Thermocouple Temperature**

(c) Mold Temperature **(d) Shell Thickness**

Figure 8.3 Heat transfer results for AK steel case

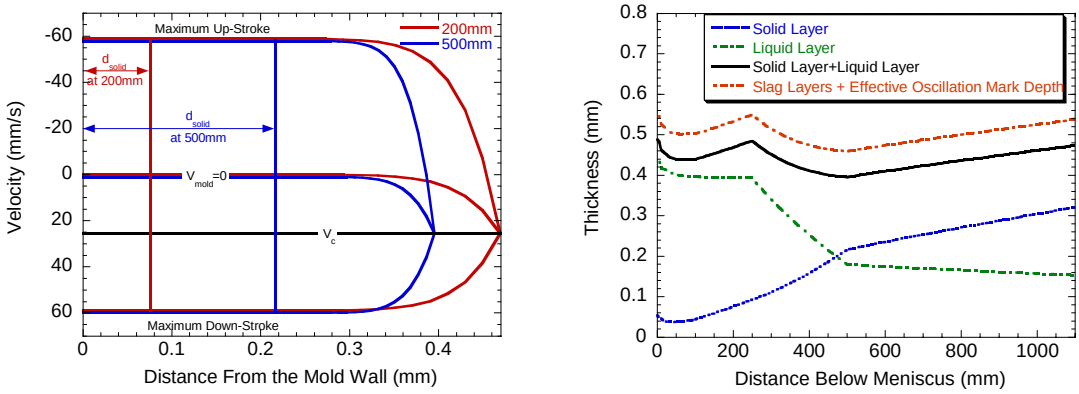

(a) Slag layer velocity distribution **(b) Slag layer thickness**

Figure 8.4 Slag layer velocity distribution and thickness

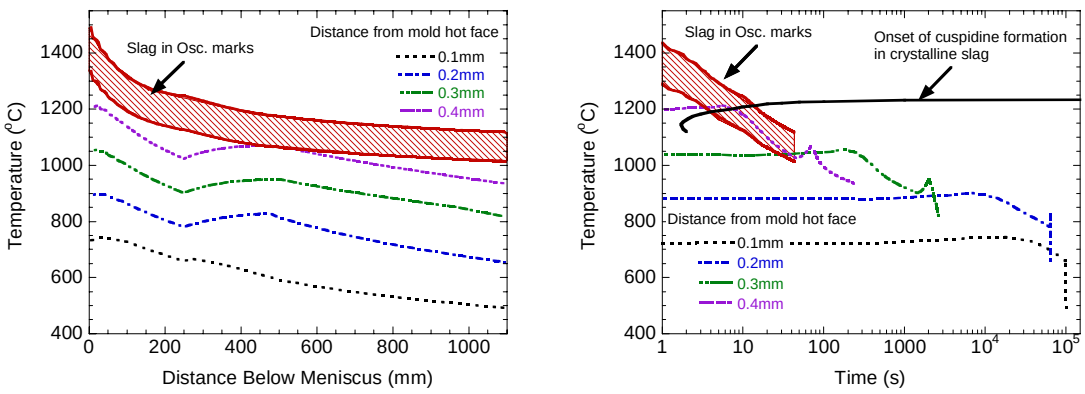

(a) Temperature vs. Distance **(b) Temperature vs. Time**

Figure 8.5 Slag layer cooling history

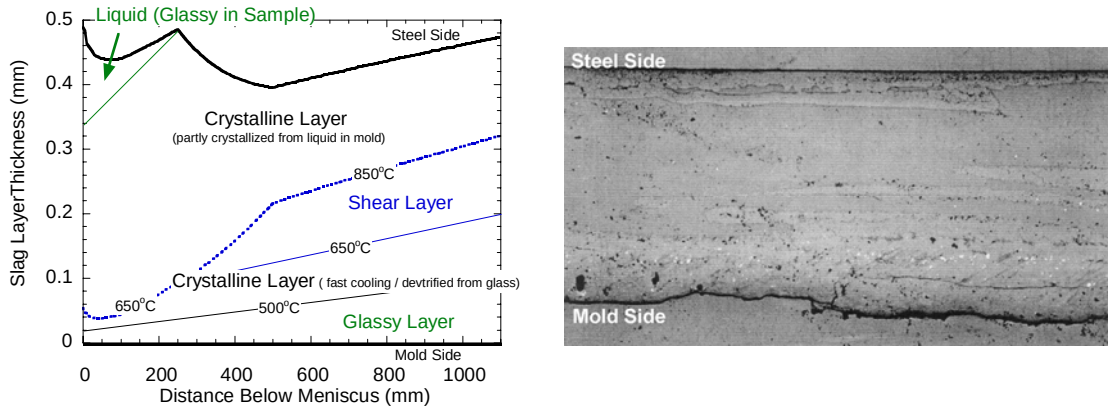

(a) Schematic of slag layer microstructure in the gap **(b) Cap-off slag film sample[29]**

Figure 8.6 Slag layer microstructure in the interfacial gap

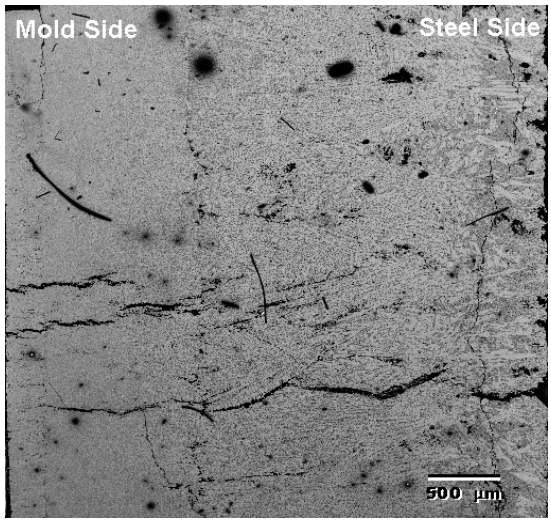

(a) Slag K1

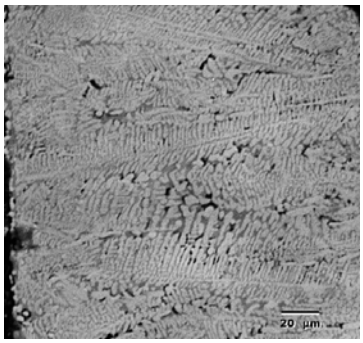

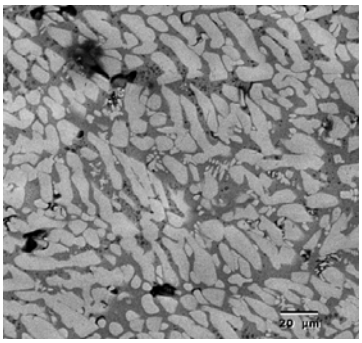

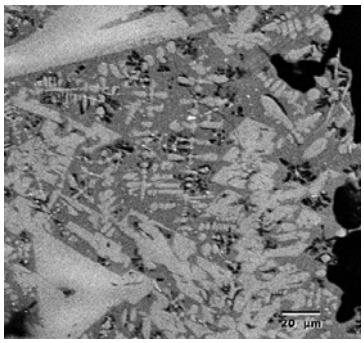

(b) Mold Side **(c) Middle Layer** **(d) Steel Side**

Figure 8.7 BSE images of slag K1 from experimental film

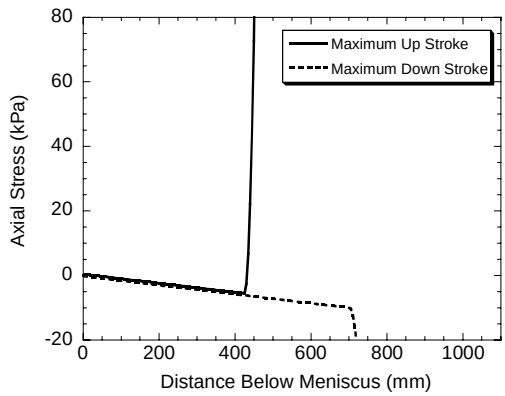

Figure 8.8 Axial stress for AK steel case

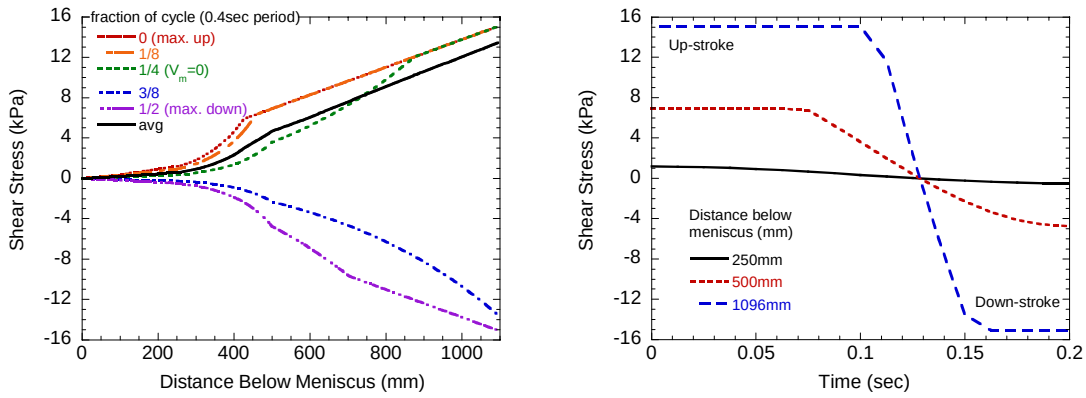

(a) Shear stress down the mold **(b) Shear stress over half oscillation cycle**

Figure 8.9 Shear stress for AK steel case

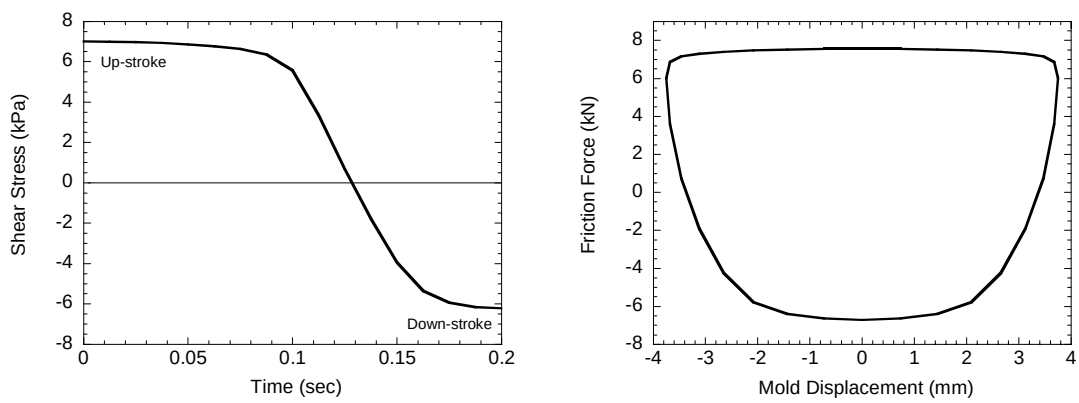

(c) Shear stress vs. Time **(b) Shear stress vs. mold displacement**

Figure 8.10 Friction force for AK steel case

CHAPTER 9. CONCLUSIONS

Analytical transient models of liquid slag flow and solid slag stress are developed and incorporated into a finite-difference model of heat transfer in the shell and mold (CON1D). All three models have been validated through numerical comparisons and extensively calibrated with measurements on operating casters, including cooling water temperature rise, mold thermocouple temperatures, breakout shell thickness, slag layer thickness, and thermocouples embedded in the steel shell. In addition to heat transfer, the model predicts thickness of the slag layers, friction in the interfacial gap, ideal mold taper, and potential quality problems such as complete slag solidification, and boiling in the water channels. It has many potential applications.

Experiments are conducted to measure the slag properties including friction coefficient at different temperatures, viscosity at low temperature, and CCT curves. The results show that increasing temperature first causes the friction coefficient to slightly decrease with an average value of 0.16 ± 0.1. A dramatic rise in friction takes place when the slag begins to soften. This temperature also extends the measurement of viscosity curves up to 10^8poise range.

XRD results show that Flourine exists as CaF_2 in pre-melted mold powder and cuspidine ($Ca_4Si_2O_7F_2$) is the predominant phase forming in re-solidified slag. The crystallization of slag highly depends on cooling rate. The critical cooling rates are 50^oC/sec for crystalline slag S1 and 20^oC/sec for glassy slag S2. The main crystalline phases in re-solidified slag are cuspidine ($Ca_4Si_2O_7F_2$), nepheline ($NaAlSiO_4$), gehlenite ($Ca_2Al_2SiO_7$), calcium silicon oxide fluoride ($Ca_2SiO_2F_4$), calcium silicate (Ca_2SiO_4, $Ca_8Si_5O_{18}$) and sodium calcium silicate ($Na_2Ca_2(SiO_3)_3$). CCT curves for both slags are

constructed. Polarized light microscopy, SEM and EDX images show crystalline and glassy layers but no severe macro-segregation in the tail-out slag film.

The models and experiment results are applied to study the effect of casting speed and mold powder properties on slag layer behavior between the oscillating mold wall and solidifying steel shell. Specific conclusions are:

Solid slag tends to remain attached to the mold wall, especially near the meniscus. When friction on the mold side cannot compensate the shear stress on the slag solid/liquid interface, axial stress builds up in the solid slag layer. If the powder consumption rate drops below a critical level, the axial stress can exceed the slag fracture strength, so the solid slag breaks and moves down the mold wall.

Crystalline slag with higher solidification temperature has a thick solid slag layer so lowers heat transfer across the mold/shell gap and increases shell surface temperature slightly.

The slag temperature-viscosity curve determines the shear stress along the mold wall and affects both the critical lubrication consumption rate, Q_{lub} and position of possible slag fracture. Crystalline slag (having a sharp viscosity transition) tends to fracture near the meniscus, but not easily (lower critical Q_{lub}). Glassy slag (having a gradual viscosity rise at lower temperature) tends to fracture near mold exit, easily (higher critical Q_{lub}). Increasing slag solidification temperature and decreasing high-temperature viscosity (such as occurs with high basicity slag) tends to lower critical Q_{lub} and make it less easy to fracture.

The following variables lower axial stress in the solid slag layer, critical Q_{lub}, and the likelihood of slag fracture.

- Increasing friction coefficient helps by encouraging the solid slag to stay attached to the mold wall.
- For a given total consumption rate, smaller oscillation marks lower gap friction and lower the danger of slag fracture.
- Decreasing casting speed lowers critical Q_{lub} and the danger of slag fracture at the meniscus, such as for slag A and for slag G cast at high speed.
- Increasing casting speed is safer for avoiding slag fracture near mold exit, such as for slag G cast at low speed.
- Increasing slag fracture strength helps slightly.

Liquid slag layer lubrication indicates a stable attached solid slag layer and can be recognized by very low mold shear stress (~1kPa) with a sinusoidal variation over each oscillation cycle.

The top half of the mold has negligible friction against the steel shell, as the liquid slag layer minimizes it. Solid slag friction begins just before the liquid slag runs out, lower down the mold. Increasing the fraction of the mold with solid slag friction can be identified by higher total mold friction and a sharper square wave shape of the friction curve over each cycle

The high friction (10~20kPa) measured in real casters might be due to any of three sources: an intermittent moving slag layer, excessive taper or mold misalignment. At low casting speed, the critical consumption rate is high, so variations in slag consumption at the meniscus can easily lead to solid slag layer fracture and movement. At high casting speed, excessive taper and mold misalignment likely increase friction problems.

The model is also applied to interpret the crystallization behavior of slag layers in the interfacial gap between the mold and the steel shell. A mechanism for the formation of this crystalline layer is proposed that combines the effects of a shift in the viscosity curve, a decrease in the liquid slag conductivity due to partial crystallization, and an increase in the solid slag layer roughness corresponding to a decrease in solid layer surface temperature with distance down the mold. When the shear stress exceeds the slag shear strength before the axial stress accumulates to the fracture strength, the slag could shear longitudinally inside the layers.

APPENDIX A. FDM SOLUTION OF STEEL SOLIDIFICATION MODEL

Figure A1 shows the simulation domain in the solidifying steel, which is a slice through the liquid steel and solid shell and moves down at casting speed, V_c. Applying the boundary conditions:

$$\left.\frac{\partial T}{\partial x}\right|_{centerline} = 0 \tag{A1}$$

$$k_{steel}\left(T_s\right)\left.\frac{\partial T}{\partial x}\right|_{steel\ surface} = -q_{int} \tag{A2}$$

Eq.(3.2) is solved at each time step using the following explicit central finite difference discretization[179]:

1) Centerline liquid node (adiabatic boundary):

$$T_1^{new} = T_1 + \frac{2\Delta t \cdot k}{\Delta x^2 \rho Cp^*}\left(T_2 - T_1\right) \tag{A3}$$

2) Interior nodes:

$$T_i^{new} = T_i + \frac{\Delta t \cdot k}{\Delta x^2 \rho Cp^*}\left(T_{i-1} - 2T_i + T_{i+1}\right) + \frac{\Delta t}{4\Delta x^2 \rho Cp^*}\frac{\partial k}{\partial T}\left(T_{i+1} - T_{i-1}\right)^2 \tag{A4}$$

3) Shell surface node (with heat flux boundary):

$$T_n^{new} = T_n + \frac{2\Delta t \cdot k}{\Delta x^2 \rho Cp^*}\left(T_{n-1} - T_n\right) + \frac{\Delta t}{\rho Cp^*}\frac{\partial k}{\partial T}\left(\frac{q_{int}}{k}\right)^2 - \frac{2\Delta t \cdot q_{int}}{\Delta x \rho Cp^*} \tag{A5}$$

The effect of superheat is included by adjusting Eq.(A4) for the first interior node with a temperature below the liquidus temperature:

$$T_i^{new} = T_i^{new} + \frac{\Delta t}{\rho C_p{}^* dx} q_{sh} \tag{A6}$$

where $dx = \Delta x$ for interior nodes, and $dx = \Delta x / 2$ for boundary nodes.

The above equations are solved at each time step (T_i^{new}) based on properties evaluated at the previous step (T_i). This simple explicit scheme is usually acceptable because property changes are generally gradual with temperature. (Refer to Figure 3.3 and Figure 3.4). However, the effective specific heat has a sudden jump when temperature drops below the liquidus temperature. To improve accuracy, and allow a larger time step, a post-iteration correction is applied to each node after the time step when it first drops below the liquidus temperature. Specifically, its temperature is increased to match the solid fraction that should have been achieved, based on converting the sensible heat extracted from that node into latent heat, according to the solid fraction curve $T(f_s)$ defined previously:

$$T_i^{new} = T\left(f_s = \frac{\left(T_{liq} - T_i^{new}\right) \cdot Cp^*\left(T_i\right)}{L_f} \right) \tag{A7}$$

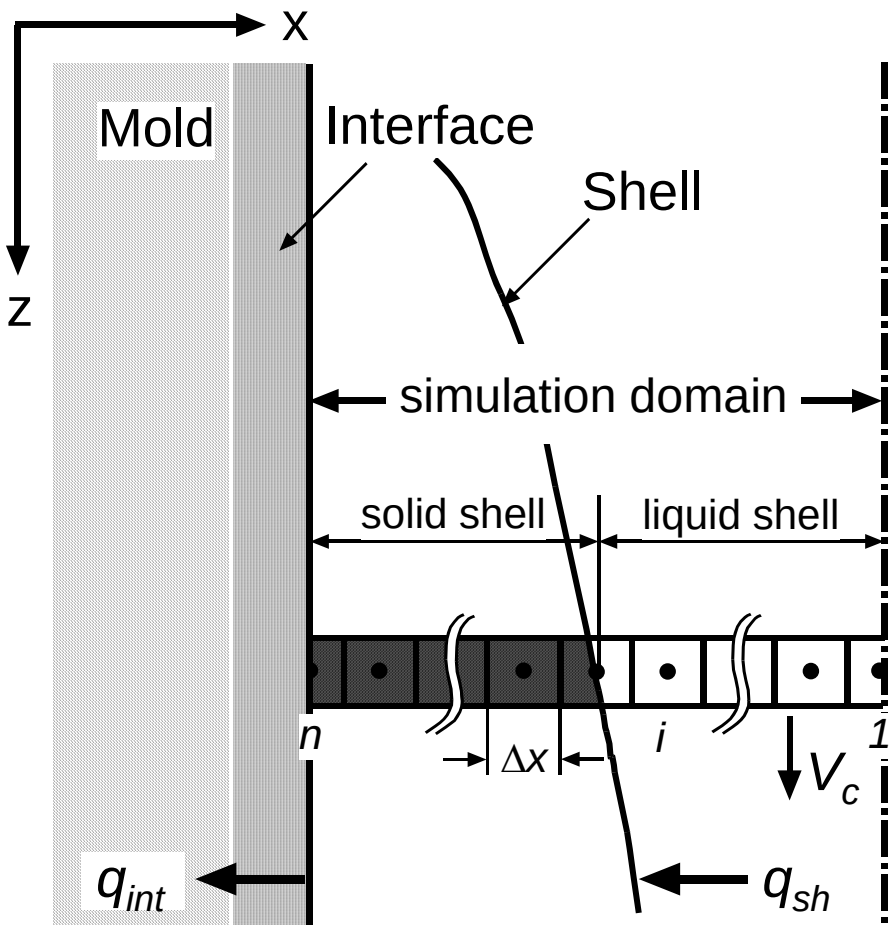

Figure A1 Simulation Domain in Shell

APPENDIX B. CARBON STEEL THERMAL PROPERTIES FUNCTIONS[159]

1. Thermal conductivities

$$k = k_\alpha f_\alpha + k_\delta f_\delta + k_\gamma f_\gamma + k_l f_l$$

where

$$\begin{aligned}
k_\alpha &= \left(80.91 - 9.9269\times10^{-2}T + 4.613\times10^{-5}T^2\right)\left(1 - a_1\left(C\%\right)^{a_2}\right) \\
k_\delta &= \left(20.14 - 9.313\times10^{-3}T\right)\left(1 - a_1\left(C\%\right)^{a_2}\right) \\
k_\gamma &= 21.6 - 8.35\times10^{-3}T \\
k_l &= 39.0 \\
a_1 &= 0.425 - 4.385\times10^{-4}T \quad a_2 = 0.209 + 1.09\times10^{-3}T
\end{aligned} \tag{B1}$$

2. Specific heat

$$C_p = C_p^\alpha f_\alpha + C_p^\delta f_\delta + C_p^\gamma f_\gamma + C_p^l f_l$$

where

$$C_p^\alpha = \begin{cases} 504.81 - 0.13T(K) - 5.19\times10^6 T(K)^{-2} & T(K) \le 800 \\ +4.49\times10^{-4}T(K)^2 & \\ -4720.32 + 4.58T(K) + 1.11\times10^9 T(K)^{-2} & 800 < T(K) \le 1000 \\ -11501.07 + 12.48T(K) & 1000 < T(K) \le 1042 \\ 34871.21 - 32.03T(K) & 1042 < T(K) \le 1060 \\ -10068.18 + 5.99T(K) + 5.22\times10^9 T(K)^{-2} & 1060 < T(K) \le 1184 \end{cases} \tag{B2}$$

$$C_p^\delta = 441.39 + 0.18T(K)$$

$$C_p^\gamma = 429.85 + 0.15T(K)$$

$$C_p^l = 824.6157$$

3. Density used for Thermal Linear Expansion Calculation

$$\rho(T) = \rho_\alpha f_\alpha + \rho_\delta f_\delta + \rho_\gamma f_\gamma + \rho_l f_l$$

where

$$\rho_\alpha = 7880.76 - 0.3244T - 2.7461\times10^{-5}T^2$$

$$\rho_\delta = \left(8010.71 - 0.4724T\right)\cdot\left(1 + \frac{C\%}{100 - C\%}\right)\cdot\left(1 + 13.43\times10^{-3}\%C\right)^{-3} \qquad \text{(B3)}$$

$$\rho_\gamma = \left(8105.91 - 0.5091T\right)\cdot\left(1 + \frac{C\%}{100 - C\%}\right)\cdot\left(1 + 8.317\times10^{-3}\%C\right)^{-3}$$

$$\rho_l = 7965.98 - 0.619T$$

APPENDIX C. HEAT LOSS FROM MOLD SLAG SOLIDIFICATION AND COOLING

To estimate the heat loss involved from slag solidification and cooling in the interfacial gap between steel and mold, a sample case is calculated following.

The slag latent heat is calculated from the components latent heat[222]. For a typical slag S1 (Table 4.1), the latent heat, L_{f_slag}, is calculated as 776.05kJ/kg based component molar fraction. The specific heat of slag, Cp_{slag}, is 0.5kJ/kgK[223] and density, ρ_{slag}, is 2500 kg/m^3.

For a typical CC run with V_c=1.0m/min, Z_{mold}=810mm, $\overline{T_s}$ =1200°C, $\overline{T_{mold}}$ =200°C, and solid layer consumption rate, q_{cons_solid}=4x10^{-6}m^2/s (corresponding total consumption rate, Q_{slag}=0.6kg/m^2 with solid slag layer speed factor f_v=0.175)[8].

The heat loss is:

$$\begin{aligned} q &= q_{latent\ heat} + q_{sensible\ heat} \\ &= q_{cons\_solid}\rho_{slag}L_{f\_slag}/Z_{mold} + q_{cons\_solid}\rho_{slag}Cp_{slag}\Delta T/Z_{mold} \\ &= \frac{4\times10^{-6}\times2500\times\left(776.05+0.5\times\frac{1200-200}{2}\right)}{810\times10^{-3}} = 12.7\,kW/m^2 \end{aligned} \tag{C1}$$

which is 0.9% of total average heat flux removed by the mold, 1400kW/m^2.

APPENDIX D. ANALYTICAL SOLUTION FOR 2-D HEAT CONDUCTION IN THE MOLD[171]

The analytical solution to Eq.(3.53) with the boundary conditions shown in Figure 3.17(a) is a cosine series:

$$T\left(x,z\right)=T_{water}+c_0\left(\frac{k_{mold}}{h_{water}}+x\right)+\sum_{n=1}^{\infty}\left(c_{2n}\cos\left(\lambda z\right)\left(c_1e^{-\lambda x}+e^{-\lambda x}\right)\right) \tag{D1}$$

where x is distance through the thickness of the mold, measured from the root of the water slot. The constants λ, c_0, c_1 and c_{2n} depend on the heat flux calculated to enter the mold hot face q_{int}, thermal conductivity k_{mold}, the effective heat transfer coefficient h_{water} and the mold length for 2-D calculation Z_{2D}.

$$\lambda=\frac{n\pi}{Z_{2D}} \tag{D2}$$

$$c_0=\frac{2\cdot\Delta z}{Z_{2D}}\left(a_j\frac{z_{j+1}+z_j}{2}+b_j\right) \tag{D3}$$

$$c_1=\frac{k_{mold}\lambda-h_{water}}{k_{mold}\lambda+h_{water}} \tag{D4}$$

$$\begin{aligned} c_{2n}&=B\frac{\frac{2}{Z_{2D}}\left(\frac{1}{\lambda}\right)^2}{e^{\lambda x}\left(1-c_1e^{-2\lambda x}\right)}\\ B&=\sum_j\left(\begin{array}{l}\left(a_jz_{j+1}+b_j\right)\sin\left(\lambda z_{j+1}\right)-\left(a_jz_j+b_j\right)\sin\left(\lambda z_j\right)\\ +\frac{a_j}{\lambda}\left(\cos\left(\lambda z_{j+1}\right)-\cos\left(\lambda z_j\right)\right)\end{array}\right)\end{aligned} \tag{D5}$$

where a_j and b_j are the linear interpolation coefficients of the interface heat flux in zone j:

$$a_j = \frac{q_{\text{int } j+1} - q_{\text{int } j}}{k_{mold}\left(z_{j+1} - z_j\right)}$$
$$b_j = \frac{q_{\text{int } j} z_{j+1} - q_{\text{int } j+1} z_j}{k_{mold}\left(z_{j+1} - z_j\right)} \tag{D6}$$

The actual hot face temperature of the mold is adjusted to account for the possible presence of mold coatings and air gaps:

$$T_{mold} = T\left(d_{mold}, z\right) + q_{\text{int}}\left(\frac{d_{ni}}{k_{ni}} + \frac{d_{cr}}{k_{cr}} + \frac{d_{poly}}{k_{poly}} + \frac{d_{air}}{k_{air}}\right) \tag{D7}$$

APPENDIX E. MOLD THICKNESS[171]

For a curved mold, the mold thickness, d_{mold} varies with distance down the mold, which is calculated for the outer and inner radius mold faces separately:

$$d_{mold}^{outer} = d_{moldo}^{outer} + \sqrt{R_O^{\,2} - \frac{1}{4}\left(Z_{mold\_total}\right)^2} - \sqrt{R_O^{\,2} - \frac{1}{4}\left(Z_{mold\_total}\right)^2 - Z_{mold\_total}^2} \qquad \text{(E1)}$$

$$d_{mold}^{inner} = d_{moldo}^{inner} - \sqrt{R_I^{\,2} - \frac{1}{4}\left(Z_{mold\_total}\right)^2} + \sqrt{R_I^{\,2} - \frac{1}{4}\left(Z_{mold\_total}\right)^2 - Z_{mold\_total}^2} \qquad \text{(E2)}$$

where d_{moldo} is the mold thickness at the top of the mold, Z_{mold_total} is the total mold length (sum of working mold length Z_{mold} and distance of meniscus from top of the mold Z_{men}) and R_O, R_I are mold outer and inner radius of curvature respectively, as shown in Figure E1.

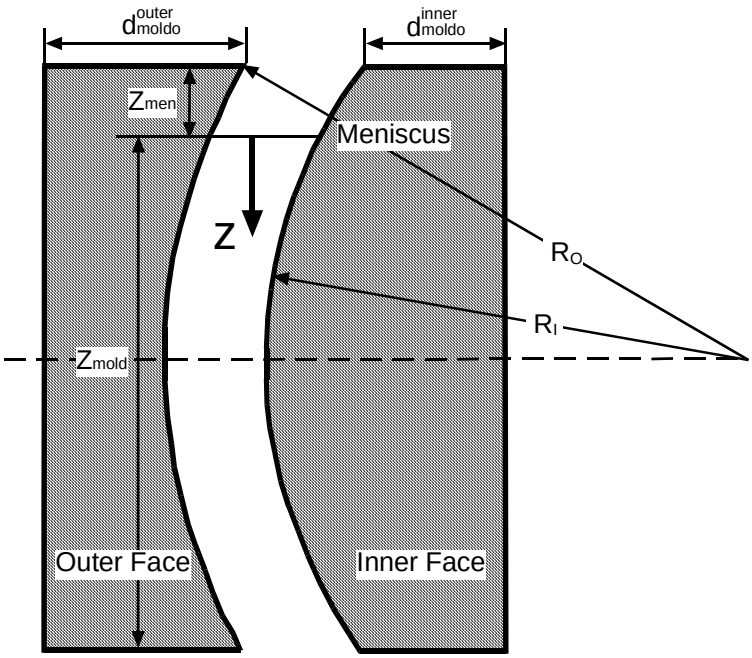

Figure E1 Mold outer and inner radius faces

APPENDIX F. WATER PROPERTIES IN MOLD COOLING CHANNEL[171]

To solve Eq.(3.57), wall temperature, T_{water}, T_{cold}, and average bulk temperature in the cooling channel, T_{film}, are used:

$$T_{film} = \frac{1}{2}\left(T_{water} + T_{cold}\right) \tag{F1}$$

The Reynolds number and the Prandtl number are calculated as following:

$$\mathrm{Re}_{waterf} = \frac{\rho_{water} V_{water} D}{\mu_{waterf}} \tag{F2}$$

$$\mathrm{Pr}_{waterw} = \frac{\mu_{waterw} Cp_{water}}{k_{waterw}} \tag{F3}$$

Water properties, such as density, viscosity and conductivity are function of temperature:

$$k_{waterm} = 0.59 + 0.001 T_{water} \tag{F4}$$

$$\rho_{water} = 1000.3 - 0.040286 T_{film} - 0.0039779 T_{film}^{2} \tag{F5}$$

$$\mu_{waterf} = 2.062 \rho_{water} \times 10^{\frac{792.42}{T_{film}+273.15} - 9} \tag{F6}$$

$$Cp_{water} = 4215 - 1.5594 T_{cold} + 0.015234 T_{cold}^{2} \tag{F7}$$

$$k_{waterw} = 0.59 + 0.001 T_{cold} \tag{F8}$$

$$\mu_{waterw} = 2.062 \rho_{water} \times 10^{\frac{792.42}{T_{cold}+273.15} - 9} \tag{F9}$$

APPENDIX G. MANUFACTURER REPORTED SLAG COMPOSITION[181-183]

Table G.1 Mold Powder Composition Reported by Suppliers (wt%)

	S1	S2	K1	H1
SiO_2	33.3	37.39	29.93	35.8
CaO	39.9	22.82	39.41	40.4
Al_2O_3	5.38	2.37	4.58	4.6
F	7.52	6.67	12.93	3.3
Na_2O	4.61	13.11	9.04	6.0
MgO	2.96	1.41	0.79	<3.0
TiO_2	<1.0	<0.5	-	<3.0
Fe_2O_3	<1.5	<1.5	0.19	<3.0
MnO	<1.0	<0.5	0.01	<3.0
K_2O	<1.0	<0.5	0.80	<3.0
Li_2O	-	<1.0	-	-
B_2O_3	-	1.38	-	-
C-Total	3.99	11.21	2.23	5.7
CO_2	3.12	3.68	2.62	-
C-Free	3.14	10.21	1.52	-
H_2O @ 105°C	<0.50	<0.50	-	-
H_2O @ 600°C	<1.0	<1.0	-	-
CaO/ SiO_2	1.20	0.61	1.32	1.13

APPENDIX H. AK STEEL BREAKOUT SHELL GROWTH

An analysis was performed by Stone et al to evaluate shell growth predictions by CON1D against measurements obtained from the AK breakout shell[32, 105]. The following table was used to convert the steady state results to transient shell growth during breakout.

Table H.1 AK Steel Breakout Shell Drainage Time vs. Distance

Drainage Time (sec)	Distance (mm)
0	0
1.1	19.84
2.4	33.06
3.3	45.18
4.5	59.51
5.8	70.53
6.7	83.75
7.7	96.98
8.7	109.1
9.4	122.32
9.9	127.84
16.4	254.69
22.2	378.77
28	509.39
33.5	633.47
39.9	764.08
45.8	894.69
52.1	1018.8
58.4	1142.9
64.9	1273.5
77.4	1449.8

APPENDIX I. CON1D VERSION 7.5 SAMPLE INPUT AND OUTPUT FILES

I.1 Input file: sample.inp

```
CON1D-7.5 Slab Casting Heat Transfer Analysis
University of Illinois, Brian G. Thomas, 2002

      Input Data                    INP

(1) CASTING CONDITIONS:
      1     Number of time-cast speed data points
            (If=1, constant casting speed)
            Next 2 lines contain time(s) and vc(m/min) data points
  0.
1.000
  1550.0    Pour temperature (C)
  230.10    Slab thickness (mm)
  1500.0    Slab width (mm)
  94.000    Distance of meniscus from top of mold (mm)
  800.00    Working mold length (mm)
  20.000    Z-distance for heat balance  (mm)
  265.00    Nozzle submergence depth (mm)

(2) SIMULATION PARAMETERS:
      0     Which shell to consider? (0=wide face; 1=narrow face)
      0     What type of mold? (0=slab, 1=funnel mold, 2=billet mold)
      2     Which moldface to consider? (0=outer, 1=inner, 2=straight)
      0     Calculate mold and interface (=0 flux casting, or 2 oil casting )
            or enter interface heat flux data (=-1)
      7     Number of zmm and q data points (if above = -1)
            Next 2 lines contain zmm(mm) and q(kW/m2) data
  0.  100.  200.  300.  400.  600.  800.
 2910. 1840. 1580. 1390. 1260. 1000.  880.
 1.000      Is superheat treated as heatflux?
            0=no; 1=yes (take default); -1=yes (enter data)
     12     Number of zmm and q data points(if above = -1)
            Next 2 lines contain zmm(mm) and q(kW/m2) data
  0.  100.  200.  260.  300.  500.  700. 1000. 1500. 2000. 3000. 10000.
  94.  97.   92.  109.  197.  211.   12.   14.   80.   20.    0.    0.
      1     Do you want (more accurate) 2d calculations in mold?
            (0=no; 1=yes; 2=yes, one extra loop for better taper)
 800.00     Max. dist. below meniscus for 2d mold calcs (mm)
            (=mold length if above = 2)
 2.00E-03   Time increment (s)
    100     Number of slab sections
 100.000    Printout interval (mm)
 0. 00      Start output at (mm)
 1500.0     Max. simulation length (must > z-distance)(mm)
 50.000     Max. simulation thickness (mm)
            (smaller of max. expected shell thickness &
            half of slab thickness)
  1000000   Max. number of iterations
      3     Shell thermocouple numbers below hot face (less than 10)
            Next line gives the distance below surface of thermocouples(mm)
  10.0  12.5  25.0
 0.3000000  Fraction solid for shell thicknesss location (-)

(3) STEEL PROPERTIES:
0.0500 1.520  0.015  0.012  0.340    %C,%Mn,%S,%P,%Si
0.0000 0.0000 0.0000 0.0000 0.0000   %Cr,%Ni,%Cu,%Mo,%Ti
0.0000 0.0000 0.0000 0.0000 0.0000   %Al,%V ,%N ,%Nb,%W
0.0000                               %Co,(additional components)
    1000    Grade flag
```

```
            (1000,304,316,317,347,410,419,420,430,999)
        1    If CK simple Seg. Model wanted for default Tliq,Tsol
            (1=yes,0=no)
  10.00000      Cooling rate used in Seg.Model(if above =1) (K/sec)
            Override defaults with following constants(-1=default)
 -1.000000      Steel liquidus temperature (C)
 -1.000000      Steel solidus temperature (C)
 -1.000000      Steel density (g/cm^3)
 -1.000000      Heat fusion of steel (kJ/kg)
 -1.000000      Steel emissivity (-)
 -1.000000      Steel specific heat (kJ/kg deg K)
 -1.000000      Steel thermal conductivity (W/mK)
 -1.000000      Steel thermal expansion coeff. (/K)

(4) SPRAY ZONE VARIABLES:
  35.00000      Water and ambient temperature after spray zone(Deg C)
                spray zone condition:(heat tran.coeff.funct:h=A*C*W^n(1-bT))
                (Nozaki Model:A*C=0.3925,n=0.55,b=0.0075)
  1.570000      A(0=off)
 0.5500000      n
 0.0075         b
  8.700000      minimum convection heat trans. coeff. (natural) (W/m^2K)
        4     Number of zones
No.  zone     rol.     water        spray      contct frac.of   spray   conv    amb.
   starts  #  rad.   flowrate   width  length  angle  q thr rol coeff   coeff   temp.
   (mm)       (m)  (l/min/row)   (m)    (m)    (Deg)                (W/m^2K) (DegC)
1   800.0   1  0.075   18.882    0.984  0.904    0.00   0.010    0.250   8.70    25.0
2  2000.0   1  0.075    9.187    0.984  0.050   10.00   0.080    0.250   8.70    25.0
3  2710.0   1  0.095    5.195    0.984  0.050   10.00   0.220    0.250   8.70    25.0
4  8700.0   5  0.095    3.897    0.984  0.050   10.00   0.200    0.250   8.70    25.0
    14000.0     End of last spray zone (mm)

(5) MOLD FLUX PROPERTIES:(flux A2 in Ref #41 by Lanyi)
32.30 36.40  0.70  5.00  1.90    %CaO,%SiO2,%MgO,%Na2O,%K2O
 3.00  0.00  0.00  0.00  0.00    %FeO,%Fe2O3,%NiO,%MnO,%Cr2O3
 8.90  0.00  3.40  0.00  0.00    %Al2O3,%TiO2,%B2O3,%Li2O,%SrO
 0.00  8.30  0.00  0.00  0.00    %ZrO2,%F,%free C,%total C,%CO2
  950.0000      Mold flux solidification temperature(c)
  1.500000      Solid flux conductivity(W/mK)
  1.500000      Liquid flux conductivity(W/mK)
  4.300000      Flux viscosity at 1300C (poise)
  2500.000      Mold flux density(kg/m^3)
  250.0000      Flux absorption coefficient(1/m)
  1.500000      Flux index of refraction(-)
            (-1 = take default f(composition)
 0.900000      Slag emissivity(-)
  1.60000      Exponent for temperature dependency of viscosity
        1       Form of mold powder consumption rate(1=kg/m^2; 2=kg/t)
 0.411000      Mold powder consumption rate
 0.0000E+00    Location of peak heat flux (m)
 0.0000E+00    Slag rim thickness at metal level (meniscus) (mm)
 0.0000E+00    Slag rim thickness at heat flux peak (mm)
  10.00000      Liquid pool depth (mm)
  8.0E+30       Solid flux tensile fracture strength (KPa)
  8.0E+30       Solid flux compress fracture strength (KPa)
 0.170000       Solid flux Poisson ratio(-)
 0.400000       Max. Static friction coeff. between solid flux and mold wall
 0.400000       Moving friction coefficient between solid flux and mold wall

(6) INTERFACE HEAT TRANSFER VARIABLES:
        1       Number of distance-vratio data points
                (1=constant ratio of solid flux velocity
                to casting speed)
                Next 2 lines contain zmm(mm) and ratio(-) data
  0.
0.06
 5.000E-09      Flux/mold or shell/mold contact resistance(m^2K/W)
 0.5000000      Mold surface emissivity(-)
 0.06           Air conductivity(W/mK)
        0       Osc.marks simulation flag(0=average,1=transient)
```

```
 0.450000        Oscillation mark depth(mm)
 4.500000        Width of oscillation mark (mm)
 1.388889        Oscillation frequency(cps)
                 (-1=take default cpm=2*ipm casting speed)
 7.800000        Oscillation stroke(mm)

(7) MOLD WATER PROPERTIES:
-1.000000        heat transfer coefficient(W/m^2K)
                 (-1=default=f(T), based on Sleicher and Rouse Eqn)
 4179.000        Water heat capacity(J/kgK)(-1=default=f(T))
 995.6000        Water density(kg/m3)(-1=default=f(T))

(8) MOLD GEOMETRY:
 51.00000        WF Mold thickness with water channel (mm),(outer rad.,top)
 51.00000        WF Mold thickness with water channel (mm),(inner rad.,top)
 51.00000        Narrow face (NF) mold thickness with water channel (mm)
 30.00000        Equivalent thickness of water box (mm)
-1.000000        Mean temperature diff between hot & cold face of NF (C)
 25.00000        25.00000    Cooling water channel depth(mm)(WF,NF)
 5.000000        5.000000    Cooling water channel width(mm)(WF,NF)
 29.00000        29.00000    Channel distance(center to center)(mm)(WF,NF)
 7672.414        2200.000    Total channel cross sectional area(mm^2)(WF,NF)
                     (served by water flow line where temp rise measured)
 315.0000        315.0000    Mold thermal conductivity(W/mK)(WF,NF)
 1.6000000E-05   Mold thermal expansion coeff. (1/K)
 30.00000        Cooling water temperature at mold top(C)
 0.2020000       Cooling water pressure(MPa)
        1      Form of cooling water velocity/flowrate(1=m/s ; 2=L/s)
 7.800000        7.800000    Cooling water velocity/flowrate per face (WF,NF)
                     (> 0 cooling water from mold top to bottom
                     < 0 cooling water from mold bottom to top)
 0.0000000E+00   funnel height (mm)
 0.0000000E+00   funnel width (mm)
 0.0000000E+00   funnel depth at mold top (mm)
 11.76000        Machine inner radius(m)
 11.98500        Machine outer radius(m)
        3      Number of mold coating/plating thickness changes down mold
 No.   Scale     Ni      Cr      Others   Air gap   Z-positions   unit
 1     0.010    1.000   0.100    0.000    0.000      0.000       (mm)
 2     0.010    1.000   0.100    0.000    0.000    400.000       (mm)
 3     0.010    1.000   0.100    0.000    0.000    800.000       (mm)
       0.550   72.100  67.000    1.000    0.060    Conductivity  (W/mK)

(9) MOLD THERMOCOUPLES:
        4      Total number of thermocouples
No.     Distance beneath     Distance below
       hot surface(mm)      meniscus(mm)
  1      19.5                -1.00
  2      19.5                20.00
  3      19.5               121.00
  4      19.5               226.00
```

I2 Output file: sample.ext

```
            CON1D-7.5 Slab Casting Heat Transfer Analysis
            University of Illinois, Brian G. Thomas, 2002

EXIT              Calculated Conditions                    EXT


    Initial casting speed:                 16.67    (mm/s)
    Carbon content:                       0.0500    (%)
    Wide face simulation:

Steel Properties:
    The following 3 temperature from Y.M.Won Segregation Model
```

```
    Liquidus Temp:                    1532.10    Deg C
    Solidus Temp:                     1515.31    Deg C
    Peritectic Temp:                     0.00    Deg C

    AE3 Temp:                         888.29    Deg C
    AE1 Temp:                         723.00    Deg C

Parameters Based on Derived Mold Values:
    Carbon equivalent:                  0.0500    (%)
    (using initial casting speed:)
     Negative strip time:                0.24    (s)
     Positive strip time:               0.48    (s)
     Velocity amplitude of mold oscillation:     34.03   (mm/s)
     Pitch(spacing betweeen oscillation marks):   12.00    (mm)
     % Time negative strip:             33.71    (%)
     Average percent negative strip velocity:    30.00    (%)

    Cooling water velocity:              7.80    (m/s)
    Cooling water flow rate per face:      59.8448    (L/s)
    Average mold flux thickness:           0.0555    (mm)
    (based on consumption rate)
    (assuming flux moves at casting speed)
    min. heat trans. coeff. on mold cold face     14.72    kW/m2K
    max. heat trans. coeff. on mold cold face     19.30    kW/m2K
    Water boiling temperature:          120.528    Deg C
    Max cold face temperature:          161.765    Deg C
    Max hot face temperature(copper only):     361.551    Deg C
    Max hot face temperature(w/coating):      404.129    Deg C
    Mold water temp diff(in hot channel):      8.2918    Deg C
    Mold water temp diff(over all channels):    6.9875    Deg C
*** Warning: There is danger of boiling in
    the water channels!
    Mean heat flux in mold:            1449.42    (kW/m^2)

Friction Values:
    Average absolute shear stress in Mold:      7.7788    (kPa)
    Average friction force in Mold:            9.3346    (kN)
    Max. shear stress in Mold:             10.2271    (kPa)
    Max friction force in Mold:            12.2726    (kN)
    Min. shear stress in Mold:             -7.6977    (kPa)
    Min friction force in Mold:            -9.2372    (kN)
    shear stress in Mold when Vmold=0:          7.5690    (kPa)
    Friction force in Mold when Vmold=0:        9.0828    (kN)
    Calculated solid flux velocity ratio        0.0000    (-)
    Calculated solid flux consumption:       0.000E+00    (m^2)
    Used solid flux consumption:            0.787E-04    (m^2)
    Calculated liquid flux consumption:      0.213E-04    (m^2)
    Used liquid flux consumption:           0.494E-04    (m^2)
    Used osc. flux consumption:             0.135E-03    (m^2)

Heat Balance at   20.00mm:
    Heat Extracted:                      4.07    (MJ/m^2)
    Heat Input to shell inside:             0.12    (MJ/m^2)
    Super Heat:                         0.01    (MJ/m^2)
    Latent Heat in mushy region:              0.77    (MJ/m^2)
    Latent Heat in Solid region:             2.51    (MJ/m^2)
    Sensible Cooling:                     0.61    (MJ/m^2)
    Total Heat:                         4.02    (MJ/m^2)
    Error In Heat Balance:                   1.30    (%)

Heat Balance at Mold Exit( 800.03mm):
    Heat Extracted:                     69.58    (MJ/m^2)
    Heat Input to shell inside:             2.49    (MJ/m^2)
    Super Heat:                         0.08    (MJ/m^2)
    Latent Heat in mushy region:              1.72    (MJ/m^2)
    Latent Heat in Solid region:            41.61    (MJ/m^2)
    Sensible Cooling:                    24.75    (MJ/m^2)
    Total Heat:                         70.64    (MJ/m^2)
    Error In Heat Balance:                   1.53    (%)
```

```
Variables Calculated at Mold Exit( 800.03mm):
    taper (per mold, narrow face):                1.79    (%)
    taper (per mold per length, narrow face):     2.24    (%/m)
    Shell thickness:                             22.37    (mm)
    Liquid flux film thickness:                   0.0207  (mm)
    Solid flux film thickness:                    1.2232  (mm)
    Total flux film thickness:                    1.2439  (mm)
    Shell surface temperature:                    1008.02 Deg C
    Mold hot face temperature:                    179.78  Deg C
    Heat flux:                                0.9445  (MW/m^2)

Predicted Thermocouple Temperatures:
  No.   distance beneath    distance below     temperature
        hot surface(mm)     meniscus(mm)          Deg C
  1     19.50               -1.00              138.26
  2     19.50               20.00              191.59
  3     19.50               121.00             181.26
  4     19.50               226.00             151.17
```

I3 Output file: sample.shl

```
#           CON1D V7.5 Slab Casting Heat Transfer Analysis
#           University of Illinois, Brian G. Thomas, 2002

# SHELL         Output Shell Temperature, Shrinkage Histories          SHL

#  Posi    time   LiqLoc SolLoc shell  Tsprime  Surf   EndWall  Endwall
#                                      Temp    Defl1   Defl2
#   mm      s      mm     mm    mm     C       C      mm       mm
#
    0.00   0.0000  0.00   0.00   0.00  1532.6  1532.6   0.000    0.000
  100.03   6.0019  6.50   5.39   5.98  1137.9  1231.0   6.436    7.575
  200.01  11.9995 10.24   8.71   9.45  1074.1  1151.4   7.782    9.960
  300.01  18.0000 13.01  11.34  12.25  1038.2  1106.3   8.540   11.411
……
  800.03  48.0049 23.50  20.97  22.37   960.3  1008.0  10.181   15.038
  900.00  54.0016 25.00  22.49  23.95  1154.4  1164.6   7.559   14.723
 1000.01  60.0003 26.50  23.79  25.43  1159.4  1179.6   7.307   14.587
```

I4 Output file: sample.mld

```
#           CON1D V7.5 Slab Casting Heat Transfer Analysis
#           University of Illinois, Brian G. Thomas, 2002

# MOLD                    Mold Output                    MLD

#   Z  Mold  TSurf      Mold Temp     Heatflux qcold  hwater    hmold   twater
#     thick          hot   hotcu  cold
#  mm   mm   Deg C       (Deg C)      MW/m^2  MW/m2   W/m^2K  W/m^2K   Deg C
#
   0.0 26.0  1532.6  307.0  244.3  109.8  4.076  1.495  18743.6   6678.2  30.00
 100.0 26.0  1231.0  349.4  317.9  147.7  2.049  2.064  17813.9   6491.9  31.87
 200.0 26.0  1151.4  283.7  258.5  122.7  1.637  1.651  18433.3   6572.4  33.17
 300.0 26.0  1106.3  248.3  226.6  109.9  1.412  1.418  18734.9   6610.3  34.25
……
 600.0 26.0  1035.0  197.6  181.1   92.8  1.069  1.071  19144.3   6660.6  36.86
 700.0 26.0  1020.3  187.9  172.5   89.7  1.001  1.002  19225.7   6670.4  37.60
 800.0 26.0  1008.0  179.8  165.3   87.8  0.944  0.955  19290.9   6678.2  38.29
```

I5 Output file: sample.gpt

```
#          CON1D V7.5 Slab Casting Heat Transfer Analysis
#          University of Illinois, Brian G. Thomas, 2002

# GAPT     Output Heat Transfer,Powder Layer Thicknesses Histories        GPT

# Z-dist   hrad     hcond     dsolid    dliquid    deff    dtotal    visc
#   (mm)  W/m^2K    W/m^2K     (mm)      (mm)      (mm)     (mm)     Poise
#
   0.0   1302.8     5693.7    0.237     0.212     0.052    0.448   0.218E+01
  100.0   930.3     6359.5    0.440     0.168     0.068    0.607   0.116E+02
  200.0   850.5     7276.7    0.611     0.135     0.071    0.746   0.226E+02
  300.0   808.5     8224.9    0.745     0.110     0.072    0.855   0.390E+02
……
  600.0   747.6    11829.2    1.056     0.052     0.075    1.108   0.201E+03
  700.0   736.0    13495.0    1.142     0.036     0.075    1.178   0.418E+03
  800.0   726.5    15551.8    1.223     0.021     0.076    1.244   0.121E+04
```

I6 Output file: sample.gpv

```
#          CON1D V7.5 Slab Casting Heat Transfer Analysis
#          University of Illinois, Brian G. Thomas, 2002

# GAPV        Output Powder Layer Consumption and Velocities          GPV

# Z-dist  qconsumpt   qosciltn   qliquid    qsolid    vliquid    vsolid
#  mm      m^2/s      m^2/s      m^2/s      m^2/s      m/s       m/s
#
   0.  0.2740E-05  0.141E-05  0.110E-05  0.237E-06  0.519E-02  0.100E-02
  100.  0.2740E-05  0.141E-05  0.894E-06  0.440E-06  0.533E-02  0.100E-02
  200.  0.2740E-05  0.141E-05  0.723E-06  0.611E-06  0.535E-02  0.100E-02
  300.  0.2740E-05  0.141E-05  0.588E-06  0.745E-06  0.535E-02  0.100E-02
……
  600.  0.2740E-05  0.141E-05  0.278E-06  0.106E-05  0.535E-02  0.100E-02
  700.  0.2740E-05  0.141E-05  0.191E-06  0.114E-05  0.535E-02  0.100E-02
```

I7 Output file: sample.spr

```
#          CON1D V7.5 Slab Casting Heat Transfer Analysis
#          University of Illinois, Brian G. Thomas, 2002

# SPRAY    Output Heat Transfer History in Spray Zones below Mold        SPR

# Z-dist   hnconv    hrad     hspray    hconv2    htot
#   (mm)   W/m^2K    W/m^2K   W/m^2K    W/m^2K    W/m^2K
#
  900.0     8.7     169.7      0.0      0.00     178.40
 1000.0     8.7     176.1    163.5      0.00     348.24
 1100.0     8.7     178.5    163.5      0.00     350.65
 1200.0     8.7     180.1    163.5      0.00     352.24
 1300.0     8.7     180.8    163.5      0.00     352.94
 1400.0     8.7     180.9    163.5      0.00     353.02
 1500.0     8.7     180.5    163.5      0.00     352.67
```

I8 Output file: sample.prf

```
#          CON1D V7.5 Slab Casting Heat Transfer Analysis
#          University of Illinois, Brian G. Thomas, 2002

# PROFILE   Temperature distribution and heat balance at mold exit        PRF


# Distance  Temperature  Super Heat  Sensible Heat  Latent Heat
#   mm       Deg C       kJ/m2       kJ/m2          kJ/m2
#
   0.0000    1008.0       0.6        602.8          501.4
   0.2500    1023.7       1.2       1174.0         1002.7
   0.7500    1039.2       1.2       1142.4         1002.7
   1.2500    1054.6       1.2       1110.8         1002.7
……
  48.7500    1532.6       0.0          0.0            0.0
  49.2500    1532.6       0.0          0.0            0.0
  49.7500    1532.6       0.0          0.0            0.0
```

I9 Output file: sample.shr

```
#          CON1D V7.5 Slab Casting Heat Transfer Analysis
#          University of Illinois, Brian G. Thomas, 2002

# Shear        Shear Stress in Gap                          SHR

# Z-dist     up axial       dn axial       max          min          Trans    Avg     Node1    Node9    Node17
# mm          Pa             Pa             Pa           Pa           Pa       Pa      Pa       Pa       Pa
#
   0.000   -0.5018E+02 -0.5018E+02  0.1286E+03 -0.5391E+02    0.0      58.7     97.6     33.8     -57.4
 100.032   -0.6134E+03 -0.1536E+04  0.9088E+03 -0.3191E+03    0.0     449.5    902.3    288.3    -325.7
 200.014   -0.2098E+04 -0.3020E+04  0.2197E+04 -0.7589E+03    0.0    1087.4   2188.0    710.0    -768.0
 300.015   -0.3584E+04 -0.4506E+04  0.4676E+04 -0.1607E+04    0.0    2316.2   4665.2   1523.6   -1618.0
……
 600.008    0.1894E+07 -0.8963E+04  0.5104E+05 -0.1749E+05    0.0   14088.2  17502.0  16760.8  -17501.0
 700.017    0.8386E+07 -0.1104E+07  0.1540E+06 -0.5275E+05    0.0   19012.9  20402.8  20402.8  -20402.8
 800.026    0.3665E+08 -0.9577E+07  0.7750E+06 -0.2655E+06    0.0   23304.0  23304.0  23304.0  -23304.0
# friction force in mold (N)
# 800.03                          76602.08  -26245.11        9334.9   12272.7    9083.1   -9237.5
```

I10 Output file: sample.tpr

```
#          CON1D V7.5 Slab Casting Heat Transfer Analysis
#          University of Illinois, Brian G. Thomas, 2002

# Taper        Output Taper Histories                          TPR

# Posi    EndWall   Endwall   WF      NF      Mold    Extra   IdealTpr  IdealTpr  IdealTpr
#         Defl-1s   Defl-2    Expn    Dstr    Dstr    Length  Def       Inst      Cumul
#  mm      mm        mm        mm      mm      mm      mm      mm        %/m       %/m
#
   0.00    0.000     0.000    -1.172  -2.343  -1.172   0.000   0.000     0.000     0.000
  100.03   6.436     7.575    -2.794  -5.588  -2.794   0.000   7.867     3.244    10.487
  200.01   7.782     9.960    -2.287  -4.575  -2.287   0.000   9.608     2.254     6.405
  300.01   8.540    11.411    -2.019  -4.039  -2.019   0.000  10.681     0.988     4.747
……
  600.01   9.732    13.960    -1.644  -3.287  -1.644   0.000  12.602     0.569     2.800
  700.02   9.976    14.539    -1.574  -3.147  -1.574   0.000  13.041     0.652     2.484
  800.03  10.181    15.038    -1.518  -3.037  -1.518   0.000  13.418     0.534     2.236
```

I11 Output file: sample.frc

```
#          CON1D V7.5 Slab Casting Heat Transfer Analysis
#          University of Illinois, Brian G. Thomas, 2002

# FRACTI        Output phase fractions:L,delta,gamma,alpha            FRC

# Posi        10.00mm below surface     |       shell surface
#  mm  Temp C  Liquid  Delta  Gamma  Alpha| Temp C  Liquid  Delta  Gamma  Alpha
#
   0. 1532.6   1.000  0.000  0.000  0.000  1532.6   1.000  0.000  0.000  0.000
  100. 1532.3   1.000  0.000  0.000  0.000  1231.0   0.000  0.000  1.000  0.000
  200. 1532.1   1.000  0.000  0.000  0.000  1151.4   0.000  0.000  1.000  0.000
  300. 1486.4   0.000  1.000  0.000  0.000  1106.3   0.000  0.000  1.000  0.000
……
  800. 1296.6   0.000  0.000  1.000  0.000  1008.0   0.000  0.000  1.000  0.000
  900. 1300.1   0.000  0.000  1.000  0.000  1164.6   0.000  0.000  1.000  0.000
 1000. 1318.1   0.000  0.000  1.000  0.000  1179.6   0.000  0.000  1.000  0.000
```

I12 Output file: sample.fxt

```
#          CON1D V7.5 Slab Casting Heat Transfer Analysis
#          University of Illinois, Brian G. Thomas, 2002

# FLUX                    Flux temperature Output              FXT

# Delta x=0.2mm
# Z          t1     T1      t2      T2      t3      T3      t4      T4      t9    Tsurf
# mm          s      C       s       C       s       C       s       C       s       C
#
 100.03  100.03  622.6   56.97  895.8    6.02  1129.7    6.00     0.0    6.00  1231.0
 200.01  200.01  501.9  156.94  720.2   51.59   938.4   12.00     0.0   12.00  1151.4
 300.01  300.01  436.6  256.96  624.8  151.59   813.1   21.91   993.7   18.00  1106.3
……
 600.01  600.01  340.1  556.95  482.6  451.63   625.2  307.19   767.7   36.01  1035.0
 700.02  700.02  321.3  656.96  454.8  551.64   588.2  407.20   721.6   42.01  1020.3
 800.03  800.03  305.7  756.97  431.6  651.65   557.6  507.21   683.5   48.00  1008.0
```

I13 Output file: sample.sst

```
#          CON1D V7.5 Slab Casting Heat Transfer Analysis
#          University of Illinois, Brian G. Thomas, 2002

# Shell        Outpput Steel Shell Temperature Below Surface          SST

# Posi  Surf    1     2     3     4     5     6     7     8     9    10
# mm     C     C     C     C     C     C     C     C     C     C     C
#       0.00  10.00  12.50  25.00  0.00  0.00  0.00  0.00  0.00  0.00  0.00
   0.0 1532.6 1532.6 1532.6 1532.6   0.0   0.0   0.0   0.0   0.0   0.0   0.0
 100.0 1231.0 1532.3 1532.4 1532.6   0.0   0.0   0.0   0.0   0.0   0.0   0.0
 200.0 1151.4 1532.1 1532.3 1532.6   0.0   0.0   0.0   0.0   0.0   0.0   0.0
 300.0 1106.3 1486.4 1532.0 1532.6   0.0   0.0   0.0   0.0   0.0   0.0   0.0
……
 800.0 1008.0 1296.6 1355.5 1532.2   0.0   0.0   0.0   0.0   0.0   0.0   0.0
 900.0 1164.6 1300.1 1346.0 1532.1   0.0   0.0   0.0   0.0   0.0   0.0   0.0
1000.0 1179.6 1318.1 1355.1 1529.9   0.0   0.0   0.0   0.0   0.0   0.0   0.0
```

I14 Output file: sample.sst

```
#          CON1D V7.5 Slab Casting Heat Transfer Analysis
#          University of Illinois, Brian G. Thomas, 2002

#SEGREGATION    Segr. Related Params. vs Dist. below Shell Surface        SEG

# Information only (not used in CON1D calculation)
#     Distance        tf          CR          SDAS        Tsol
#       mm          sec         K/sec         um          C

      0.0000       0.1500      111.9019      12.9697     1515.3097
      0.2500       0.4180       40.1561      21.5070     1515.3119
      0.7500       0.6520       25.7444      26.7830     1515.3129
      1.2500       0.6960       24.1171      27.6601     1515.3130
……
     22.2500       9.7107        1.7285     101.5632     1515.3182
     22.7500      10.2224        1.6420     104.1701     1515.3184
     23.2500      10.8900        1.5413     107.4738     1515.3185
# At 1000.04mm below meniscus, liquid still exists from 23.75mm below shell surface
```

I15 Output file: sample.liq

```
#          CON1D V7.5 Slab Casting Heat Transfer Analysis
#          University of Illinois, Brian G. Thomas, 2002

# Liquid Phase              Concentration Output                LIQ

# Information only (not used in CON1D calculation)
# Position: surface
#   Z   time    Temp    fl      C%      Si%     Mn%     P%      S%
#  mm  sec     Deg C
   0.5  0.03 1519.49 0.787  0.0604  0.3582  1.6059  0.0144  0.0188
   1.0  0.06 1517.24 0.578  0.0760  0.3798  1.7104  0.0180  0.0251
   1.5  0.09 1513.70 0.371  0.1020  0.4063  1.8436  0.0241  0.0374
   2.0  0.12 1508.45 0.203  0.1412  0.4332  1.9857  0.0337  0.0625
   2.5  0.15 1499.80 0.073  0.2012  0.4589  2.1287  0.0497  0.1307
   3.0  0.18 1486.54 0.002  0.2620  0.4753  2.2250  0.0680  0.3258
# From     3.5mm below meniscus only solid phase exists
```

I16 Output file: sample.sol

```
#          CON1D V7.5 Slab Casting Heat Transfer Analysis
#          University of Illinois, Brian G. Thomas, 2002

# Solid Phase               Concentration Output                SOL

# Information only (not used in CON1D calculation)
# Position: surface
#   Z   time   Temp    fs    fd    fg     C%     Si%     Mn%     P%     S%
#   mm    sec   Deg C
   0.5  0.03 1519.49 0.213 0.213 0.000  0.0115  0.2758  1.2204  0.0033  0.0009
   1.0  0.06 1517.24 0.422 0.422 0.000  0.0144  0.2924  1.2999  0.0041  0.0013
   1.5  0.09 1513.70 0.629 0.629 0.000  0.0194  0.3128  1.4011  0.0055  0.0019
   2.0  0.12 1508.45 0.797 0.797 0.000  0.0268  0.3336  1.5091  0.0077  0.0031
   2.5  0.15 1499.80 0.927 0.927 0.000  0.0382  0.3533  1.6178  0.0114  0.0065
   3.0  0.18 1486.54 0.998 0.998 0.000  0.0498  0.3660  1.6910  0.0157  0.0163
# From     3.5mm below meniscus only solid phase exists
```

REFERENCES

1. Irving, W.R.: *Continuous Casting of Steel*, The Institute of Materials, London, 1993.
2. "World Steel in Figures", *World Steel in Figures*, International Iron and Steel Institute, 2003
3. Tanner, A.H.: *Continuous Casting: A Revolution in Steel*, Write Stuff Enterprises, INC., 1998.
4. Huang, X. and Thomas, B.G.: "Modeling of Steel Grade Transition in Continuous Slab Casting Processes", *Metallurgical Transactions B (USA)*, 1993, vol. 24B (2), pp. 379-393.
5. Wolf, M.M.: "Mold Heat Transfer and Lubrication Control Two Major Functions of Caster Productivity and Quality Assurance", *Continuous Casting 1997*, vol. Volume 9: Initial Solidification and Strand Surface Quality of Peritectic Steels, ISS/AIME, Warrendale, PA, pp. 211-222, 1997
6. Pinheiro, C.A., Samarasekera, I.V. and Brimacombe, J.K.: "Mold Flux for Continuous Casting of Steel Part Xv: Heat Transfer", *Iron and Steelmaker (USA)*, 1995, vol. 22 (12), pp. 43-44.
7. Billany, T.J.H., Normanton, A.S., Mills, K.C. and Grieveson, P.: "Surface Cracking in Continuously Cast Producs", *Ironing and Steelmaking*, 1991, vol. 18 (6), pp. 403-410.
8. Meng, Y. and Thomas, B.G.: "Heat Transfer and Solidification Model of Continuous Slab Casting: Con1d", *Metall. Mater. Trans. B (USA)*, 2003, vol. 34B (5), pp. 685-705.
9. Najjar, F.M., Thomas, B.G. and Hershey, D.E.: "Numerical Study of Steady Turbulent Flow through Bifurcated Nozzles in Continuous Casting", *Metall. Mater. Trans. B (USA)*, 1995, vol. 26B (4), pp. 749-765.
10. Kubrik, B.I.: "Effects of Thermal and Physical Properties of Slag and Coefficients of Thermal Conductivity of Mould Walls on Heat Transfer in Mould", *Steel USSR*, 1987, vol. 17 (12), pp. 573-575.
11. Machingawuta, N.C., Bagha, S. and Grieveson, P.: "Heat Transfer Simulation for Continuous Casting", *Steelmaking Conference Proceedings*, (Washington, D.C., USA, 14-17 Apr. 1991), ISS, Warrendale, PA, 1991, pp. 163-170.
12. Cimarelli, T.: "Mould Powder Influence on Continuous Casting Operations and on Slabs Surface Quality", *Metallurgia Italiana (Italy)*, 1997, vol. 89 (9), pp. 31-37.
13. Takeuchi, E. and Brimacombe, J.K.: "The Formation of Oscillation Marks in the Continuous Casting of Steel Slabs", *Metall. Trans. B*, 1984, vol. 15B (3), pp. 493-509.

14. Pinheiro, C.A., Samarasekera, I.V. and Brimacombe, J.K.: "Mold Flux for Continuous Casting of Steel Part Xvii Mold Flux Related Defects", *Iron and Steelmaker (USA)*, 1996, vol. 23 (2), pp. 59-60.

15. Suzuki, M., Mizukami, H., Kitagawa, T., Kawakami, K., Uchida, S. and Komatsu, Y.: "Development of a New Mold Oscillation Mode for High-Speed Cc of Steel Slabs", *ISIJ International (Japan)*, 1991, vol. 31 (3), pp. 254-261.

16. Nakamori, Y., Fujikake, Y. and Tokiwa, K.: "Development of Friction Measuring System in a Continuous Casting Mold", *Tetsu-to-Hagane (J. Iron Steel Inst. Jpn.)*, 1984, vol. 70 (9), pp. 1262-1268.

17. DiLellio, J.A. and Young, G.W.: "Asymptotic Model of the Mold Region in a Continuous Steel Caster", *Metallurgical and Materials Transactions B: Process Metallurgy and Materials Processing Science*, 1995, vol. 26B (6), pp. 1225-1441.

18. Wolf, M.M.: "Review of Mould Fricrtion", *BHM*, 2000, vol. 145 (7), pp. 270-275.

19. Lawson, G.D., Sander, S.C., Emling, W.H., Moritra, A. and Thomas, B.G.: "Prevention of Shell Thinning Breakouts Associated with Widening Width Changes", *77th Steelmaking Conference*, (Chicago, IL, USA, 20-23 Mar. 1994), ISS/AIME, Warrendale, PA, 1994, pp. 329-336.

20. Thomas, B.G., Moitra, A. and McDavid, R.: "Simulation of Longitudinal Off-Corner Depressions in Continuously Cast Steel Slabs", *Iron and Steelmaker (USA)*, 1996, vol. 23 (4), pp. 57-70.

21. Thomas, B.G. and Ojeda, C.: "Ideal Taper Prediction for Slab Casting", *ISSTech Steelmaking Conference*, (Indianapolis, IN, USA, April 27-30, 2003), 2003, pp. 396-308.

22. Tony, W.A.: "Small Ticket Item Proving to Have Big Impact", *Iron and Steelmaker (USA)*, 1992, vol. 19 (4), pp. 17-20.

23. Mills, K.C.: "The Performance of Casting Powders", *Steel Technol. Int.*, 1994, pp. 161-166.

24. Nakato, H., Takeuchi, S., Fujii, T., Nozaki, T. and Washio, M.: "Characteristics of New Mold Fluxes for Strand Casting of Low and Ultra Low Carbon Steel Slabs", *Steelmaking Conference Proceedings*, (Washington, D.C., USA, 14-17 Apr. 1991), 1991, pp. 639-646.

25. Moore, J.A., Phillips, R.J. and Gibbs, T.R.: "An Overview for the Requirements of Continuous Casting Mold Fluxes", *Steelmaking Conference Proceedings*, (Washington, D.C., USA, 14-17 Apr. 1991), 1991, pp. 615-621.

26. Pinheiro, C.A., Samarasekera, I.V. and Brimacombe, J.K.: "Mold Flux for Continuous Casting of Steel Part V: Crystallization Temperature", *I&SM*, 1995, vol. 22 (2), pp. 37-39.

27. Bhamra, M.S., Charlesworth, M.G., Wong, S., Sawyers-Villers, D. and Cramb, A.W.: "Crystallization of Fluxes under Varying Cooling Rates", *54th Electric Furnace Conference*, (Dallas, Texas, USA, 9-12 Dec. 1996), ISS/AIME, Warrendale, PA, 1996, pp. 551-564.

28. Orrling, C., Cramb, A.W., Tilliander, A. and Kashiwaya, Y.: "Observations of the Melting and Solidification Behavior of Mold Slags", *Iron and Steelmaker (USA)*, 2000, vol. 27 (1), pp. 53-63.

29. O'Malley, R.J.: "Observations of Various Steady State and Dynamic Thermal Behaviors in a Continuous Casting Mold", *82nd Steelmaking Conference*, (Chicago, IL, USA, 21-24 Mar. 1999), ISS/AIME, Warrendale, PA, 1999, pp. 13-33.

30. Thomas, B.G., Ho, B. and Li, G.: "Heat Flow Model of the Continuous Slab Casting Mold, Interface, and Shell", *Alex McLean Symposium: Process Fundamentals, Liquid Metal Processing for Cleanliness, Novel and Conventional Casting, and Novel Process Technologies*, (Toronto, Ontario, Canada, 12-14 July 1998), Iron and Steel Society/AIME, Alex McLean Symposium Proceedings (USA), 1998, pp. 177-193.

31. Ho, B.: *Characterization of Interfacial Heat Transfer in the Continuous Slab Casting Process*, Master Thesis, UIUC, 1992.

32. Stone, D.T.: *Mathematical Modeling of Interfacial Heat Transfer in the Continuous Slab Casting Process*, M.S. Thesis, University of Illinois, Champaign-Urbana, 2000.

33. Nakato, H., Omiya, S., Habu, Y., Hamagami, K. and Koshikawa, T.: "Optimizing Mold Lubrication for High-Speed Continuous Casting of Slabs", *Journal of metals*, 1984, vol. 36 (3), pp. 44-50.

34. Thomas, B.G., O'malley, R.J., Shi, T., Meng, Y., Creech, D. and Stone, D.: "Validation of Fluid Flow and Solidification Simulation of a Continuous Thin-Slab Caster", *Modeling of Casting, Welding and Advanced Solidification Process IX*, (Aachen, Germany, Aug. 20-25, 2000), TMS, Warrendale, PA, 2000, pp. 769-776.

35. Thomas, B.G. and Morthland, T.: *3-D Heat Transfer Analysis of Columbus Slab Casting Mold*, Columbus Steel, Urbana, IL, 2001.

36. Park, J.K., Thomas, B.G. and Samarasekera, I.V.: "Analysis of Thermo-Mechnical Behavior in Billet Casting with Different Mold Cornerradii", *ironmaking and Steelmaking*, 2002, vol. 29 (5), pp. 359-375.

37. Lin, K.J. and Thomas, B.G.: "Thermal Stress Analysis of Bulging with Roll Misalignment for Various Slab Cooling Intensities", *China Steel Technical Report (Taiwan)*, 2002, vol. 16 (Dec.), pp. 9-14.

38. Thomas, B.G.: "Mathematical Modeling of the Continuous Slab Casting Mold: A State of the Art Review", *1991 Steelmaking Conference*, ISS, Warrendale, PA, 1991, pp. 69-82.

39. Thomas, B.G.: "Modeling of the Continuous Casting of Steel - Past, Present and Future", *Metall. Mater. Trans. B (USA)*, 2002, vol. 33B (6), pp. 795-812.

40. Thomas, B.G. and Zhang, L.: "Mathematical Modeling of Fluid Flow in Continuous Casting", *ISIJ International (Japan)*, 2001, vol. 41 (10), pp. 1181-1193.

41. Hills, A.W.D.: "A Generlized Intergral-Profile Method for the Analysis of Unidirectional Heat Flow During Solidification", *Transactions TMS-AIME*, 1969, vol. 245, pp. 1471-1479.

42. Mizikar, E.A.: "Mathematical Heat Transfer Model for Solidification of Continuosly Cast Steel Slabs", *AIME MET SOC TRANS*, 1967, vol. 239 (11), pp. 1747-1758.

43. Lait, J.E., Brimacombe, J.K. and Weinberg, F.: "Mathematical Modelling of Heat Flow in the Continuous Casting of Steel", *ironmaking and Steelmaking*, 1974, vol. 1 (2), pp. 90-97.

44. Grill, A., Sorimachi, K. and Brimacombe, J.K.: "Heat Flow, Gap Formation and Break-Outs in the Continuous Casting of Steel Slabs", *Metall. Trans. B*, 1976, vol. 7B (2), pp. 177-189.

45. Upton, E.A., Rao, T.R.S., Dauby, P.H. and Knechtges, R.C.: "Physical Metallurgy and Mathematical Modeling as Tools for Continuous Casting Optimization at Ltv Steel", *Iron Steelmaker*, 1988, vol. 15 (5), pp. 51-57.

46. Davies, R., Blake, N. and Campbell, P.: "Solidification Modelling--an Aid to Continuous Casting", *4th International Conference Continuous Casting. Preprints. Vol. 2*, (Brussels, Belgium, 17-19 May 1988), Verlag Stahleisen, P.O. Box 8229, D-4000, Dusseldorf 1, FRG, 1988, pp. 645-654.

47. Mahapatra, R.B., Brimacombe, J.K. and Samarasekera, I.V.: "Mold Behavior and Its Influence on Quality in the Continuous Casting of Steel Slabs. Ii. Mold Heat Transfer, Mold Flux Behavior, Formation of Oscillation Marks, Longitudinal Off-Corner Depressions, and Subsurface Cracks", *Metall. Trans. B*, 1991, vol. 22B (6), pp. 875-888.

48. Brimacombe, J.K.: "Design of Continuous Casting Machine Based on a Heat Flow Analysis: State-of-the-Art Review", *Canadian Metallurgical Quarterly*, 1976, vol. 15 (2), pp. 163-175.

49. Kristiansson, J.O.: "Thermomechanical Behavior of the Solidifying Shell within Continuous-Casting Billet Molds - a Numerical Approach", *Journal of Thermal Stresses*, 1984, vol. 7, pp. 209-226.

50. Moitra, A. and Thomas, B.G.: "Application of a Thermo-Mechanical Finite Element Model of Steel Shell Behavior in the Continuous Slab Casting Mold", *76th Steelmaking Conference*, (Dallas, TX, 28-31 Mar. 1993), ISS, Warrendale, PA, 1993, pp. 657-667.

51. Aboutalebi, M.R., Guthrie, R.I.L. and Hasan, M.: "Thermal Modelling and Stress Analysis in the Continuous Casting of Arbitrary Sections", *Steel Research*, 1994, vol. 65 (6), pp. 225-233.

52. Wimmer, F., Thone, H. and Lindorfer, B.: "Thermomechanically-Coupled Analysis of the Steel Solidification Process in the Continuous Casting Mold as a Basis for the Development of a High Speed Casting Mold", *Berg- und Huttenmannische Monatshefte (Austria)*, 1996, vol. 141 (5), pp. 185-191.

53. Nam, H., Park, H.S. and Yoon, J.K.: "Numerical Analysis of Fluid Flow and Heat Transfer in the Funnel Type Mold of a Thin Slab Caster", *ISIJ International (Japan)*, 2000, vol. 40 (9), pp. 886-892.

54. Choudhary, S.K. and Mazumdar, D.: "Mathematical Modelling of Transport Phenomena in Continuous Casting of Steel", *ISIJ International (Japan)*, 1994, vol. 34 (7), pp. 584-592.

55. Lee, J.E., Yeo, T.J., Oh, K.H., Yoon, J.K. and Yoon, U.S.: "Prediction of Cracks in Continuously Cast Steel Beam Blank through Fully Coupled Analysis of Fluid Flow, Heat Transfer, and Deformation Behavior of a Solidifying Shell", *Metallurgical and Materials Transactions A (USA)*, 2000, vol. 31A (1), pp. 225-237A.

56. Ohler, C., Odenthal, H.J., Pfeifer, H. and Lemanowicz, I.: "Numerical Simulation of the Fluid Flow and Solidification Phenomena in a Thin Slab Caster", *Stahl und Eisen (Germany)*, 2002, vol. 122 (3), pp. 55-63.

57. Flint, P.: "A Three-Dimensional Finite Difference Model of Heat Transfer Fluid Flow and Solidification in the Continuous Slab Caster", *Procedings of 73rd Steel Making Conference*, (Detroit, ISS/AIME, Warrendale, PA, 1990, pp. 481-490.

58. Thomas, B.G., Storkman, W.R. and Moitra, A.: "Optimizing Taper in Continuous Slab Casting Molds Using Mathematical Models", *IISC. The Sixth International Iron and Steel Congress*, (Nagoya, Japan, Oct 21-26, 1990), ISIJ, Tokyo, Japan, 1990, pp. 348-355.

59. Li, C. and Thomas, B.G.: "Analysis of the Potential Productivity of Continuous Cast Molds", *The Brimacombe Memorial Symposium*, (Vancouver, British Columbia, Canada, 1-4 Oct. 2000), Canadian Institute of Mining, Metallurgy and Petroleum, Montreal PQ, Canada, 2000, pp. 595-611.

60. Laitinen, E. and Neittaanmaki, P.: "On Numerical Simulation of the Continuous Casting Process", *Journal of Engineering Mathmatics*, 1988, vol. 22, pp. 335-354.

61. Huang, X., Thomas, B.G. and Najjar, F.M.: "Modeling Superheat Removal During Continuous Casting of Steel Slabs", *Metall. Mater. Trans. B (USA)*, 1992, vol. 23B (6), pp. 339-356.

62. Birat, J.P., Larrecq, M., Lamant, J.Y. and Petegnief, J.: "The Continuous Casting Mold: A Basic Tool for Surface Quality and Strand Productivity", *1991 Steelmaking Conference*1991), 1991, pp. 3-14.

63. Samarasekera, I.V. and Brimacombe, J.K.: "Thermal and Mechanical Behavior of Continous-Casting Billet Molds", *ironmaking and Steelmaking*, 1982, vol. 9 (1), pp. 1-15.

64. Thomas, B.G., Li, G., Moitra, A. and Habing, D.: "Analysis of Thermal and Mechanical Behavior of Copper Molds During Continuous Casting of Steel Slabs", *80th Steelmaking Conference*, (Chicago, IL, Iron and Steel Society, 1997, pp. 183-201.

65. Park, J.K., Samarasekera, I.V., Thomas, B.G. and Yoon, U.S.: "Analysis of Thermal and Mechanical Behavior of Copper Mould During Thin Slab Casting", *83rd Steelmaking Conference*, (Pittsburgh, PA, USA, 26-29 Mar. 2000), ISS/AIME, Warrendale, PA, 2000, pp. 9-21.

66. Mahapatra, R.B., Brimacombe, J.K., Samarasekera, I.V., Walker, N., Paterson, E.A. and Young, J.D.: "Mold Behavior and Its Influence on Quality in the Continuous Casting of Steel Slabs. I. Industrial Trials, Mold Temperature Measurements, and Mathematical Modeling", *Metall. Trans. B,* 1991, vol. 22B (6), pp. 861-874.

67. Pinheiro, C.A.M., Samarasekera, I.V. and Walker, B.N.: "Mould Heat Transfer and Continously Cast Billet Quality with Mould Flux Lubrication Part 1: Mould Heat Transfer", *Ironmaking and Steelmaking (UK),* 2000, vol. 27 (1), pp. 37-54.

68. Samarasekera, I.V. and Brimacombe, J.K.: "The Thermal Field in Continuous-Casting Moulds", *Canadian Metallurgical Quarterly,* 1979, vol. 18, pp. 251-266.

69. Gilles, H.L., Byrne, M., Russo, T.J. and DeMasi, G.A.: "The Use of an Instrumented Mold in the Development of High Speed Slab Casting", *Process Technology Conference Proceedings. Vol. 9. Use of Instrumentation to Optimize the Continuous Casting Process*, (Detroit, Michigan, USA, 25-28 Mar. 1990), Iron and Steel Society, 1990, pp. 123-138.

70. Kapaj, N., Pavlicevic, M. and Poloni, A.: "Exceeding the Casting Speed of Bloom Cc Machines by Three Times", *Steelmaking Conference*, (Baltimore, Maryland USA, March 25-28, 2001), 2001, pp. 67-78.

71. Li, C.: *Thermal-Mechanical Model of Solifying Steel Shell Behavior and Its Application in High Speed Continuous Casting of Billets*, Ph.D Thesis, University of Illinois, Urbana-Champaign, 2004.

72. Wolf, M.M.: "Mold Length in Slab Casting--a Review", *Iron and Steelmaker (USA),* 1996, vol. 23, pp. 47-51.

73. Dippenaar, R.J., Samarasekera, I.V. and Brimacombe, J.K.: "Mold Taper in Continuous Casting Billet Machines", *ISS Transactions,* 1986, (7), pp. 331-343.

74. Chandra, S., Brimacombe, J.K. and Samarasekera, I.V.: "Mould-Strand Interaction in Continuous Casting of Steel Billets. Iii. Mould Heat Transfer and Taper", *Ironmaking and Steelmaking (UK),* 1993, vol. 20 (2), pp. 104-112.

75. Park, J.K., Thomas, B.G., Samarasekera, I.V. and Yoon, U.S.: "Thermal and Mechanical Behavior of Copper Molds During Thin-Slab Casting. Ii. Mold Crack Formation", *Metall. Mater. Trans. B (USA),* 2002, vol. 33b (3), pp. 437-449B.

76. Samarasekera, I.V., Anderson, D.L. and Brimacombe, J.K.: "The Thermal Distortion of Continuous Casting Billet Molds", *Metall. Mater. Trans. B (USA)*, 1982, vol. 13 (March), pp. 91-104.

77. Wimmer, F., Thone, H. and Lindorfer, B.: "Thermomechanically-Coupled Analysis of the Steel Solidification Process as a Basis for the Development of a High Speed Billet Casting Mold", *The International Conference on Modelling and Simulation in Metallurgical Engineering and Materials Science*, (Beijing, China, 11-13, June 1996), Metallurgical Industry Press, Beijing, China, 1996, pp. 366-371.

78. Tiedje, N. and Langer, E.W.: "Metallographic Examination of Breakouts from a Continuous Billet Caster", *Scandinavian Journal of Metallurgy (Denmark)*, 1992, vol. 21 (5), pp. 211-217.

79. Bagha, S., Machingawuta, N.C. and Grieveson, P.: "Heat Transfer Simulation for Continuous Casting", *3rd International Conference on Molten Slags and Fluxes*, (Glasgow, UK, June 27-29, 1988), The Institute of Metals, 1 Carlton House Terrace, London SW1Y 5DB, UK, 1989, pp. 235-240.

80. Ohmiya, S., Tacke, K.H. and Schwerdtfeger, K.: "Heat Transfer through Layers of Casting Fluxes", *ironmaking and Steelmaking*, 1983, vol. 10 (1), pp. 24-30.

81. Ridolfi, M.R., Thomas, B.G., Li, G. and Foglia, U.D.: "The Optimization of Mold Taper for the Ilva-Dalmine Round Bloom Caster", *Rev. Metall., Cah. Inf. Tech. (France)*, 1994, vol. 91 (4), pp. 609-620.

82. Jenkins, M.S.: "Characterization of Heat Transfer in a Continuous Casting Mold", *Continuous Casting*, vol. 9, Initial Solidification and Strand Surface Quality of Peritectic Steels (USA), Iron and Steel Society/AIME, pp. 239-244, 1997

83. Riboud, P.V. and Larrecq, M.: "Lubrication and Heat Transfer in a Continuous Casting Mold", *Steelmaking Proceedings*, (Detroit, Mich., USA, TMS/AIME, 1979, pp. 78-92.

84. Kor, G.J.W.: "An Analysis of the Fluid Flow of Liquid Mold Powder in the Space between the Cc Mold and the Steel Shell", *Continuous Casting of Steel, 2nd Process Technology Conf.*, (Chicago, Ill., USA, 23-25 Feb. 1981), ISS/AIME, Warrendale, PA, 1981, pp. 124-132.

85. Bland, D.R.: "Flux and the Continuous Casting of Steel", *IMA Journal of Applied Mathematics*, 1984, vol. 32, pp. 89-112.

86. Hill, J.M. and Wu, Y.H.: "On a Nonlinear Stefan Problem Arising in the Continuous Casting of Steel", *Acta mech.*, 1994, vol. 107 (1-4), pp. 183-198.

87. Kelly, J.E., Michalek, K.P., O'Connor, T.G., Thomas, B.G. and Dantzig, J.A.: "Initial Development of Thermal and Stress Fields in Continuously Cast Steel Billets", *Metall. Trans. A*, 1988, vol. 19A (10), pp. 2589-2602.

88. Bommaraju, R. and Saad, E.: "Mathematical Modelling of Lubrication Capacity of Mold Fluxes", *73th Steelmaking Conference*, (Detroit, Michigan, USA, 25-28, Mar. 1990), ISS, Warrendale, PA, 1990, pp. 281-296.

89. Itoyama, S., Washio, M. and Nishikawa, H.: "Reduction of Friction Force in Mold and Prevention of Sticking Type Breakout for High Speed Cc of Slabs", *Tetsu-to-Hagane (J. Iron Steel Inst. Jpn.),* 1988, vol. 74 (7), pp. 1274-1281.

90. Hering, L. and Fenzke, H.W.: "On-Line Monitoring of Heat Flow Density in Slab Continuous Casting", *Stahl und Eisen (Germany),* 1992, vol. 112 (7), pp. 91-95.

91. Anzai, E., Shigezumi, T., Nakano, T., Ando, T. and Ikeda, M.: "Hydrodynamic Behavior of Molten Powder in Meniscus Zone of Continuous Casting Mold", *Nippon Steel Tech. Rep.,* 1987, (34), pp. 31-40.

92. Risteski, I.B.: "A Mathematical Model of the Movement of Molten Powder in the Vicinity of the Meniscus During the Continuous Casting of Steel", *Revista de Metalurgia (Spain),* 1992, vol. 28 (5), pp. 288-296.

93. Ogibayashi, S.: "Mathematical Modeling of Mold Powder Infiltration and Heat Extraction near Meniscus in Continuous Casting", *85th Steelmaking Conference,* (Nashville, TN, USA, 10-13 Mar. 2002), ISS/AIME, Warrendale, PA, 2002, pp. 175-183.

94. Yamauchi, A., Emi, T. and Seetharaman, S.: "A Mathematical Model for Prediction of Thickness of Mould Flux Film in Continuous Casting Mould", *ISIJ International (Japan),* 2001, vol. 42 (10), pp. 1084-1093.

95. Chavez, J.F., Celaya, A., Barron, M.A. and Morales, R.D.: "Heat Transfer in Mold Flux-Layers During Slab Continuous Casting", *Seventy Ninth Conference of the Steelmaking Division of the Iron and Steel Society,* (Pittsburgh, PA, USA, 24-27 Mar. 1996), ISS/AIME, Warrendale, PA, 1996, pp. 321-329.

96. Nakajima, K.: "Heat Transfer and Lubrication Behavior in Mold at High-Speed Continuous Casting of Steel Slabs", *Curr. Adv. Mater. Process.,* 1992, vol. 5 (4), pp. 1221-1224.

97. Hiraki, S., Nakajima, K., Murakami, T. and Kanazawa, T.: "Influence of Mold Heat Fluxes on Longitudinal Surface Cracks During High Speed Continuous Casting of Steel Slab", *77th Steelmaking Conference,* (Chicago, IL, USA, 20-23 Mar. 1994), ISS/AIME, Warrendale, PA, 1994, pp. 397-403.

98. Takashi, K., Sei, H., Masayuki, K., Ken, N., Kazuharu, H. and Toshihiko, M.: "Behavior of Lubrication and Heat Transfer in Mold at High Speed Continuous Casting", *Tetsu-to-Hagane (Journal of the Iron and Steel Institute of Japan) (Japan),* 1997, vol. 83 (11), pp. 701-706.

99. Riboud, P.V., Roux, Y., Lucas, L.D. and Gaye, H.: "Improvement of Continuous Casting Powders", *Fachberichte Huttenpraxis Metallweiterverarbeitung,* 1981, vol. 19 (8), pp. 859-869.

100. Lanyi, M.D. and Rosa, C.J.: "Viscosity of Casting Fluxes Used During Continuous Casting of Steel", *Metall. Trans. B,* 1981, vol. 12B (2), pp. 287-298.

101. Mills, K.C. and Sridhar, S.: "Viscosities of Ironmaking and Steelmaking Slags", *Ironmaking and Steelmaking (UK),* 1999, vol. 26 (4), pp. 262-268.

102. Nakato, H., Nozaki, T., Habu, Y. and Oka, H.: "Improvement of Surface Quality of Continuously Cast Slabs by High Frequency Mold Oscillation", *68th Steelmaking Conference*, (Detroit, Michigan, USA, 14-17 Apr. 1985), ISS/AIME, Warrendale, PA, 1985, pp. 361-365.

103. Schwerdtfeger, K. and Sha, H.: "Depth of Oscillation Marks Forming in Continuous Casting of Steel", *Metallurgical and Materials Transactions B (USA)*, 2000, vol. 31B (4), pp. 813-826B.

104. Singh, S.N. and Blazek, K.E.: "Heat Transfer and Skin Formation in a Continuous Casting Mold as a Function of Steel Carbon Content", *Journal of metals*, 1974, vol. 26 (10), pp. 17-27.

105. Thomas, B.G., O'Malley, R.J. and Stone, D.: "Measurement of Temperature, Solidification, and Microstructure in a Continuous Cast Thin Slab", *Modeling of Casting, Welding, and Advanced Solidification Processes VIII*, (San Diego, June 7-12, 1998), TMS, Warrendale, PA, 1998, pp. 1185-1199.

106. Badri, A.B. and Cramb, A.W.: "Heat Flux Calculation from Thermocouples-What Can Be Measured?" *85th Steelmaking Conference*, (Nashville, TN, USA, Mar. 10-13, 2002), Iron and Steel Society, 2002, pp. 65-76.

107. Brimacombe, J.K., Samarasekera, I.V., Walker, N., Bakshi, I., Bommaraju, R., Weinberg, F. and Hawbolt, E.B.: "Mould Behaviour and Solidification in the Continuous Casting of Steel Billets, Part I: Industrial Trials", *ISS Transactions*, 1984, vol. 5, pp. 70-78.

108. Bakshi, I.A., Brendzy, J.L., Walker, N., Chandra, S., Samarasekera, I.V. and Brimacombe, J.K.: "Mould--Strand Interaction in Continuous Casting of Steel Billets. I. Industrial Trials", *Ironmaking and Steelmaking (UK)*, 1993, vol. 20 (1), pp. 54-62.

109. Pinheiro, C.A.M.: *Mould Thermal Response, Billet Surface Quality and Mould-Flux Behavior in Billet Casting with Powder Lubrication*, PhD Thesis, UBC, 1997.

110. Ozgu, M.R. and Kocatulum, B.: "Thermal Analysis of the Burns Harbor No. 2 Slab Caster Mold", *76th Steelmaking Conference*, (Dallas, Texas, USA, 28-31 Mar. 1993), ISS, Warrendale, PA, 1993, pp. 301-308.

111. Jenkins, M.S., Thomas, B.G., Chen, W.C. and Mahapatra, R.B.: "Investigation of Strand Surface Defects Using Mold Instrumentation and Modelling", *1994 Steelmaking Conference*, (Chicago, IL, USA, 20-23 Mar. 1994), 1994, pp. 337-345.

112. Emling, W.H. and Dawson, S.: "Mold Instrumentation for Breakout Detection and Control", *74th Steelmaking Conference*, (Washington, D.C., USA, 14-17, Apr. 1991), ISS, Warrendale, PA, 1991, pp. 197-217.

113. Geist, G.A.: "Establishing Mold Thermal Stability and Lubrication During Continuous Casting of High Carbon Steel Grades", *83rd Steelmaking Conference*, (Pittsburgh, PA, USA, 26-29 Mar. 2000), ISS/AIME, Warrendale, PA, 2000, pp. 389-396.

114. Mairy, B., Ramelot, D. and Dutrieux, M.: "Mold Lubrication and Oscillation Monitoring for Optimizing Continuous Casting", *5th Process Technology Conference: Measurement and Control Instrumentation in the Iron and Steel Industry*, (Detroit, Michigan, USA, 14-17 Apr. 1985), ISS/AIME, Warrendale, PA, 1985, pp. 101-117.

115. Brendzy, J.L., Bakshi, I.A., Samarasekera, I.V. and Brimacombe, J.K.: "Mould--Strand Interaction in Cc of Steel Billets. Ii. Lubrication and Oscillation Mark Formation", *Ironmaking and Steelmaking (UK)*, 1993, vol. 20 (1), pp. 63-74.

116. Schergen, P., Houbart, M. and Heard, R.: "Vibromold, a Flexible Tool for Succcessful High Speed Casting of Sensitive Steel Grades", *3rd International Metallurgical Conference on CC of Billets*, (Trinec, Czech Republic, 26-27 Oct. 1999), Trinecke Zelezarny, Trinec, 739 70, Czech Republic, 1999, pp. 67-77.

117. Ozgu, M.R., Rego, D.N., Kocatulum, B., Simms, J.K., Fenicle, T.W., Burcaw, K.R., Bentley, W.T. and Idstein, D.J.: "Use of Instrumentation to Evaluate Mold Powders and Practices at the Burns Harbor No. 2 Slab Caster", *1st European Conference on Continuous Casting*, (Florence, Italy, Sept.23-25, 1991), Associazione Italiana di Metallurgia, Piazzale Rodolfo Morandi, 2, I-20121 Milano, Italy, 1991, pp. 73-82.

118. Gurton, R.M.: *Mould Response and Its Impact on Billet Quality*, PhD Thesis, UBC, 1997.

119. Cho, J., Shibata, H., Emi, T. and Suzuki, M.: "Thermal Resistance at the Interface between Mold Flux Film and Mold for Continuous Casting of Steels", *ISIJ International (Japan)*, 1998, vol. 38 (5), pp. 440-446.

120. Mills, K.C., Sridhar, S., Normanton, A.S. and Mallaband, S.T.: "Mould Flux Behaviour in Continuous Casting", *The Brimacombe Memorial Symposium*, (Vancouver, British Columbia, Canada, 1-4 Oct. 2000), Canadian Institute of Mining, Metallurgy and Petroleum, Montreal, PQ, Canada, 2000, pp. 781-794.

121. Chavez, J.F., Rodriguez, A., Morales, R. and Tapia, V.H.: "Laboratory and Plant Studies on Thermal Properties of Mold Powders", *Steelmaking Conference Proceedings*, (Nashville, Tennessee, USA, 2-5 Apr. 1995), ISS/AIME, Warrendale, PA, 1995, pp. 679-686.

122. Yamauchi, A., Sorimachi, K. and Yamauchi, T.: "Effect of Solidus Temperature and Crystalline Phase of Mould Flux on Heat Transfer in Continuous Casting Mould", *ironmaking and Steelmaking*, 2002, vol. 29 (3), pp. 203-207.

123. Watanabe, T., Fukuyama, H. and Nagata, K.: "Stability of Cuspidine (3cao2sio Sub 2 Caf Sub 2) and Phase Relations in the Caosio Sub 2 Caf Sub 2 System", *ISIJ International (Japan)*, 2002, vol. 42 (5), pp. 489-497.

124. Levin, E.M., Robbins, C.R. and McMurdie, H.F.: *Phase Diagram for Ceramists*, vol. 1, M.K. Reser, ed. The American Ceramic Society, Columbus, Ohio, 1964.

125. Pinheiro, C.A., Samarasekera, I.V. and Brimacombe, J.K.: "Mold Flux for Continuous Casting of Steel Part Iii: Mold Flux Properties", *I&SM*, 1994, vol. 21 (12), pp. 12-14.

126. Doremus, R.H.: *Glass Science*, John Wiley & Sons, Inc., New York, 1994.

127. Varshneya, A.K.: *Fundamentals of Inorganic Glasses*, Academic Press, Inc., San Diego, 1993.

128. Kingery, W.D., Bowen, H.K. and Uhlmann, D.R.: *Introduction to Ceramics*, 2nd ed., John Wiley & Sons, New York, 1975.

129. Turkdogan, E.T.: *Physicochemical Properties of Molten Slags and Glasses*, The metal society, London, 1983.

130. Koyama, K., Nagano, Y., Nagano, K. and Nakano, T.: "Design for Chemical and Physical Properties of Continuous Casting Powders", *Nippon Steel Tech. Rep.*, 1987, vol. 34, pp. 41-47.

131. Jenkins, M.S.: *Heat Transfer in the Continuous Casting Mould*, Ph D Thesis, Monash University, Australia, 1998.

132. Pinheiro, C.A., Samarasekera, I.V. and Brimacombe, J.K.: "Mold Flux for Continuous Casting of Steel Part Ii: Chemical Composition of Mold Fluxes", *I&SM*, 1994, vol. 21 (11), p. 62.

133. Sardemann, J. and Schrewe, H.: "The Influence of Casting Powder on the Formation of Cracks in Continuous Slab Casting", *74th Steelmaking Conference*, (Washington, D.C., USA, Apr. 14-17, 1991), Iron and Steel Society, Inc., 410 Commonwealth Dr., Warrendale, Pennsylvania 15086, USA, 1991, pp. 719-728.

134. Terada, S., Ryu, K., Kaneko, S. and Mitsumune, T.: "Development of a New Type of Viscometer and Estimation of Viscosity and Solidifying Point by Calculation Formula", *Steelmaking Conference*, (Chicago, IL, USA, 20-23 Mar. 1994), Iron and Steel Society/AIME (USA), 1994, pp. 457-459.

135. Lee, I.R., Kim, J.W., Choi, J., Kwon, O.D. and Shin, Y.K.: "Development of Mould Powder for High Speed Continuous Casting", *Conference on Continuous Casting of Steel in Developing Countries*, (Beijing, China, 14-18 Sept. 1993), Chinese Society of Metals, 1993, pp. 814-822.

136. Sridhar, S., Mills, K.C., Afrange, O.D.C., Lorz, H.P. and Carli, R.: "Break Temperatures of Mould Fluxes and Their Relevance to Continuous Casting", *Ironmaking and Steelmaking (UK)*, 2000, vol. 27 (3), pp. 238-242.

137. Taylor, R. and Mills, K.C.: "Physical Properties of Casting Powders Iii: Thermal Conductivities of Casting Powders", *Ironmaking and Steelmaking (UK)*, 1988, vol. 15 (4), pp. 187-194.

138. Stone, D.T. and Thomas, B.G.: "Measurement and Modeling of Heat Transfer across Interfacial Mold Flux Layers", *Canadian Metallurgical Quarterly (Netherlands)*, 1999, vol. 38 (5), pp. 363-375.

139. Susa, M., Mills, K.C., Richardson, M.J., Taylor, R. and Stewart, D.: "Thermal Properties of Slag Films Taken from Continuous Casting Mould", *Ironmaking and Steelmaking (UK)*, 1994, vol. 21 (4), pp. 279-286.

140. Yamauchi, A., Sorimachi, K., Sakuraya, T. and Fujii, T.: "Heat Transfer between Mold and Strand through Mold Flux Film in Continuous Casting of Steel", *ISIJ International (Japan)*, 1993, vol. 33 (1), pp. 140-147.

141. Wang, Q., Xie, B. and Chi, J.: "Study on Cc Fluxes with High Basic and High Glassy Properties", *Conference on Continuous Casting of Steel in Developing Countries*, (Beijing, China, 14-18 Sept. 1993), Chinese Society of Metals, Beijing, China, 1993, pp. 842-851.

142. Watanabe, K., Suzuki, M., Murakami, K., Kondo, H., Miyamoto, A. and Shiomi, T.: "The Effect of Mold Powder Crystallization on Heat Transfer in Continuous Casting Mold", *NKK Technical Review (Japan)*, 1997, vol. 77, pp. 20-26.

143. Kashiwaya, Y., Cicutti, C.E. and Cramb, A.W.: "An Investigation of the Crystallization of a Continuous Casting Mold Slag Using the Single Hot Thermocouple Technique", *ISIJ International (Japan)*, 1998, vol. 38 (4), pp. 357-365.

144. Orrling, C., Sridhar, S. and Cramb, A.W.: "In Situ Observation of the Role of Alumina Particles on the Crystallization Behavior of Slags", *ISIJ International (Japan)*, 2000, vol. 40 (9), pp. 877-885.

145. Seetharaman, S.: "Chapter 2: Pertinent Properties for Metals and Slags in Continuous Casting", *The Making, Shaping and Treationg of Steel 11th Ed.*, vol. Casting, AISE Steel Foundation, 2003

146. Kashiwaya, Y., Cicutti, C.E. and Cramb, A.W.: "Crystallization Behavior of Mold Slags", *Steel Making Conference*, 1998, pp. 185-191.

147. Cramb, A.W., Orrling, C., Fang, Y., Phinichka, N. and Sridhar, S.: "Observing and Measuring Solidification Phenomena at High Temperatures", *JOM (USA)*, 1999, vol. 51 (7), p. 11.

148. Orrling, C., Tilliander, A., Kashiwaya, Y. and Cramb, A.W.: "Melting and Solidification of Mold Slags", *82nd Steelmaking Conference*, (Chicago, IL, USA, Mar. 1999), Iron and Steel Society/AIME, 1999, pp. 417-424.

149. Orrling, C., Sridhar, S., Kashiwaya, Y. and Cramb, A.W.: "Crystallization Phenomenon in Slags", *58th Electric Furnace Conference and 17th Process Technology Conference*, (Orlando, FL, USA, 12-15 Nov. 2000), ISS/AIME, Warrendale, PA, 2000, pp. 211-221.

150. Tsutsumi, K., Ohtake, J.I., Nagasaka, T. and Hino, M.: "Crystallization Behavior of Li2o-Sio2, Na2o-Sio2 and Na2o-Cao-Sio2 Galsses", *Tetsu-to-Hagane (J. Iron Steel Inst. Jpn.)*, 1998, vol. 84 (6), pp. 464-469.

151. Larson, D.: "Criteria for Selecting Mold Powders to Optimize Continuous Cast Steel Quality", *Industrial Heating*, 1986, vol. 53 (4), pp. 16-17.

152. Lanyi, M.D. and Rosa, C.J.: "Casting Fluxes: Physical Properties Affecting Strand Lubrication", *ironmaking and Steelmaking*, 1982, vol. 9 (1), pp. 25-31.

153. Lin, K.J. and Chung, Y.H.: "Selection of Casting Powder", *China Steel Technical Report (Republic of China)*, 1992, (6), pp. 71-79.

154. Sankaranarayanan, S.R. and Apelian, D.: "Evaluation of Mold Powder Performance Via Crystallization Analysis", *Steelmaking Conference Proceedings*, (Toronto, Ontario, Canada, 5-8 Apr. 1992), Iron and Steel Society, 1992, pp. 607-625.

155. Kishimoto, M., Maeda, M. and Kawai, Y.: "Thermal Conductivity and Specfic Heat of Metallurgical Slags", 1984, pp. 891-905.

156. Wolf, M.M.: "On the Interaction between Mold Oscillation and Mold Lubrication", *Electric Furnace Conference Proceedings*, (Kansas City, Mo., U.S.A., 7-10 Dec. 1982), 1983, pp. 335-346.

157. Ogibayashi, S., Mukai, T. and Mimura, Y.: "Mold Powder Technology for Continuous Casting of Low-Carbon Aluminium-Killed Steel", *Nippon Steel Tech. Rep.*, 1987, (34), pp. 1-10.

158. Mills, K.C.: "Chapter 8: Mold Powders for Continuos Casting", *The Making, Shaping and Treationg of Steel 11th Ed.*, vol. Casting, AISE Steel Foundation, 2003

159. Harste, K.: *Investigation of the Shinkage and the Origin of Mechanical Tension During the Solidification and Successive Cooling of Cylindrical Bars of Fe-C Alloys*, PhD Dissertation Thesis, Technical University of Clausthal, 1989.

160. Kagawa, A. and Okamoto, T.: "Influence of Alloying Elements on Temperature and Composition for Peritectic Reaction in Plain Carbon Steels", *Mater. Sci. Technol.*, 1986, vol. 2 (10), pp. 997-1008.

161. Won, Y.M. and Thomas, B.G.: "Simple Model of Microsegregation During Solidification of Steels", *Metallurgical and Materials Transactions A (USA)*, 2001, vol. 32A (7), pp. 1755-1767.

162. Pehlke, R.D., Jeyarajan, A. and Wada, H.: *Summary of Thermal Properties for Casting Alloys and Mold Materials*, Univ. of Michigan, Ann Arbor, 1982.

163. Poirier, D.R. and Geiger, G.H.: *Transport Phenomena in Materials Processing*, TMS, 1994, p. 339.

164. Shibata, H., Kondo, K. and Suzuki, M.: "Thermal Resistance between Solidifying Steel Shell and Continuous Casting Mold with Intervening Flux Film", *ISIJ Int. (Japan)*, 1996, vol. 35 (Suppl.), pp. S179-S182.

165. Ichikawa, K., Morita, A. and kawabe, Y.: "Behavior of Powder Slag Film and Influence of Powder Slag on Mold Heat Transfer Rate", *Shinagawa Technical Report*, 1993, vol. 36, pp. 99-107.

166. Mikrovas, A.C., Argyropoulos, S.A. and Sommerville, I.D.: "Measurements of the Effective Thermal Conductivity of Liquid Slags", *Iron and Steelmaker (USA)*, 1991, vol. 18 (12), pp. 51-61.

167. *Matlab6.1 Users Manual*, The Mathworks, Inc., Natick, MA, 2001.

168. *Ansys6.1 Users Manual*, ANSYS, Inc., Canonsburg, PA, 2002.

169. Watzinger, J. and Flick, A.: "Online Mold Friction Monitoring System in Continuous Casting", *84th Steelmaking Conference*, (Baltimore, MD, USA, 25-28 Mar. 2001), ISS/AIME, Warrendale, PA, 2001, pp. 205-213.

170. Carslaw, H.S. and Jaeger, J.C.: *Conduction of Heat in Solids*, 2nd ed., Oxford University Press, 1986.

171. Thomas, B.G. and Meng, Y.: *Con1d Users Manual*, University of Illinois, 2002.

172. Burmesiter, L.C.: *Convective Heat Transfer*, 2 ed., Wiley, New York, 1993, p. 484.

173. Sleicher, C.A. and Rouse, M.W.: "A Convenient Correlation for Heat Transfer to Constant and Variable Property Fluids in Turbulent Pipe Flow", *International Journal of Heat & Mass Transfer*, 1975, vol. 18 (5), pp. 677-683.

174. Dittus, F.W. and Boelter, L.M.K.: "Heat Transfer in Automobile Radiators of the Tubular Type", *University of California Publications in Engineering*, 1930, (2), pp. 443-461.

175. Langeneckert, M.M.: *Influence of Mold Geometry on Heat Transfer, Thermocouple and Mold Temperatures in the Continuous Casting of Steel Slabs*, Master Thesis, University of Illinois, Champaign-Urbana, 2001.

176. Brimacombe, J.K., Agarwal, P.K., Hibbins, S., Prabhaker, B. and Baptista, L.A.: "Spray Cooling in the Continuous Casting of Steel", vol. 2, Continuous Casting, ISS/AIME, Warrendale, PA, pp. 109-123, 1984

177. Nozaki, T.: "A Secondary Cooling Pattern for Preventing Surfcace Cracks of Continuous Casting Slab", *Trans. ISIJ*, 1978, vol. 18, pp. 330-338.

178. Hardin, R.A., Shen, H. and Beckermann, C.: "Heat Transfer Modeling of Continuous Steel Slab Caster Using Realistic Spray Patterns", *Modelling of Casting, Welding and Advanced Solidification Processes IX*, (Aachen, Germany, 20-25 Aug. 2000), TMS, Warrendale, PA, 2000, pp. 729-736.

179. Pehlke, R.D.: "Computer Simulation of Continuous Casting", *Enginneering Summer Conference: Continuous Casting of Steel*May 17-23, 1980), Univ. of Michigan, Ann Arbor, MI, 1980, pp. Section VII, 1-17.

180. Voller, V.R., Swaminathan, C.R. and Thomas, B.G.: "Fixed Grid Techniques for Phase Change Prolems: A Review", *International Journal for Numerical Methods in Engineering*, 1990, vol. 30, pp. 875-898.

181. Sturgill, D.: "Stollberg, Inc Mold Powder Chemical Properties", *private communication*, 2001.

182. O'Malley, R.J.: "Metallurgica Mold Powder Chemical Properties", *private communication*, 1999.

183. Jenkins, M.S., Thomas, B.G. and mahapatra, R.B.: "Investigation of Strand Surface Defects Using Mold Instrumentation and Modeling", *ironmaking and Steelmaking*, 2003, (submitted).

184. McCauley, W.L. and Apelian, D.: "Temperature Dependence of the Viscosity of Liquids", *Proceeding of 2nd International Symposium on Metallurgical Slags and Fluxes*, Meallurigical Society of AIME, Warrendale, PA, 1984, pp. 925-947.

185. "Hight Temperature Pin-on_Disc Tribology Apparatus Manual", Advanced Mechanical Technology, INC., 1988

186. Lui, D.T.K.: *Effect of Oscillation Marks on Heat Transfer in Continuous Casting Molds*, Master Thesis, UIUC, 1995.

187. Sliney, H.E. and Dellacorte, C.: "Friction and Wear of Ceramic/Ceramic and Ceramic/Metal Combinations in Sliding Contact", *Lubrication Engineering*, 1994, vol. 50 (7), pp. 571-576.

188. Jenkins, M.S.: "Characterisation and Modification of the Heat Transfer Performance of Mold Powders", *Steelmaking Conference Proceedings*, (Nashville, Tennessee, USA, 2-5 Apr. 1995), ISS/AIME, Warrendale, PA, 1995, pp. 669-677.

189. Emi, M.: "The Mechanisms for Sticking Type Break-Outs and New Developments in Continuous Casting Mold Fluxes", *Steelmaking Conference Proceedings*, (Washington, D.C., USA, 14-17 Apr. 1991), 1991, pp. 623-630.

190. Kyoden, H., Doihara, T. and Nomura, O.: "Development of Mold Powders for High Speed Continuous Casting of Steel", *Steelmaking Proceedings*, (Washington, D.C., USA, 6-9 Apr. 1986), 1986, pp. 153-159.

191. Nakato, H., Sakuraya, T., Nozaki, T., Emi, T. and Nishikawa, H.: "Physical and Chemical Properties of Casting Powders Affecting the Mold Lubrication During Continuous Casting", *Steelmaking Proceedings*, (Washington, D.C., USA, 6-9 Apr. 1986), 1986, pp. 137-143.

192. Prasad, A. and Henein, H.: "Cct Diagram for Mold Flux Crystallization Studies", *ISSTech 2003*, (Indianapolis, IN, April 27~30), 2003, pp. 257-262.

193. Prasad, A., Henein, H. and Gandin, C.A.: "A Study of Microsegregation in Al-Cu Alloys Using Impulse Atomization as an Rsp", *Light Metals 2002 Métaux Légers*, (Montreal, Quebec, Canada, 11-14 Aug. 2002), 2002, pp. 101-114.

194. Mills, K.C., Olusanya, A., Brooks, R., Morrell, R. and Bagha, S.: "Physical Properties of Casting Powders. Iv. Physical Properties Relevant to Fluid and Thermal Flow", *ironmaking and Steelmaking*, 1988, vol. 15 (5), pp. 257-264.

195. Watanabe, T., Fukuyama, H., Susa, M. and Nagata, K.: "Phase Diagram Cuspidine (3cao2sio Sub 2 Caf Sub 2)-Caf Sub 2", *Metallurgical and Materials Transactions B (USA)*, 2000, vol. 31B (6), pp. 1273-1281B.

196. Hardin, R.A., Liu, K. and Beckermann, C.: "Development of a Model for Transient Simulation and Control of Continous Steel Slab Caster", *Materials Processing in the Computer Age*, 2000, vol. 3, pp. 61-74.

197. Grieveson, P., Bagha, S., Machingawuta, N., Liddell, K. and Mills, K.C.: "Physical Properties of Casting Powders. Ii. Mineralogical Constitution of Slags Formed by Powders", *Ironmaking Steelmaking*, 1988, vol. 15 (4), pp. 181-186.

198. O'malley, R.J.: "Glass Film Isothermal Aging Study", *private communication*, 2003.

199. *Polarized Light Microscopy*, Lerner Research Institute, 2003, http://www.lerner.ccf.org/bme/valve/techniques/polarized_light.php.

200. Jenkins, M.S. and Thomas, B.G.: "An Investigation of Some Mold Powder Related Startup Problems", *Steelmaking Conference Proceeding 1997*, (Chicago, IL, USA, 13-16 Apr. 1997), ISS/AIME, Warrendale, PA, 1997, pp. 285-293.

201. Thomas, B.G., Lui, D. and Ho, B.: "Effect of Transverse Depressions and Oscillation Marks on Heat Transfer in the Continuous Casting Mold", *Sensors and Modeling in Materials Processing: Techniques and Applications*, (Orlando, Florida, USA, Minerals, Metals and Materials Society/AIME, 420 Commonwealth Dr., P.O. Box 430, Warrendale, PA 15086, USA, 1997, pp. 117-142.

202. Collur, M.M.: *Use of Con1d Model to Determine If the Casting Speed Can Be Increased for Chrome-Nickel Grades at 8-3 Caster*, Allegheny Ludlum Corporation Technical Center, Brackenridge, PA, 1996.

203. Paidipati, J., Sharos, B., Slayton, C. and Wood, J.: *Thin-Slab Continuous Casting Mold Taper Design*, University of Illinois, Champaign-Urbana, 2002.

204. Park, J.K.: *Thermo-Mechanical Phenomena in High Speed Continuous Casting Processes*, PhD Thesis, University of British Columbia, Vancouver, BC, Canada, 2002.

205. Thomas, B.G.: "Modeling Study of Intermixing in Tundish and Strand During a Continuous-Casting Grade Transition", *79th Conference of the Steelmaking Division of the Iron and Steel Society*, (Pittsburgh, PA, USA, 24-27 Mar. 1996), ISS/AIME, Warrendale, PA, 1996, pp. 519-531.

206. Sobolewski, R., Sander, S.C., Kuczma, J.G. and Rumler, A.J.: "An Experimental, Instrumented Mold for Heat Transfer and Operating Conditions Study", *Steelmaking Conference Proceedings*, (Detroit, Michigan, USA, 25-28 Mar. 1990), ISS, Warrendale, PA, 1990, pp. 275-280.

207. Moitra, A.: *Thermo-Mechanical Model of the Steel Shell Behavior in Continuous Slab Casting*, PhD Thesis, University of Illinois, Urbana-Chamapign, 1993.

208. Gaskell, D.R.: *Ann Introduction to Transport Phenomena in Materials Engineering*, Macmillan Publishing Co., 1992, p. 210.

209. Tsutsumi, K., Murakami, H., Nishioka, S.I., Tada, M., Nakada, M. and Komatsu, M.: "Estimation of Mold Powder Consumption in Continuous Casting", *Tetsu-to-Hagane (Journal of the Iron and Steel Institute of Japan) (Japan)*, 1998, vol. 84 (9), pp. 617-624.

210. Abratis, H., Hofer, F., Junemann, M., Sardemann, J. and Stoffel, H.: "Heat Transfer at the Continuous Casting Permanent Mold for Different Slag Producing Powder Additives", *Stahl und Eisen (Germany)*, 1996, vol. 116 (9), pp. 73-78.

211. Yamauchi, A.: *Heat Transfer Phenomena and Mold Flux Lubrication in Continuous Casting of Steel*, PhD Thesis, Royal Institute of Technology, Stockholm, Sweden, 2001.

212. Cho, J.W., Emi, T., Shibata, H. and Suzuki, M.: "Heat Transfer across Mold Flux Film in Mold During Initial Solidification in Continuous Casting of Steel", *ISIJ International (Japan)*, 1998, vol. 38 (8), pp. 834-842.

213. Konishi, J., Militzer, M., Brimacombe, J.K. and Samarasekera, I.V.: "Modeling the Formation of Longitudinal Facial Cracks During Continuous Casting of Hypoperitectic Steel", *Metallurgical and Materials Transactions B (USA)*, 2002, vol. 33B (3), pp. 413-423B.

214. *Crc Handbook of Chemistry and Physics*, R.C. Weast, ed. the Chemical Rubber Co., Cleveland, Ohio, 1971.

215. Hamagami, K., Sorimachi, K., Kuga, M., Koshikawa, T. and Saigusa, M.: "Studies on Quality Improvement in Strand Cast Slabs at Chiba Works", *Steelmaking Conference*, 1982, pp. 358-364.

216. Okazaki, T., Tomono, H., Ozaki, K. and Akahane, H.: "Effect of Short Stroke High Cycle Oscillation on the Strand Surface Quality", *Tetsu-to-Hagane (J. Iron Steel Inst. Jpn.)*, 1982, vol. 68 (10), p. 265.

217. Inagaki, M.: "Improvement Technology of Surface Quality at Velocity Change", *CAMP-ISIJ*, 1989, (2), p. 309.

218. Lorento, D.P.: *Internal Report*, Accumold, Ontario Canada, 2001.

219. Nagata, K. and Goto, K.S.: "Heat Conductivity and Mean Free Path of Phonons in Metallurgical Slags", 1984, pp. 875-889.

220. O'Malley, R.J.: *private communication*, 2003.

221. O'Malley, R.J. and Neal, J.: "An Examination of Mold Flux Film Structures and Mold Gap Behavior Using Mold Thermal Monitoring and Petrographic Analysis at Armco's Mansfield Operations", *Proc. METEC Congress 99*, (Dusseldorf, Germany, 13-15 June, 1999), Verein Deutscher Eisenhuttenleute, Dusseldorf, Germany, 1999, pp.

222. *Crc Materials Science and Engineering Handbook*, 2 ed., J.F. Shackelford, ed. CRC press, 1994.

223. *Specific Heat Capacities for Different Solids*, The Engineering ToolBox, 2004, http://www.engineeringtoolbox.com/24_154.html.

VITA

Ya Meng was born in Jiangxi, China on Jun 17, 1974. She graduated from Central South University of Technology, Changsha, China with a bachelor degree in 1995 and a master degree in 1998, both in Materials Science and Engineering.

In the Fall of 1998, Ya began pursuing her Ph. D in the Department of Materials Science and Engineering at the University of Illinois at Urbana-Champaign. Under the guidance of Professor Brian G. Thomas, she worked on modeling continuous casting of steel. Her research interests are in the area of computational and experimental materials processing, heat transfer and finite element analysis.